

RESONANCE COMPENSATION STUDIES AT THE FNAL RECYCLER RING

By

Cristhian Gonzalez-Ortiz

A DISSERTATION

Submitted to  
Michigan State University  
in partial fulfillment of the requirements  
for the degree of

Physics—Doctor of Philosophy

2024

## ABSTRACT

Circular accelerators, such as the ones in the Fermilab Accelerator Complex, are indispensable tools driving scientific discovery by propelling particles to high energies and high intensities. In the context of the Proton Improvement Plan II (PIP-II) at Fermilab, the Recycler Ring (RR) is confronted with the challenge of high-intensity operation. The space charge tune shifts at these intensities necessitate the mitigation of third-order resonances. By measuring the Resonance Driving Terms (RDTs) for each resonance line, their strengths and damaging effects can be quantified.

The study is focused on the utilization of dedicated normal and skew sextupoles for the compensation of these resonance lines. By employing the response matrix method to measure the Resonance Driving Terms (RDTs) relative to the currents in these sextupoles, a methodical approach to simultaneously compensate individual and multiple third-order resonances has been developed and assessed. The assessment and verification incorporate mapping out beam losses through dynamic and static tune scans, along with the utilization of the Ion Profile Monitor (IPM) system for beam size measurements.

Furthermore, optimization algorithms have been explored and incorporated into the resonance compensation scheme. Parallel, to the work done at Fermilab, the study extends its scope by performing related experiments at the CERN Proton Synchrotron Booster (PSB). For these experiments, multiple resonance lines in the tune diagram were compensated by optimizing the currents in the compensation elements with the aid of advanced optimization algorithms.

High-intensity operation of the Recycler Ring involves understanding the interplay between the space charge tune spread, resonance lines, and specialized subsystems such as transverse dampers. The following study also delves into experiments that try to discern each of these phenomena, while highlighting challenges still ahead. Overall, these studies indicate the feasibility of compensating for multiple third-order resonances, contributing to the objectives of PIP-II for the reliable delivery of a 1.2 MW proton beam to experimental facilities.

## ACKNOWLEDGEMENTS

I would like to acknowledge Dr. Robert Ainsworth for taking those couple of nutmegs when we played footy together. Thank you, Rob, for making me a better scientist and teaching me so many valuable life lessons. Thank you for always having my back.

I would like to acknowledge the instrumental role of Dr. Peter Ostroumov in these years of my Ph.D. at Michigan State University. Thank you, Peter, for pushing me to be a better physicist and scientist, every day. Thank you for believing in me, even in the moments I didn't believe in myself.

Thank you to the members of my doctoral committee, Steve Lund, Yue Hao, Paul Gueye and Kendall Mahn. I truly value every comment and every word of encouragement at all of our meetings. We did not meet frequently, but your guidance was crucial through this process. Also thank you to whole support network at MSU and FRIB—these are institutions where you will never feel alone and always have someone support you when needed.

I would like to acknowledge the whole MI/RR department at Fermilab. Thank you, Kyle, Adam, Nino, Osama, Betiay, Denton, Marty, Mike, Phil, MaryKate, Matilda and Meiqin, and whoever I might have left out. Thank you for having the patience and your unconditional support while I pushed through with my experiments. You guys always had a smile even when I asked the most basic questions. Special acknowledgement to the operations team at Fermilab for always being open to questions and discussion. Thank you for having the patience to withstand me when I would continuously trip the permit on beam losses. I would also like to acknowledge the hospitality and awesomeness of our CERN collaborators, specially Foteini and Tirsi.

Luisa. Tú has sido el soporte y la inspiración estos últimos años para poder estar a puertas de cruzar la meta. Gracias por siempre estar ahí y no rendirte nunca con lo nuestro. Vamos a lograr grandes cosas juntos. Ya casi adoptamos un perrito, manguitos szah.

Gracias a toda mi familia, incluyendo a esos amigos que considero mi familia, por apoyarme en este camino. Desde Bogotá hasta llegar a Chicago pasando por Lansing. Nunca pensé en llegar tan lejos de la loma. No hubiera podido terminar este doctorado sin el apoyo de todos ustedes. Gracias por estar ahí en cada momento de mi vida. Thank you, Sjuju, the great celestial whale overseer.

## TABLE OF CONTENTS

LIST OF ABBREVIATIONS . . . . .	vi
CHAPTER 1: INTRODUCTION . . . . .	1
1.1: Circular Accelerators and Storage Rings . . . . .	2
1.2: Fermilab . . . . .	3
1.3: Outline . . . . .	6
CHAPTER 2: BEAM DYNAMICS IN RINGS . . . . .	7
2.1: Introductory Accelerator Physics . . . . .	7
2.2: Lie Maps in Accelerator Physics . . . . .	13
2.3: One-turn Map and Normal Form . . . . .	15
2.4: Resonances in Circular Accelerators . . . . .	18
2.5: Resonance Driving Terms . . . . .	22
2.6: Amplitude-Dependent Tune Shift . . . . .	24
2.7: Space Charge Tune Shift . . . . .	28
CHAPTER 3: THE FNAL RECYCLER RING . . . . .	35
3.1: Introduction . . . . .	35
3.2: General Description . . . . .	37
3.3: Tune Diagram and Resonances . . . . .	43
3.4: High Intensity and Tune Footprint . . . . .	45
3.5: Diagnostic Devices . . . . .	47
3.6: Sextupoles for Resonance Compensation . . . . .	51
CHAPTER 4: COMPENSATION OF THIRD-ORDER RESONANCES AT LOW INTENSITIES . . . . .	54
4.1: Global RDTs and Lattice Model . . . . .	54
4.2: Measurement of Third Order RDTs . . . . .	57
4.3: Compensation of RDTs . . . . .	71
4.4: Optimization of Compensation Currents . . . . .	86
4.5: Experimental Verification of Compensation . . . . .	89
4.6: Additional Sextupoles for Resonance Compensation . . . . .	100
CHAPTER 5: RESONANCE COMPENSATION STUDIES AT THE CERN PRO- TON SYNCHROTRON BOOSTER . . . . .	108
5.1: General Description . . . . .	108
5.2: Tune Diagram and Operation . . . . .	109
5.3: Optimization Algorithms for Resonance Compensation . . . . .	113
5.4: Experimental Verification of Compensation . . . . .	124
CHAPTER 6: HIGH INTENSITY STUDIES . . . . .	126
6.1: Space Charge Tune Shift . . . . .	126
6.2: Measurement of Tune Spread . . . . .	127
6.3: Intensity-Dependent Effects and Non-Gaussian Beam Profiles . . . . .	130

6.4: Static Tune Scans at Different Intensities . . . . .	132
6.5: Effect of Transverse Dampers . . . . .	140
<b>CHAPTER 7: CONCLUSIONS AND FUTURE WORK . . . . .</b>	<b>143</b>
7.1: Conclusions . . . . .	143
7.2: Future Work . . . . .	145
<b>BIBLIOGRAPHY . . . . .</b>	<b>149</b>

## LIST OF ABBREVIATIONS

<b>MSU</b>	Michigan State University
<b>FNAL</b>	Fermilab National Accelerator Laboratory
<b>RR</b>	Recycler Ring
<b>MI</b>	Main Injector
<b>RDTs</b>	Resonance Driving Terms
<b>NuMI</b>	Neutrinos at the Main Injector
<b>PSB</b>	CERN Proton Synchrotron Booster
<b>ACNET</b>	Accelerator Control Network
<b>TbT</b>	Turn-by-Turn Data
<b>NAFF</b>	Numerical Analysis of Fundamental Frequencies
<b>GFCs</b>	Generating Function Coefficients

## CHAPTER 1

### INTRODUCTION

Particle accelerators are the workhorses for modern scientific discoveries. Experimental nuclear and particle physics research benefits greatly from the progress of accelerator physics and technology. Accelerator physics is a rich field of applied physics living on the intersection of electromagnetism, solid-state and atomic physics, nonlinear mechanics, plasma physics, and quantum mechanics, just to name a few [1]. Furthermore, the design and operation of modern accelerator projects require costly enterprises of scientists, engineers, operators, and politicians coming together under one metaphorical roof. Everyone coming together to perform “megascience” [2].

The scientific principle of particle accelerators involves accelerating, steering, and/or storing charged particles through electromagnetic manipulations. These manipulations occur through a plethora of devices and components that can control electromagnetic fields, e.g., magnets and electrical cavities. The group of particles subject to this electromagnetic handling is called "the beam". The field of beam dynamics studies the interaction between the beam and the steering devices, as well as the Coulomb interactions between the beam itself—this is known as space charge physics. One can make an additional distinction when these steering devices are configured circularly or linearly. This is the distinction between circular accelerators and linear accelerators (Linacs).

Furthermore, one can categorize particle accelerators by the type of elementary particles composing the beam and how close to the speed of light they travel. The first category refers to the distinction between hadrons and leptons—particles that interact or do not interact through the strong force, respectively [3]. For example, protons and heavy ions are considered hadrons, while electrons and muons are considered leptons. The second category refers to whether particles in the machine travel at high or low energy. An example of a low-energy hadron machine is the heavy ion Linac at FRIB (Facility for Rare Isotope Beams) [4]. An example of a high-energy lepton machine was the Stanford Linear Accelerator located at SLAC National Accelerator Laboratory [5]. The two most famous high-energy hadron machines in history are the Tevatron [6], which operated

at Fermilab, and the LHC (Large Hadron Collider), operating at CERN [7]. Furthermore, there are accelerator projects that encompass several categories, such as the future EIC (Electron-Ion Collider) being built at Brookhaven National Laboratory [8], which will use an electron ring—a lepton machine—and a heavy-ion circular accelerator—a hadron machine—to probe new physics. A plethora of accelerator projects worldwide are either operational, under commissioning, or being designed.

The following thesis will explore the beam dynamics of a circular machine. The research results will be applied to the Fermilab Recycler Ring, which stores high-energy protons.

### 1.1 Circular Accelerators and Storage Rings

As will become more apparent in Ch. 2, a particle accelerator can be thought of as a composition of accelerator-themed LEGO® bricks [9]. Each elemental LEGO® brick can be thought of as an accelerator component performing some mapping on the charged particles entering it. As it turns out, one can assemble these LEGO® bricks circularly to give rise to circular accelerators. The assembly of these blocks in a particular shape gives rise to what is known as the lattice of the accelerator.

The acceleration part of these structures comes from elements inside the lattice that introduce some electromotive force in the longitudinal direction. The most common example for these blocks is radio-frequency (RF) cavities [1], with super-conducting RF cavities also as an established technology [10]. Particles that go through these elements gain energy on every pass. In the case where there are no acceleration blocks on these structures, a storage ring arises. Nevertheless, storage rings can also have RF cavities just for longitudinal beam manipulation but no overall acceleration—such is the case of the Recycler Ring.

Circular accelerators are unique since particles have to pass thousands or even millions of turns through the same LEGO® blocks. This multipass feature gives birth to exciting and complex dynamics inside these machines. One of these phenomena is called betatron resonances. The most simple lattice of a high-energy machine is composed of focusing and steering blocks, which are dipole and quadrupole magnets, i.e., the lowest-order multipole magnets. For reasons that will

become apparent in Ch. 2, these elements, in combination with free drift spaces, represent linear blocks. For the simplest circular machine, these linear LEGO® bricks are assembled to create a linear lattice. One can design a linear lattice with stable particle orbits around the accelerator. Nevertheless, accounted or unaccounted elements, described by linear or nonlinear blocks, around the machine can perturb the stable orbits. Ultimately, the effect of these perturbations can add up coherently over many turns to push the beam out of the acceptance of the lattice, i.e., the particles hit the enclosing vacuum pipe and create beam loss. This whole process is known as a betatron resonance in a circular accelerator. Chapter 2 provides a mathematical description of this process.

The following thesis describes an effort to mitigate the deleterious effect of these resonances in the Recycler Ring. After dipole and quadrupole, the third order of multipole magnetic fields is the sextupole component. Therefore, sextupole fields around the lattice are the source of third-order betatron resonances. Specifically, this thesis explores mitigation techniques to these third-order resonances, mainly in the Fermilab Recycler Ring (see Ch. 3, Ch. 4 and Ch. 6), but also with some experiments done at the CERN Proton Synchrotron Booster (see Ch. 5).

## 1.2 Fermilab

The best introduction to Fermilab is to cite an excerpt from Ref. [2]:

[...] A passenger peers through the window of an airplane. As his plane flies into Chicago's O'Hare Field from the west, he notices a large ring on the ground below (see Fig. 1.1). Near it, he sees a towering white structure, a group of colorful smaller buildings, an expanse of forest, open fields, and lakes.

"What is that ring?" he asks his neighbor.

"Fermilab," she replies. "It's a physics laboratory. The government supports research there into what the universe is made of."

"Why the ring?"

"It's the four-mile-round main ring of a machine called the Tevatron. It turns protons into tools for looking inside the atomic nucleus. Huge magnets steer the protons

around the ring, while high voltages accelerate them. [...]" (pp. 1)



Figure 1.1 Aerial view of the Fermi National Accelerator Laboratory (FNAL) located in Batavia, IL, USA [11].

The Fermi National Accelerator Laboratory (FNAL), better known as Fermilab, has a long and rich history of designing, building, and operating high-energy particle accelerators. Ever since the founding director of Fermilab, Robert R. Wilson, envisioned the 400 GeV Main Ring back in 1967, Fermilab has been at the forefront of accelerator physics [2, 6, 12]. The most famous accelerator project hosted by Fermilab has been the Tevatron, a proton-antiproton circular collider with a circumference of around 6.28 km. This machine took protons and antiprotons from smaller machines still in operation or repurposed as of 2024, e.g., the Recycler Ring. The Tevatron operated up until 2011, leaving an indelible legacy in the field of high energy and accelerator physics. Nostalgia aside, Fermilab still hosts a deluge of particle physics experiments connected to its main accelerator complex.

Figure 1.2 summarizes the current layout of the Fermilab Accelerator Complex. As of 2024, the Fermilab Accelerator Complex is composed of an  $H^-$  source that connects to a linear accelerator, accelerating the ions to an energy of 400 MeV. This linear accelerator feeds to the first circular machine—the Booster—where protons are achieved and accelerated to an energy of 8 GeV. After the Booster, the protons are transported to the Recycler Ring (RR), which is the second circular machine. The Recycler Ring stores and stacks protons to increase the beam intensity delivered to the Main Injector (MI). This last circular accelerator is where protons are accelerated from an energy of 8 GeV to 120 GeV. Once at this energy, the protons are transported to the Neutrinos at the Main Injector (NuMI) experiment to create the world’s most intense neutrino beam [13]. Nevertheless, throughout the chain of accelerators, the beam is also delivered to many other experiments. Therefore, the facility has several modes of operation depending on the online experiments. A more detailed and technical study of the current Fermilab Accelerator Complex, focusing on the Recycler Ring, is given in Ch. 3.

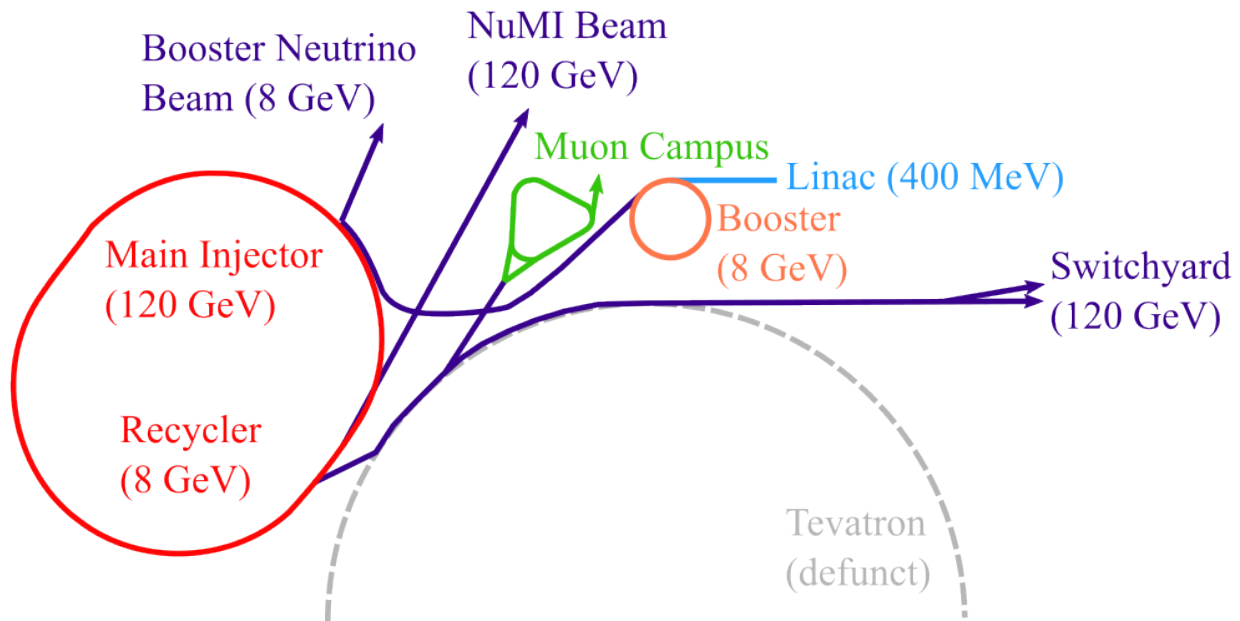


Figure 1.2 Schematic layout of the Fermilab Accelerator Complex as of 2024. Original plot provided by R. Ainsworth, first published on Ref. [14].

### 1.3 Outline

The following thesis will explore the compensation of third-order resonances in the Fermilab Recycler Ring. Chapter 1 introduces the motivation behind this thesis work. Chapter 2 summarizes single particle dynamics with exponential Lie operators' help and introduces a relevant concept of collective beam dynamics: the space charge tune shift. This theoretical overview gives a segue into this thesis' Ch. 3, where the Recycler Ring is introduced and described in detail. This chapter motivates the compensation of third-order resonances under the framework of the current and future operation of the RR. With the basic physics concepts and the description of the machine put in place, Ch. 4 describes in full detail the scheme and experiments developed to compensate for third-order resonances at low intensities. Before moving to explore the Recycler Ring at high intensities, Ch. 5 provides an interlude to show a series of experiments done at the CERN PS Booster. These experiments explore the use of advanced optimization algorithms to compensate for multiple resonance lines simultaneously. Coming back to Fermilab, Ch. 6 showcases the studies and experiments done at high intensities in the RR to understand the interplay between the compensation of resonance lines and space charge effects. Finally, Ch. 7 brings down the curtain by providing some general conclusions and future work stemming from this thesis.

## CHAPTER 2

### BEAM DYNAMICS IN RINGS

#### 2.1 Introductory Accelerator Physics

The basic building blocks of a particle accelerator are the elements that steer and focus the beam in the transverse direction. This is done by utilizing and manipulating the Lorentz force  $\vec{F}_L$  by means of the electromagnetic fields  $\vec{E}$  and  $\vec{B}$  to act on some particle with charge  $q$  and velocity  $\vec{v}$ , i.e.,  $\vec{F}_L = q(\vec{E} + \vec{v} \times \vec{B})$ . While a handful of electromagnetic devices can do this, the most prominent ones in high-energy accelerators are magnets with no electric field,  $\vec{E} = 0$ . In particular, there are pure dipole magnets for steering and pure quadrupole magnets for focusing. Nevertheless, some machines such as the Recycler Ring have combined function magnets with both types of magnets—and even higher order magnets—embedded in one to steer and focus the particles. The previous information assumes that every magnet can be expanded and described as a decomposition of magnetic multipoles, where dipole and quadrupole components are the lowest order terms of the expansion. Therefore, using the Beth representation [1], the multipole expansion for an arbitrary multipole magnet reads:

$$\frac{1}{[B\rho]} (B_y(x, y) + iB_x(x, y)) = -\frac{1}{\rho} \sum_{n=0}^{\infty} (b_n + ia_n) (x + iy)^n, \quad (2.1)$$

where  $b_n$  and  $a_n$  are the multipole coefficients defined by

$$b_n = \frac{1}{B_0 n!} \left. \frac{\partial^n B_y}{\partial x^n} \right|_{x=y=0}, \quad a_n = \frac{1}{B_0 n!} \left. \frac{\partial^n B_x}{\partial x^n} \right|_{x=y=0}. \quad (2.2)$$

For Eqs. 2.1 and 2.2,  $x$  and  $y$  represent the Cartesian coordinates, the product  $[B\rho]$  represents the magnetic rigidity of the beam with  $B_0$  being the main dipole field and  $\rho$  is the bending radius. At the same time,  $B_x$  and  $B_y$  are the transverse magnetic fields in the magnets. Specifically, the coefficients  $b_n$  and  $a_n$  represent the multipole coefficient of the magnet with the dipole coefficient defined as  $b_0 = 1$ , such that  $B_0 b_0 = -[B\rho]/\rho$ . Following the expansion, the term  $a_0$  is known as the dipole roll coefficient,  $b_1$  as the quadrupole coefficient,  $a_1$  as the skew quadrupole coefficient,  $b_2$  as the sextupole coefficient,  $a_2$  for the skew sextupole coefficient,  $b_3$  for the octupole coefficient,  $a_3$  for the skew octupole coefficient, and so forth. This expansion follows the U.S. convention.

The most basic circular accelerator of circumference  $C$  is composed of LEGO® blocks chosen from a pile of dipoles, quadrupoles, and free drift spaces. Equations 2.1 and 2.2 describe each of these elements, i.e., for the quadrupole case, the only non-zero coefficient is  $b_1$ . The particles inside this ring have a longitudinal relativistic velocity of  $v = \beta_L c$ , and therefore have a revolution frequency of  $f_{rev} = \beta_L c / C$ . The Hamiltonian of a single particle with position coordinates  $x, y$  and momentum coordinates  $p_x, p_y$  traversing through such a system at an independent time coordinate  $s$  is:

$$H = \frac{1}{2} \left( K_x(s)x^2 + K_y(s)y^2 + p_x^2 + p_y^2 \right), \quad (2.3)$$

where  $K_x(s), K_y(s)$  are the effective focusing functions and are defined as:

$$K_x(s) = \frac{1}{\rho^2} - \frac{b_1(s)}{\rho}, \quad K_y(s) = \frac{b_1(s)}{\rho} \quad (2.4)$$

assuming the definition of  $b_1(s)$  in 2.2 extends to describe the distribution of the horizontal quadrupole coefficient around the ring. For the case where  $\rho \gg 1$  (high-energy limit), the function  $K_y(s) = -K_x(s)$ , i.e., horizontally focusing quadrupoles will have a defocusing effect in the vertical direction and vice versa.

In classic accelerator references, such as Refs. [1, 15, 16], the equations of motion derived from the Hamiltonian in Eq. 2.3 are known as Hill's equations. The usual accelerator-physics method to solve this type of equation is to introduce transfer matrices for each type of linear element. This will define linear mappings bringing some initial state vector  $\vec{X}_0 = (x_0, x'_0, y_0, y'_0)$  to a final vector  $\vec{X}_f = (x_f, x'_f, y_f, y'_f)$  using a symplectic matrix  $M$ , i.e.,  $\vec{X}_f = M\vec{X}_0$ . Table 2.1 shows the 4D transfer matrices for common linear elements found in accelerators. It is worth noting that these 4D matrices can include coupling elements that couple the  $x - y$  plane. For this case, the off-block coefficients of the matrices would be non-zero. An example of this last case is shown in Table 2.1 through the thin skew quadrupole case. Nevertheless, the starting point of this work is to consider a circular accelerator built from linear non-coupling elements, while other coupling or nonlinear elements are considered perturbative. In Sec. 2.2, Lie operators extend these mappings to the nonlinear regime.

Table 2.1 Transfer matrices for common accelerator elements in the high-energy regime and paraxial approximation

Element	4D Transfer Matrix
Drift space of length $L$	$M = \begin{bmatrix} 1 & L & 0 & 0 \\ 0 & 1 & 0 & 0 \\ 0 & 0 & 1 & L \\ 0 & 0 & 0 & 1 \end{bmatrix}$
Dipole of bending radius $\rho$ , length $\ell$ and orbiting angle $\theta = \ell/\rho$	$M = \begin{bmatrix} \cos \theta & \rho \sin \theta & 0 & 0 \\ -\frac{1}{\rho} \sin \theta & \cos \theta & 0 & 0 \\ 0 & 0 & 1 & \ell \\ 0 & 0 & 0 & 1 \end{bmatrix}$
Thin quadrupole of focal length $f = \lim_{\ell \rightarrow 0} \frac{1}{k\ell} > 0$	$M = \begin{bmatrix} 1 & 0 & 0 & 0 \\ -1/f & 1 & 0 & 0 \\ 0 & 0 & 1 & 0 \\ 0 & 0 & 1/f & 1 \end{bmatrix}$
Thick quadrupole of strength $k > 0$ and length $\ell$	$M = \begin{bmatrix} \cos \sqrt{k}\ell & \frac{1}{\sqrt{k}} \sin \sqrt{k}\ell & 0 & 0 \\ -\sqrt{k} \sin \sqrt{k}\ell & \cos \sqrt{k}\ell & 0 & 0 \\ 0 & 0 & \cosh \sqrt{ k }\ell & \frac{1}{\sqrt{ k }} \sinh \sqrt{ k }\ell \\ 0 & 0 & \sqrt{ k } \sinh \sqrt{ k }\ell & \cosh \sqrt{ k }\ell \end{bmatrix}$
Thin skew quadrupole of focal length $f_s = \lim_{\ell \rightarrow 0} \frac{1}{k_s \ell} > 0$	$M = \begin{bmatrix} 1 & 0 & 0 & 0 \\ 0 & 1 & 1/f_s & 0 \\ 0 & 0 & 1 & 0 \\ 1/f_s & 0 & 0 & 1 \end{bmatrix}$

Like stacking LEGO® bricks, one can stack these transfer matrices to calculate the total mapping through a stack of elements. The total linear mapping of a consecution of accelerator elements is just the matrix multiplication of the corresponding transfer matrices, i.e., for a lattice with  $N$  linear

blocks, the total transfer matrix reads:

$$M_{Total} = M_N M_{N-1} \dots M_1. \quad (2.5)$$

One can introduce the Courant-Snyder (CS) parametrization and Twiss parametrization to understand linear lattices further. One can parametrize any linear element or stack of linear elements functions by the Twiss parameters  $\beta_u(s)$ ,  $\alpha_u(s)$  and  $\gamma_u(s)$  and a phase advance defined as  $\phi_u(s) = \int_0^s ds/\beta_u(s)$ , where  $u$  stands for either the  $x$  or  $y$  plane. This results in the following transfer matrix from location  $s = 0$  to an arbitrary location  $s$ :

$$M(s) = \begin{bmatrix} M_x(s) & 0_{2 \times 2} \\ 0_{2 \times 2} & M_y(s) \end{bmatrix}, \quad (2.6)$$

where  $M_u$  is a square matrix defined as:

$$M_u = \begin{bmatrix} \sqrt{\frac{\beta_u(s)}{\beta_u(0)}} (\cos \phi_u(s) + \alpha_u(0) \sin \phi_u(s)) & \sqrt{\beta_u(s)\beta_u(0)} \sin \phi_u(s) \\ \frac{\alpha_u(0)-\alpha_u(s)}{\beta_u(s)\beta_u(0)} \cos \phi_u(s) - \frac{1+\alpha_u(0)\alpha_u(s)}{\beta_u(s)\beta_u(0)} \sin \phi_u(s) & \sqrt{\frac{\beta_u(0)}{\beta_u(s)}} (\cos \phi_u(s) - \alpha_u(s) \sin \phi_u(s)) \end{bmatrix}, \quad (2.7)$$

and  $0_{2 \times 2}$  is a square matrix of size  $2 \times 2$  with zeros in all of its entries. As a consequence of the Twiss parametrization, one can express the position coordinates at an arbitrary  $s$  along a linear lattice as:

$$u(s) = \sqrt{2J_u\beta_u(s)} \cos(\phi_u(s) + \phi_{u0}), \quad (2.8)$$

where  $J_u$  is a constant of motion known as the action and  $\phi_{u0}$  is an arbitrary phase constant. Equation 2.8 describes what is known as betatron oscillations. Additionally, the action  $J_u$  can be calculated as

$$2J_u = \gamma_u u^2 + 2\alpha_u uu' + \beta_u u'^2, \quad (2.9)$$

for any  $s$  using the property  $\beta_u \gamma_u = 1 + \alpha_u^2$ . Therefore, the particles traversing through the lattice will exhibit oscillatory motion, with amplitude dictated by the  $\beta_u(s)$  function and frequency dictated by the  $\phi_u(s)$  function.

Until now, one can apply this formalism to a linear or circular accelerator. No assumption has been made on how the stacking of the LEGO® bricks in the lattice affects this formalism.

Nevertheless, in a circular accelerator of circumference  $C$ , there is an additional constraint on the Twiss functions given that periodic boundary conditions exist, i.e.,  $\beta(s) = \beta(s + C)$ , and similarly for the other Twiss functions. Another critical parameter for a circular lattice is the tune  $Q_u$ , defined as the total phase advance over one turn of the machine, i.e.,

$$2\pi Q_u = \phi_u(C) = \int_s^{s+C} \frac{ds}{\beta_u(s)}. \quad (2.10)$$

With the definition of the tune  $Q_u$ , Eq. 2.7 can be rewritten in order to calculate the one-turn matrix  $M(C)$  of the circular accelerator, such that:

$$M(C) = \begin{bmatrix} M_x(C) & 0_{2 \times 2} \\ 0_{2 \times 2} & M_y(C) \end{bmatrix}, \quad (2.11)$$

where each plane will have its one-turn transfer matrix reading:

$$M_u(C) = \begin{bmatrix} \cos 2\pi Q_u + \alpha_u(C) \sin 2\pi Q_u & \beta_u(C) \sin 2\pi Q_u \\ -\gamma_u(C) \sin 2\pi Q_u & \cos 2\pi Q_u - \alpha_u(C) \sin 2\pi Q_u \end{bmatrix}. \quad (2.12)$$

Ultimately, Eq. 2.12 can be used to calculate the particle's state vector after  $N$  turns, where the total transfer matrix  $M_u(NC)$  will be  $M_u(NC) = M_u(C)^N$ . If one tracks a particle with some initial conditions for enough turns and its geometrical coordinates  $(x, x', y, y')$  are recorded through some diagnostic device every turn, the resulting trajectory would lie on an ellipse—the phase space ellipse. The astute reader would have already identified that Eq. 2.9 hinted at this fact, given that this is just the implicit definition for an ellipse. In essence, the Twiss parametrization will give the geometry to describe the ellipse fully. Figure 2.1 illustrates these statements by associating the phase space ellipse geometry with the Twiss functions.

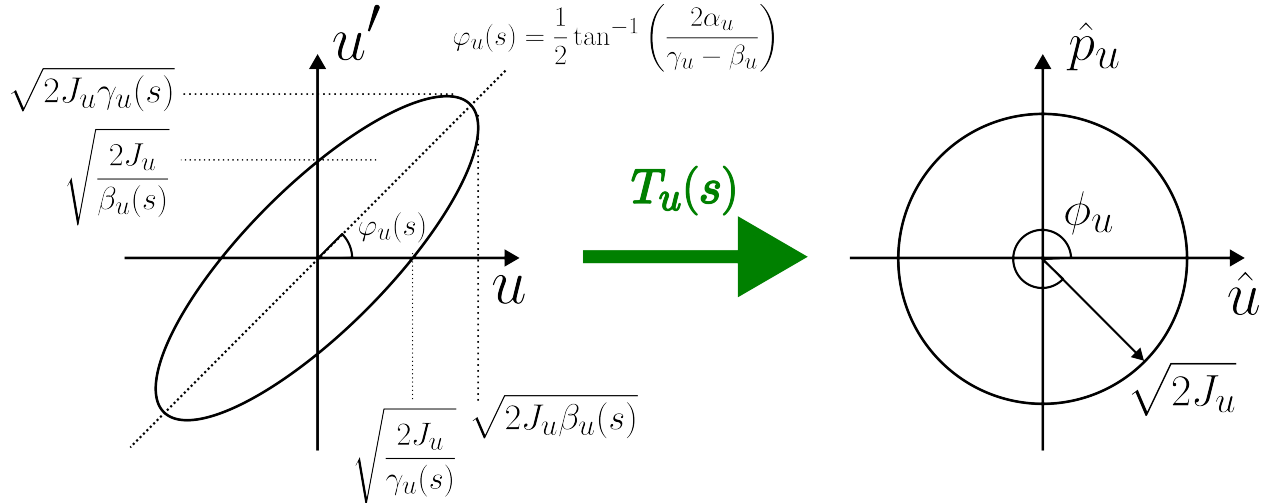


Figure 2.1 Phase space ellipse in geometrical coordinates with Twiss parametrization and its counterpart transformation in normalized phase space.

Figure 2.1 also hints that one can do a linear transformation  $T_u(s)$  to transform the phase space ellipse into a circle. This transformation is known as a Floquet transformation. Therefore, a change of coordinates from geometrical coordinates  $(u, u')$  to normalized coordinates  $(\hat{u}, \hat{p}_u)$  can be achieved through the following linear transformation:

$$\begin{bmatrix} \hat{u} \\ \hat{p}_u \end{bmatrix} = \begin{bmatrix} \frac{1}{\sqrt{\beta_u}} & 0 \\ \frac{\alpha_u}{\sqrt{\beta_u}} & \sqrt{\beta_u} \end{bmatrix} \begin{bmatrix} u \\ u' \end{bmatrix} = \sqrt{2J_u} \begin{bmatrix} \cos \phi_u(s) \\ -\sin \phi_u(s) \end{bmatrix}. \quad (2.13)$$

Ultimately, one can express the one-turn Hamiltonian for circular accelerators as:

$$H_0 = 2\pi Q_x J_x + 2\pi Q_y J_y, \quad (2.14)$$

which is simpler and more succinct than the Hamiltonian in Eq. 2.3. Conclusively, one can map all the dynamics of a linear-circular accelerator with its intricacies to rotations on a simple circle. The rotation matrix  $R(s)$  summarizes the dynamics in normalized phase space, which will depend on the lattice itself and is analogous to the transfer matrices  $M(s)$  in geometrical space. Therefore,

the following commutative diagram summarizes the linear dynamics:

$$\begin{array}{ccc}
 \begin{pmatrix} x, x' \\ y, y' \end{pmatrix}_0 & \xrightarrow{M(s)} & \begin{pmatrix} x, x' \\ y, y' \end{pmatrix}_f \\
 T(s) \downarrow & & \downarrow T(s) \\
 \begin{pmatrix} J_x, \phi_x \\ J_y, \phi_y \end{pmatrix}_0 & \xrightarrow{R(s)} & \begin{pmatrix} J_x, \phi_x \\ J_y, \phi_y \end{pmatrix}_f
 \end{array} \quad (2.15)$$

Lie operators are introduced in the following sections to generalize to non-linear mappings. For a linear-circular accelerator, the last section has shown that starting from Hill's equation, linear transformations can be applied to a complex machine such as an accelerator in order to end up with a simple mathematical equation such as the one described in Eq. 2.14. Put, nonlinear elements will distort the phase space circle of Fig. 2.1, destroying the system's linearity. The premise here is that non-linear elements in circular accelerators are inevitable, and they will come from anywhere and everywhere in the lattice, either from accounted or unaccounted sources. Therefore, one can use higher-tier mathematical tools to describe non-linear dynamics in a circular accelerator. Linear matrices will only get us so far.

## 2.2 Lie Maps in Accelerator Physics

The most basic element of a particle accelerator can be considered a LEGO® brick acting as a black box transformation for a single particle. This black box takes some single charged particle with initial transverse coordinates  $(x_0, x'_0, y_0, y'_0)$ , as defined in a Frenet-Serret coordinate system, and maps them to some final coordinates  $(x_f, x'_f, y_f, y'_f)$ . For simplicity, this analysis will not consider any longitudinal effect, but it can be easily incorporated. By gathering the initial coordinates into a vector, i.e.,  $\vec{X}_0 = (x_0, x'_0, y_0, y'_0)$ , and doing the same for the final coordinates, i.e.,  $\vec{X}_f = (x_f, x'_f, y_f, y'_f)$ , one can define the mapping  $\mathcal{M}$  that relates both vectors, such that:

$$\vec{X}_f = \mathcal{M}\vec{X}_0. \quad (2.16)$$

Unlike the previous section,  $\mathcal{M}$  need not be a linear mapping. For a charged particle inside some accelerator element (described using Hamiltonian dynamics), Poisson brackets and exponential Lie operators can help describe this mapping  $\mathcal{M}$  [9, 15, 17–19].

Let  $\vec{X} = (q_1, p_1, \dots, q_n, p_n)$  be a  $2n$  dimensional vector, made from  $n$  pairs of canonical coordinates  $(q_i, p_i)$  that make up the  $2n$  dimensional phase space. Moreover, let two arbitrary functions  $f(\vec{X}; s)$  and  $g(\vec{X}; s)$  be functions of  $\vec{X}$  and  $s$ , where  $s$  plays the role of the independent "time" coordinate. The Poisson brackets  $[\bullet, \bullet]$  can be defined as:

$$[f, g] = \sum_{i=1}^n \frac{\partial f}{\partial q_i} \frac{\partial g}{\partial p_i} - \frac{\partial f}{\partial p_i} \frac{\partial g}{\partial q_i}. \quad (2.17)$$

Using this definition, one can explicitly write the Poisson bracket definition for a four-dimensional phase space described by state vector  $\vec{X} = (x, x', y, y')$ . This definition reads:

$$[f, g] = \frac{\partial f}{\partial x} \frac{\partial g}{\partial x'} - \frac{\partial f}{\partial x'} \frac{\partial g}{\partial x} + \frac{\partial f}{\partial y} \frac{\partial g}{\partial y'} - \frac{\partial f}{\partial y'} \frac{\partial g}{\partial y}. \quad (2.18)$$

The Lie operator :  $f$  : acts on some function  $g$  and is the adjoint operator of the Poisson bracket operator. Its definition reads:

$$: f : g = [f, g]. \quad (2.19)$$

This specific :  $\bullet$  : notation allows a compact notation to define the exponential Lie operator. The exponential Lie operator of an arbitrary function  $f$  is defined as

$$e^{:f:} \bullet = \sum_{k=0}^{\infty} \frac{1}{k!} (: f :)^k \bullet. \quad (2.20)$$

For a Hamiltonian system, the mapping of coordinates from  $\vec{X}_0$  to  $\vec{X}_f$  follows the expression:

$$\vec{X}_f = e^{-\ell:H} \vec{X} \Big|_{\vec{X}=\vec{X}_0}, \quad (2.21)$$

which is known as a Lie Map [17]. In this case,  $\ell$  corresponds to the integration length of the independent coordinate. For example, for a particle traversing a magnet with length  $L$ , the integration length is  $\ell = L$ . When looking at the one-turn map, the integration length corresponds

to the circumference  $C$  of the accelerator over an effective Hamiltonian  $H_{eff}$ . Furthermore, the integration length  $\ell$  would be the phase advance  $\mu$  if working with action-angle variables.

### 2.3 One-turn Map and Normal Form

LEGO® bricks can be stacked together to create complex structures. Analogously, one can assemble accelerator elements to create complex ring-shaped structures such as circular accelerators. In such structures, particles will experience the same one-turn mapping over thousands or millions of turns. The one-turn map  $\mathcal{M}_1$  of a circular accelerator is the composition ( $\circ$ ) of mappings from every LEGO® element in the ring. Choosing an arbitrary initial point at  $s = 0$  and going around the ring, the one-turn map describes the transformation of coordinates after one turn, i.e.,  $\vec{X}_{N=1} = \mathcal{M}_1 \vec{X}_0$ . This map composition reads:

$$\mathcal{M}_1 = M_{N+1} \circ e^{:h_N:} \circ \dots \circ e^{:h_2:} \circ M_2 \circ e^{:h_1:} \circ M_1 = M_{N+1} e^{:h_N:} \dots e^{:h_2:} M_2 e^{:h_1:} M_1, \quad (2.22)$$

where  $M_i$  is the matrix representation of a linear mapping that does not couple the  $x - y$  plane, e.g., drift space mapping or quadrupole mapping. On the other hand, the map  $e^{:h_i:}$  represents any linear or non-linear mapping that can be found around the machine and can be considered a perturbation to the ideal lattice, including coupling elements, e.g., skew quadrupoles, higher order multipole elements. Figure 2.2 illustrates the procedure to build the one-turn map for a circular accelerator.

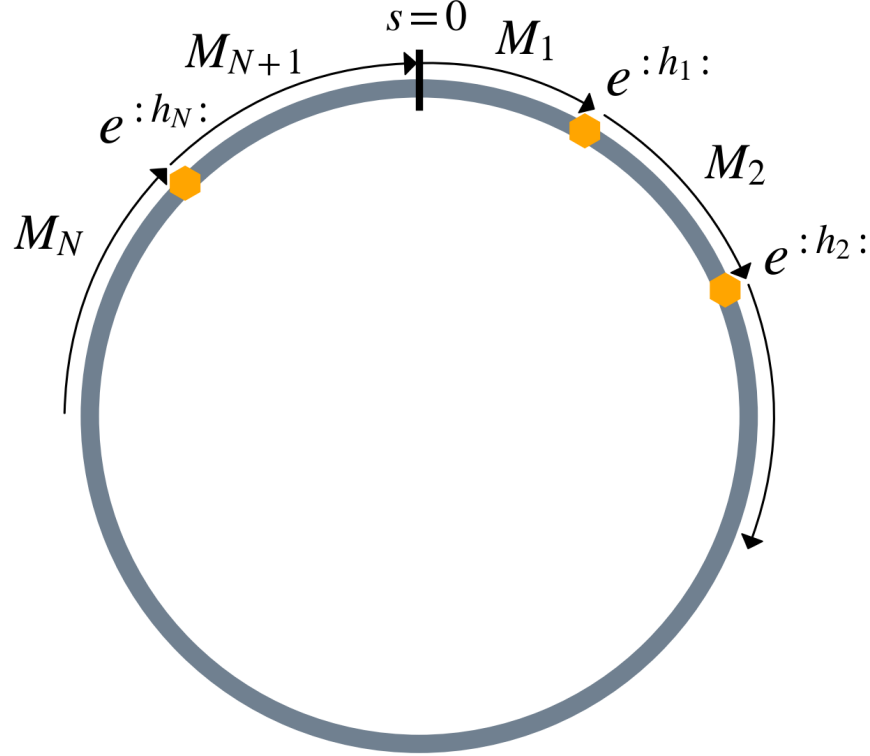


Figure 2.2 Diagram of an arbitrary circular accelerator to illustrate the one-turn map.

Through the use of the Baker-Campbell-Hausdorff formula [20], Eq. 2.22 can be collapsed to the expression

$$\mathcal{M}_1 = e^{-C:H_{eff}:}, \quad (2.23)$$

where  $C$  is the circumference of the ring, and  $H_{eff}$  is the effective Hamiltonian of the machine over one turn. As mentioned earlier, for most cases, it is of interest to look at the perturbations to the linear uncoupled dynamics of the design lattice. With this in mind, Eq. 2.23 can be rewritten as:

$$\mathcal{M}_1 = e^{(h)} R, \quad (2.24)$$

where  $R$  is a rotation matrix encoding the linear uncoupled dynamics of the ideal lattice. On the other hand, the term  $e^{(h)}$  encodes the perturbations to this ideal situation. It is worth pointing out that for the case  $h = 0$ , the traditional Courant-Snyder variables are recovered.

One can write the Courant-Snyder variables  $(\hat{x}, \hat{p}_x, \hat{y}, \hat{p}_y)$  or normalized phase space coordinates for a linear uncoupled case as:

$$\hat{u} = \sqrt{2J_u} \cos(\phi_u + \phi_{u_0}); \quad (2.25)$$

$$\hat{p}_u = -\sqrt{2J_u} \sin(\phi_u + \phi_{u_0}), \quad (2.26)$$

where  $u$  can stand either for the  $x$  or  $y$  coordinate,  $J_u$  and  $\phi_u$  correspond to the action-angle variables and  $\phi_{u_0}$  corresponds to the initial phase. For the case where perturbations exist, i.e.,  $h \neq 0$ , the action  $J_u$  is not constant anymore and will be a function of  $\phi_u$ .

The Normal Form formalism is introduced at this point in order to find action-angle coordinates  $I_u$  and  $\psi_u$ , such that the motion depends on  $\psi_u$  at a constant  $I_u$ , with some initial phase  $\psi_{u_0}$ . These are known as non-linear action-angle variables. The variables  $I_u$  and  $\psi_u$  are calculated from the transformation  $e^{-:F:}$  acting on  $J_u$  and  $\phi_u$ . The whole point is to find these variables that allow the Hamiltonian to be only amplitude-dependent. The following commutative diagram can summarize these Normal Form gymnastics:

$$\begin{array}{ccc} \left( \begin{matrix} J_x, \phi_x \\ J_y, \phi_y \end{matrix} \right)_0 & \xrightarrow{e^{:h(J_u, \phi_u):_R}} & \left( \begin{matrix} J_x, \phi_x \\ J_y, \phi_y \end{matrix} \right)_f \\ e^{-:F:} \downarrow & & \downarrow e^{-:F:} \\ \left( \begin{matrix} I_x, \psi_x \\ I_y, \psi_y \end{matrix} \right)_0 & \xrightarrow{e^{:H(I_u):}} & \left( \begin{matrix} I_x, \psi_x \\ I_y, \psi_y \end{matrix} \right)_f. \end{array} \quad (2.27)$$

Without loss of generality, the generating function  $F$  can be written as a Fourier expansion over the objective space  $(I_x, \psi_x, I_y, \psi_y)$  such that:

$$F = \sum_{jklm} f_{jklm} (2I_x)^{\frac{j+k}{2}} (2I_y)^{\frac{l+m}{2}} e^{i[(j-k)(\psi_x + \psi_{x0}) + (l-m)(\psi_y + \psi_{y0})]}. \quad (2.28)$$

Similarly, the argument of the Lie operator  $e^{:h:}$  from Eq. 2.24 can be expanded as:

$$h = \sum_{jklm} h_{jklm} (2J_x)^{\frac{j+k}{2}} (2J_y)^{\frac{l+m}{2}} e^{i[(j-k)(\phi_x + \phi_{x0}) + (l-m)(\phi_y + \phi_{y0})]}. \quad (2.29)$$

For Eqs. 2.28 and 2.29, the integer indices  $j, k, l, m$  run from 0 to infinity and correspond to the four degrees of freedom for transverse phase space.

The terms  $f_{jklm}$  are known as generating function coefficients. The terms  $h_{jklm}$  are known as Hamiltonian coefficients or resonance driving terms (RDTs). Section 2.5 describes the non-linear dynamics of accelerators using RDTs. The generating function coefficients  $f_{jklm}$  can be related to the Hamiltonian resonance driving terms  $h_{jklm}$  through the following relation [18, 21]:

$$f_{jklm} = \frac{h_{jklm}}{1 - e^{2\pi i[(j-k)Q_x + (l-m)Q_y]}}, \quad (2.30)$$

where  $Q_x$  and  $Q_y$  represent the transverse uncoupled and unperturbed tunes of the accelerator. The transverse tunes of a circular accelerator are defined as the phase advances in each plane over one turn, in units of  $2\pi$ , i.e.,  $Q_u = \phi_u(s = C)/2\pi$ .

The terms  $h_{jklm}$  are generally defined by the order in which they enter the one-turn normal form Hamiltonian [21]. With the assumption of thin elements around the ring, the general expression to define RDTs reads:

$$h_{jklm} = \Xi_{jklm} \sum_i L_i K_{n-1,i} \beta_{x,i}^{\frac{j+k}{2}} \beta_{y,i}^{\frac{l+m}{2}} e^{i[(j-k)\phi_{x,i} + (l-m)\phi_{y,i}]}, \quad (2.31)$$

where  $\Xi_{jklm}$  is just a constant defined as:

$$\Xi_{jklm} = -\frac{1}{2^n} \frac{1}{n!} \binom{n}{l+m} \binom{j+k}{j} \binom{l+m}{l}. \quad (2.32)$$

For Eqs. 2.31 and 2.32,  $n = j + k + l + m$  represents the order of the RDT. The sum over  $i$  is done over all multipoles of order  $n$  and length  $L_i$  that either have a normal component  $K_{n-1,i} = b_{n-1,i}/\rho$  if  $l + m$  is even, or a skew component  $K_{n-1,i} = K_{n-1,i}^{(s)} = a_{n-1,i}/\rho$  if  $l + m$  is odd, remembering  $\rho$  is the bending radius as it appeared on Eq. 2.1. The notation  $K_{n-1,i}$  is to keep up with the MAD-X convention for naming normal multipole coefficients [22]. The symbols for  $\beta_{x,i}$ ,  $\beta_{y,i}$ ,  $\phi_{x,i}$  and  $\phi_{y,i}$  represent the unperturbed beta functions and phase advances in each plane, respectively.

## 2.4 Resonances in Circular Accelerators

Equation 2.30 diverges when the denominator tends to zero. Specifically, this defines a condition reading:

$$(j - k) Q_x + (l - m) Q_y = p, \quad (2.33)$$

where  $p$  can be any integer. Equation 2.33 defines resonance lines in tune space of order  $n = j + k + l + m$ . Suppose the accelerator is tuned to operate on top of these resonances. In that case, the perturbations will add up coherently turn-to-turn and kick the resonant particles out of their original trajectory. Operating close to or on top of a resonance line is generally harmful as particles will be lost. This is especially true for lower-order resonances, i.e., for  $n < 4$ . Generally, the higher the resonance order, the weaker it is [16]. This thesis focuses on third-order resonances, i.e.,  $n = 3$ , and how to mitigate their deleterious effect.

Figure 2.3 shows the tune diagram with resonance lines, as defined by Eq. 2.33, drawn up to the fifth order. The integer part of both tunes is chosen to include the actual area of operation of the Recycler Ring. Nevertheless, only the fractional part of the tune carries significant information for resonance diagrams. In particular, Ch. 3 describes the operation and tune diagram for the Recycler Ring in more detail. Typically, one designs the operation point of a circular accelerator to be clear of any resonance line and as far away as possible from integer ( $n = 1$ ) and half-integer ( $n = 2$ ) resonances.

Nevertheless, in reality, two concepts complicate things. The first relates that resonance lines are not infinitely thin and have some stop bandwidth. The second one concerns that particles will not have localized tunes at high intensities but rather a distribution of tunes with some tune spread, i.e., a tune footprint. Section 2.7 looks at the space charge tune shift. Ultimately, choosing the operation point on Fig. 2.3 involves localizing a resonance-free region where the intensity-dependent tune footprint can be placed.

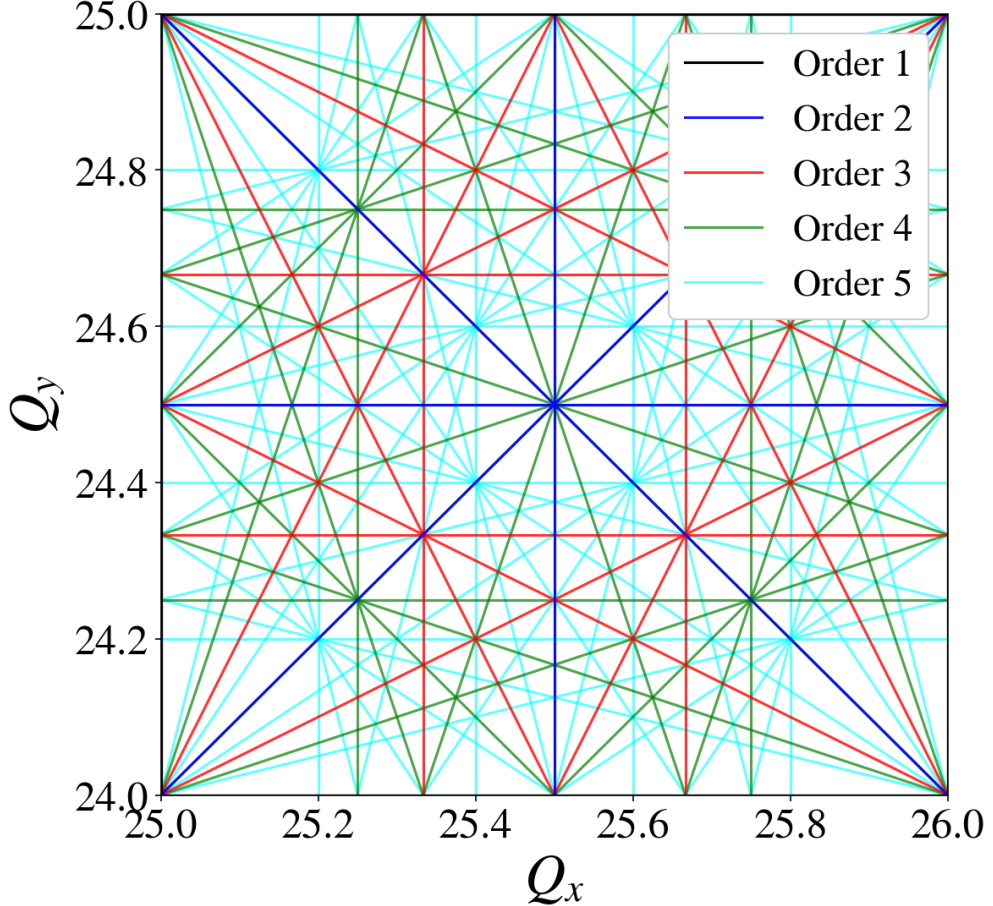


Figure 2.3 Tune diagram with resonance lines up to fifth order, enclosing the operation point of the Recycler Ring.

It is worth stopping here and asking what is the driving force behind each of these resonance lines. Classic accelerator references such as Refs. [1, 15, 16] will derive Eq. 2.33 by perturbing Hill's equation with different magnetic multipole orders. A closer look into each perturbation term reveals that half-integer resonances are caused by quadrupole terms, third-order resonances by sextupole-like terms, and fourth-order resonances by octupole terms, following the pattern to higher orders. Nevertheless, the story is complicated when one considers that pure multipole magnets can feed down or up to other order terms if installation misalignments exist, e.g., a misaligned sextupole feed to skew quadrupole-like terms.

Figure 2.4 zooms into the region of interest for the Recycler Ring operation in the tune diagram, as shown in Fig. 2.3. As mentioned before, the operation point of an accelerator in the tune diagram

is not a singular point but a footprint. While the lattice can be tuned to a specific nominal point, the particles will interact with other particles through the Coulomb force. Consequently, each particle will feel a different tune shift depending on its position within the bunch of particles. This effect is called the incoherent space charge tune shift, and it will be the largest for particles in the core of the bunch, i.e., the beam core. At low particle intensities, such as the one used to produce Fig. 2.4, the tune spread of the particles in the bunch is small enough to approximate the physics to single-particle dynamics. For beams with low particle intensities and a minor tune spread, such as the one depicted in Fig. 2.4, operating clear from any low-order resonance lines is not generally a problem. Nevertheless, at high intensities, the situation changes.

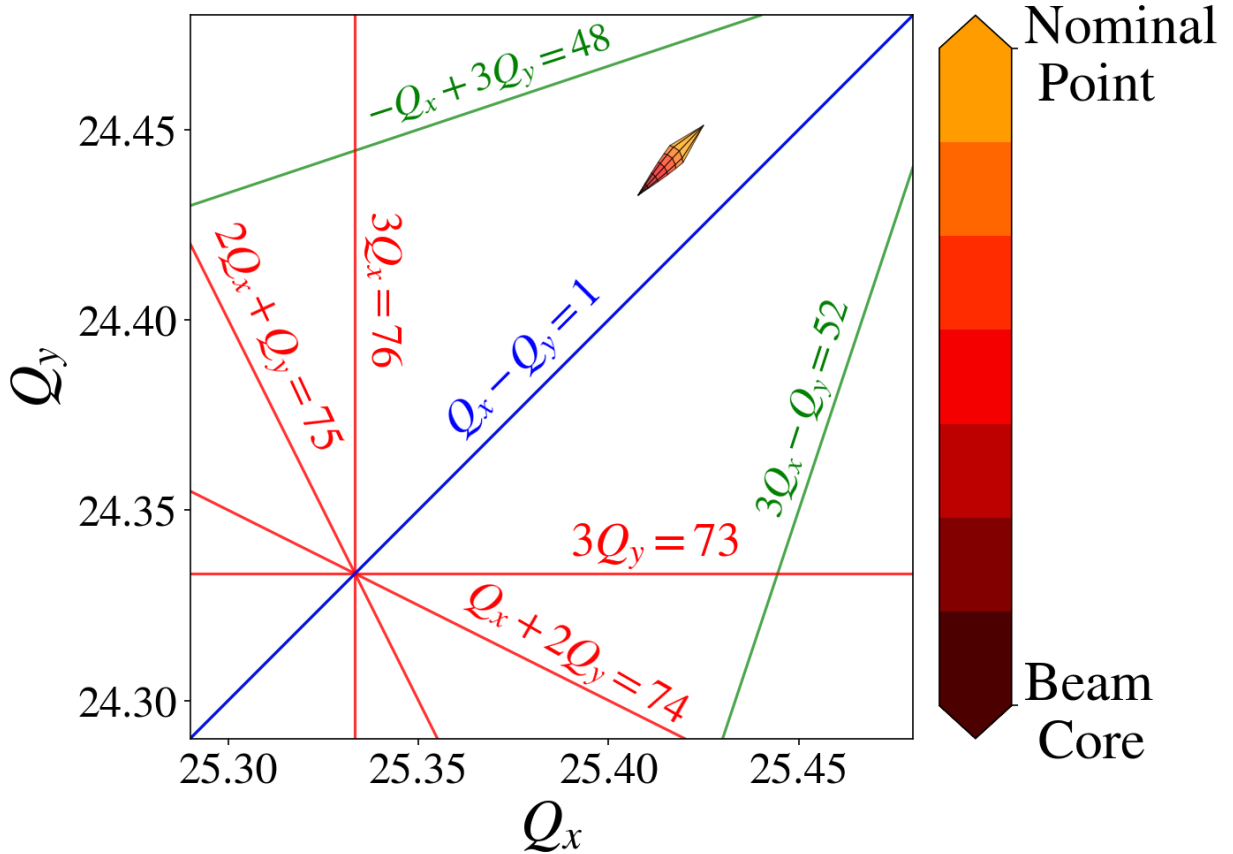


Figure 2.4 Approximate operational tune footprint at low intensities calculated with PySCRDT [23], i.e., 1e10 particles per bunch.

Figure 2.4 plots all resonance lines up to fourth order in this region of interest. The half-integer line  $Q_x - Q_y = 1$ , known as a difference coupling resonance, is usually driven by solenoidal and

skew-quadrupole fields in the lattice. Sextupole-like fields drive the third-order lines  $3Q_x = 76$  and  $Q_x + 2Q_y = 74$ . Skew sextupole terms drive the other third-order lines  $3Q_y = 73$  and  $2Q_x + Q_y = 75$ . Moreover, finally, octupole-like fields drive the fourth order lines  $-Q_x + 3Q_y = 48$  and  $3Q_x - Q_y = 52$ . This assumes a rectangular multipole expansion notation of the magnetic field, such as the one presented in Eq. 2.1.

## 2.5 Resonance Driving Terms

The RDTs  $h_{jklm}$  are related to the strength of the resonance  $(j - k)Q_x + (l - m)Q_y$ . Therefore, controlling and measuring these RDTs is of special interest to accelerator physics. The following section explains how to get to a useful expression that can be used in order to measure the  $h_{jklm}$  terms through Fourier expansions.

The whole point of introducing the Normal Form coordinates  $(I_u, \psi_u)$  through the transformation  $e^{-iF}$  as defined in Eq. 2.28 is to transfer complicated non-linear dynamics to simple dynamics that lie on a circle— $I_u$  and  $\dot{\psi}_u$  are constant. When this happens, a set of canonical coordinates  $\vec{\zeta} = (\zeta_x^+, \zeta_x^-, \zeta_y^+, \zeta_y^-)$  can be defined as:

$$\zeta_u^\pm = \sqrt{2I_u} e^{\mp i(\psi_u + \psi_{u_0})}, \quad (2.34)$$

always keeping in mind that  $I_u$  is a constant of motion and  $\psi_{u_0}$  is a constant initial phase set by the initial conditions. The Poisson brackets for a pair of these quantities are:

$$[\zeta_u^+, \zeta_u^-]_{\psi_u, J_u} = \frac{\partial \zeta_u^+}{\partial \psi_u} \frac{\partial \zeta_u^-}{\partial J_u} - \frac{\partial \zeta_u^+}{\partial J_u} \frac{\partial \zeta_u^-}{\partial \psi_u} = -2i, \quad (2.35)$$

for the same plane  $u$  and using a reduced form of Eq. 2.18. In this notation, the subindices from  $[\bullet, \bullet]_{\psi_u, J_u}$  refer to the variables used to calculate the Poisson brackets. Using Eq. 2.35, the following useful property can be derived:

$$[\zeta_x^{+j} \zeta_x^{-k} \zeta_y^{+l} \zeta_y^{-m}, \zeta_x^-]_{\psi_x, J_x} = (\zeta_y^{+l} \zeta_y^{-m}) [\zeta_x^{+j} \zeta_x^{-k}, \zeta_x^-]_{\psi_x, J_x} = -2ij \zeta_x^{+j-1} \zeta_x^{-k} \zeta_y^{+l} \zeta_y^{-m}, \quad (2.36)$$

where the last step is achieved using the Leibnitz rule for Poisson brackets, i.e.,  $[fg, h] = [f, h]g + f[g, h]$ .

On the other hand, going back to the Courant-Snyder phase space, a set of coordinates known as a resonance basis  $\vec{h} = (h_x^+, h_x^-, h_y^+, h_y^-)$  can be defined. Similarly to Eq. 2.34, the resonance basis reads:

$$h_u^\pm = \hat{u} \pm \hat{p}_u = \sqrt{2J_u} e^{\mp i(\phi_u + \phi_{u_0})}, \quad (2.37)$$

always keeping in mind that in the Courant-Snyder phase space, the action  $J_u$  is a function of the phase  $\phi_u$ , i.e.,  $J_u = J_u(\phi_u)$  and is not constant. The initial phase  $\phi_{u_0}$  is again a constant set by the initial conditions.

The basis grouped in  $\vec{h}$  and the one grouped in  $\vec{\zeta}$  are related by the transformation:

$$\vec{h} = e^{:F(\vec{\zeta}):} \vec{\zeta}, \quad (2.38)$$

where  $F(\vec{\zeta})$  is the generating function written in terms of the basis  $\vec{\zeta}$ . The inverse transformation to Eq. 2.38 reads:

$$\vec{\zeta} = e^{-:F(\vec{\zeta}):} \vec{h}. \quad (2.39)$$

Writing out the generating function  $F(\vec{\zeta})$  in a general polynomial form, this functions reads:

$$F(\vec{\zeta}) = \sum_{jklm} f_{jklm} (\zeta_x^+)^j (\zeta_x^-)^k (\zeta_y^+)^l (\zeta_y^-)^m. \quad (2.40)$$

Inserting the definitions in Eq. 2.34 into Eq. 2.40, the proposed definition in Eq. 2.28 can be recovered.

Expanding Eq. 2.38 by using the exponential Lie operator definition from Eq. 2.20 reads:

$$\vec{h} = \vec{\zeta} + [F(\vec{\zeta}), \vec{\zeta}] + \frac{1}{2} [F[F(\vec{\zeta}), \vec{\zeta}]] + \dots, \quad (2.41)$$

where this expression was truncated to second order in the Poisson brackets. By taking only the first two terms of the expansion and introducing the expression from Eq. 2.40, one can find an approximated expression for  $h_x^-$  which reads:

$$h_x^- \approx \zeta_x^- + [F(\vec{\zeta}), \zeta_x^-] = \zeta_x^- + \sum_{jklm} f_{jklm} [\zeta_x^{+j} \zeta_x^{-k} \zeta_y^{+l} \zeta_y^{-m}, \zeta_x^-], \quad (2.42)$$

At this point, the usefulness of Eq. 2.36 comes into play. Introducing the explicit result from Eq. 2.36 into Eq. 2.42 yields the following expression:

$$h_x^- \approx \zeta_x^- - 2i \sum_{jklm} j f_{jklm} \zeta_x^{+j-1} \zeta_x^{-k} \zeta_y^{+l} \zeta_y^{-m}. \quad (2.43)$$

Manipulating this expression further, the definition for  $\zeta_u$  as described in Eq. 2.34 can be introduced into Eq. 2.43. This yields:

$$\begin{aligned} h_x^-(N) = & \sqrt{2I_x} e^{i(\psi_x + \psi_{x_0})} \\ & - 2i \sum_{jklm} j f_{jklm} (2I_x)^{\frac{j+k-1}{2}} (2I_y)^{\frac{l+m}{2}} e^{i[(1-j+k)(\psi_x + \psi_{x_0}) + (m-l)(\psi_y + \psi_{y_0})]}. \end{aligned} \quad (2.44)$$

At this point, Eq. 2.44 is starting to look like a useful Fourier expansion. Ultimately, the diagnostic data from a circular accelerator will come from a diagnostic device triggered every turn, i.e., turn-by-turn data. For that reason, it will be useful to rewrite Eq. 2.44 in terms of the  $N$  number of turns of particles in the accelerator. The expression relating the phase advances to the turn number reads:

$$\psi_u = 2\pi Q_u N, \quad (2.45)$$

where  $2\pi Q_u$  is the respective phase advance over one turn of the accelerator, i.e., the tune of the circular accelerator.

Therefore, one can build the resonance basis by getting the quantity  $h_u^\pm = \hat{u} \pm \hat{p}_u$  in terms of the number of turns  $N$  and using Eq. 2.45. Specifically, for  $h_x^-$  this reads:

$$\begin{aligned} h_x^-(N) = & \sqrt{2I_x} e^{i(2\pi Q_x N + \psi_{x_0})} \\ & - 2i \sum_{jklm} j f_{jklm} (2I_x)^{\frac{j+k-1}{2}} (2I_y)^{\frac{l+m}{2}} e^{i[(1-j+k)(2\pi Q_x N + \psi_{x_0}) + (m-l)(2\pi Q_y N + \psi_{y_0})]}, \end{aligned} \quad (2.46)$$

where  $Q_x$  and  $Q_y$  are the horizontal and vertical uncoupled tunes. Note that one can extend this analysis to calculate the other elements in  $\vec{h}$ .

## 2.6 Amplitude-Dependent Tune Shift

The RDT formalism allows one to calculate an important quantity in accelerator physics called the amplitude-dependent tune shift. The Hamiltonian for a single particle in a linear-circular lattice

with perturbation elements reads:

$$H(x, y, s) = H_0(J_x, J_y) + H_1(J_x, \phi_x, J_y, \phi_y), \quad (2.47)$$

where  $H_0$  is the unperturbed linear Hamiltonian with tunes  $Q_x$  and  $Q_y$ , and  $H_1$  is the perturbation Hamiltonian stemming from linear and non-linear unaccounted blocks in the lattice.

From Secs. 2.1 and 2.3, the expressions for  $H_0$  and  $H_1$  have been explicitly written in Eqs. 2.14 and 2.29 in terms of  $J_x, \phi_x, J_y, \phi_y$ , therefore the sum of both expression reads:

$$H_0 + H_1 = 2\pi Q_x J_x + 2\pi Q_y J_y + \sum_{jklm} h_{jklm} (2J_x)^{\frac{j+k}{2}} (2J_y)^{\frac{l+m}{2}} e^{i[(j-k)(\phi_x + \phi_{x0}) + (l-m)(\phi_y + \phi_{y0})]}. \quad (2.48)$$

Nevertheless, it is essential to remember that  $H_1$  is the compilation of all perturbations after one turn to the linear Hamiltonian  $H_0$  and is therefore perturbative.

Consequently, for Eq. 2.48, the independent time variable is the number of turns  $N$ . For this case, the equations of motion taking  $N$  as the number of turns around the circular accelerator are just:

$$\frac{\partial J_u}{\partial N} = -\frac{\partial H}{\partial \phi_u} = -\frac{\partial H_1}{\partial \phi_u}, \quad (2.49)$$

and

$$\frac{\partial \phi_u}{\partial N} = \frac{\partial H}{\partial J_u} = 2\pi Q_u + \frac{\partial H_1}{\partial J_u}. \quad (2.50)$$

This last term  $\partial H_1 / \partial J_u$  in Eq. 2.50 will define the amplitude-dependent tune shift. If the whole lattice were linear, the betatron oscillations would gain a phase change of  $2\pi Q_u$  every turn, i.e.,  $\Delta\phi(N) = 2\pi Q_u N$ . Nevertheless, given that this new term  $H_1$  perturbs the dynamics in the accelerator, the phase change will now depend on the amplitude  $J_u$  of the betatron oscillations of the single particle. Therefore, given that this effect acts on each particle, it is incoherent. The effective result from this new term is to detune the circular lattice from its original tune  $Q_u$  for each particle.

Explicitly calculating the expression from Eq. 2.50 for  $J_x$  and  $\phi_x$  using the Hamiltonian in Eq. 2.47 yields

$$\frac{\partial \phi_x}{\partial N} = 2\pi Q_x + \sum_{jklm} h_{jklm} (j+k) (2J_x)^{\frac{j+k}{2}-1} (2J_y)^{\frac{l+m}{2}} e^{i[(j-k)(\phi_x + \phi_{x0}) + (l-m)(\phi_y + \phi_{y0})]}. \quad (2.51)$$

In particular, looking at the average limit where particles have undergone many turns around the circular accelerator  $N \rightarrow \infty$  is interesting. This is done to wash out any oscillatory behavior in  $\partial H_1 / \partial J_u$ . Therefore, the following quantity is of interest:

$$\lim_{N \rightarrow \infty} \left\langle \frac{\partial \phi_x}{\partial N} \right\rangle_N = \lim_{N \rightarrow \infty} \frac{1}{N} \int_0^N dN' \frac{\partial \phi_x}{\partial N'}, \quad (2.52)$$

which is just the definition for the average of  $\partial \phi_x / \partial N$  over  $N$  turns, for many turns. Explicitly calculating this quantity gives:

$$\begin{aligned} \lim_{N \rightarrow \infty} \left\langle \frac{\partial \phi_x}{\partial N} \right\rangle_N &= 2\pi Q_x \\ &+ \sum_{jklm} h_{jklm} (j+k) \lim_{N \rightarrow \infty} \frac{1}{N} \int_0^N dN' (2J_x)^{\frac{j+k}{2}-1} (2J_y)^{\frac{l+m}{2}} e^{i[(j-k)(\phi_x + \phi_{x0}) + (l-m)(\phi_y + \phi_{y0})]}. \end{aligned} \quad (2.53)$$

In general, it is known that  $J_u, \phi_u$  depend on the number of turns, i.e.,  $J_u, \phi_u = J_u(N), \phi_u(N)$ . Nevertheless, Eq. 2.53 can be approximated by inserting the unperturbed solution of  $H_0$ , which means that  $J_u$  is constant and  $\phi_u = 2\pi Q_u N$ . With this in mind and assuming the constants  $\phi_{u0} = 0$  without loss of generality, Eq. 2.53 reduces to

$$\begin{aligned} \lim_{N \rightarrow \infty} \left\langle \frac{\partial \phi_x}{\partial N} \right\rangle_N &= 2\pi Q_x \\ &+ \sum_{jklm} h_{jklm} (j+k) (2J_x)^{\frac{j+k}{2}-1} (2J_y)^{\frac{l+m}{2}} \lim_{N \rightarrow \infty} \frac{1}{N} \int_0^N dN' e^{2\pi i [(j-k)Q_x + (l-m)Q_y]N'}. \end{aligned} \quad (2.54)$$

A closer look into the integral in Eq. 2.54 reveals that this integral in the limit where  $N \rightarrow \infty$  is just a delta function reading  $\delta((j-k)Q_x + (l-m)Q_y)$ . As a reminder, the RDT approximation breaks down if Eq. 2.33 holds. Therefore, the delta function can only be zero if  $j = k$  and  $l = m$ . Thus, this delta function effectively becomes two Kronecker deltas— $\delta_{jk}$  and  $\delta_{lm}$ . Inserting this into Eq. 2.54 yields:

$$\lim_{N \rightarrow \infty} \left\langle \frac{\partial \phi_x}{\partial N} \right\rangle_N = 2\pi Q_x + \sum_{jklm} h_{jklm} (j+k) (2J_x)^{\frac{j+k}{2}-1} (2J_y)^{\frac{l+m}{2}} \delta_{jk} \delta_{lm}. \quad (2.55)$$

Reducing this expression further with the properties of Kronecker deltas reads:

$$\lim_{N \rightarrow \infty} \left\langle \frac{\partial \phi_x}{\partial N} \right\rangle_N = 2\pi Q_x + 2 \sum_{jl} h_{jllj} (2J_x)^{j-1} (2J_y)^l. \quad (2.56)$$

Equation 2.56 states that the terms where  $j = k$  and  $l = m$  define the constant detuning terms in the accelerator. As a consequence of Eq. 2.31, for this case, the RDTs will be real numbers, i.e.,  $h_{jklm} \in \mathbb{R}$ . Therefore, the constant detuning terms will come from even orders of  $n = j + k + l + m$ . It is worth remembering that this is a first approximation given that the assumption is that the dynamics are mainly governed by  $H_0$ . Higher-order approximations would involve recursively solving Eqs. 2.49 and 2.50 as a Taylor expansion of the actions  $J_u$  [24].

For example, Eq. 2.56 can be used to calculate the detuning due to horizontal quadrupole errors  $n = 2$ . For this, the calculation would only involve calculating  $h_{1100}$  from Eq. 2.31, the only surviving term. Therefore, the detuning in  $x$  due to quadrupole errors would read

$$\lim_{N \rightarrow \infty} \left\langle \frac{\partial \phi_x}{\partial N} \right\rangle_N = 2\pi Q_x + 2h_{1100} = 2\pi Q_x - \frac{1}{2} \sum_i L_i K_{1,i} \beta_{x,i} = 2\pi Q_x - \frac{1}{2} \sum_i L_i \frac{b_{1,i}}{\rho} \beta_{x,i}, \quad (2.57)$$

where the sum over  $i$  goes around all the quadrupole errors in the ring. Equation 2.57 gives a well-known result in accelerator physics [1].

Another example is calculating the detuning terms due to octupole components around the ring, i.e.,  $n = 4$ . In this case, the calculation yields

$$\lim_{N \rightarrow \infty} \left\langle \frac{\partial \phi_x}{\partial N} \right\rangle_N = 2\pi Q_x + 4h_{1111} J_y + 8h_{2200} J_x, \quad (2.58)$$

where if  $h_{1100}$  and  $h_{2200}$  are explicitly calculated from Eq. 2.31, this gives:

$$\lim_{N \rightarrow \infty} \left\langle \frac{\partial \phi_x}{\partial N} \right\rangle_N = 2\pi Q_x + \frac{J_y}{4} \sum_i L_i K_{3,i} \beta_{x,i} \beta_{y,i} + \frac{J_x}{8} \sum_i L_i K_{3,i} \beta_{x,i}^2. \quad (2.59)$$

It is essential to clarify that the sum over  $i$  goes around all the octupole perturbations in the ring.

To summarize, the amplitude-dependent tune shift  $\Delta(2\pi Q_u)$  is an important quantity that will change the dynamics of particles inside a circular accelerator. In order to calculate this incoherent effect to first order in perturbation theory, the quantity:

$$\Delta(2\pi Q_u) = 2\pi Q_u - \lim_{N \rightarrow \infty} \left\langle \frac{\partial \phi_u}{\partial N} \right\rangle_N = \lim_{N \rightarrow \infty} \left\langle \frac{\partial H_1}{\partial J_u} \right\rangle_N, \quad (2.60)$$

needs to be calculated.

## 2.7 Space Charge Tune Shift

Up to this point, the beam dynamics of high-energy particle accelerators has been explained in terms of single-particle dynamics. Up until now, there are a couple of implicit assumptions: (a) particles do not interact with each other, and (b) the basic blocks composing the lattice have been idealized to create the fields but without supplying any electromagnetic boundary conditions. Nevertheless, to have a model closer to reality, one has to consider the interaction between particles through the Coulomb force. Furthermore, particles also interact with the electromagnetic properties of the basic elements, ultimately creating unwanted electromagnetic wake fields. This latter phenomenon opens another branch of accelerator physics that studies collective beam instabilities [25]. However, the scope of this thesis is only interested in the first bullet point regarding direct particle-particle interactions through the Coulomb force—widely known as space charge physics. It is worth specifying that this restricts the analysis to a single bunch of particles.

As mentioned in Sec. 2.4, the Coulomb force will act as a detuning force on each individual particle. In order to explain this statement using a Hamiltonian formalism, the starting point needs to be the single-particle Hamiltonian that includes the Coulomb potential from the charge distribution in the bunch [26]. The expression for this system reads:

$$H(x, y) = H_0(x, y) + H_1(x, y) + \Psi(x, y, \tilde{z}), \quad (2.61)$$

keeping in mind that  $x$  and  $y$  are interchangeable for their respective action-phase variables  $J_x, \phi_x, J_y, \phi_y$ . For a bunched beam, the variable  $\tilde{z} = z - z_b$  is introduced in order to represent the longitudinal distance from the center of the bunch, always keeping in mind that the reference system moves with the bunch as described by a Frenet-Serret coordinate system. The center of the bunch with coordinates  $(0, 0, z_b)$  is determined from the centroid of the longitudinal charge distribution. The one-turn space-charge potential  $\Psi$ , is the average potential from all the space charge kicks around the accelerator for one turn. Nevertheless, the functional form should be similar to Eq. 2.31, to apply the same methods of Sec. 2.6. Therefore, this reads:

$$\Psi(J_x, \phi_x, J_y, \phi_y, \tilde{z}) = \sum_{jklm} G_{jklm} (2J_x)^{\frac{j+k}{2}} (2J_y)^{\frac{l+m}{2}} e^{i[(j-k)(\phi_x + \phi_{x0}) + (l-m)(\phi_y + \phi_{y0})]}. \quad (2.62)$$

Analogous to Eq. 2.31, the terms  $G_{jklm}$  are named the global space-charge resonance driving terms (GSCRDTs). One can calculate these terms as the one-turn average of the instantaneous driving terms of order  $l, j, k$  and  $m$ , which have an explicit  $s$  dependence. Therefore, the definition for the GSCRDTs  $G_{jklm}$  reads:

$$G_{jklm} = \frac{1}{C} \int_{s_0}^{s_0+C} \tilde{V}_{jklm}(s) e^{i[(j-k)(\phi_x(s)+\phi_{x0})+(l-m)(\phi_y(s)+\phi_{y0})]} ds, \quad (2.63)$$

where the terms  $\tilde{V}_{jklm}(s)$  are the instantaneous driving terms of the expansion for the self-field potential  $\psi$  of the bunch at a point  $s$  of the accelerator, i.e.,

$$\psi(J_u, \phi_u, \tilde{z}, s) = f(\tilde{z}) + \sum_{jklm} \tilde{V}_{jklm}(s) (2J_x)^{\frac{j+k}{2}} (2J_y)^{\frac{l+m}{2}} e^{i[(j-k)(\phi_x+\phi_{x0})+(l-m)(\phi_y+\phi_{y0})]}. \quad (2.64)$$

The term  $f(\tilde{z})$  will hold any longitudinal dependence of the potential, but it is generally irrelevant to the space charge detuning calculation. This approach is similar to the one taken by Ref. [27]. This assumes the self-field potential has been calculated and a Floquet transformation has been performed using Eq. 2.8. The self-potential  $\psi(x, y, \tilde{z}, s)$  is determined self-consistently from the 3D Poisson equation with a particle number density of the bunch  $n_b(x, y, \tilde{z}, s)$  reading:

$$\left( \frac{\partial}{\partial x} + \frac{\partial}{\partial y} + \frac{\partial}{\partial \tilde{z}} \right) \psi(x, y, \tilde{z}, s) = -\frac{2\pi K_b}{N_b} n_b(x, y, \tilde{z}, s), \quad (2.65)$$

where  $K_b$  is a dimensionless parameter known as the self-field perveance defined as

$$K_b = \frac{2N_b e_b^2}{\gamma_L^3 m_b \beta_L^2 c^2}, \quad (2.66)$$

with  $N_b$  being the total number of particles in the bunch defined as  $N_b = \int dx dy d\tilde{z} n_b(x, y, \tilde{z}, s)$ ,  $e_b$  is the charge of one beam particle,  $m_b$  is the rest mass of one beam particle,  $\gamma_L$  and  $\beta_L$  being the relativistic longitudinal factors of a beam with total energy  $E_T = \gamma_L m_b c^2$ , and  $c$  being the speed of light.

One can find the solution to Eq. 2.65 in any book of mathematical methods for physics, see Refs. [28, 29]. The solution to this equation involves using Green's function and finding the convolution with the particle number density  $n_b(x, y, \tilde{z}, s) = n_b(\vec{r}, s)$ . This reads:

$$\psi(x, y, \tilde{z}, s) = -\frac{2\pi K_b}{N_b} \int_{\mathbb{R}^3} d\vec{r}' \frac{n_b(\vec{r}, s)}{|\vec{r} - \vec{r}'|}. \quad (2.67)$$

In section 2.6, it was interesting to look at how particles at different amplitudes undergo different detuning due to  $H_1$  given their  $J_u$  coordinates. The same will be valid for the effect of  $\Psi$  on the single-particle dynamics. The quantity of interest will be the detuning due to Coulomb forces—the space-charge tune shift. Nevertheless, it is essential to note that the space charge will be a continuous force around the accelerator. Therefore, the terms  $G_{jklm}$  in order to enter the one-turn Hamiltonian in Eq. 2.61 will have to be an average of the space-charge force around the ring for a single particle—as defined in Eq. 2.63. Ultimately, the space-charge tune shift will also be an incoherent quantity.

For now, let  $H_1 = 0$ , but let space-charge dictate the functional form of  $\Psi$ . For this case, and in analogy to Eq. 2.50, the space charge tune shift will be dictated by:

$$\frac{\partial \phi_u}{\partial N} = \frac{\partial H}{\partial J_u} = 2\pi Q_u + \frac{\partial \Psi}{\partial J_u}. \quad (2.68)$$

The non-trivial part of this calculation is figuring  $\partial\Psi/\partial J_u$  for a specific bunch distribution after calculating the integral in Eq. 2.67.

The first case to analyze is when the bunch has a uniform charge density enclosed in a 3D ellipsoid. The charge bunch distribution reads:

$$n_b(x, y, \tilde{z}, s) = \begin{cases} \hat{n}_b(s), & \text{if } 0 \leq \frac{x^2}{a^2(s)} + \frac{y^2}{b^2(s)} + \frac{\tilde{z}^2}{c^2(s)} \leq 1 \\ 0, & \text{if else.} \end{cases}, \quad (2.69)$$

where  $a(s)$ ,  $b(s)$  and  $c(s)$  are the length of the semi-axes of the ellipsoid around the accelerator and can be calculated from the beam-envelope equations [26]. Additionally, the constant particle number density over an ellipsoid is defined as  $\hat{n}_b = N_b/V_e$ , where  $V_e$  is the volume of an ellipsoid reading  $V_e = (4/3)\pi abc$ . Inputting this distribution into Eq. 2.67 gives the expression for the potential. This involves solving a 3D integral inside the ellipsoid. This reads:

$$\psi(x, y, \tilde{z}, s) = -\frac{2\pi K_b \hat{n}_b}{N_b} \int_{\mathbb{S}} d\vec{r}' \frac{1}{|\vec{r} - \vec{r}'|}, \quad (2.70)$$

where  $\mathbb{S}$  is the region enclosed by the ellipsoid. The integral has been studied with ellipsoidal coordinates, and the solution can be found in Refs. [26, 30]. In these references, it is shown that

the solution can be expressed as a quadratic function of  $x$ ,  $y$  and  $\tilde{z}$  such that:

$$\psi(x, y, \tilde{z}, s) = -\frac{\pi K_b \hat{n}_b abc}{N_b} [-Ax^2 - By^2 - \tilde{C}\tilde{z}^2 + D], \quad (2.71)$$

such that  $A$ ,  $B$ ,  $\tilde{C}$  and  $D$  are calculated as:

$$A(s) = \int_0^\infty \frac{d\varsigma}{(a^2 + \varsigma) \sqrt{(a^2 + \varsigma)(b^2 + \varsigma)(c^2 + \varsigma)}}, \quad (2.72)$$

$$B(s) = \int_0^\infty \frac{d\varsigma}{(b^2 + \varsigma) \sqrt{(a^2 + \varsigma)(b^2 + \varsigma)(c^2 + \varsigma)}}, \quad (2.73)$$

$$\tilde{C}(s) = \int_0^\infty \frac{d\varsigma}{(c^2 + \varsigma) \sqrt{(a^2 + \varsigma)(b^2 + \varsigma)(c^2 + \varsigma)}}, \quad (2.74)$$

$$D(s) = \int_0^\infty \frac{d\varsigma}{\sqrt{(a^2 + \varsigma)(b^2 + \varsigma)(c^2 + \varsigma)}}. \quad (2.75)$$

Furthermore, Eq. 2.71 can be rewritten using Eq. 2.8 to highlight the dependence on  $J_u, \phi_u$  explicitly. This reads:

$$\begin{aligned} \psi(J_u, \phi_u, \tilde{z}, s) = & -\frac{\pi K_b \hat{n}_b abc}{N_b} \left[ -A (2\beta_x J_x) \left( \frac{e^{2i(\phi_x + \phi_{x0})} + e^{-2i(\phi_x + \phi_{x0})} + 2}{4} \right) \right. \\ & \left. - B (2\beta_y J_y) \left( \frac{e^{2i(\phi_y + \phi_{y0})} + e^{-2i(\phi_y + \phi_{y0})} + 2}{4} \right) - \tilde{C}\tilde{z}^2 + D \right]. \end{aligned} \quad (2.76)$$

Equation 2.76 can be cross-examined using Eq. 2.64 in order to retrieve the driving terms  $\tilde{V}_{jklm}$  and  $f(\tilde{z})$ . Therefore, for a uniform distribution, the following expansion for the self-potential holds:

$$\begin{aligned} \psi(J_u, \phi_u, \tilde{z}, s) = & f_0(\tilde{z}) + \tilde{V}_{2000} J_x e^{2i(\phi_x + \phi_{x0})} + \tilde{V}_{0200} J_x e^{-2i(\phi_x + \phi_{x0})} + \tilde{V}_{1100} J_x \\ & + \tilde{V}_{0020} J_y e^{2i(\phi_y + \phi_{y0})} + \tilde{V}_{0002} J_y e^{-2i(\phi_y + \phi_{y0})} + \tilde{V}_{0011} J_y. \end{aligned} \quad (2.77)$$

The instantaneous driving terms  $\tilde{V}_{jklm}$  from Eq. 2.77 are summarized in Table 2.2. Table 2.2 also shows how to calculate the SCRTs  $G_{jklm}$  from averaging out the  $\tilde{V}_{jklm}(s)$  all around the circular accelerator as an example of using Eq. 2.63. One can calculate the integrals for the  $G_{jklm}$  with previous knowledge of the unperturbed beta functions and phase advances around the ring. The

envelope equations, as described in Ref. [26], should also be solved in order to get  $a(s)$ ,  $b(s)$  and  $c(s)$  around the lattice, ultimately, aiding in the evaluation of  $A(s)$ ,  $B(s)$  and  $C(s)$ .

Table 2.2 Instantaneous driving terms and GSCRDTs for a uniform beam

$\tilde{V}_{jklm}$	$\tilde{V}_{jklm}(s)$	$G_{jklm}$	$G_{jklm}$
$\tilde{V}_{2000}$	$\frac{3}{8}K_b A(s)\beta_x(s)$	$G_{2000}$	$\frac{3K_b}{8C} \int_{s_0}^{s_0+C} A(s)\beta_x(s)e^{2i(\phi_x(s)+\phi_{x0})} ds$
$\tilde{V}_{0200}$	$\frac{3}{8}K_b A(s)\beta_x(s)$	$G_{0200}$	$\frac{3K_b}{8C} \int_{s_0}^{s_0+C} A(s)\beta_x(s)e^{-2i(\phi_x(s)+\phi_{x0})} ds$
$\tilde{V}_{1100}$	$\frac{3}{4}K_b A(s)\beta_x(s)$	$G_{1100}$	$\frac{3K_b}{4C} \int_{s_0}^{s_0+C} A(s)\beta_x(s) ds$
$\tilde{V}_{0020}$	$\frac{3}{8}K_b B(s)\beta_y(s)$	$G_{0020}$	$\frac{3K_b}{8C} \int_{s_0}^{s_0+C} B(s)\beta_y(s)e^{2i(\phi_y(s)+\phi_{y0})} ds$
$\tilde{V}_{0002}$	$\frac{3}{8}K_b B(s)\beta_y(s)$	$G_{0002}$	$\frac{3K_b}{8C} \int_{s_0}^{s_0+C} B(s)\beta_y(s)e^{-2i(\phi_y(s)+\phi_{y0})} ds$
$\tilde{V}_{0011}$	$\frac{3}{4}K_b B(s)\beta_y(s)$	$G_{0011}$	$\frac{3K_b}{4C} \int_{s_0}^{s_0+C} B(s)\beta_y(s) ds$

Just like in Sec. 2.6, looking at the terms where  $j = k$  and  $l = m$  is interesting. This calculation will give nonlinear detuning terms due to a uniform charge distribution. Therefore, similar to Eq. 2.56, the nonlinear detuning terms due to space charge for the horizontal plane are:

$$\lim_{N \rightarrow \infty} \left\langle \frac{\partial \phi_x}{\partial N} \right\rangle_N = 2\pi Q_x + 2 \sum_{jl} G_{jllj} (2J_x)^{j-1} (2J_y)^l. \quad (2.78)$$

Therefore, it is interesting to look at the terms  $G_{1100}$  and  $G_{0011}$ , which will cause constant detuning of the unperturbed tunes.

One can do the previous analysis for a uniform beam, i.e., the particle number density is constant inside the bunch. Nevertheless, this is an idealized case for a circular accelerator. A more realistic approach would be to consider a Gaussian distribution. This multivariate distribution, assuming no correlation, reads:

$$n_b(x, y, \tilde{z}, s) = \frac{1}{(2\pi)^{3/2} \sigma_x \sigma_y \sigma_{\tilde{z}}} e^{-\frac{x^2}{2\sigma_x^2} - \frac{y^2}{2\sigma_y^2} - \frac{\tilde{z}^2}{2\sigma_{\tilde{z}}^2}} \quad (2.79)$$

This approach is the approach taken in Refs. [23, 27]. Specifically, the Python library developed at CERN called PySCRDT [23] allows for the calculation of GSCRDTs and the tune footprint for a Gaussian beam distribution. As mentioned before in the discussion of Fig. 2.4, the tune footprint depends on the intensity of the beam interchangeable with the beam space charge perveance parameter  $K_b$ . Figure 2.5 shows the space charge tune footprint for the Recycler Ring for typical beam parameters used in studies. One can calculate the footprint using PySCRDT. Nevertheless, the approach behind PySCRDT is similar to the example provided with a uniform beam distribution. One special feature of the Gaussian beam is that the space charge potential is its largest at the core of the beam. Hence, the detuning is largest for particles close to the middle of the bunch. In contrast, the particles away from the core of the beam will not be subject to the full space charge potential and, therefore, will oscillate close to the unperturbed nominal tune of  $Q_u$ . Figure 2.5 illustrates this concept by drawing a color map at different actions, close to the beam core and  $3\sigma_u$  away from the center of the bunch—location where particles oscillate close to nominal tunes.

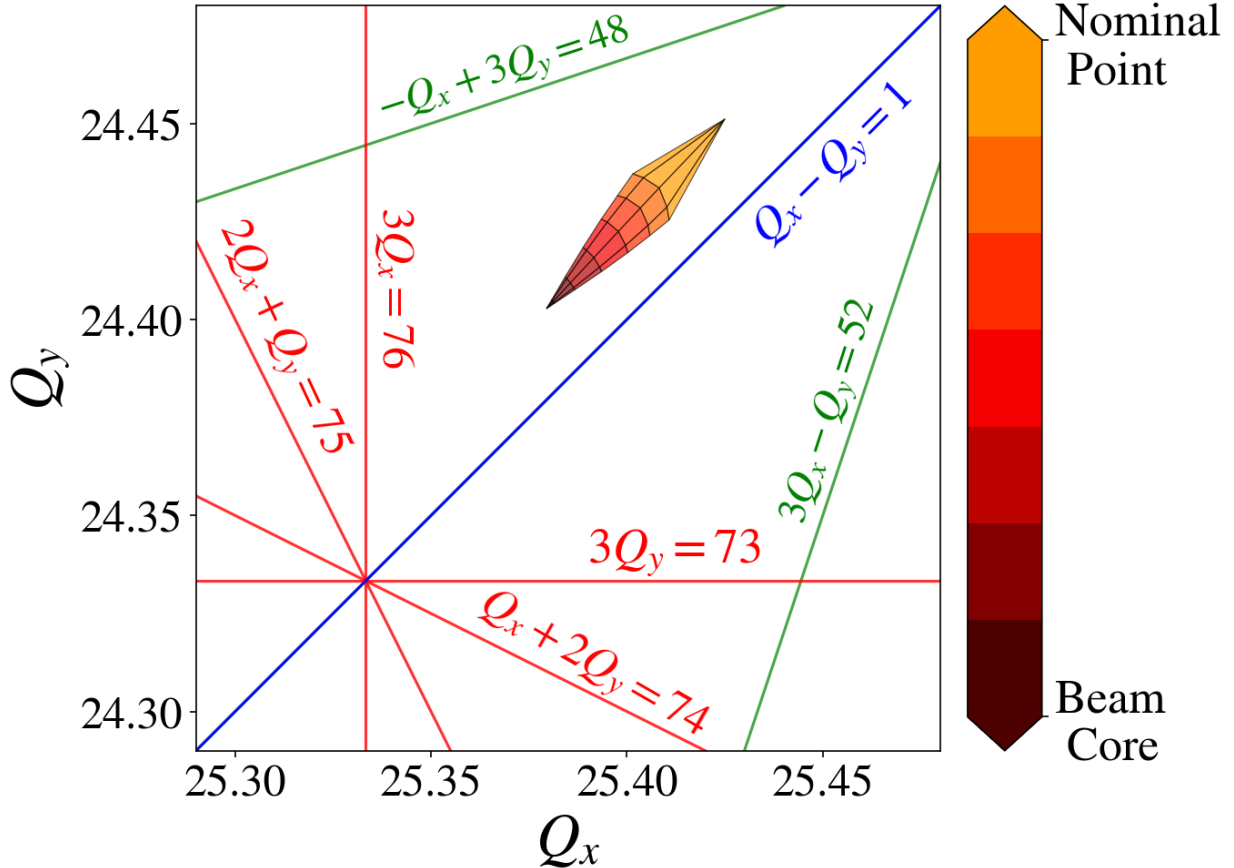


Figure 2.5 Tune footprint for a Gaussian beam in the Recycler Ring at an intensity of 5e10 particles per bunch created with PySCRDT.

Up until now, the assumption  $H_1 = 0$  has held for this section. Nevertheless, there will be an interplay between the nonlinear Hamiltonian and the space charge potential in high-intensity particle accelerators. Ultimately, the terms  $h_{jklm}$  and  $G_{jklm}$  will dictate the perturbation to the linear Hamiltonian by their effective detuning. Therefore, the following Hamiltonian will describe the perturbation due to nonlinear elements in the circular lattice and due to space charge forces:

$$H(J_x, \phi_x, J_y, \phi_y, \tilde{z}) = 2\pi Q_x J_x + 2\pi Q_y J_y + \sum_{jklm} (h_{jklm} + G_{jklm}) (2J_x)^{\frac{j+k}{2}} (2J_y)^{\frac{l+m}{2}} e^{i[(j-k)(\phi_x + \phi_{x0}) + (l-m)(\phi_y + \phi_{y0})]}. \quad (2.80)$$

## CHAPTER 3

### THE FNAL RECYCLER RING

#### 3.1 Introduction

The Fermilab Recycler Ring (RR) is one of the circular accelerators located in the Fermilab Accelerator Complex. It was originally designed to store and accumulate antiprotons that remained from a Tevatron event [31]. The recycling of antiprotons was deemed ineffective and was never operationally implemented [32]. Since 2011, the RR has been repurposed as a pre-injector to the Main Injector (MI) by storing and accumulating protons [14]. It is worth pointing out that the MI and the RR share the same tunnel, with a circumference of 3.319 km (2.062 mi). The work done for this thesis focuses on the Recycler Ring. The following chapter starts by giving a general description of the operation and physics of the Recycler Ring. The following sections introduce and motivate the compensation of third-order resonances for high-intensity operation.

The MI/RR complex is fed protons by the Proton Source, which by itself consists of the Pre-Accelerator, the Linear Accelerator (Linac), and the Booster. The Pre-Accelerator systems provide  $H^-$  ions to the Linac, where they are accelerated to an energy of 400 MeV. After this, the beam is injected into the Booster Ring. The Booster is a rapid-cycling synchrotron operating at a 15 Hz repetition rate. During this injection process, the  $H^-$  beam passes through a carbon stripping foil and incorporates into the circulating proton beam. The Booster ramps the energy up from 400 MeV to 8 GeV. This 8 GeV proton beam can either go to the Booster Neutrino Experiments or get injected into the Recycler Ring. Once in RR, the beam has two possible destinations: 1) high-energy neutrino experiments through MI or 2) Muon Campus. For the latter, the proton beam gets rebunched from 53 MHz to 2.5 MHz and transported to the Muon Campus. The proton beam gets slip-stacked for high-energy neutrino experiments, doubling the intensity injected into the Main Injector. Once in MI, the beam is accelerated to 120 GeV and sent to the NuMI (Neutrinos at the Main Injector) beam facility [13, 14, 32]. Figure 3.1 describes the current accelerator complex, including the experimental beamlines that feed neutrino, muon, and fixed target experiments.

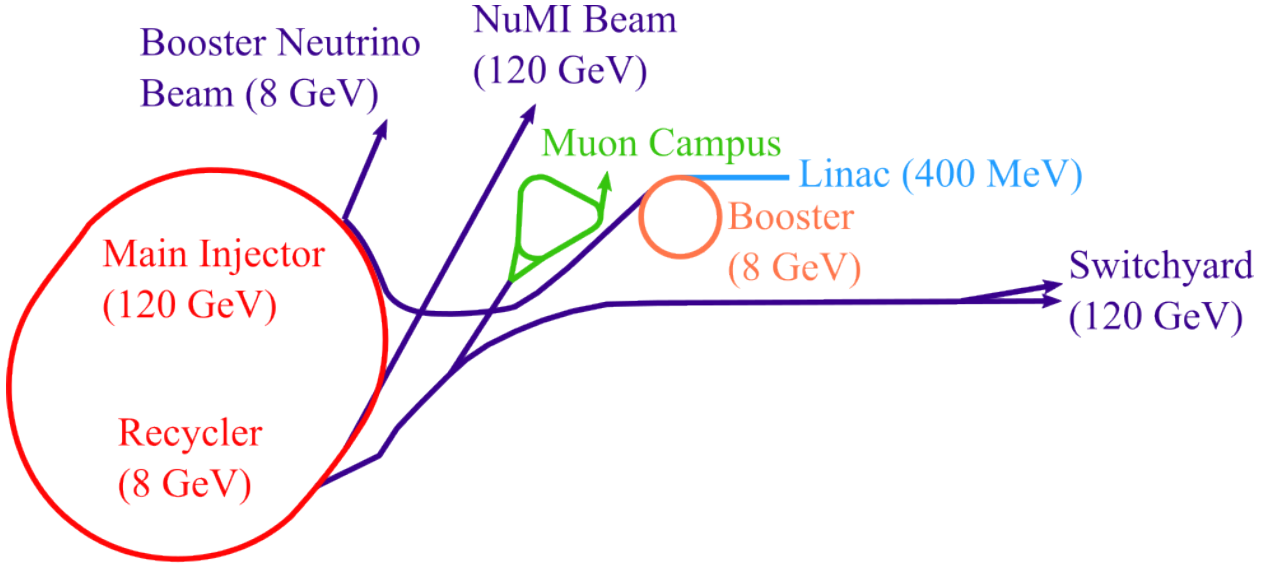


Figure 3.1 Current operational layout of the Fermilab Accelerator Complex as of 2024. The original plot was provided by R. Ainsworth, first published on Ref. [14], but modified for this document.

The Proton Improvement Plan II (PIP-II) is the first step in establishing the Fermilab Accelerator Complex as a multi-MW proton facility [33]. The near-future objective is to deliver a 1.2 MW proton beam to the Deep Underground Neutrino Experiment (DUNE) through the Long-Baseline Neutrino Facility (LBNF) [34], still in construction. In order to meet this goal, Fermilab is planning several upgrades in the accelerator complex, including a new 800 MeV superconducting linear accelerator. The plan for the layout of the Fermilab Accelerator Complex is shown in Fig. 3.2. With minimal upgrades to the Main Injector and Recycler Ring but a substantial overhaul of the Booster Ring, this will allow for a 50% increase in particles per pulse intensity. Table 3.1 also specifies some upgrades that will happen for the PIP-II era. Some examples include an increase of the particle per bunch intensity, a shortening of the Main Injector acceleration ramp, and an increase in the Booster ramping rate. As the Recycler Ring starts to deal with higher intensities from the PIP-II upgrade, it is important to mitigate the effects of space charge, as discussed in Secs. 2.4 and 2.7. Particles along the bunch will experience space charge forces leading to detuning in their betatron frequencies. Given the incoherent nature of this process, this leads to the beam having a larger tune spread in the tune diagram and having particles operate on top of resonances.

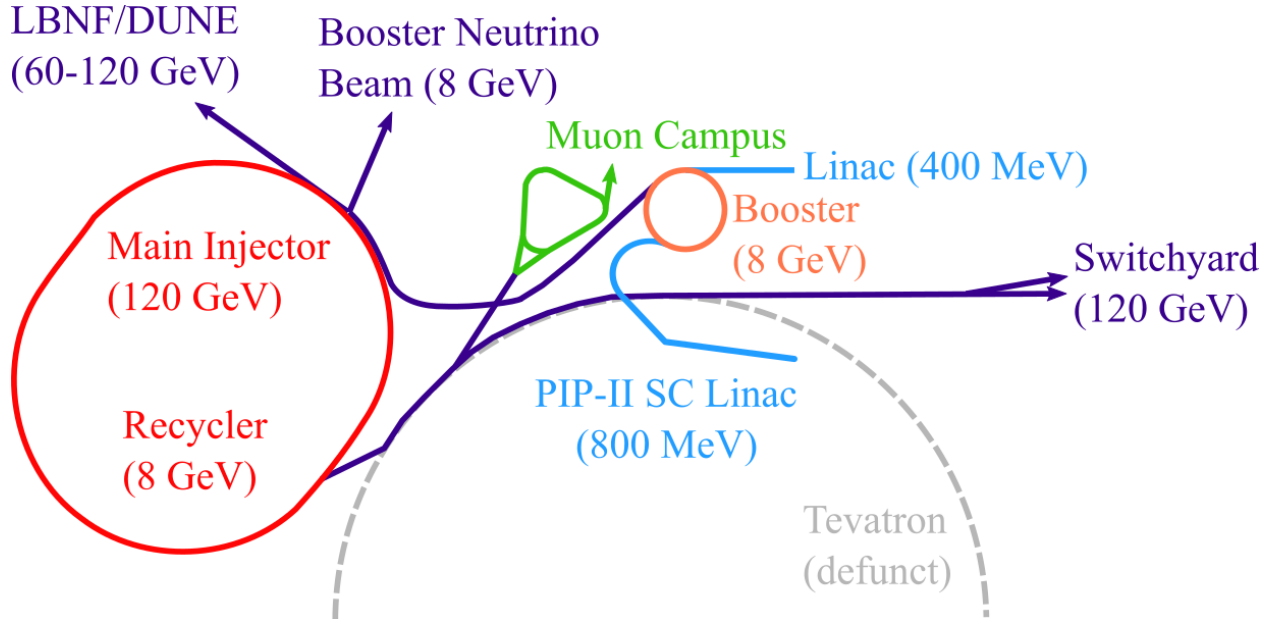


Figure 3.2 Future layout of the Fermilab Accelerator Complex for the Proton Improvement Plan II (PIP-II). The original plot was provided by R. Ainsworth, first published on Ref. [14], but modified for this document.

### 3.2 General Description

The RR is a permanent magnet storage ring operating at a fixed momentum of 8.835 GeV/c, equivalent to an energy of 8 GeV. The basic cell structures of this machine are FODO (Focusing Quadrupole - Drift - Defocusing Quadrupole - Drift) cells. During its conception, the need for a quick and non-expensive design spurred the idea of combining quadrupole and dipole magnets into one combined function magnet. Figure 3.3 shows these combined function magnets as the green-covered magnets on the top ring—the Recycler Ring. In order to further reduce costs during its construction, these magnets were chosen to be permanent magnets made out of a strontium ferrite [31]. One advantage of having permanent magnets is that there is no need for power supplies, cooling systems, or power distribution cables. Consequently, these types of magnets are very stable against time and temperature. Nevertheless, the magnetic field of such magnets does degrade over time. Reference [14] shows how the fields in RR-type magnets can degrade around 1% after 20 years. Ultimately, this slightly changes the nominal energy in the machine.



Figure 3.3 Picture of the Main Injector (blue and red magnets in the bottom) and the Recycler Ring (green magnets up top) tunnel.

Figure 3.3 reminds the reader that the Main Injector and the Recycler Ring share the same tunnel. This tunnel is divided into six sections with labels: 100, 200, 300, 400, 500 and 600. Injection from the Booster Ring into the Recycler takes place just after the beginning of section 100. Specifically, this happens at a Lambertson magnet labeled as LAM102. This case is just an example of how every RR or MI element will be labeled according to its position in one of these sections. Figure 3.4 shows a schematic of the Recycler Ring section with some labels for critical subsystems inside them. In particular, it shows the location close to 232, where the beam is transferred from the Recycler Ring to the Main Injector. Figure 3.4 also presents the location in section 500 where the beam is transferred from RR to the Muon Campus, as well as the location after 401 where the beam is dumped towards the abort line [14, 35].

As highlighted in Fig. 3.4, a critical subsystem is the tune trombone. The RR has two of them, one in sections 601-609 and another in 301-309. A tune or phase trombone is a linear insert

composed of quadrupoles introducing local phase advances. These quadrupoles are powered to add a controlled phase advance while leaving the Twiss parameters unchanged at the end of the insert and matched to the start of the trombone [31, 36]. Ultimately, these subsystems introduce local tune changes that allow the control of both tunes in a  $\pm 0.5$  range, i.e.,  $\Delta Q_u = \pm 0.5$ . The Recycler Ring has accelerator applications through ACNET that allow the control of these tune trombones and set the tunes to some desired values. Furthermore, this application allows tune ramps and continuous linear changes in the tunes. This feature is crucial for building dynamic loss maps—an important tool to probe resonance lines as will be described in Sec. 4.5.1.

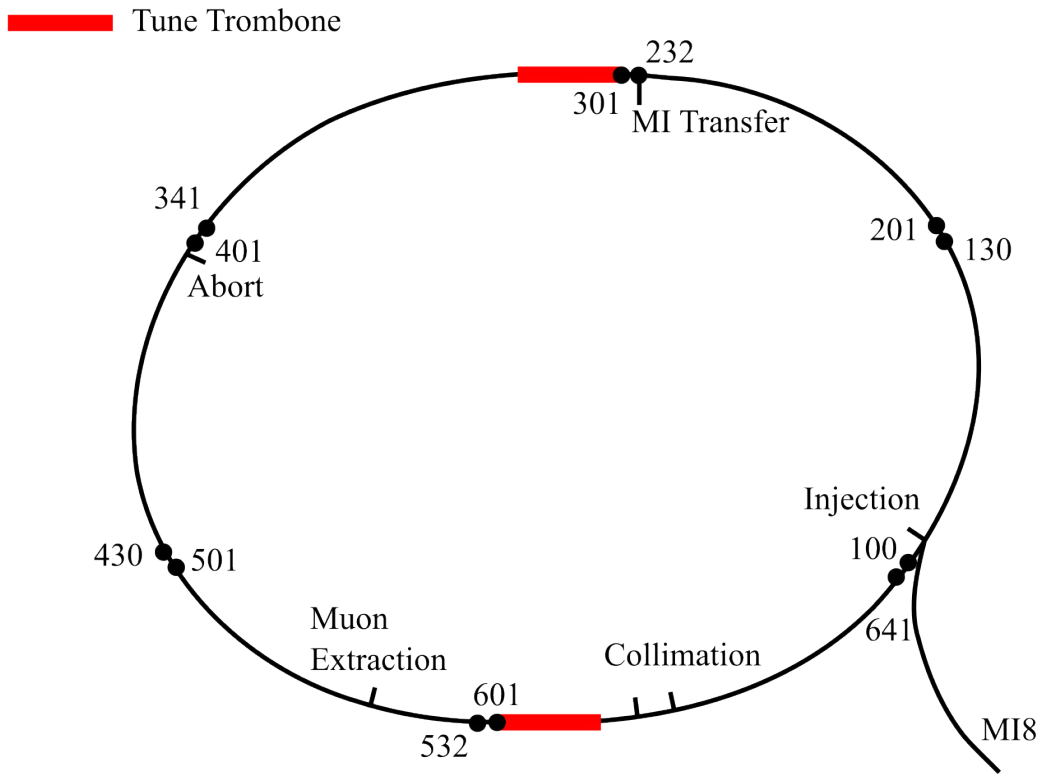


Figure 3.4 Schematic layout of the Recycler Ring and its corresponding sections. Original plot provided by R. Ainsworth, first published on Ref. [14].

The Recycler Ring has 104 FODO cells distributed into three main groups around its 3319.4-meter circumference [31]. The first group of cells comprises two permanent magnet quadrupoles arranged so that each cell has a phase advance of  $90^\circ$ . There are 18 cells of this first group throughout the Recycler. The second group comprises a cell with two combined function magnets

to simultaneously bend and focus the beam. This type of cell also has a phase advance of  $90^\circ$ , with 54 cells of this type in the RR. Ultimately, the configuration of these cells will dictate the Twiss parameters around the ring. Figure 3.5 shows the beta functions  $\beta_u(s)$  around the Recycler Ring tuned to some particular set of tunes. Some horizontal BPMs are marked in the upper horizontal axis to note the corresponding section in the tunnel.

Before describing the third group, it is worth clarifying to the reader that the transverse motion inside any circular accelerator is dictated by:

$$u(s) = u_\beta(s) + D_u(s)\delta, \quad (3.1)$$

where  $u$  is either the  $x$  or  $y$  plane,  $u_\beta(s)$  is the betatron motion as described by Eq. 2.8,  $D_u(s)$  is known as the dispersion function and  $\delta = \Delta p/p_0$  is the fractional momentum deviation of an individual particle with respect to the reference longitudinal momentum  $p_0$ . In Ch. 2, specifically in Sec. 2.2, an assumption was made that the transverse coordinates were not going to be influenced by any longitudinal property, focusing on on-momentum particles, i.e.,  $\delta = 0$ . Nevertheless, for this section, it is relevant to introduce the dispersion function  $D_u(s)$  to describe the Recycler Ring in all its glory and detail. The dispersion function depends on the distribution of quadrupole and dipole components throughout the ring [1]. Even so, the scope of this work regarding resonance compensation will not consider any longitudinal-transverse coupling.

With all this said, the third group comprises special dispersion suppressor cells,  $D_x(s) = 0$  for these regions. Each one has two combined function magnets and globally has a betatron phase advance of again  $90^\circ$ . This cell type will allow dispersion-free regions necessary for the Recycler's injection, extraction, and other particular subsystems. There are 32 cells of this type. Figure 3.6 shows the dispersion functions for the Recycler Ring. Thanks to this third type of FODO cells, the horizontal dispersion function  $D_x(s)$  has regions of close-to-zero values. The vertical dispersion is negligible, i.e.,  $D_y(s) \approx 0$ .

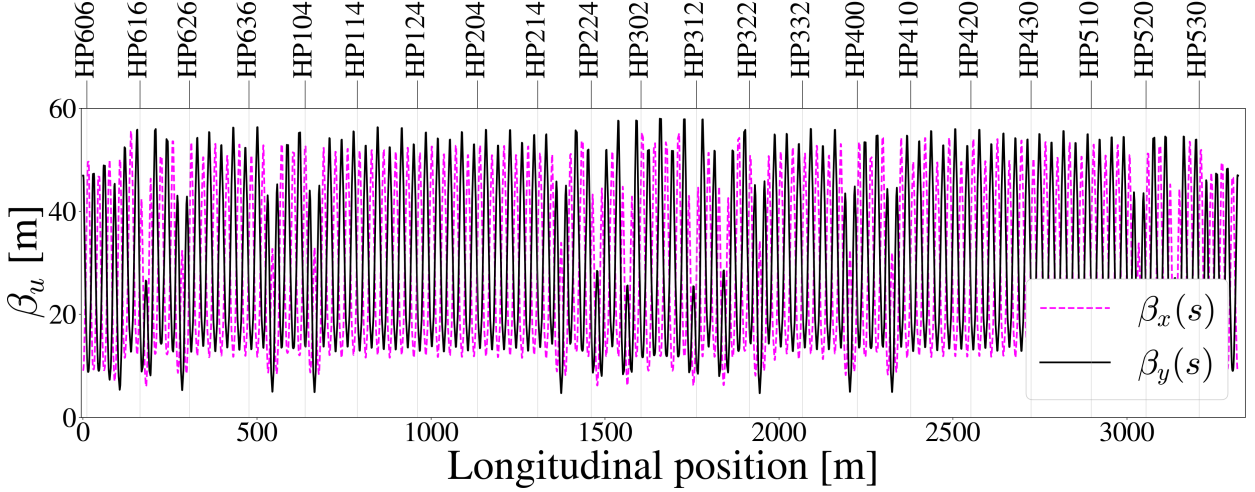


Figure 3.5 Beta functions for the Recycler Ring lattice tuned to  $Q_x = 25.44$  and  $Q_y = 24.39$ . Lattice functions are calculated from the lattice file using SYNERGIA.

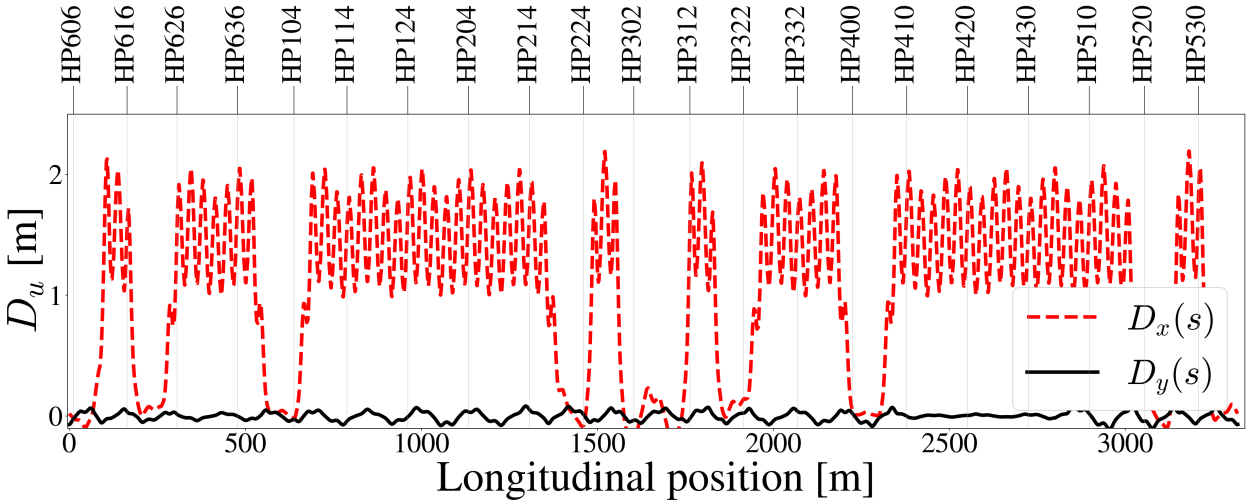


Figure 3.6 Dispersion functions for the Recycler Ring lattice tuned to  $Q_x = 25.44$  and  $Q_y = 24.39$ . Lattice functions are calculated from the lattice file using SYNERGIA.

The ultimate role of the Recycler Ring is to smooth the way for high-intensity proton beam injection into the Main Injector. In particular, for the high-intensity beam delivered to the neutrino experiments, the Recycler performs a beam manipulation known as slip-stacking. Although this longitudinal manipulation is out of the main scope of this thesis, it is relevant to briefly explain this procedure since this is the Recycler Ring's main feature. Slip-stacking is the process through which a pair of bunches are manipulated in longitudinal phase space to merge them into one higher-intensity bunch [35]. In particular, the RR utilizes two RF stations to decelerate and accelerate

trains of bunches. The Recycler can fit 7 Booster Rings. Hence, 6+6 beam batches are injected and slip-stacked, while 1 batch space is left as a gap for the kickers to fire. Each batch is composed of 81 bunches following the harmonic number of the Recycler. A more detailed explanation of the Recycler Ring's slip-stacking procedure can be found in Refs. [14, 35, 37]. Ultimately, this slip-stacking process is relevant because it doubles the particles per bunch intensity (ppb), which has significant consequences for the transverse dynamics, as explained in Sec. 2.7. Furthermore, Table 3.1 summarizes some important parameters for the RR slip-stacking and the general operation of the neutrino-bound beam.

Table 3.1 Typical Recycler Ring properties for beam sent to NuMI, with some PIP-II nominal parameters.

Parameter	Value	Unit
Circumference	3319.4	m
Momentum	8.835	GeV/c
Revolution Period	11.1	$\mu$ s
Revolution Frequency	90.1	kHz
RF Frequency	52.8	MHz
RF Voltage	80	kV
Harmonic Number	588	
Synchrotron Tune	0.0028	
Slip Factor	$-8.6 \times 10^{-3}$	
Superperiodicity	2	
Horizontal Tune	25.43	
Vertical Tune	24.445	
Horizontal Chromaticity	-6	
Vertical Chromaticity	-7	
95% Normalized Emittance	15	$\pi$ mm mrad
95% Longitudinal Emittance	0.08	eV s
Intensity	$5 \times 10^{10}$	ppb
	$8 \times 10^{10}$ (PIP-II)	ppb
MI Ramp Time	1.2	s
	1.133	s
	1.067	s
Booster Frequency	15	Hz
	20 (PIP-II)	Hz

### 3.3 Tune Diagram and Resonances

Table 3.1 specifies nominal horizontal and vertical tunes for the operation of the Recycler Ring. While this pair of tunes can be switched around during operation to reduce losses, they will always stay clear of the surrounding transverse betatron resonances, as introduced in Sec. 2.4. Figure 3.7 plots the resonance lines relevant to the Recycler Ring operation, with their corresponding order in the multipole expansion. Specifically, this study looks at normal sextupole lines  $3Q_x = 76$  and  $Q_x + 2Q_y = 74$ , plus skew sextupole lines  $3Q_y = 73$  and  $2Q_x + Q_y = 75$ .

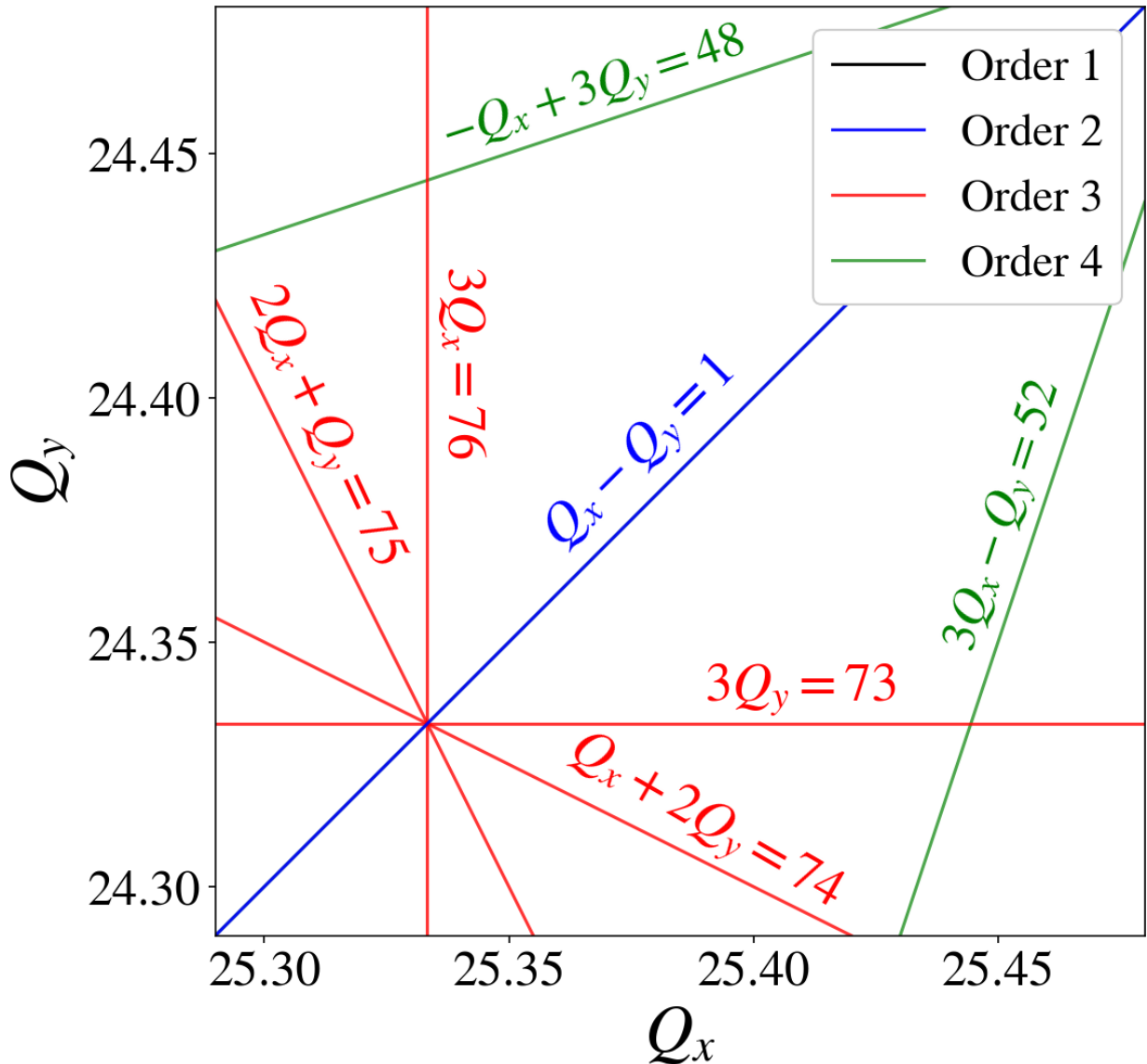


Figure 3.7 Portion of the tune diagram enclosing the operational tunes of the Recycler Ring.

Starting from the lowest order resonance line, Fig. 3.7 shows the second-order linear coupling line  $Q_x - Q_y = 1$ . This resonance line comes from the skew-quadrupole component accumulated all around the ring. While operating on this resonance line will not lead to chaotic motion, the dynamics are characterized by action exchange between the betatron modes [1]. This exchange can cause emittance growth, eventually leading to beam loss. Due to this fact, the Recycler Ring has two families of skew quadrupoles, which correct this resonance line. Consequently, operating close to this resonance line is feasible with this correction.

The third-order resonance lines are the main focus of this thesis. They are driven by normal- and skew-sextupole components distributed around the ring. In particular, it is known that the combined function magnets are the main drivers of these resonance lines. Even though these magnets were designed to be quadrupole and dipole only, they can still have sextupole components from construction errors. Nevertheless, since they are permanent magnets, little can be done about the magnets themselves. As a result, the following work explores a compensation technique to bring down the lattice RDTs that drive these resonance lines. A summary of the RDTs, their corresponding resonance line, and the frequency position of their spectral lines are summarized in Table 3.2. The spectral lines are a concept critical to the measurement of RDTs, and it is introduced in the next chapter. The compensation of these RDTs involves the usage of additional compensation sextupoles. Section 3.6 describes these elements. Chapter 4 goes into a deep dive explaining this approach from a theoretical and experimental point of view.

Table 3.2 Corresponding RDTs and location of spectral lines for each resonance line.

<b>Resonance Line</b>	<b>Source</b>	<b>RDT</b>	<b>Hor. Spect.</b>	<b>Vert. Spect.</b>
$3Q_x = 76$	Normal Sextupole	$h_{3000}$	(-2,0)	-
$Q_x + 2Q_y = 74$	Normal Sextupole	$h_{1020}$	(0,-2)	(-1,-1)
$3Q_y = 73$	Skew Sextupole	$h_{0030}$	-	(0,-2)
$2Q_x + Q_y = 75$	Skew Sextupole	$h_{2010}$	(-1,-1)	(-2,0)

Finally, there are also fourth-order resonance lines close to the nominal operation of the Recycler. Octupole components around the ring drive these lines. In practice,  $-Q_x + 3Q_y = 48$  and  $3Q_x - Q_y = 52$  are not particularly concerning to the operation of the RR. Their corresponding lattice RDTs

are not large enough to consider them dangerous during the RR cycle, i.e., the beam is stored for approximately 1 second. Nevertheless, these lines are interesting because fourth-order resonance lines are susceptible to being amplified by the space charge potential through the SCRDTs, as described in Sec. 2.7.

### 3.4 High Intensity and Tune Footprint

In order to achieve the PIP-II beam power objective, the Recycler will be required to store and accumulate 50% more beam than current operations [33]. As explained in Sec. 2.7, larger beam intensities lead to larger space charge tune spread. Figure 3.8 shows how, for the typical operation to the neutrino experiments under future PIP-II specifications, there is a space charge tune spread of around 0.1 in both planes. At nominal tunes, it is clear that for high-intensity operation, the particles in the core of the beam will start to operate on top of third-order resonances. One feature further complicates this picture: particles will undergo synchrotron oscillations within the diamond-shaped region. Particles will go from the core of the beam to its outskirts, and its incoherent space charge tune shift will fluctuate accordingly. Therefore, particles will cross in and out of these third-order resonances at a synchrotron period. Ultimately, Fig. 3.8 just tries to take a snapshot of the region of these excursions.

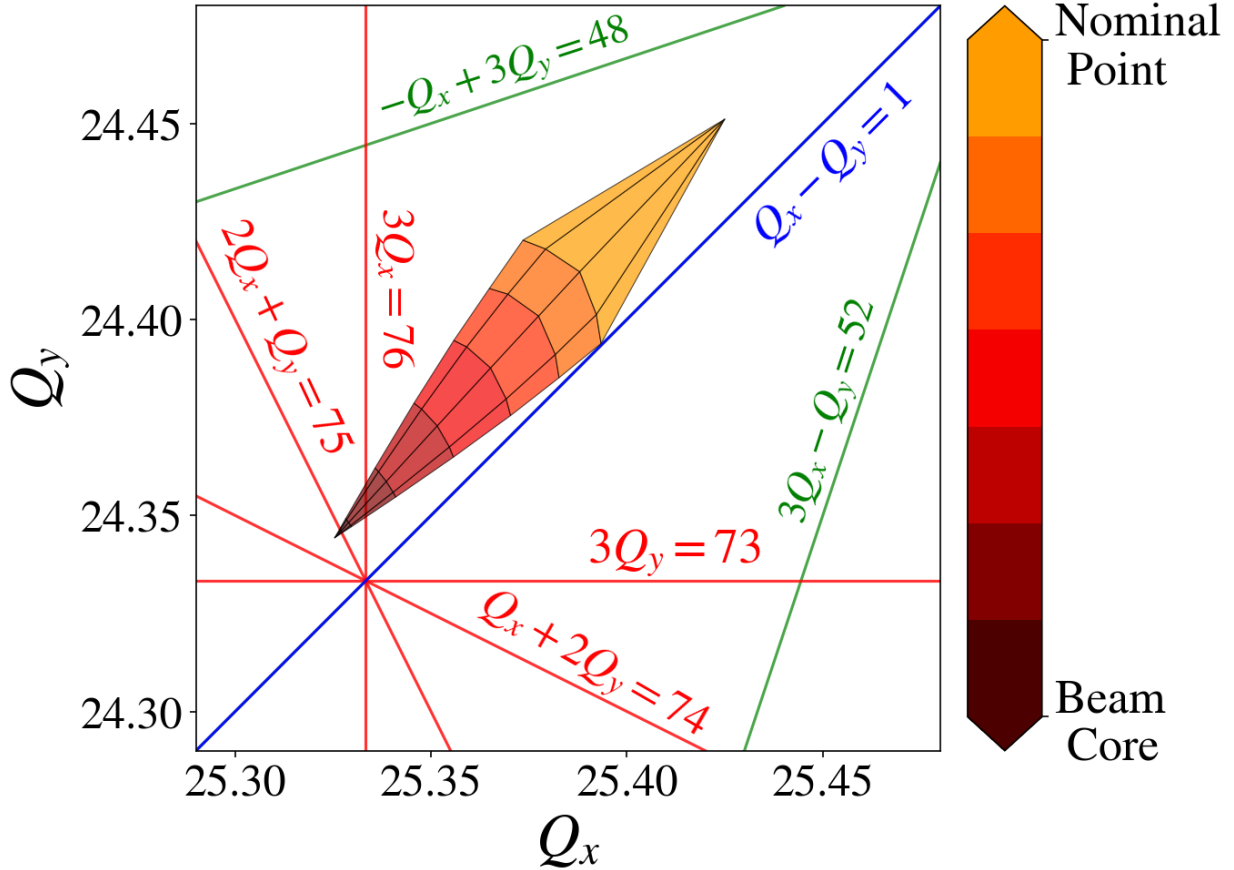


Figure 3.8 Approximate operational tune footprint at high intensities, i.e., 1e11 particles per bunch.

Figure 3.8 and the latter discussion motivate the need for mitigating the deleterious effects of  $3Q_x = 76$  and  $Q_x + 2Q_y = 74$ , and weaker effects from  $3Q_y = 73$  and  $2Q_x + Q_y = 75$ . If one reduces the RDT of each resonance line, then their strength becomes less, losses in those regions are reduced, and ultimately there will be a larger area in the tune diagram for operation. This mechanism is desirable for PIP-II. Nevertheless, Ch. 4 describes compensating one resonance line might make another one worse and vice versa. Here lies the difficulty of this approach. Additionally, these third-order resonance lines must be adequately characterized at low intensities before going to PIP-II intensities. Experimentally, everything starts to blend together in the tune diagram at high intensities due to the space charge tune shift. This amalgam of phenomena motivates the fact to have a distinction between Ch. 4 and 6.

### 3.5 Diagnostic Devices

The Recycler Ring has two primary diagnostic devices that fall under the scope of this work: the Beam Position Monitors (BPMs) and the Ion Profile Monitors (IPMs). Although both systems quantify the properties of the beam, each one gives different information about the beam distribution. In particular, BPMs probe the first moment of the transverse distribution, i.e., the bunch's mean position or beam centroid. Depending on the BPM system, this measurement is done in one plane or simultaneously in both planes. On the other hand, IPMs go one order higher and give information about the second-order moment of the transverse beam distribution—information about the variance and spread of the bunch. Specifically for the Recycler case, there is one IPM for the horizontal direction and another for the vertical case.

There are 208 BPMs in the Recycler Ring in total. Specifically, there are 104 horizontal BPMs and 104 vertical BPMs. Each class is oriented in order to measure the corresponding plane. The BPMs are labeled according to their position around the ring as described in Sec. 3.2 and in Fig. 3.4. One BPM consists of two parallel pick-up electrodes that produce an electric signal once the beam passes. The beam position is determined from the relative amplitude between the signals of the opposing channels [38]—also known as the  $(A - B)/(A + B)$  signal. This signal is digitized and calibrated to include the scaling factors and offsets, ultimately, in order to represent the transverse beam position. The digitized signal from all 208 BPMs is interfaced with ACNET for accelerator applications. The resulting data is digitized every turn, which is called turn-by-turn (TbT) data. Figure 3.9 shows an example of this TbT BPM data for a beam pinged in the horizontal direction and recorded for 2048 turns.

## R:HP620 READING

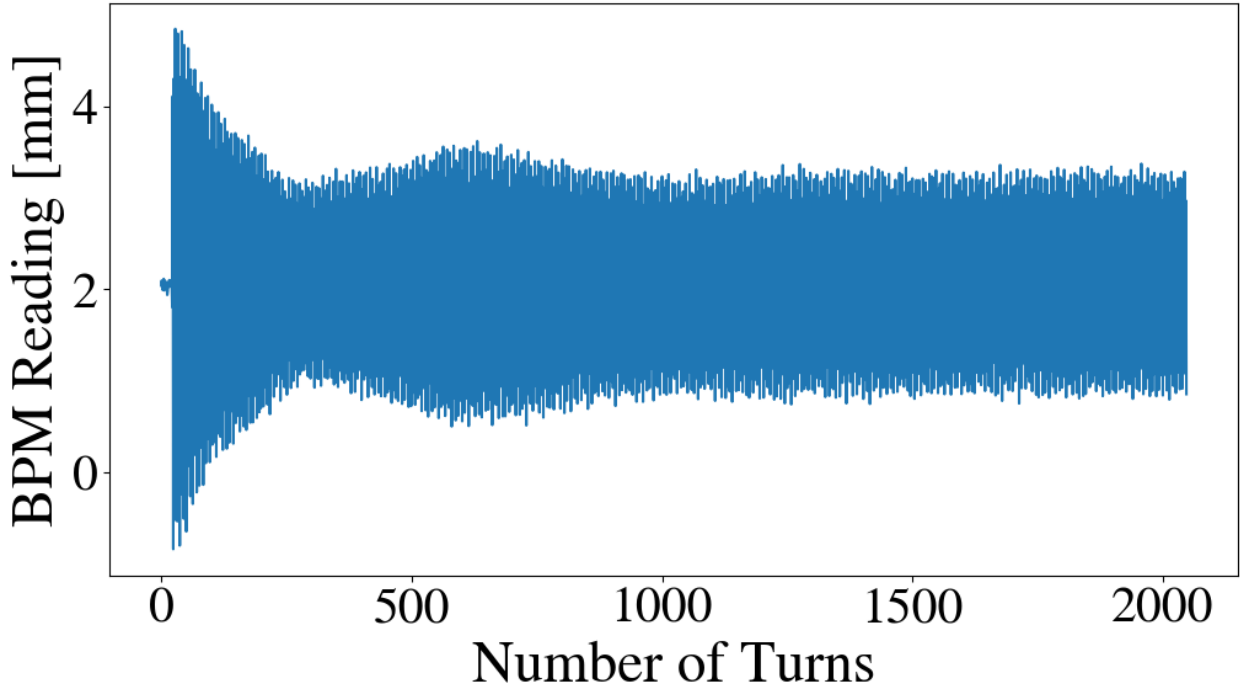


Figure 3.9 BPM turn-by-turn data for an arbitrary kick at horizontal BPM R:HP620.

One important example of using TbT data is using it to perform tune measurements. As mentioned in Sec. 2.1, specifically in Eq. 2.8, the motion inside the Recycler Ring will exhibit betatron oscillations. In particular, the tune frequency dictates the main harmonic of these oscillations. Say a particular set of BPM TbT data has been recorded for  $N$  number of turns. Therefore, a Fast-Fourier Transform (FFT) will help uncover and measure FFT accuracy— $\sigma_Q \approx 1/N$ —the main frequency of these oscillations. Figure 3.10 shows how the prominent peak of the FFT can be identified to measure the horizontal tune  $Q_x$  of the circular accelerator. Furthermore, Ch. 4 will explore how a more involved Fourier Transform algorithm, such as NAFF (Numerical Analysis of Fundamental Frequencies) [39], will help analyze the spectrum of TbT data and measure higher order harmonics, ultimately, leading to the measurement of RDTs in the RR.



Figure 3.10 Fast Fourier Transform amplitude for the turn-by-turn data presented in Fig. 3.9.

The second type of diagnostics relevant to this work are the Ion Profile Monitors (IPMs). As mentioned before, this device measures the beam size in the Recycler Ring. The RR has two IPM systems: one for the horizontal plane and another one for the vertical. One unique characteristic of IPMs relies on their non-destructive nature. The working principle of this system is to collect ions created in the interaction between the proton beam and residual molecules in the vacuum. Micro-channel plates (MCP) detect the secondary ions and are biased at an arbitrary high voltage [40]. The counts at each MCP are logged in and digitized to be compatible with ACNET. Similar to the BPM systems, an application was developed to control and use the IPM system.



Figure 3.11 Reconstructed beam profile for the horizontal plane assuming Gaussian distributions along 1024 turns for an arbitrary beam in the Recycler Ring.

Figure 3.11 shows the reconstruction of the horizontal beam profile from the raw data of the IPM micro-channel plates. At every turn, the raw count data from each of the 96 MCP is fit to Gaussian beam distribution, resulting in some variance  $\sigma$ . The color map shows the evolution of this beam profile along 1024 turns. The IPM system can record up to 65000 turns. Nevertheless, it batches the data into a  $1024 \times 96$  array. In particular, Fig. 3.11 shows how, for these arbitrary experimental conditions, the size of the beam grows with the number of turns—this is pointing at emittance growth. Other distributions different from a Gaussian can be used to fit the raw data to extract more information about the skewness or tail population of the beam, e.g., a q-Gaussian or a Skew-Gaussian distribution. In particular, Ch. 6 shows how to use q-Gaussian distributions to quantify beam tail population.

### 3.6 Sextupoles for Resonance Compensation

The ideal linear lattice of a circular accelerator would be composed only of dipoles and quadrupoles—assuming the beam is composed of mono-energetic particles. Nevertheless, this is a strong assumption, given that a bunch of particles will always have an energy spread. Particles orbiting at different energies will feel different quadrupole fields, resulting in betatron detuning. This wording is the definition of chromaticity, and therefore, its mathematical definition reads:

$$C_u = \frac{d(\Delta Q_u)}{d\delta}. \quad (3.2)$$

Every real ring will have a non-zero chromaticity. Sextupoles are crucial to control and correct chromaticity [1]. Therefore, they are indispensable in any lattice. Nevertheless, as explained in Ch. 2, introducing non-linear elements inevitably leads to driving betatron resonances, e.g., sextupoles will drive third-order resonances. In this sense, and dramatically speaking, sextupoles are double-edged swords. They are essential for chromaticity correction but deleterious by inducing resonances in the accelerator.

The Recycler Ring has 76 sextupoles, including normal and skew sextupoles. Additionally, as described in Sec. 3.2, each gradient magnet has end shims on both ends and is used to correct the field shape [41]. These end shims can also induce a sextupole-like field on the beam. It is also worth reminding the reader that the gradient magnets also have sextupole components in their permanent fields. All of these build up to the fact that the chromaticity of the Recycler Ring can be controlled in a range of -2 to -20 in both planes, i.e.,  $Q_u \in (-2, -20)$ .

Table 3.3 List of sextupoles used to compensate third-order resonances in the Recycler Ring.

Name	Type
SC220(a/b)	Normal Sextupole
SC222(a/b)	Normal Sextupole
SC319(a/b)	Normal Sextupole
SC321(a/b)	Normal Sextupole
SS222(a/b)	Skew Sextupole
SS319(a/b)	Skew Sextupole
SS321(a/b)	Skew Sextupole
SS323(a/b)	Skew Sextupole

In particular, out of all the sextupoles in the Recycler Ring, this thesis work is interested in the ones listed in Table 3.3. These elements have been placed in the Recycler Ring with the sole objective of mitigating the harmful effect of the third-order resonances [37]. The elements listed in Table 3.3 are in regions of close-to-zero dispersion,  $D_x \approx 0$ , to cancel out any additional chromaticity due to their inclusion. In principle, normal sextupoles are used to correct  $3Q_x = 76$  and  $Q_x + 2Q_y = 74$ , while skew sextupoles are used to correct  $3Q_y = 73$  and  $2Q_x + Q_y = 75$ . Nevertheless, normal sextupoles can have small tilts around the magnetic axis, introducing a skew-sextupole field and vice versa.

Figure 3.12 shows an example of these sextupoles installed in the Recycler Ring. As can be seen, two yellow-coated elements appear in the top ring. The same power supply powers both elements. Hence, the notation in Table 3.3 alludes to a and b elements, e.g., normal sextupole SC220(a/b). The numbers in the name allude to their location in the RR/MI tunnel, as illustrated in Fig. 3.4. Given that each pair of elements, a and b, are connected to the same power supply, these two elements effectively become one knob. The currents for the power supply are controlled through ACNET. This concept is important for the reader to remember, given that in Ch. 4, the currents of the sextupoles listed in Table 3.3 will be the main knobs turned in order to mitigate the strength of these resonances.



Figure 3.12 Picture of compensation sextupoles (yellow magnets on top) installed in the Recycler Ring. Picture provided by Dr. Robert Ainsworth.

## CHAPTER 4

### COMPENSATION OF THIRD-ORDER RESONANCES AT LOW INTENSITIES

#### 4.1 Global RDTs and Lattice Model

The following chapter explores how to mitigate the effect of third-order resonances from the Recycler Ring by minimizing the Resonance Driving Terms (RDTs) that drive each resonance. The resonances in question are introduced in Figs. 3.7 and 3.8, and are summarized in Table 4.1. The RDTs for these third-order resonance lines can be calculated from Eqs. 2.31 and 2.32. Table 4.1 shows the explicit expression for each third-order RDT relevant to this work. The sum over  $i$  goes through each element of the lattice beam line and asks if it has some sextupole component in its definition—it can be normal  $K_{2,i}$  or skew  $K_{2,i}^{(s)}$  sextupole component. If it has this multipole, it will add it to the RDT sum by weighting it with the beta functions  $\beta_{u,i}$  and phase advances  $\phi_{u,i}$  from the linear approximation at those particular locations. Ultimately, the  $h_{jklm}$  RDT will be a complex number whose amplitude  $|h_{jklm}|$  should be minimized.

Table 4.1 Corresponding RDTs for each resonance line.

Resonance Line	RDT Expression
$3Q_x = 76$	$h_{3000} = -\frac{1}{48} \sum_i K_{2,i} L_i \beta_{x,i}^{\frac{3}{2}} e^{3i\phi_{x,i}}$
$Q_x + 2Q_y = 74$	$h_{1020} = -\frac{1}{16} \sum_i K_{2,i} L_i \beta_{x,i}^{\frac{1}{2}} \beta_{y,i} e^{i[\phi_{x,i} + 2\phi_{y,i}]}$
$3Q_y = 73$	$h_{0030} = -\frac{1}{48} \sum_i K_{2,i}^{(s)} L_i \beta_{y,i}^{\frac{3}{2}} e^{3i\phi_{y,i}}$
$2Q_x + Q_y = 75$	$h_{2010} = -\frac{1}{16} \sum_i K_{2,i}^{(s)} L_i \beta_{x,i} \beta_{y,i}^{\frac{1}{2}} e^{i[2\phi_{x,i} + \phi_{y,i}]}$

Figure 4.1 shows a visual representation for calculating the  $h_{3000}$  RDT. It shows the amplitude of the complex cumulative sum as it goes around the ring (thick, solid orange line). This plot also shows the amplitude of each contribution for every  $i$ -th element in the lattice with a sextupole component (thin purple line). This quantity visualizes where and how the sextupole component is distributed around the ring. Ultimately, after doing this sum around the ring, the final result is

a complex number with amplitude and phase corresponding to the  $h_{3000}$  RDT, as calculated from some arbitrary location in the lattice. The amplitude of the  $h_{3000}$  term is plotted in Fig. 4.1 with a red dashed line. Figure 4.2 shows a similar exercise for the  $h_{1020}$  term. These calculations are done with a lattice model with a list of components and magnet coefficients, which should be very close to what is inside the tunnel. The particular RR model used was the RR2020V0922FLAT lattice model, provided by R. Ainsworth and M. Xiao.

A question that promptly arises is: does the arbitrary starting position for the sum of Eq. 2.31 change the RDT result? The short answer is yes; the RDT will change depending on the initial position for the sum. Reference [19], specifically in its Ch. 5, goes into depth on how to correlate the RDT calculated from a starting point  $s_1$  to one measured at starting point  $s_2$ . The difference in this case relates to the amount of multipole component between both calculation points, e.g., the amount of elements that have sextupole component between an  $s_1$  and  $s_2$  observation point. Nevertheless, given that there is an infinite amount of  $s_1$  and  $s_2$  observation points and only so much real state in this thesis, the plots are for an arbitrary observation point in the lattice. Additionally, given that the sextupole components are evenly distributed around the ring, the RDT values will not oscillate much.

As mentioned in Ch. 3, the Recycler Ring comprises permanent gradient magnets. From looking at Figs. 4.1 and 4.2, one can see that the sextupole component is evenly distributed around some sections of the ring. If one were to plot the distribution of permanent gradient on these plots, their location would coincide with the peaks of the individual contributions to the RDT of Figs. 4.1 and 4.2. Therefore, the sources that drive the Recycler Ring's normal sextupole resonances come from the permanent magnets themselves—this is known as a systematic-driven resonance instead of a random-error-driven resonance. Highly periodic and linear machines use the fluctuations between RDT measurements from BPMs to locate any sextupole errors in the lattice and try to fix them [19]. Nevertheless, this is not the case for the Recycler, given its low superperiodicity of 2 and its uniform sextupole component distribution.

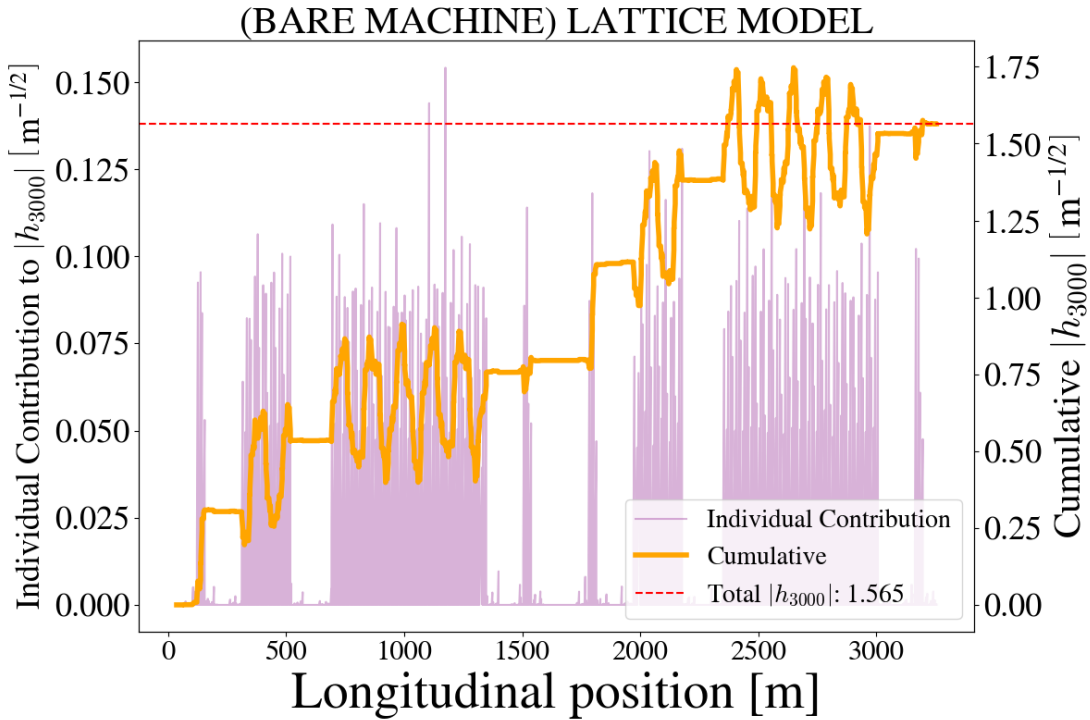


Figure 4.1 Distribution of the  $h_{3000}$  term around the ring with individual contributions from each relevant element and the cumulative sum from an arbitrary starting point.

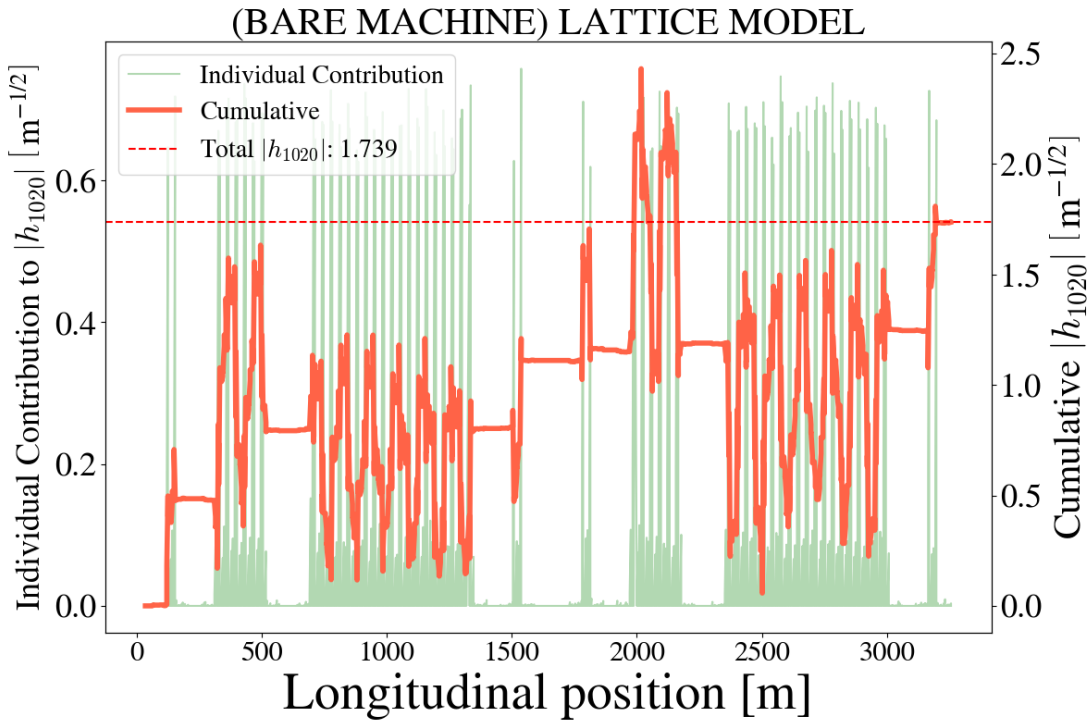


Figure 4.2 Distribution of the  $h_{1020}$  term around the ring with individual contributions from each relevant element and the cumulative sum from an arbitrary starting point.

## 4.2 Measurement of Third Order RDTs

Calculating the theoretical RDTs from the lattice model is a matter of calculating the sums outlined in Table 4.1. Nevertheless, measuring the third-order RDTs requires following a long and involved recipe. This recipe is based on previous work from Refs. [19, 21], but with many original steps specifically developed for the Recycler Ring. In summary, these are the steps used in order to measure RDTs at the Recycler:

1. Kick the beam with dipole kickers and save turn-by-turn BPM data for offline analysis.
2. Go through data and estimate momentum coordinates with previously calculated transfer matrices from the lattice model.
3. Estimate Twiss parameters and normalized coordinates  $(\hat{u}, \hat{p}_u)$  at every BPM location.
4. Create resonance basis  $h_u^\pm$  (see Eq. 2.37).
5. Get spectrum of resonance basis using NAFF (Numerical Analysis of Fundamental Frequencies) through the SUSSIX software [42].
6. Identify resonance lines from the spectrum corresponding to the RDT of interest.
7. Calculate the RDT at each BPM location from the equivalence relation of spectral lines and RDT expansion (see Eq. 2.46).

The following subsections will explore the steps outlined in the previous list in more detail.

### 4.2.1 Dipole Kick and BPM data

The first step towards measuring RDTs is to kick (or ping) the beam in either transverse direction(s) to excite betatron oscillations. Betatron oscillations are the natural oscillations of particles around their equilibrium orbit in a circular accelerator. Horizontal and vertical dipole kickers induce a kick in the beam. In particular, the devices used for this were the kicker devices with ACNET names R:K4XXX and R:KVXXX, horizontally and vertically, respectively. In principle, these are the Recycler abort kickers—devices used to send the beam to the abort line in Recycler.

Nevertheless, these pingers' high-voltage settings and timings can be changed to give a small kick to the beam—a ping that is small enough not to steer the beam to the abort line but large enough to excite betatron oscillations in one or both transverse directions. The beam was kicked exclusively in the horizontal direction in order to measure purely horizontal RDTs, e.g.,  $h_{3000}$ , solely in the vertical direction for vertical RDTs, e.g.,  $h_{0030}$ , or pinged in both directions for all of them, including coupling RDTs, e.g.,  $h_{1020}$  and  $h_{2010}$ .

Once the kickers are set correctly, the next step is to take BPM data. As mentioned in Sec. 3.5, ACNET applications allow gathering and saving BPM data for offline analysis. The BPM data from all 208 BPMs (104 horizontal and 104 vertical) can be saved in one file. Figure 4.3 shows an instance of kicking the beam in the horizontal direction and recording beam centroid data for 2048 turns at an arbitrary BPM. The amount of turns recorded is also a customizable quantity. The ping shown in Fig. 4.3 happens early in the cycle, at around 50 turns. The next hundred turns hold information about the betatron oscillations. This data is used to extract the tunes  $Q_u$  and RDTs of the machine.

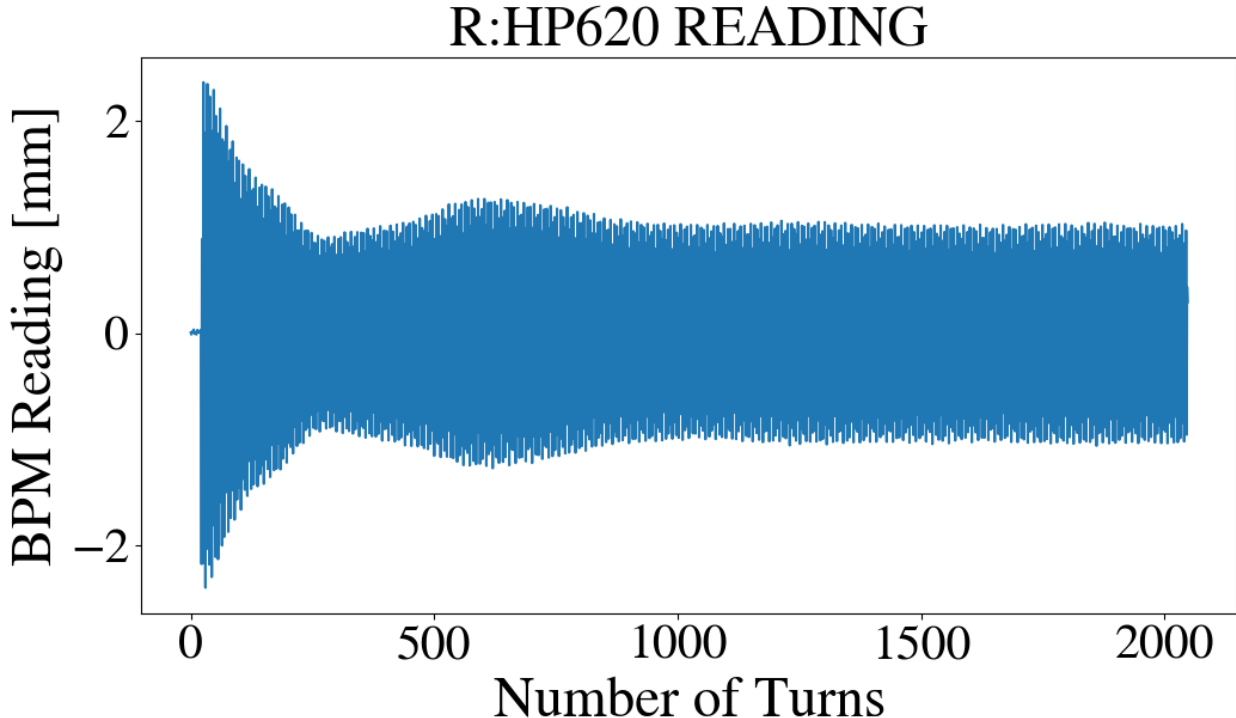


Figure 4.3 BPM data of an arbitrary horizontal kick in the beam at horizontal BPM R:HP620.

The physics of a kicked beam is well explained in Refs. [43, 44]. Once the beam is pinged, the centroid response will oscillate at betatron tunes  $Q_u$ . Nonlinearities and chromaticity of the machine will dictate the envelope of these oscillations. How fast this envelope decays is a measure of the decoherence of the beam. Decoherence of a particle beam in accelerator physics refers to the process by which a beam that initially has particles oscillating in phase—meaning they have similar amplitudes and frequencies—gradually becomes out of phase over time. This decoherence effect results in a spread in the particles’ positions and momenta, leading to a more diffuse beam. This decoherence is caused by nonlinearities in the machine and the transverse chromaticities that will detune the beam out of coherence, as explained by Eqs. 2.51 and 3.2. Ultimately, this process will diffuse and maim the signal recorded by the BPMs.

Therefore, when the BPM data for the kicked beam is taken, special care must be taken to sustain coherent oscillations. This is done by manipulating the machine’s chromaticities using specialized sextupoles. Table 3.1 showed the nominal chromaticities at which the Recycler Ring operates. For these RDT measurements, the vertical chromaticity was changed between the range of -7 and -3 to find sustained vertical oscillations. For the horizontal case, a chromaticity of -5 would usually be enough for 1 mm oscillations. The other system that affects decoherence is the transverse dampers. As per its name, these devices dampen any oscillation in the beam. Therefore, they were turned off for these particular studies. Considering these factors, one could get consequential oscillations in both transverse planes as a first step to measure Resonance Driving Terms.

#### 4.2.2 Estimation of Momentum Coordinate

At the most fundamental level, BPM data holds only information about the centroid position of the beam. Nevertheless, in a particle accelerator, it is of interest to look at the whole phase space picture ( $\hat{u}, \hat{p}_u$ )—including the momentum coordinate. Therefore, explaining how the momentum coordinate is calculated from the TbT position from every BPM is relevant. The approach used involves a model-based perspective. Therefore, the lattice model plays a crucial role in the momentum estimation.

The approach to estimating the momentum coordinate involves solving a least-squares problem.

This approach is developed in Ref. [45]. The first step is to calculate the model's transfer matrices (linear approximation) from one fixed point in the accelerator to all the horizontal and vertical BPM locations—in total, there should be 208 transfer matrices. For these studies, the fixed point chosen was the starting point of the turn count, which is the location of the vertical BPM R:VP601. For example, the following paragraphs show how to calculate the horizontal phase space coordinates, including the relative momentum deviation  $\delta$ . In particular, the main objective is to calculate the  $X_0$  matrix with dimensions  $3 \times 2048$ , which corresponds to the phase space coordinates  $(\vec{x}_0, \vec{x}'_0, \vec{\delta}_0)$  at the location of R:VP601. The  $X_0$  array will have the following definition:

$$X_0 = \begin{pmatrix} \vec{x}_0 \\ \vec{x}'_0 \\ \vec{\delta}_0 \end{pmatrix} = \begin{pmatrix} [x_0(N=1), x_0(N=2), \dots, x_0(N=2048)] \\ [x'_0(N=1), x'_0(N=2), \dots, x'_0(N=2048)] \\ [\delta_0(N=1), \delta_0(N=2), \dots, \delta_0(N=2048)] \end{pmatrix}, \quad (4.1)$$

and holds the information over the 2048 turns. The least squares problem is defined as the solution to the following system:

$$AX_0 = B, \quad (4.2)$$

where  $A$  is the matrix made from the horizontal coefficients of the model's transfer matrices, and it reads:

$$A = \begin{pmatrix} (M_{11} & M_{12} & M_{13})_{BPM(i-10)} \\ & \vdots & \\ (M_{11} & M_{12} & M_{13})_{BPM(i)} \\ & \vdots & \\ (M_{11} & M_{12} & M_{13})_{BPM(i+10)} \end{pmatrix}. \quad (4.3)$$

The notation  $(\dots)_{BPM(j)}$  means that all the matrix coefficients inside the parenthesis are indexed by the BPM(j) and should be copied from that particular transfer matrix correlating the fixed point to BPM(j). For this case, the BPM(i) corresponds to the particular BPM location where one wants to calculate the phase space coordinates  $X_{BPM(i)}$ , after calculating  $X_0$ . One can note that only the ten upstream BPMs and ten downstream BPMs of BPM(i) are included in this calculation. This

number is easily customizable in this estimation but should not be too large, i.e., no larger than 30, to preserve some sense of locality.

One can define the  $B$  matrix from the BPM observations, and its transpose is just the BPM responses stacked horizontally. This notation reads explicitly:

$$B^T = \begin{pmatrix} \vdots & \vdots & \vdots \\ \left\langle x_{BPM(i-10)} \right\rangle & \dots & \left\langle x_{BPM(i)} \right\rangle & \dots & \left\langle x_{BPM(i+10)} \right\rangle \\ \vdots & \vdots & \vdots & & \vdots \end{pmatrix}. \quad (4.4)$$

For Eq. 4.4, the triangular bracket notation  $\langle \dots \rangle$  is used to specify that the BPM data inside the brackets has already been averaged out—the oscillations recorded in the BPM data is centered around 0. Again, to use least-squares approximation, this calculation should take the 10 BPMs upstream and the 10 BPMs downstream of the BPM(i), whose phase space coordinates are being calculated.

The least-squares solution  $\hat{X}_0$  to this problem is given by:

$$\hat{X}_0 = (A^T A)^{-1} A^T B. \quad (4.5)$$

Once  $\hat{X}_0$  is calculated from the data of 10 BPMs upstream and downstream of BPM(i). The phase space coordinates  $\hat{X}_{BPM(i)}$  at BPM(i) can be calculated from:

$$\hat{X}_{BPM(i)} = \begin{pmatrix} \vec{x} \\ \vec{x}' \\ \vec{\delta} \end{pmatrix}_{BPM(i)} = \begin{pmatrix} [x(N=1), \dots, x(N=2048)] \\ [x'(N=1), \dots, x'(N=2048)] \\ [\delta(N=1), \dots, \delta(N=2048)] \end{pmatrix} = [M_{11} \quad M_{12} \quad M_{13}]_{BPM(i)} \hat{X}_0. \quad (4.6)$$

The hat notation  $\hat{X}$  symbolizes data estimated based on the least-squares solution to Eq. 4.5.

Similar to the horizontal case, for the vertical case, the phase space coordinates at each BPM location can be estimated by first estimating the phase space coordinates  $Y_0$  at an arbitrary location in the lattice—vertical BPM R:VP601 for this case. At this location, the  $Y_0$  array will be defined as:

$$Y_0 = \begin{pmatrix} \vec{y}_0 \\ \vec{y}'_0 \end{pmatrix} = \begin{pmatrix} [y_0(N=1), y_0(N=2), \dots, y_0(N=2048)] \\ [y'_0(N=1), y'_0(N=2), \dots, y'_0(N=2048)] \end{pmatrix}. \quad (4.7)$$

The least-squares estimate  $\hat{Y}_0$  for the array in Eq. 4.7 from the recorded BPM data will be given by:

$$\hat{Y}_0 = (A_y^T A_y)^{-1} A_y^T B_y, \quad (4.8)$$

where similar to the horizontal case, the matrix  $A_y$  is defined by:

$$A_y = \begin{pmatrix} (M_{21} & M_{22})_{BPM(i-10)} \\ \vdots \\ (M_{21} & M_{22})_{BPM(i)} \\ \vdots \\ (M_{21} & M_{22})_{BPM(i+10)} \end{pmatrix}, \quad (4.9)$$

and  $B_y$  is defined by

$$B_y^T = \begin{pmatrix} \vdots & \vdots & \vdots \\ \left\langle y_{BPM(i-10)} \right\rangle & \dots & \left\langle y_{BPM(i)} \right\rangle & \dots & \left\langle y_{BPM(i+10)} \right\rangle \\ \vdots & \vdots & \vdots & \vdots & \vdots \end{pmatrix}. \quad (4.10)$$

Once one calculates  $\hat{Y}_0$ , it can be transferred to the location of BPM(i) utilizing the transfer matrices.

This is the way of calculating  $\hat{Y}_{BPM(i)}$ , which reads

$$\hat{Y}_{BPM(i)} = \begin{pmatrix} \vec{y} \\ \vec{y}' \end{pmatrix}_{BPM(i)} = \begin{pmatrix} [y(N=1), \dots, y(N=2048)] \\ [y'(N=1), \dots, y'(N=2048)] \end{pmatrix} = [M_{21} \quad M_{22}]_{BPM(i)} \hat{Y}_0. \quad (4.11)$$

It is worth pointing out that for the vertical case, one picks out the appropriate elements of the transfer matrices, i.e.,  $M_{21}$  and  $M_{22}$  instead of the horizontal coefficients  $M_{11}$ ,  $M_{12}$  and  $M_{13}$ . The other thing to note is that any momentum dependence is dropped for the vertical case, given that the vertical dispersion is negligible in the Recycler Ring, as shown in Fig. 3.6. The previous procedure of calculating  $\hat{U}_{BPM(i)}$  is done and saved for each of the 104 horizontal and 104 vertical BPMs— $\hat{X}_{BPM(i)}$  or  $\hat{Y}_{BPM(i)}$ , accordingly. Figure 4.4 shows an application of this momentum reconstruction technique for a horizontal BPM R:HP620 and its vertical neighbor R:VP621.

With model-based approaches, it is important to be confident that the model is as close to the real accelerator as possible. The beta-beating measures how well the model's beta functions

describe the beta functions from the real-world accelerator. In particular, M. Xiao has shown that the beta-beating along the Recycler is below 10% [46]—an acceptable quantity for modern accelerators. Therefore, this proves that the model used is reliable up to some significance level. The beta-beating quantity is ultimately limited by how linear the accelerator is and any ripple noise from the power supplies feeding the quadrupole and dipoles.

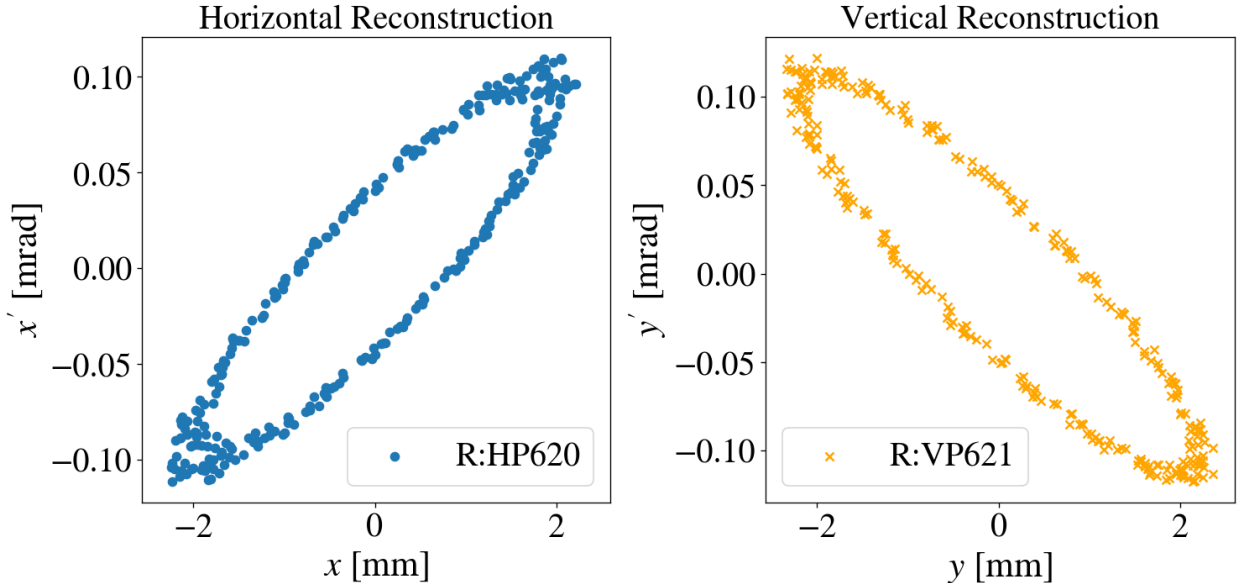


Figure 4.4 Phase space coordinates reconstruction for two neighboring BPMs—one horizontal R:HP620 and one vertical R:VP621—windowed for 300 turns.

#### 4.2.3 Twiss Parameters and Normalized Phase Space

The next step to measure RDTs, once the phase space coordinates have been reconstructed for every BPM, is to build the normal phase space coordinates  $(\hat{u}, \hat{p}_u)$ . This is done by using Eqs. 2.9 and 2.13, and the information provided in Fig. 2.1. In order to build the normalized phase space, the Twiss parameters first have to be estimated. This is done by performing a least-squares fit to estimate the ellipse parameters of reconstructed phase space, such as the one shown in Fig. 4.4. Therefore, an ellipse is fit to the data, and after that, the Twiss parameters are retrieved from the fit, including the centroid action  $2\pi\langle J_u \rangle = \varepsilon_x$  (see Eq. 2.9).

Figure 4.5 shows an example of this procedure. The left plot shows reconstructed phase space data with the best ellipse fit. The parameters indicated on the inset provide detailed characteristics

of this particular fit: (a)  $\beta_x$  (beta function) describes the spatial spread of the beam, (b)  $\alpha_x$  (alpha function) relates to the angle the beam particles make with the reference orbit, and it is a measure of the beam divergence, and (c)  $\varepsilon_x$  (centroid emittance) quantifies the area of the phase space that the beam centroid occupies. In particular, the centroid action can be calculated from  $2\pi\langle J_u \rangle = \varepsilon_x$ .

The right plot of Fig. 4.5 shows the reconstructed normalized phase space using the Twiss parameters, as estimated from the ellipse fit. This normalization process involves scaling by the square root of the Twiss parameter  $\beta_u$  at that particular location, per Floquet's transformation as defined in Eq. 2.13. This procedure is done for the reconstructed data of every BPM, and, finally  $(\hat{u}, \hat{p}_u)$  is recorded.

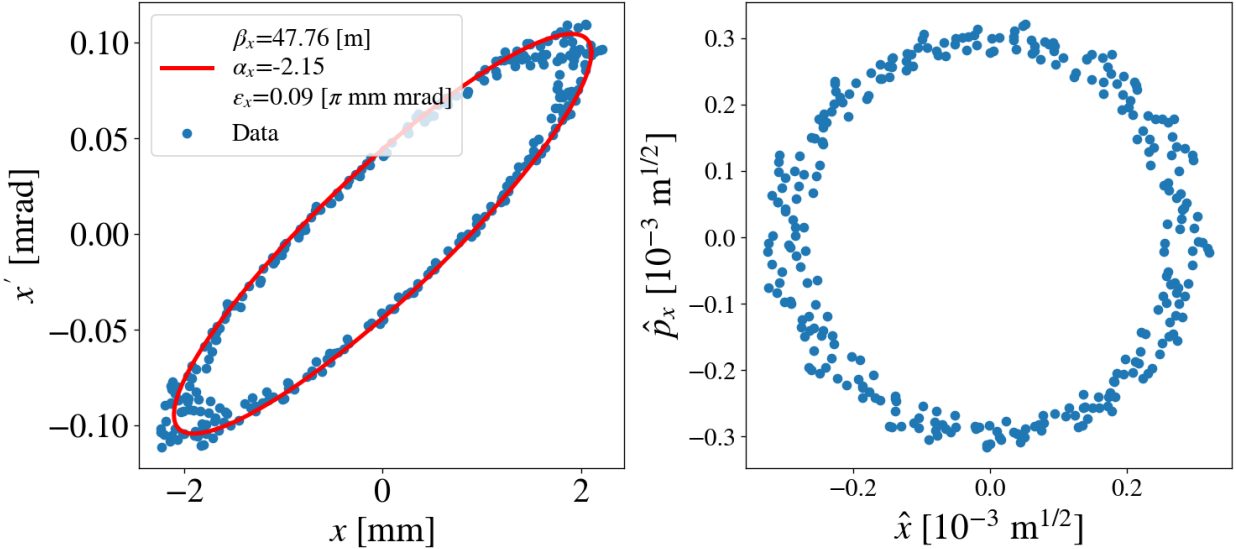


Figure 4.5 Reconstructed phase space data with the best ellipse fit (left plot). The right plot shows the reconstructed normalized phase space using Eq. 2.13 with the Twiss parameters, as estimated from the ellipse fit. This data corresponds to the horizontal data shown in Fig. 4.4 for the R:HP620 BPM.

#### 4.2.4 Resonance Basis and Spectral Decomposition

Once one reconstructs the normalized phase space coordinates for every BPM, the next step is to build the resonance basis  $h_u^\pm(N)$ , as defined in Eq. 2.37, i.e.,  $h_u^\pm = \hat{u} \pm \hat{p}_u$ . This resonance basis is a function of the number of turns  $N$  that have elapsed. As shown in Eq. 2.46, this quantity can have a spectral decomposition as a Fourier series. In general, this spectral decomposition in the

horizontal dimension reads:

$$h_x^-(N) = \hat{x} - i\hat{p}_x = \sum_{jklm} HSL_{jklm} e^{2\pi i N [(1-j+k)Q_x + (m-l)Q_y]}, \quad (4.12)$$

and in the vertical dimension:

$$h_y^-(N) = \hat{y} - i\hat{p}_y = \sum_{jklm} VSL_{jklm} e^{2\pi i N [(k-j)Q_x + (1-l+m)Q_y]}. \quad (4.13)$$

These sums run over the  $(j, k, l, m)$  indices. Theoretically, they run to infinity, but one can truncate them. The  $HSL_{jklm}$  term corresponds to the complex amplitude defining the horizontal spectral line at frequency location  $(1-j+k)Q_x + (m-l)Q_y$ . The  $VSL_{jklm}$  term corresponds to the complex amplitude defining the vertical spectral line at location  $(k-j)Q_x + (1-l+m)Q_y$ . Moreover, as always,  $Q_u$  corresponds to the betatron tunes. These definitions help to understand the experimental data in order to measure RDTs.

Nevertheless, from the theoretical point of view, the spectral decomposition can be calculated with the Lie algebra gymnastics shown in Sec. 2.5. These spectral decompositions read for the horizontal plane:

$$\begin{aligned} h_x^-(N) &= \sqrt{2I_x} e^{i(2\pi Q_x N + \psi_{x_0})} \\ &- 2i \sum_{jklm} j f_{jklm} (2I_x)^{\frac{j+k-1}{2}} (2I_y)^{\frac{l+m}{2}} e^{i[(1-j+k)(2\pi Q_x N + \psi_{x_0}) + (m-l)(2\pi Q_y N + \psi_{y_0})]}, \end{aligned} \quad (4.14)$$

and for the vertical case:

$$\begin{aligned} h_y^-(N) &= \sqrt{2I_y} e^{i(2\pi Q_y N + \psi_{y_0})} \\ &- 2i \sum_{jklm} l f_{jklm} (2I_x)^{\frac{j+k}{2}} (2I_y)^{\frac{l+m-1}{2}} e^{i[(k-j)(2\pi Q_x N + \psi_{x_0}) + (1-l+m)(2\pi Q_y N + \psi_{y_0})]}. \end{aligned} \quad (4.15)$$

The RDT calculation exploits the equivalence between Eqs. 4.12 and 4.13 to Eqs. 4.14 and 4.15. Therefore, the generating function coefficients ( $f_{jklm}$ ) can be related to the horizontal and spectral line coefficients ( $HSL_{jklm}$  and  $VSL_{jklm}$ ). Ultimately, the  $f_{jklm}$  terms can be related to Resonance Driving Terms  $h_{jklm}$  through Eq. 2.30.

A quick comparison between Eqs. 4.12 and 4.14 allow the building of an equivalence table between the generating function coefficients (GFCs) and the spectral lines. Table 4.2 is the result

of this. One can find the original table in Refs. [21, 42]. Table 4.2 shows how to calculate the GFCs from its corresponding spectral line. In particular, the amplitude and phase of a spectral line will be given by  $|USL_{jklm}|$  and  $\arg(USL_{jklm})$ , while its location in its corresponding frequency space will be given by  $Q(USL_{jklm})$ . It is worth pointing out that in this notation,  $U$  can be either the horizontal or vertical plane.

Table 4.2 Equivalence table between the generating function coefficients and the spectral lines.

	<b>Generating Function Coefficient</b>	<b>Spectral Line</b>
<b>Amplitude</b>	$ f_{jklm} $	$ HSL_{jklm}  = 2 j (2I_x)^{\frac{j+k-1}{2}} (2I_y)^{\frac{l+m}{2}}  f_{jklm} $ $ VSL_{jklm}  = 2 l (2I_x)^{\frac{j+k}{2}} (2I_y)^{\frac{l+m-1}{2}}  f_{jklm} $
<b>Phase</b>	$\phi_{jklm} = \arg(f_{jklm})$	$\arg(HSL_{jklm}) = \phi_{jklm} + \psi_{x_0} - \frac{\pi}{2}$ $\arg(VSL_{jklm}) = \phi_{jklm} + \psi_{y_0} - \frac{\pi}{2}$
<b>Spectral Harmonic</b>	N/A	$Q(HSL_{jklm}) = (1 - j + k)Q_x + (m - l)Q_y$ $Q(VSL_{jklm}) = (k - j)Q_x + (1 - l + m)Q_y$

#### 4.2.5 Resonance Basis Spectrum

As mentioned in the last section, the resonance basis spectral lines hold enough information to reconstruct the generating function coefficients (GFCs) and, ultimately, the resonance driving terms (RDTs). Therefore, it is interesting to have a program that reconstructs the spectral lines from  $h_u^\pm(N)$  data. This is exactly what SUSSIX [42] does. SUSSIX is a software developed at CERN, and it utilizes the Numerical Analysis of Fundamental Frequencies (NAFF) algorithm to identify and calculate the resonance lines up to an arbitrary order. SUSSIX can calculate spectral lines for the horizontal, the vertical plane, or both planes.

Figure 4.6 shows an example of spectrum data calculated using SUSSIX. The horizontal axis

represents the frequency (or tune) of the spectral lines, while the vertical axis shows the amplitude of the lines, i.e.,  $|HSL_{jklm}|$ . All the lines that show up in Fig. 4.6 represent the harmonics present in  $h_x^-(N)$ . The largest peak corresponds to the horizontal tune  $Q_x$ . In this case, the second-largest tune corresponds to the vertical tune  $Q_y$ , indicating some residual coupling. The lines  $HSL_{2010}$ ,  $HSL_{3000}$  and  $HSL_{1020}$  are also marked with their location at the plot. One can use these lines to calculate relevant GFCs and corresponding RDTs. Other unmarked spectral lines illustrate how higher-order harmonics and RDTs might be present in the oscillations. It is especially worth highlighting how several RDTs can feed to the line at  $Q_x = 0$ . Figure 4.7 shows this exercise done but for the vertical resonance basis  $h_y^-(N)$ . In this case, the largest peak corresponds to the vertical tune  $Q_y$ , while the second-largest corresponds to the horizontal tune  $Q_x$ . The lines  $VSL_{2010}$ ,  $VSL_{3000}$ , and  $VSL_{1020}$  also show up, but at different locations than their horizontal counterparts, as expected. The amplitudes of these spectral lines are at least three orders of magnitude less than the main harmonic of the oscillations.

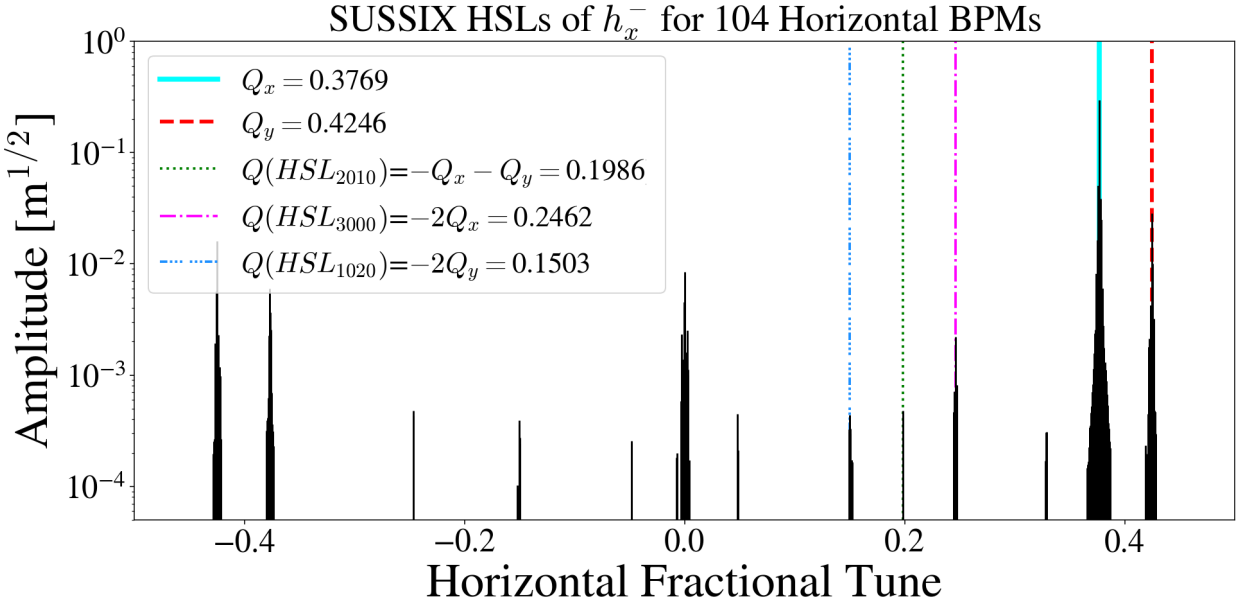


Figure 4.6 Spectral lines of  $h_x^-$  calculated with SUSSIX [42]. The  $h_x^-$  signal was reconstructed for the 104 Horizontal BPMs. The spectrum for all BPMs is superimposed in this plot.

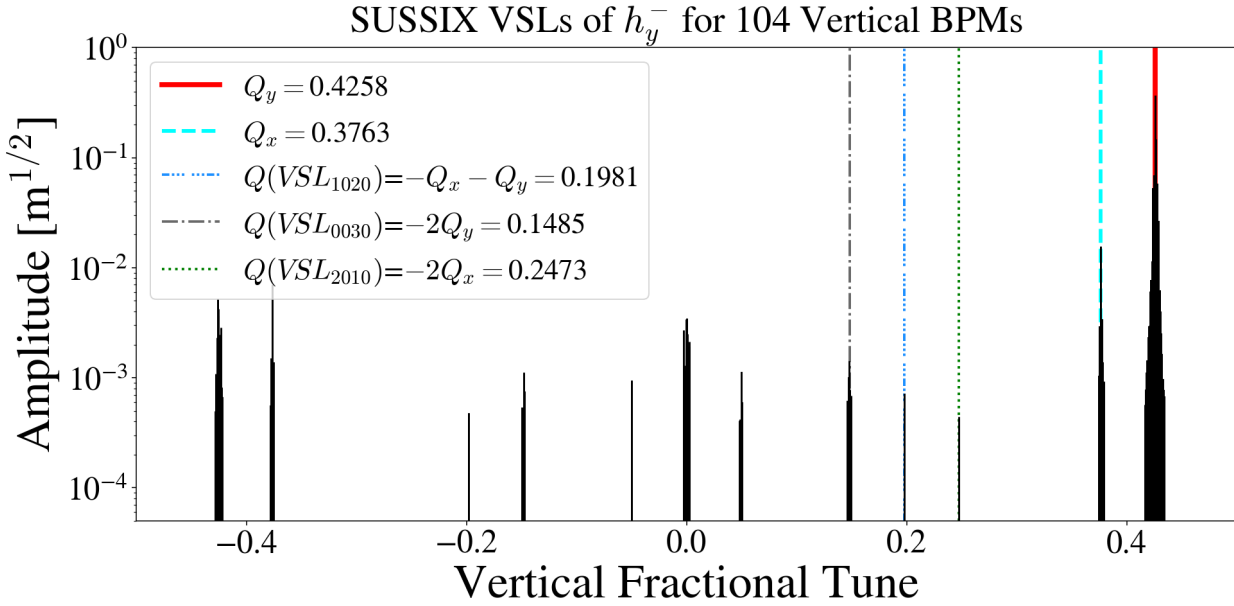


Figure 4.7 Spectral lines of  $h_y^-$  calculated with SUSSIX [42]. The  $h_y^-$  signal was reconstructed for the 104 Vertical BPMs. The spectrum for all BPMs is superimposed in this plot.

#### 4.2.6 Spectral Lines and RDT calculation

The spectral lines  $HSL_{3000}$ ,  $HSL_{2010}$ , and  $HSL_{1020}$  identified in Fig. 4.6 are the necessary lines to calculate the  $h_{3000}$ ,  $h_{2010}$  and  $h_{1020}$  RDTs. In combination with the  $VSL_{0030}$  spectral line and its corresponding  $h_{0030}$  RDT, these are all the spectral lines needed to calculate the RDTs for each resonance line shown in Fig. 3.7 and specified in Table 3.2. Table 4.3 shows the explicit expressions for each resonance line RDT as a function of its GFC. Once one calculates the  $f_{jklm}$  terms using the expressions in Table 4.2, the RDT is just one multiplication away.

Table 4.3 Corresponding RDTs from GFCs for each resonance line.

Resonance Line	RDT
$3Q_x = 76$	$h_{3000} = f_{3000} (1 - e^{6\pi i Q_x})$
$Q_x + 2Q_y = 74$	$h_{1020} = f_{1020} (1 - e^{2\pi i [Q_x + 2Q_y]})$
$3Q_y = 73$	$h_{0030} = f_{0030} (1 - e^{6\pi i Q_y})$
$2Q_x + Q_y = 75$	$h_{2010} = f_{2010} (1 - e^{2\pi i [2Q_x + Q_y]})$

#### 4.2.7 Third Order RDTs at every BPM location

Once one transforms the data from spectral lines to GFCs  $f_{jklm}$ , it is just a matter of using the expressions in Table 4.3 to calculate the RDTs  $h_{jklm}$ . Figure 4.8 shows several measurements of the  $h_{3000}$  term for the Recycler Ring from one particular BPM, i.e., R:HP620. This figure is a polar plot to indicate the amplitude and phase of this complex quantity. The left plot displays a set of 36 vectors representing individual measurements of the  $h_{3000}$  term at a specific Beam Position Monitor (BPM) located at R:HP620. From this plot, one can see some spread in the data from each measurement. This spread is due to changes in the beam from Booster for every injection and to noise in BPM data. The right plot shows the average vector of the measurements, with its spread indicated by the shaded area. This spread signifies the variance in the data from measurement to measurement.

### SUSSIX: $h_{3000}$ for bare machine at R:HP620

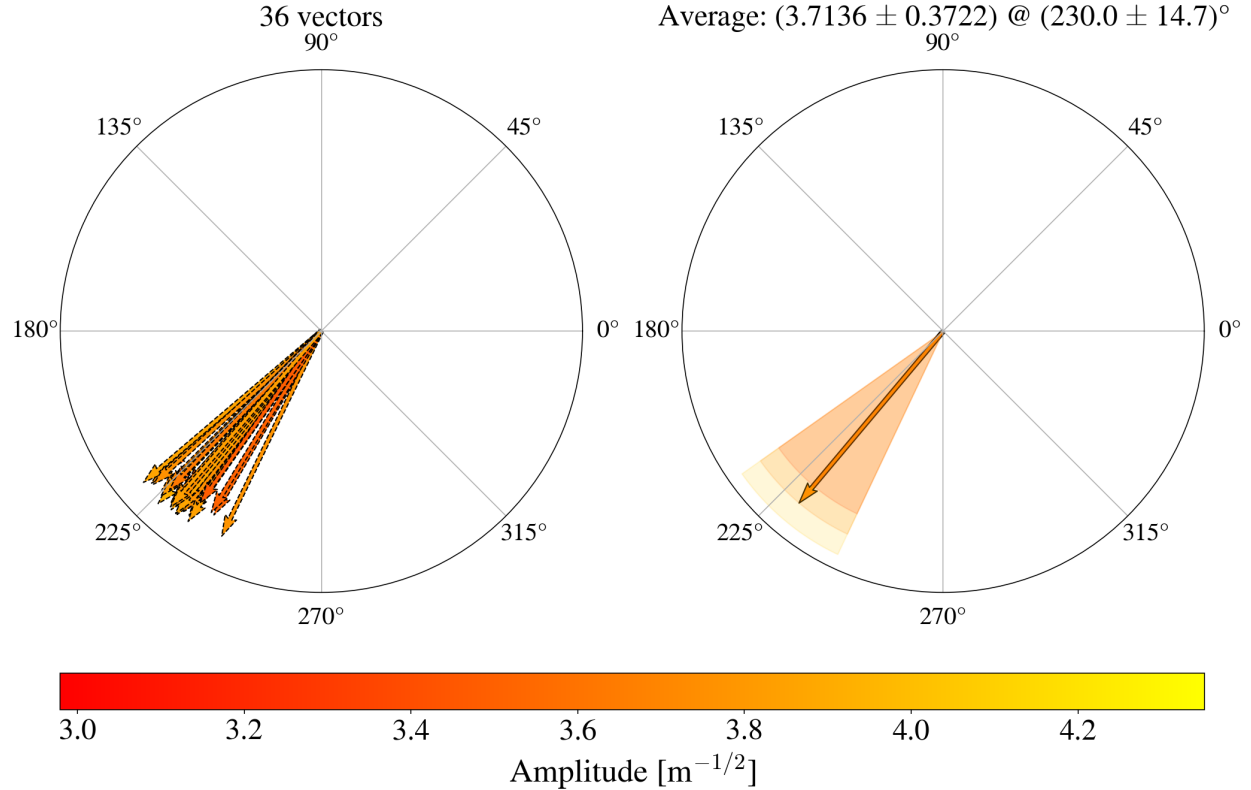


Figure 4.8 Polar plot for the measurement of  $h_{3000}$  for 36 measurements at horizontal BPM R:HP620.

For every BPM, measurements like those presented in Fig. 4.8 are done. In the case of the  $h_{3000}$ , one can use the 104 horizontal BPMs. For the case of the  $h_{0030}$  term, the 104 vertical BPMs are used. Figure 4.9 shows a plot of the amplitude of the measured  $h_{3000}$  as a function of the BPM used. Each label (e.g., R:HP100, R:HP106,..., R:HP638) corresponds to a different BPM in the accelerator. The labels are ordered according to their physical positions along the Recycler Ring. Each point represents the amplitude of  $h_{3000}$  measured at the corresponding BPM. The error bars on each data point indicate the uncertainty in the measurement, coming from the statistical variance as shown in Fig. 4.8. The shaded background of Fig. 4.9 visually emphasizes the spread and distribution of the data points around the average. While there is a global spread, the local variations of  $h_{3000}$  from BPM to BPM correspond to the amount of sextupole between them. Nevertheless, the large discontinuity at the 600 region—before R:HP602—comes from the

momentum-estimation method, which calculates the coordinates at R:VP601. Following all the previous steps in this recipe will allow us to measure the RDTs at the Recycler Ring.

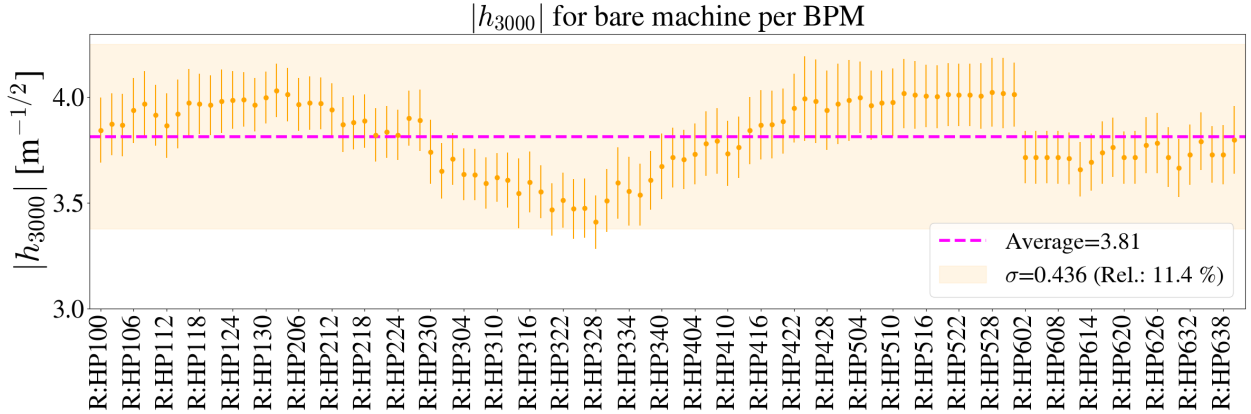


Figure 4.9 Measurements of  $h_{3000}$  at all horizontal BPMs around the ring. The average (dashed line) corresponds to the average  $h_{3000}$  from all the measurements.

## 4.3 Compensation of RDTs

### 4.3.1 Theoretical Approach from Lattice Model

Once there is a way to measure and calculate RDTs, the next step is to find a way to cancel out the RDTs. As mentioned in Sec. 3.6, four normal sextupoles and four skew sextupoles have been installed previously for this particular purpose. They have also been included in the lattice model. This section focuses on canceling the RDTs from a lattice model perspective—just from theoretical considerations. One can calculate the RDTs from the lattice model as shown in Sec. 4.1.

The first step is to understand how to cancel out a single RDT—a single resonance line. For example, to compensate the  $3Q_x$  line, the  $h_{3000}$  would need to be canceled. In order to cancel this term, one needs to set the appropriate  $K_2$  coefficients to the sextupoles. This procedure is equivalent to setting the appropriate currents in the sextupoles. The appropriate  $K_2$  coefficients are

calculated from the following equation:

$$\begin{bmatrix} -|h_{3000}| \cos \psi_{3000} \\ -|h_{3000}| \sin \psi_{3000} \\ 0 \\ 0 \end{bmatrix}_{(Bare)} = \mathbf{M} \begin{bmatrix} K_2^{(sc220)} \\ K_2^{(sc222)} \\ K_2^{(sc319)} \\ K_2^{(sc321)} \end{bmatrix}, \quad (4.16)$$

where the  $h_{3000}$  RDT is a complex quantity with a real and imaginary part, i.e.,  $h_{3000} = |h_{3000}| e^{i\psi_{3000}} = |h_{3000}| \cos \psi_{3000} + i|h_{3000}| \sin \psi_{3000}$ . The  $\mathbf{M}$  term corresponds to the RDT response matrix. Finally, the  $K_2^{(i)}$  corresponds to the  $i$ -th compensation sextupole coefficient. The response matrix for compensating only  $3Q_x$  and arbitrarily setting two sextupole currents to the negative of each other reads:

$$\mathbf{M} = \begin{bmatrix} M_{11} & M_{12} & M_{13} & M_{14} \\ M_{21} & M_{22} & M_{23} & M_{24} \\ 1 & 1 & 0 & 0 \\ 0 & 0 & 1 & 1 \end{bmatrix}, \quad (4.17)$$

where the theoretical matrix coefficients are calculated from the derivatives of the expressions in Table 4.1 concerning  $K_2^{(i)}$ , and they read:

$$M_{11} = \frac{1}{48} l_{sc} \beta_{x(sc220)}^{3/2} \cos 3\phi_{x(sc220)}, \quad (4.18)$$

$$M_{12} = \frac{1}{48} l_{sc} \beta_{x(sc222)}^{3/2} \cos 3\phi_{x(sc222)}, \quad (4.19)$$

$$M_{13} = \frac{1}{48} l_{sc} \beta_{x(sc319)}^{3/2} \cos 3\phi_{x(sc319)}, \quad (4.20)$$

$$M_{14} = \frac{1}{48} l_{sc} \beta_{x(sc321)}^{3/2} \cos 3\phi_{x(sc321)}, \quad (4.21)$$

$$M_{21} = \frac{1}{48} l_{sc} \beta_{x(sc220)}^{3/2} \sin 3\phi_{x(sc220)}, \quad (4.22)$$

$$M_{22} = \frac{1}{48} l_{sc} \beta_{x(sc222)}^{3/2} \sin 3\phi_{x(sc222)}, \quad (4.23)$$

$$M_{23} = \frac{1}{48} l_{sc} \beta_{x(sc319)}^{3/2} \sin 3\phi_{x(sc319)}, \quad (4.24)$$

$$M_{24} = \frac{1}{48} l_{sc} \beta_{x(sc321)}^{3/2} \sin 3\phi_{x(sc321)}, \quad (4.25)$$

where each beta function  $\beta_{u(i)}$  and phase evaluation  $\phi_{u(i)}$  in the  $u$  plane—horizontal or vertical—is taken at the location of the  $i$ -th compensation element. Every compensation magnet has the same length of  $l_{sc}$ .

Once one calculates the response matrix, the solution can be found by calculating its inverse and operating on the bare machine RDT vector. This RDT vector is a known quantity that can be calculated from the lattice model. The solution for compensation thus reads:

$$\begin{bmatrix} K_2^{(sc220)} \\ K_2^{(sc222)} \\ K_2^{(sc319)} \\ K_2^{(sc321)} \end{bmatrix}_{(Comp)} = \mathbf{M}^{-1} \begin{bmatrix} -|h_{3000}| \cos \psi_{3000} \\ -|h_{3000}| \sin \psi_{3000} \\ 0 \\ 0 \end{bmatrix}_{(Bare)}. \quad (4.26)$$

Table 4.4 shows this equation’s solution for arbitrary lattice tunes. It is worth pointing out that the RDT response matrix, as defined in Eq. 4.17, should have an inverse. Nevertheless, one can relax the problem constraints by dropping the two last rows of Eq. 4.17. For this case, the corresponding equation to Eq. 4.26 would involve calculating the pseudo-inverse using a least-squares approach. In this case, every sextupole should have different values for the  $K_2$  coefficients that compensate  $h_{3000}$ .

Table 4.4  $K_2$  coefficients that cancel out the  $h_{3000}$  term. These values were calculated for a Recycler lattice tuned to  $Q_x = 25.4422$  and  $Q_y = 24.3915$ .

Sextupole	$K_2$ [m <sup>-3</sup> ]
SC220	-0.594702
SC222	0.594702
SC319	0.930019
SC321	-0.930019

Figure 4.10 shows the calculation of the  $h_{3000}$  RDT once one sets the  $K_2$  coefficients in the sextupoles to the values in Table 4.4. For this case, as opposed to the bare machine calculation from

Fig. 4.1, the cumulative sum of  $h_{3000}$  goes to 0 at the end of the sum. This compensation means that one has canceled the global RDT. Furthermore, if Fig. 4.1 is compared to Fig. 4.10, one can see the big spikes in the middle of the lattice that corresponds to the individual contributions from the compensation sextupoles. These kicks ultimately bring the  $h_{3000}$  term to zero.

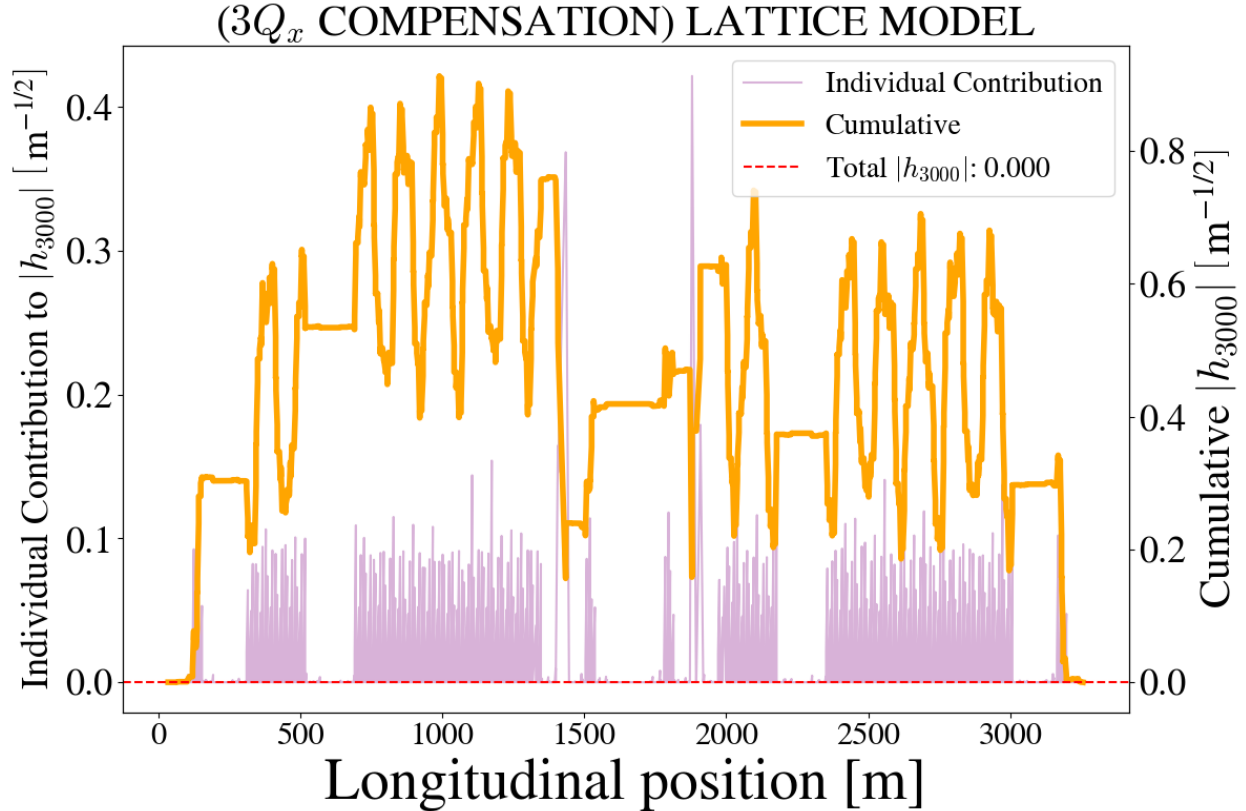


Figure 4.10 Distribution of the  $h_{3000}$  term around the ring with individual contributions from each relevant element and the cumulative sum from an arbitrary starting point when correction elements are set to compensate  $3Q_x = 76$ , i.e.,  $h_{3000} = 0$ .

On the other hand, there is the  $h_{1020}$  term. This one also gets affected if normal sextupole components are changed in the lattice, as explained by the expressions in Table 4.1. Therefore, looking at how  $h_{1020}$  changes as  $h_{3000}$  is compensated is interesting. Figure 4.11 shows the calculation for this term as one compensates  $3Q_x$ . Again, four additional spikes show up in the individual contribution plot exactly where the compensation sextupoles are placed. If one compares this plot to Fig. 4.2, it can also be seen that the total sum of the  $h_{1020}$  term increases from  $1.739 \text{ m}^{-1/2}$  to  $1.988 \text{ m}^{-1/2}$ . This shows that by compensating the  $h_{3000}$  RDT, the  $h_{1020}$  increases. This effect

means that compensating one resonance line might worsen other lines.

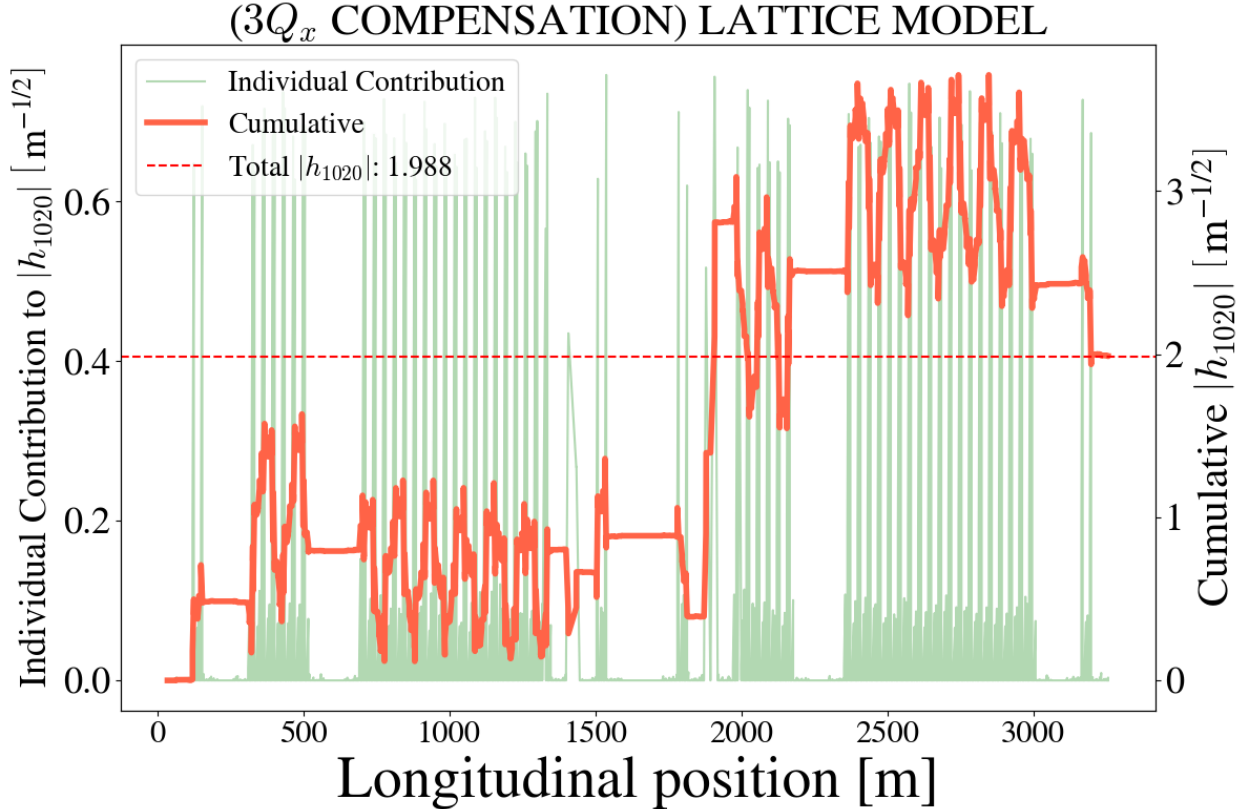


Figure 4.11 Distribution of the  $h_{1020}$  term around the ring with individual contributions from each relevant element and the cumulative sum from an arbitrary starting point when correction elements are set to compensate  $3Q_x = 76$ , i.e.,  $h_{3000} = 0$ .

An effort can be made to extend Eq. 4.16 to include the cancellation of  $h_{1020}$ . The simultaneous compensation of the  $h_{3000}$  and the  $h_{1020}$  term is given by the following equation:

$$\begin{bmatrix} -|h_{3000}| \cos \psi_{3000} \\ -|h_{3000}| \sin \psi_{3000} \\ -|h_{1020}| \cos \psi_{1020} \\ -|h_{1020}| \sin \psi_{1020} \end{bmatrix}_{(Bare)} = \mathbf{M} \begin{bmatrix} K_2^{(sc220)} \\ K_2^{(sc222)} \\ K_2^{(sc319)} \\ K_2^{(sc321)} \end{bmatrix}. \quad (4.27)$$

For this case, one needs to modify the response matrix  $\mathbf{M}$ . This new response matrix reads:

$$\mathbf{M} = \begin{bmatrix} M_{11} & M_{12} & M_{13} & M_{14} \\ M_{21} & M_{22} & M_{23} & M_{24} \\ M_{31} & M_{32} & M_{33} & M_{34} \\ M_{41} & M_{42} & M_{43} & M_{44} \end{bmatrix}, \quad (4.28)$$

where the first two rows are defined the same as before by Eqs. 4.19-4.25. Similarly, the coefficients in the last two rows are defined by:

$$M_{31} = \frac{1}{16} l_{sc} \beta_{x(sc220)}^{1/2} \beta_{y(sc220)} \cos(\phi_{x(sc220)} + 2\phi_{y(sc220)}), \quad (4.29)$$

$$M_{32} = \frac{1}{16} l_{sc} \beta_{x(sc222)}^{1/2} \beta_{y(sc222)} \cos(\phi_{x(sc222)} + 2\phi_{y(sc222)}), \quad (4.30)$$

$$M_{33} = \frac{1}{16} l_{sc} \beta_{x(sc319)}^{1/2} \beta_{y(sc319)} \cos(\phi_{x(sc319)} + 2\phi_{y(sc319)}), \quad (4.31)$$

$$M_{34} = \frac{1}{16} l_{sc} \beta_{x(sc321)}^{1/2} \beta_{y(sc321)} \cos(\phi_{x(sc321)} + 2\phi_{y(sc321)}), \quad (4.32)$$

$$M_{41} = \frac{1}{16} l_{sc} \beta_{x(sc220)}^{1/2} \beta_{y(sc220)} \sin(\phi_{x(sc220)} + 2\phi_{y(sc220)}), \quad (4.33)$$

$$M_{42} = \frac{1}{16} l_{sc} \beta_{x(sc222)}^{1/2} \beta_{y(sc222)} \sin(\phi_{x(sc222)} + 2\phi_{y(sc222)}), \quad (4.34)$$

$$M_{43} = \frac{1}{16} l_{sc} \beta_{x(sc319)}^{1/2} \beta_{y(sc319)} \sin(\phi_{x(sc319)} + 2\phi_{y(sc319)}), \quad (4.35)$$

$$M_{44} = \frac{1}{16} l_{sc} \beta_{x(sc321)}^{1/2} \beta_{y(sc321)} \sin(\phi_{x(sc321)} + 2\phi_{y(sc321)}), \quad (4.36)$$

as calculated from the derivative of  $h_{1020}$  with respect to  $K_2^{(i)}$ , with the explicit expression in Table 4.1.

The solution to Eq. 4.27 is just given by the inverse of the response matrix applied to the bare machine RDT vector. This perspective is equivalent to the approach in Eq. 4.26. The result of this approach is the calculation of the  $K_2$  coefficients in the compensation sextupoles that cancel out both the  $h_{3000}$  and the  $h_{1020}$  term. The solution to Eq. 4.27 is given in Table 4.5 for an arbitrarily tuned lattice. One thing to note is that these values are almost one order of magnitude larger than those in Table 4.4.

Table 4.5  $K_2$  coefficients that cancel out the  $h_{3000}$  and  $h_{1020}$  term. These values were calculated for a Recycler lattice tuned to  $Q_x = 25.4422$  and  $Q_y = 24.3915$ .

<b>Sextupole</b>	$K_2$ [m $^{-3}$ ]
SC220	6.039888
SC222	4.826964
SC319	-4.529674
SC321	-6.167827

Once one inputs the magnet coefficients from Table 4.5 into the lattice model, the RDT calculations can be done to verify that the terms effectively go to 0. Figures 4.12 and 4.13 show these calculations. Moreover, one can see how the RDT sums add up to 0. Nevertheless, it can be seen from these plots how the spikes are now very large compared to the previous cases and compared to the individual contributions from around the lattice. This effect means the sextupole component will be localized in the compensation sextupoles' locations. This is an unwanted effect, given that these large sextupole kicks will overfocus the beam in these locations. In particular, the sextupole component will no longer be perturbative in these locations.

## (COMPENSATION ON) LATTICE MODEL

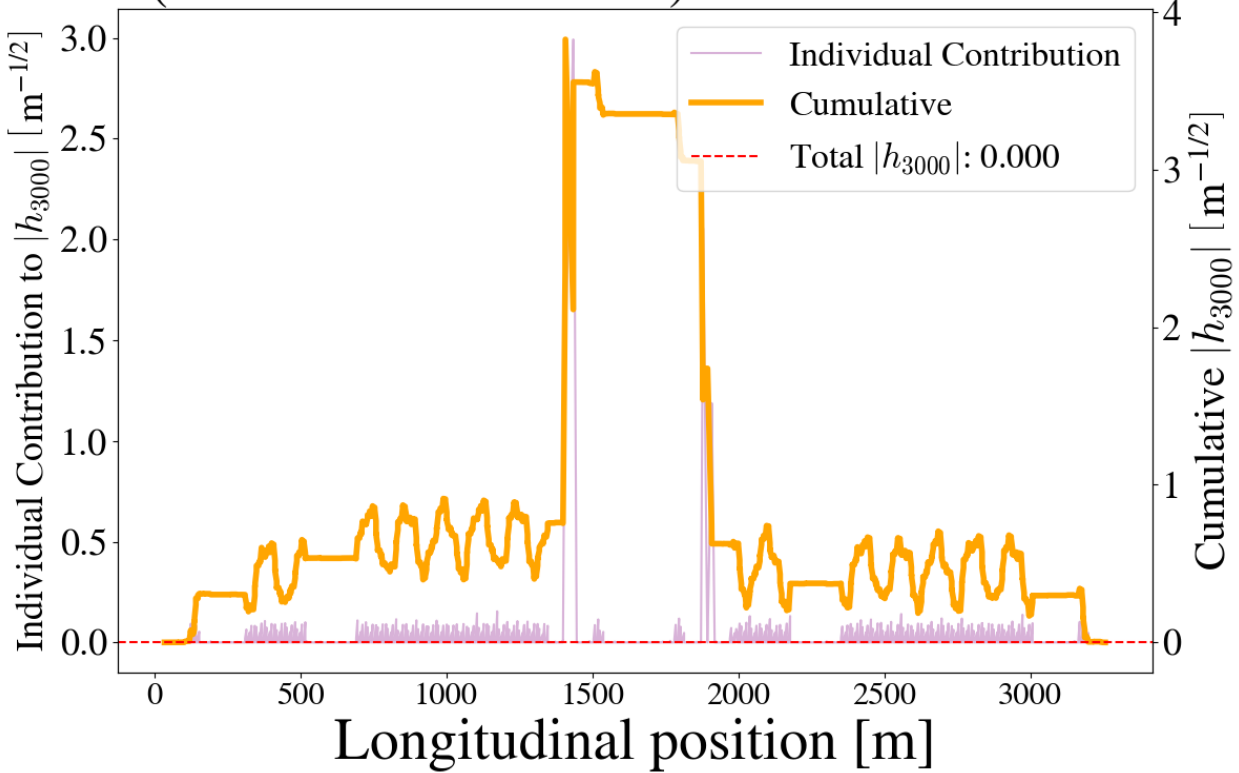


Figure 4.12 Distribution of the  $h_{3000}$  term around the ring with individual contributions from each relevant element and the cumulative sum from an arbitrary starting point. This sum is done with existing sextupoles powered at the correct currents to simultaneously cancel out  $h_{3000}$  and  $h_{1020}$ .

The results from solving Eq. 4.27, as specified in Table 4.5, indicate that the  $K_2$  coefficients are very large compared to the case where there was only  $h_{3000}$  compensation. Experimentally, the currents in the sextupoles that compensate both  $h_{3000}$  and  $h_{1020}$  are too large and exceed the range of operational limits. While there are no limits for  $K_2$  in the sextupoles from the lattice model, the solutions are very large. Suppose one were to translate the operational current limits of the sextupoles to the lattice model  $K_2$  coefficients. In that case, one can show that the solutions lie out of this range, i.e., the maximum  $K_2$  coefficients are around  $1 \text{ m}^{-3}$ . Therefore, this solution does not work for the operational beam. Section 4.6 shows how to circumvent this by adding two additional sextupoles in the lattice at optimized locations to effectively bring down the compensation  $K_2$  coefficients—the compensation currents.

## (COMPENSATION ON) LATTICE MODEL

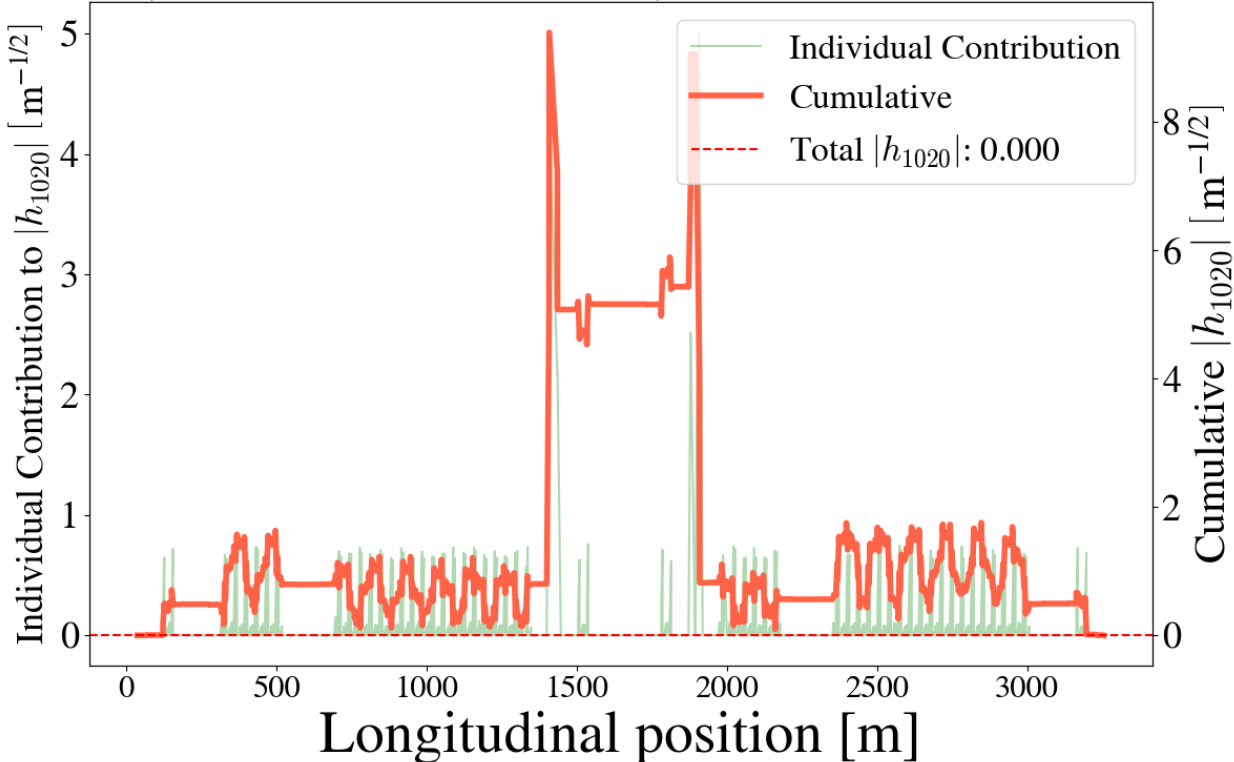


Figure 4.13 Distribution of the  $h_{1020}$  term around the ring with individual contributions from each relevant element and the cumulative sum from an arbitrary starting point. This distribution is with existing sextupoles powered at the correct currents to simultaneously cancel out  $h_{3000}$  and  $h_{1020}$ .

While the previous section focused only on the normal sextupole RDTs, all of this can easily be extended to the skew sextupole RDTs, i.e.,  $h_{0030}$  and  $h_{2010}$ . All of this assumes the lattice model has a good approximation of the skew sextupole distribution around the ring. For the Recycler Ring, the skew sextupole resonances are not as strong as the normal sextupole resonance  $3Q_x = 76$ . This resonance dominates the losses in this region. Therefore, special attention has been paid to the  $3Q_x = 76$  resonance and its  $h_{3000}$  resonance driving term. Nevertheless, using the skew sextupole correctors, this procedure works for  $3Q_y = 73$  and  $2Q_x + Q_y = 75$  and its corresponding RDTs.

### 4.3.2 Response Matrix Approach

The next step is translating the procedure from the previous section to the real machine. This step is done by measuring the response matrix. As mentioned before, for resonance compensation there are four dedicated normal sextupoles with currents that can be set to  $(I_{sc220}, I_{sc222}, I_{sc319}, I_{sc321})$

and four dedicated skew sextupoles with currents that can be set to  $(I_{ss323}, I_{ss323}, I_{ss319}, I_{ss321})$ . As shown in the previous section, one RDT can be canceled out with the right kick from the correction elements, which means the resonances are corrected to the first order.

Nevertheless, compensating for one resonance line might worsen other resonances. This is why, for simultaneous compensation, compensation currents will vary depending on the subsets of resonances to compensate. In principle, the currents  $I_x$  needed in each correction element in order to cancel out the four bare machine RDTs are given by the solution to this linear system of equations:

$$\begin{bmatrix} -|h_{3000}| \cos(\psi_{3000}) \\ -|h_{3000}| \sin(\psi_{3000}) \\ -|h_{1020}| \cos(\psi_{1020}) \\ -|h_{1020}| \sin(\psi_{1020}) \\ -|h_{0030}| \cos(\psi_{3000}) \\ -|h_{0030}| \sin(\psi_{3000}) \\ -|h_{2010}| \cos(\psi_{1020}) \\ -|h_{2010}| \sin(\psi_{1020}) \end{bmatrix}_{(Bare)} = \mathbf{M} \begin{bmatrix} I_{sc220} \\ I_{sc222} \\ I_{sc319} \\ I_{sc321} \\ I_{ss223} \\ I_{ss323} \\ I_{ss319} \\ I_{ss321} \end{bmatrix} \quad (4.37)$$

where  $M_{ij}$  is the response matrix for the RDTs with respect to the currents and includes any roll that can happen for the correction sextupoles. It is worth emphasizing that one can calculate the response matrix from measurements instead of the model for this approach. This response matrix  $M_{ij}$  can be calculated by scanning the currents in each correction element and looking at the response from the real and imaginary part of the RDTs, i.e.,  $h_{jklm} = |h_{jklm}| e^{i\psi_{jklm}}$ .

In reality, there are limitations to solving Eq. 4.37. First, all the RDTs ( $h_{jklm}$ ) may not be accessible for measurement, given that they may not show up as a spectral line. Another limitation is that the solution for the currents may be outside the maximum limits for the correction elements.

One can also try canceling a subset of RDTs from Eq. 4.37, including only one RDT. For example, in order to compensate  $3Q_x = 76$ , the system of equations to be solved is:

$$\begin{bmatrix} -|h_{3000}| \cos(\psi_{3000}) \\ -|h_{3000}| \sin(\psi_{3000}) \\ 0 \\ 0 \end{bmatrix}_{(Bare)} = \begin{bmatrix} M_{11} & M_{12} & M_{13} & M_{14} \\ M_{21} & M_{22} & M_{23} & M_{24} \\ 1 & 1 & 0 & 0 \\ 0 & 0 & 1 & 1 \end{bmatrix} \begin{bmatrix} I_{sc220} \\ I_{sc222} \\ I_{sc319} \\ I_{sc321} \end{bmatrix}, \quad (4.38)$$

which is analogous to Eq. 4.16, only now the sextupole currents are the knobs. Nevertheless, in this case, the RDT is measured from the procedure shown in Sec. 4.2 for the bare machine—no compensation sextupoles turned on. In order to measure the response matrix  $\mathbf{M}$ , the  $h_{3000}$  RDT has to be measured as a function of the compensation currents in the sextupoles. The procedure summarizing all of this is the following:

1. Measure the bare machine RDT vector for several shots, e.g., measure  $h_{3000}$  for 20 instances.
2. Choose a compensation sextupole for the first scan.
3. Set the compensation sextupole to the lower limit of the scan range, e.g., -10 Amps.
4. Measure the  $h_{3000}$  RDT (or arbitrary RDT) using following the recipe in Sec. 4.2.
5. Increase the current in the compensation sextupole by some step size, e.g., by 2 Amps, and repeat the RDT measurement.
6. Repeat steps 2-4 until the upper limit of the scan range, e.g., 10 Amps.
7. For every measurement, decompose the RDT into its real and imaginary part, e.g.,  $h_{3000} = |h_{3000}| \cos \psi_{3000} + i|h_{3000}| \sin \psi_{3000}$ .
8. Plot the real and imaginary part of the RDT as a function of sextupole current and perform a linear fit. The slopes of these fits are the corresponding  $M_{ij}$  response matrix coefficients.
9. Repeat steps 2-8 for the other compensation sextupoles until the response matrix is fully calculated. This procedure can be done for a subset of correctors, reducing the dimension of the response matrix.

10. Once the response matrix is specified, calculate its inverse (or pseudo-inverse) and operate on to the bare machine RDT vector in order to get the compensation currents on every BPM (see Fig. 4.16).

Figures 4.14 and 4.15 show an example of performing two of these scans for the  $h_{3000}$  term. In Fig. 4.14, it can be seen how the relationship between the real part and the imaginary part follows a linear relation within the shaded region. The fit for these plots was done only for this region, given that prior empirical data showed that the currents should not exceed the absolute value of 7 Amps. One can extract the response matrix coefficients from the slope values provided by the fit.

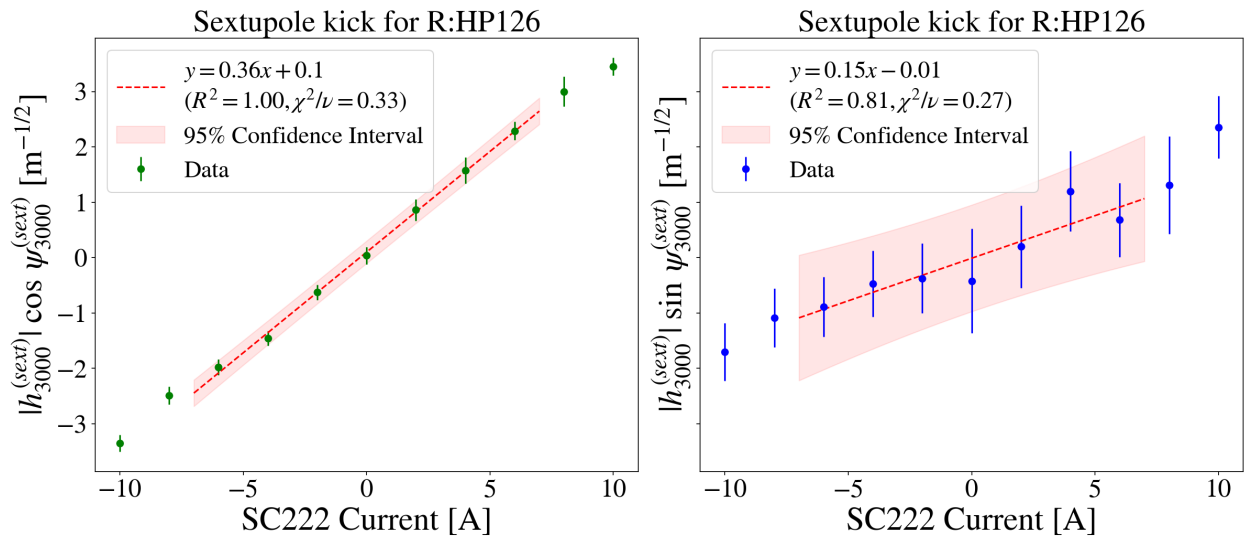


Figure 4.14 Real and imaginary part of  $h_{3000}$  as a function of current fed to compensation sextupole SC222. Measurement is shown for R:HP126 data.

Figures 4.14 and 4.15 are taken at two different BPMs, i.e., horizontal BPMs R:HP126 and R:HP612. Comparing both plots shows that the RDT sensitivity of  $h_{3000}$  changes depending on the sextupole used. Furthermore, at high currents, it can be seen that some non-linear behavior starts to kick in. This behavior was present in almost all BPMs. Nevertheless, this only happened at high currents far from the region of interest, which was capped at an absolute value of 6 Amps.

After performing this process, the result is an array of compensating currents predicted by every BPM. Figure 4.16 shows an example of these results. The bars at each BPM represent the predicted compensation current for a particular sextupole. While each BPM will give a local approximation

of what currents minimize the  $h_{3000}$  RDT, the sextupoles can only take one input. One must average all these currents to get a global compensation current that minimizes the RDT at every location. Nevertheless, given some uncertainty on the bare machine RDTs and the response matrix coefficients, this needs to be included in developing this global solution.

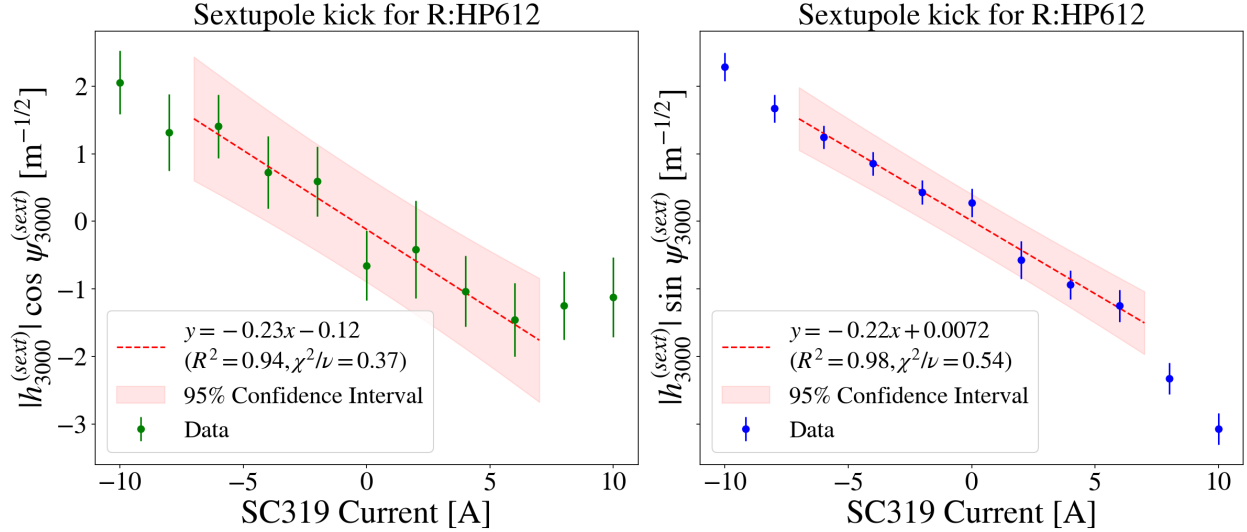


Figure 4.15 Real and imaginary part of  $h_{3000}$  as a function of current fed to compensation sextupole SC319. Measurement is shown for R:HP612 data.

In order to build a final setting for the compensation currents, not all BPMs are necessarily used. For this prediction, the BPMs that showed the most linear fit from the RDT scan as a function of current were used. One can use the R-squared statistics and the reduced  $\chi^2$  to quantify this linearity. Once the best BPMs were selected, the compensation currents were selected. This selection is why not all BPMs are plotted in Fig. 4.16. One can build a prediction function assuming that the currents predictions shown in Fig. 4.16 follow a bi-Gaussian distribution centered at the mean values with a variance equal to the uncertainty in the error bar. The prediction function is just the sum of all the bi-Gaussian distributions. A contour plot example of such a prediction function is shown in Fig. 4.17. Ultimately, this prediction function will specify a region in the currents' space of each sextupole where the best setting lies.

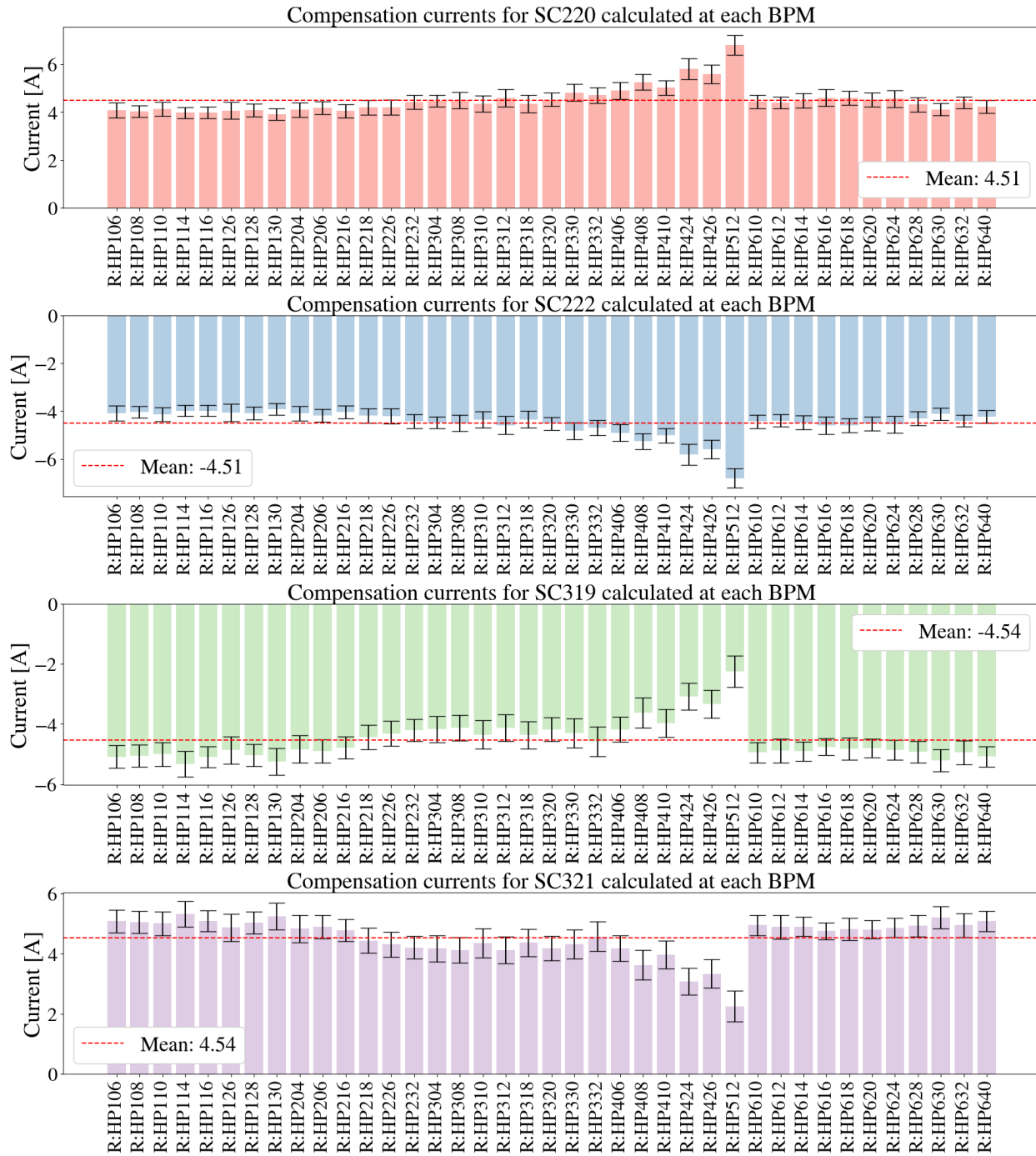


Figure 4.16 Compensation currents calculated from BPMs that showed the best R-square statistic from the RDT scans.

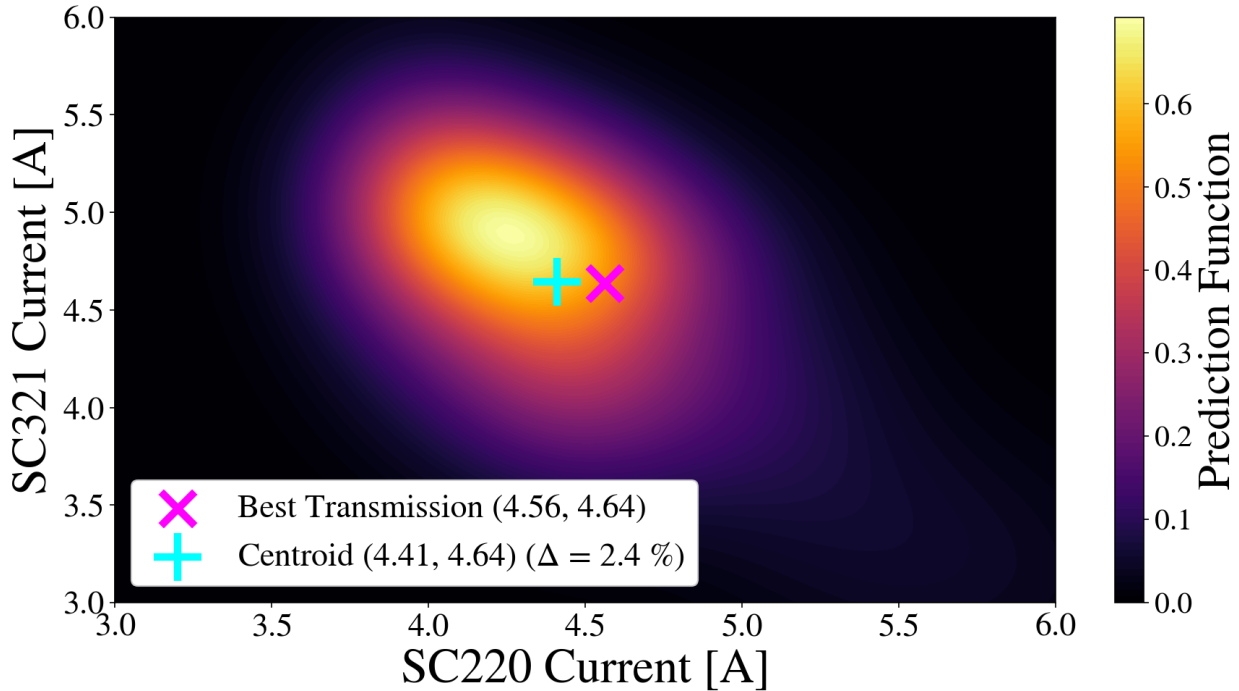


Figure 4.17 Prediction function built from the best R-squared statistics BPMs to predict the best global currents for  $h_{3000}$  compensation.

The prediction function in Fig. 4.17 can be used to predict an optimal setting for the currents in the compensation sextupoles. Specifically, the centroid of this prediction distribution can be calculated and used as the optimum setting. This centroid corresponds to the cyan cross in Fig. 4.17. Later in this chapter, a whole section is dedicated to verifying the compensation of resonances; see Sec. 4.5. Nevertheless, a quick way to verify resonance compensation is to use a dynamic tune ramp that crosses the  $3Q_x = 76$ . Uncorrected for, around 95% of the beam is lost once this resonance is crossed. One can use the interval where the prediction function thinks it is best to operate and scan the parameter space (sextupole currents) while recording beam transmission across the  $3Q_x$  resonance. The fuchsia X in Fig. 4.17 shows the setting with the best transmission—the best transmission now corresponds to less than 5% losses. The centroid of the prediction function is around 2.4% (relative distance) away from this experimental value. This difference shows that the predicted value from the response matrix approach does indeed reduce the losses from the  $3Q_x = 76$  line—meaning the  $h_{3000}$  RDT is minimized in this region.

#### 4.4 Optimization of Compensation Currents

The last section showed how to predict the optimum setting for the sextupoles by measuring the response matrix. Nevertheless, this procedure takes a few hours of study time and might not be accessible for routine operations. Therefore, one can perform this procedure once or twice per run. It is interesting to explore optimization algorithms that can help predict the optimum setting that minimizes losses from the resonance lines.

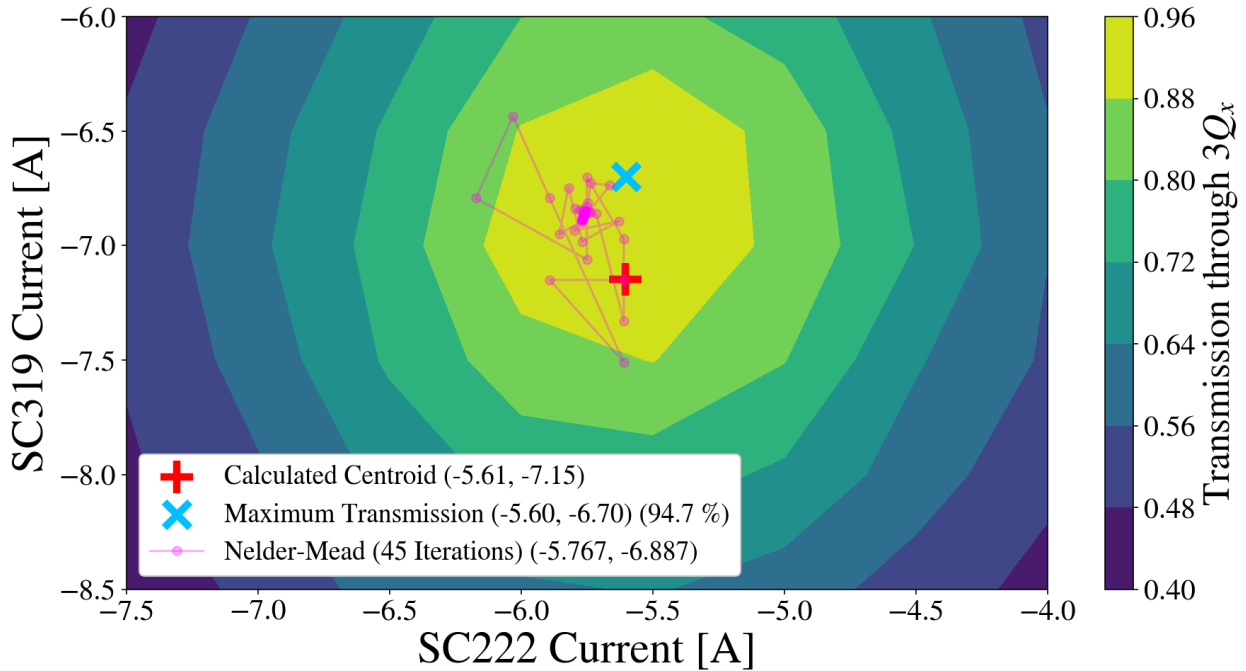


Figure 4.18 Nelder-Mead optimization from an instance where the response matrix prediction was used as the initial point. The contour plot shows the transmission through  $3Q_x$  as a function of the currents.

Figure 4.18 shows an example of using a Simplex (Nelder-Mead) optimization procedure to find the optimum setting in the compensation sextupoles. In the background of this plot, the contour plot corresponds to the experimentally measured transmission through  $3Q_x$ . This Nelder-Mead instance was started with the currents predicted from the response matrix approach. After 45 iterations, the optimization algorithm converged to the value specified in the legend of Fig. 4.18. This value is fairly close to the value predicted by the response matrix approach. The maximum transmission from the contour plot (red cross in Fig. 4.18) agrees up to some significance with

the currents from the optimization procedure and the response matrix approach. They are all fairly close within a region. Therefore, by taking the response-matrix predicted currents as an initial point, one can fine-tune this configuration using this optimization algorithm. In principle, any numerical optimization algorithm should converge to the answer given that the underlying function is not especially difficult—in the context of numerical optimization.

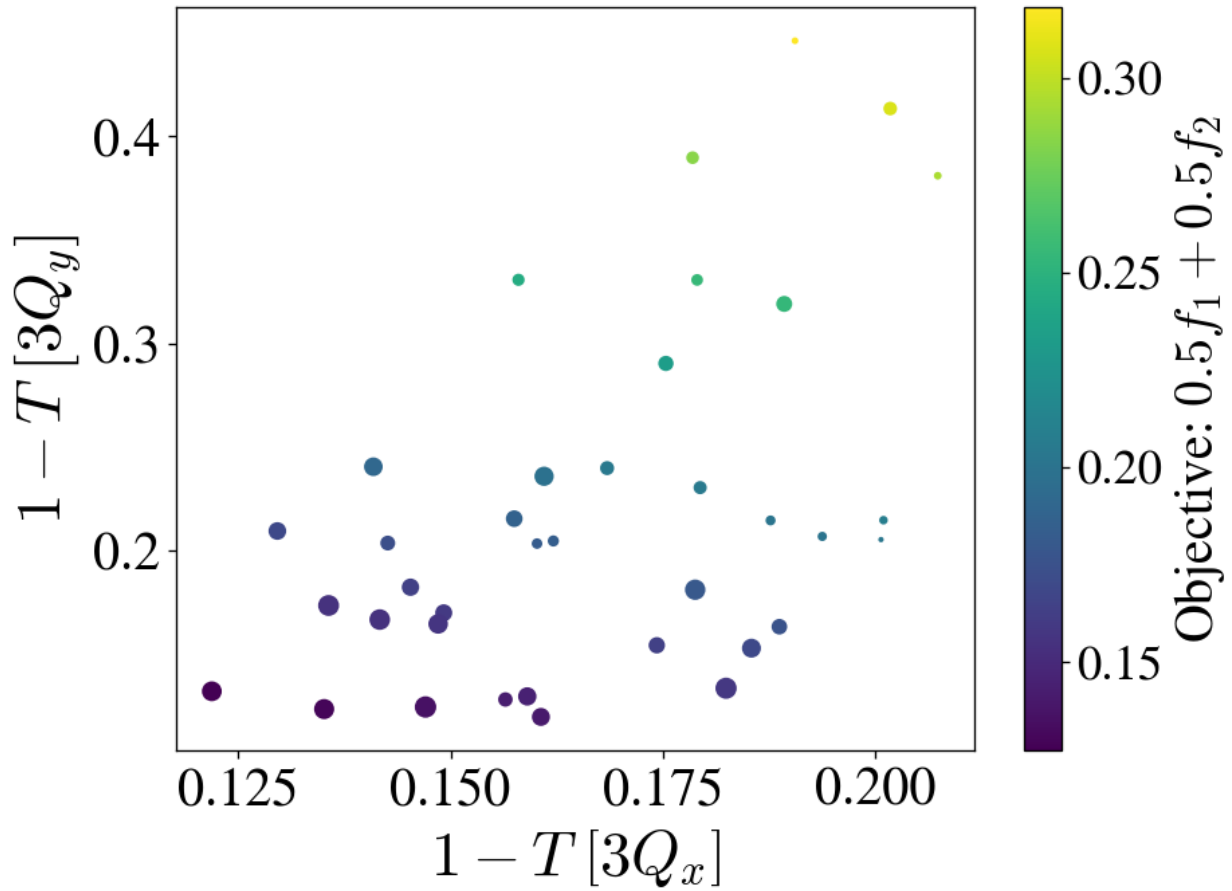


Figure 4.19 Multiobjective Nelder-Mead optimization of the transmission through  $3Q_x$  and  $3Q_y$ . The objective function to be minimized was defined as an equally weighted sum of both minus transmissions—corresponding to the fractional losses through the resonance lines.

Figure 4.19 takes this further by performing multiobjective optimization on two resonance lines, i.e.,  $3Q_x$  and  $3Q_y$ . The eight compensation sextupoles (see Table 3.3), including normal and skew, were used for this optimization. While, in principle, powering up the normal compensation sextupoles should not affect the  $3Q_y$  line, it was observed that the losses due to this line increased when  $3Q_x$  was corrected. This observation motivated the multiobjective optimization of both

lines. Figure 4.19 shows how the other one got worse by trying to correct one line. Ultimately, the best configuration would lie on the Pareto front of these functions. The y-axis in Fig. 4.19 represents the fractional beam loss when crossing the resonance lines. The objective function minimized by a Nelder-Mead algorithm was defined as an equally weighted sum of both fractional losses. Ultimately, Fig. 4.19 shows how the algorithm slowly drifts toward the best solution to this problem.

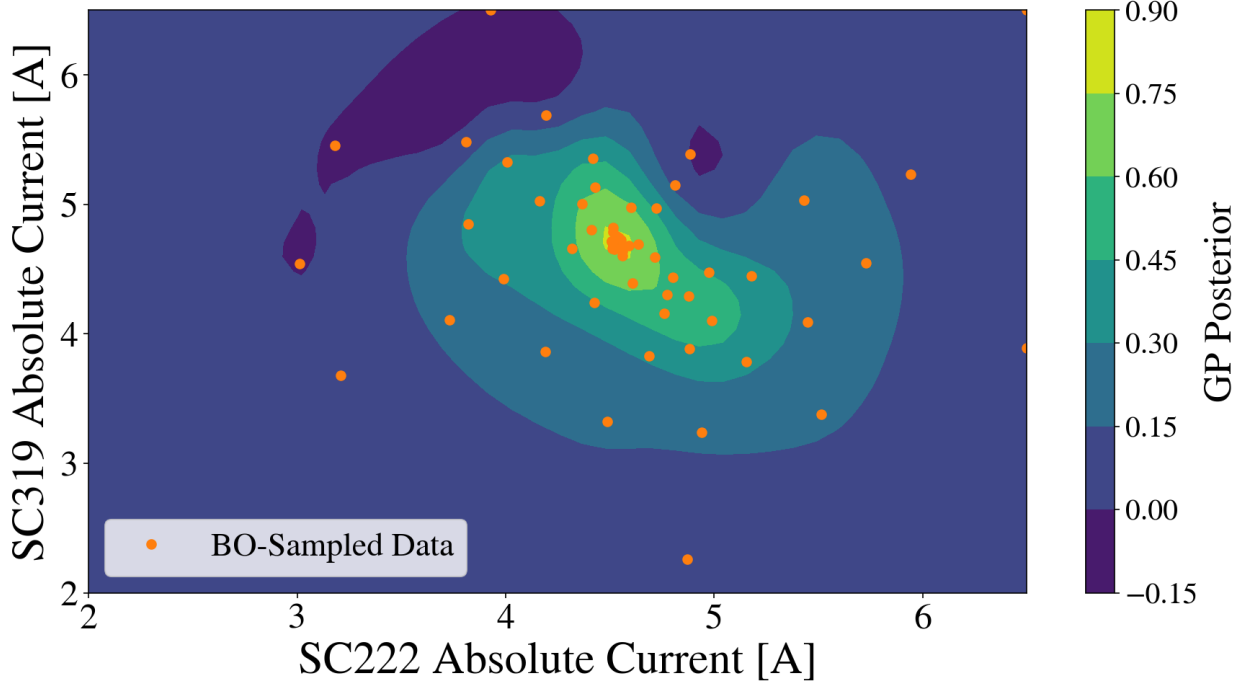


Figure 4.20 Bayesian optimization of the compensation currents for  $3Q_x$  transmission. The contour plot shows the Gaussian Process Posterior function trained by the sampled data (orange dots).

One can use more advanced optimization algorithms to fine-tune the best optimization currents in the compensation sextupoles. Figure 4.20 shows an instance where Bayesian optimization was used for this purpose. A summary of Bayesian optimization can be found in Ref. [47]. It is worth clarifying that the optimum currents from Fig. 4.20 differ from the ones in 4.18 given that the first plot was generated from data taken in the 2022-2023 run and the other one from the 2021-2022 run. The tuning of the machine changes from year to year—even from week to week. The background contour plot of Fig. 4.20 corresponds to the Gaussian Process posterior trained from the Bayesian-guided transmission sampling through  $3Q_x$ . Ultimately, the cluster of points

around the maximum shows how the algorithm converged and found the best configuration to feed the sextupoles. These currents are close to the ones shown in Fig. 4.17. Chapter 5 shows some studies done at the Proton-Synchrotron Booster (PSB) at CERN, where this optimization approach is fully embraced to compensate resonance lines.

## 4.5 Experimental Verification of Compensation

### 4.5.1 Dynamic Loss Maps

One effective method for visualizing resonance compensation involves constructing dynamic loss maps. In order to generate these loss maps, specialized quadrupoles responsible for controlling the tune of the Recycler are gradually adjusted to map out the desired tune area. These are quadrupoles inside the tune trombone region. The beam loss rate is measured using DCCT devices across the specified region throughout this process. This procedure is done in the horizontal and vertical directions. One generates the initial horizontal scan by maintaining a constant vertical tune while implementing a horizontal tune ramp ranging from  $Q_x = 25.47$  to  $Q_x = 25.31$ . Subsequently, the vertical tune, initially set as *constant* at  $Q_y = 24.47$ , is adjusted incrementally to  $Q_y = 24.31$  in steps of 0.005, with intensity data recorded at each step. Conversely, the roles are reversed for the vertical scan: the horizontal tune remains constant while a vertical tune ramp progresses from  $Q_y = 24.47$  to  $Q_y = 24.31$ . Then, the *constant* horizontal tune is varied from  $Q_x = 25.47$  to  $Q_y = 25.31$  in steps of 0.005. The resulting intensity data from both scans can be differentiated, normalized by the instantaneous intensity, and interpolated within a two-dimensional grid to construct plots akin to those depicted in Figs. 4.21 and 4.22. Figure 4.21 demonstrates the initial machine scan without compensation. If plotted alongside the theoretical positions of the lines as in Fig. 4.22, the beam loss bands align with the resonance lines.

Figure 4.22 illustrates the correspondence between the loss patterns and the theoretical positions of resonance lines. A slight deviation exists between the set and actual tunes due to calibration adjustments from the tune trombone program. However, despite this variance, the resonance line configuration within the loss pattern facilitates the visualization of each resonance's strengths. Specifically, a higher normalized loss at a particular tune location indicates a stronger Resonance

Driving Term (RDT) for the corresponding resonance line. Inside Figs. 4.21 and 4.22, third, fourth, and even traces of fifth-order resonance lines are discernible, with third-order resonance lines exhibiting the greatest prominence.

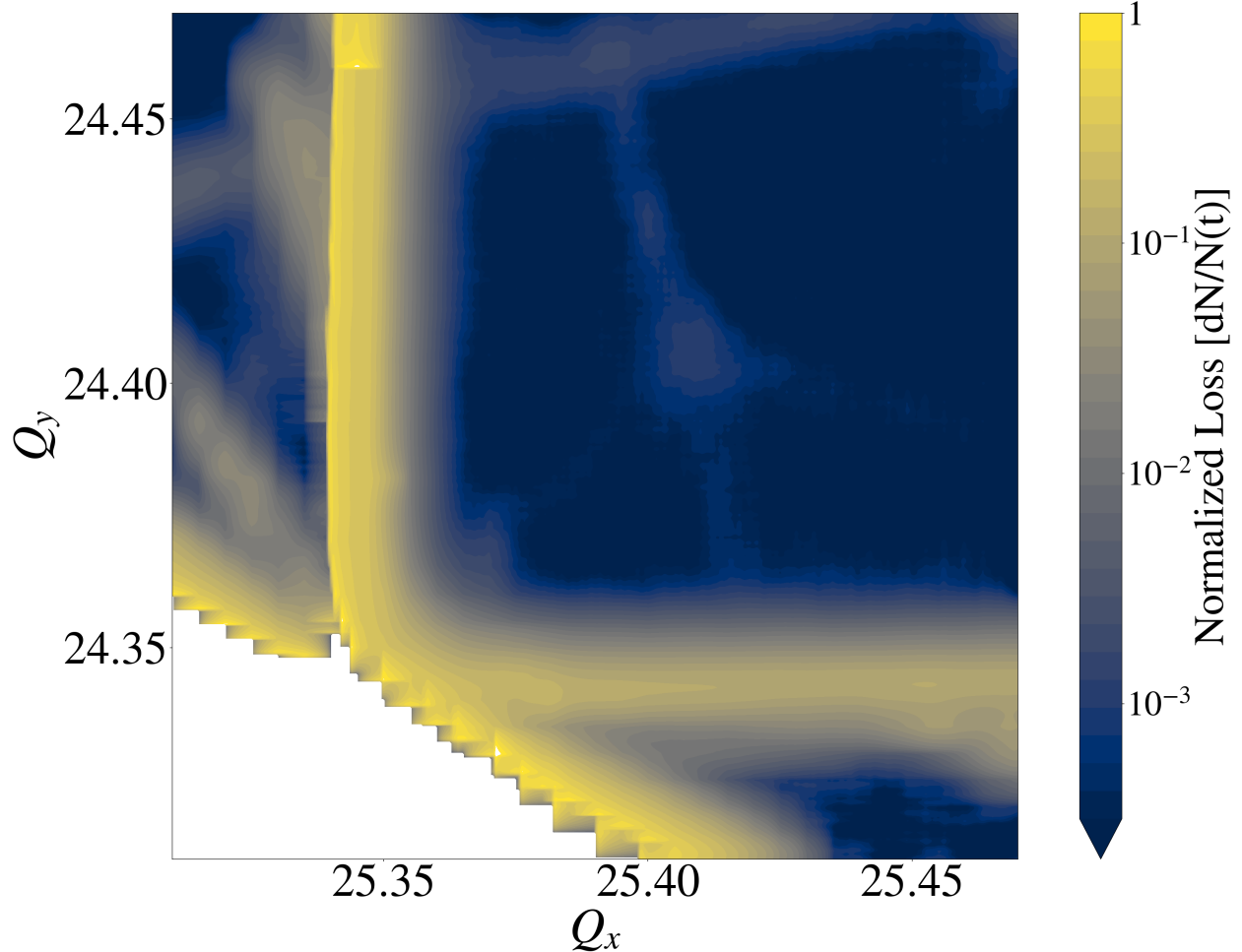


Figure 4.21 Dynamic loss map from ramping the tunes with an interval of  $\Delta Q_u = 0.005$  in both directions. The directions of the scan are from left to right and top to bottom. The results are superimposed in this plot.

Figure 4.23 depicts dynamic loss maps representing various configurations of the compensation sextupoles. Specifically, Fig. 4.23a illustrates the loss map for the bare machine, where no compensation sextupoles are activated, while Fig. 4.23b and Fig. 4.23c demonstrate compensation for a single resonance line each. For  $3Q_x$  compensation, one can set the four normal sextupoles to the calculated compensation currents using the RDT response matrix method. Moreover, a comparison between Fig. 4.23b and Fig. 4.23a indicates a reduction of normalized losses by two

orders of magnitude at the  $3Q_x$  line with compensation. This observation also holds for the  $3Q_y$  compensation, as shown in Fig. 4.23c.

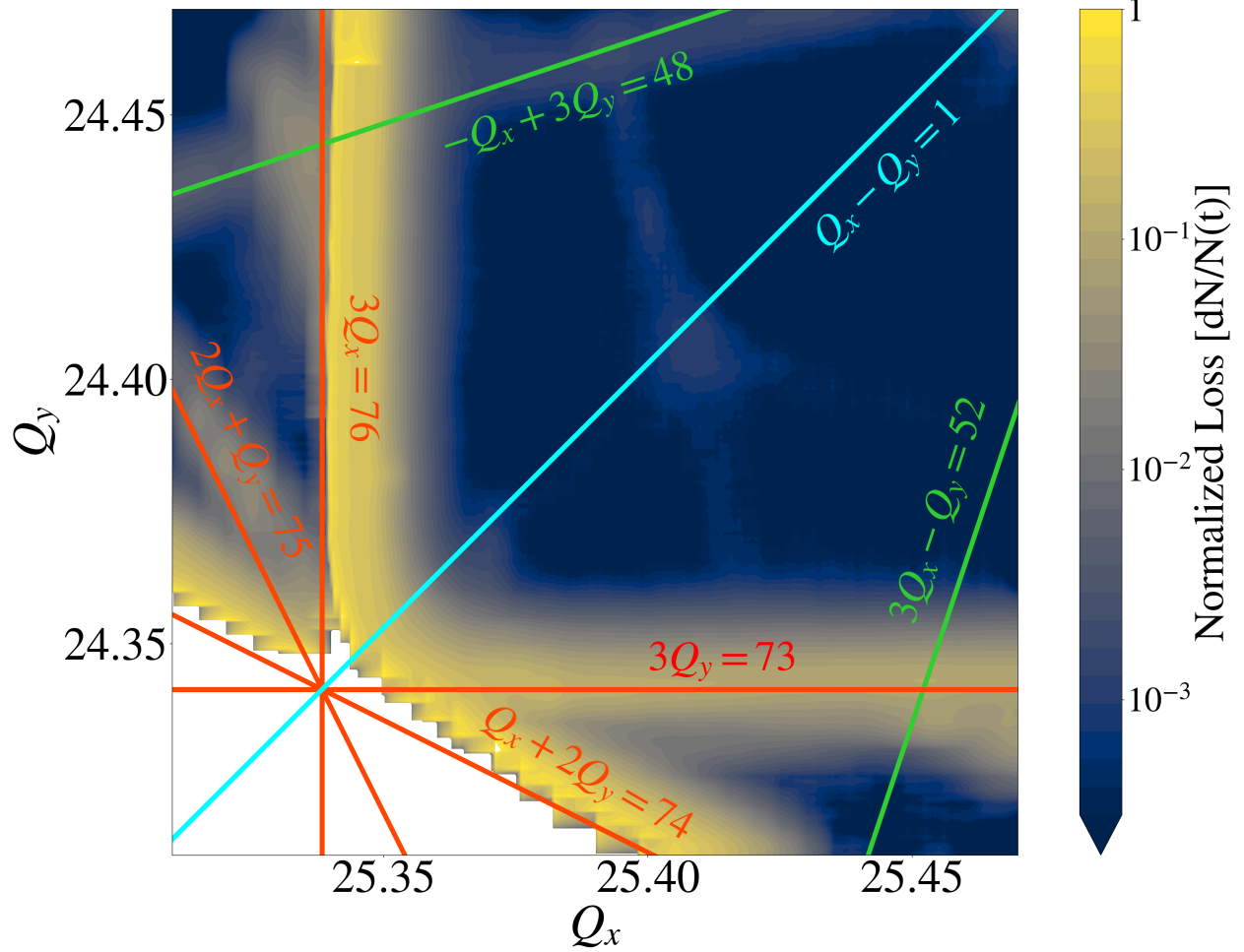


Figure 4.22 Dynamic loss map with the corresponding lines from Fig. 3.7 drawn on top.

Figures 4.23d, 4.23e, and 4.23f showcase the optimal configurations of compensation sextupoles designed to address multiple resonance lines simultaneously. It is important to note that while attempting to compensate for one or multiple resonance lines, there is a possibility that other resonance lines may strengthen. This effect is evident in the explicit case depicted in Fig. 4.23f, where compensating for  $3Q_y$  and  $Q_x + 2Q_y$  leads to the amplification of the  $2Q_x + Q_y$  resonance. Such occurrences pose a limitation when aiming to compensate for more than two resonance lines, as the compensation currents tend to increase. There exists a constraint on the currents supplied to the compensation sextupoles. For instance, the required currents exceed the current limits when

compensating both normal sextupole lines,  $3Q_x$  and  $Q_x + 2Q_y$ . Ongoing efforts are focused on reducing the compensation currents in this specific scenario. Section 4.6 summarizes some of these efforts, where additional sextupoles have been installed in order to decrease the currents that cancel out both the  $h_{3000}$  and  $h_{1020}$  RDTs.

Another notable detail is evident in Figs. 4.23a-4.23f is the presence of white areas within the loss maps, indicating regions with insufficient beam particles to map out the losses accurately. In certain configurations of the compensation sextupoles, the combined weakening of the third-order resonance lines occurs in a manner that leaves some beam remaining beyond these lines. One can argue that conducting two additional scans, injected from the left and bottom, could effectively map out these inaccessible regions. Such an enhancement could be considered a future upgrade to these dynamic loss maps. Ultimately, all the plots presented in Fig. 4.23 demonstrate various potential configurations that open up regions of tune space for utilization during operations, enabling the accommodation of high-intensity beams.

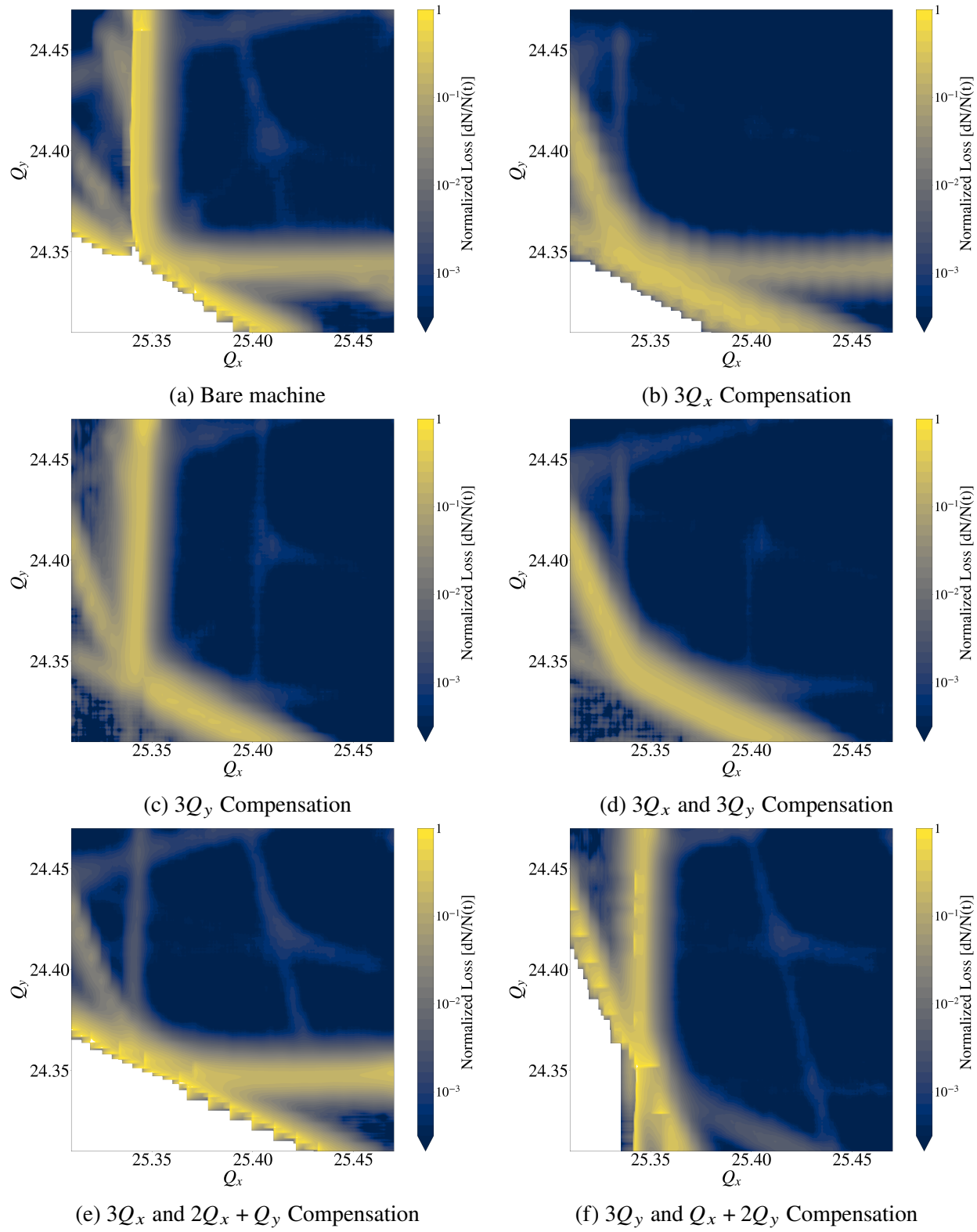


Figure 4.23 Dynamic loss maps for several configurations of compensation sextupoles

#### 4.5.2 Static Tune Scans

Another method for visualizing resonance compensation involves using static tune scans. While the loss maps detailed earlier illustrate the dynamic crossing of resonances, an alternative method entails setting the tune to a specific value and assessing the beam survival ratio alongside the beam size over a defined time interval. This time interval was around 0.8 seconds, which is equivalent to approximately 72800 turns. The beam survival ratio was calculated from the beam intensity data captured from the DC Current Transformer (DCCT). The beam size is quantified using the Ion Profile Monitor System (IPM) introduced in Sec. 3.5.

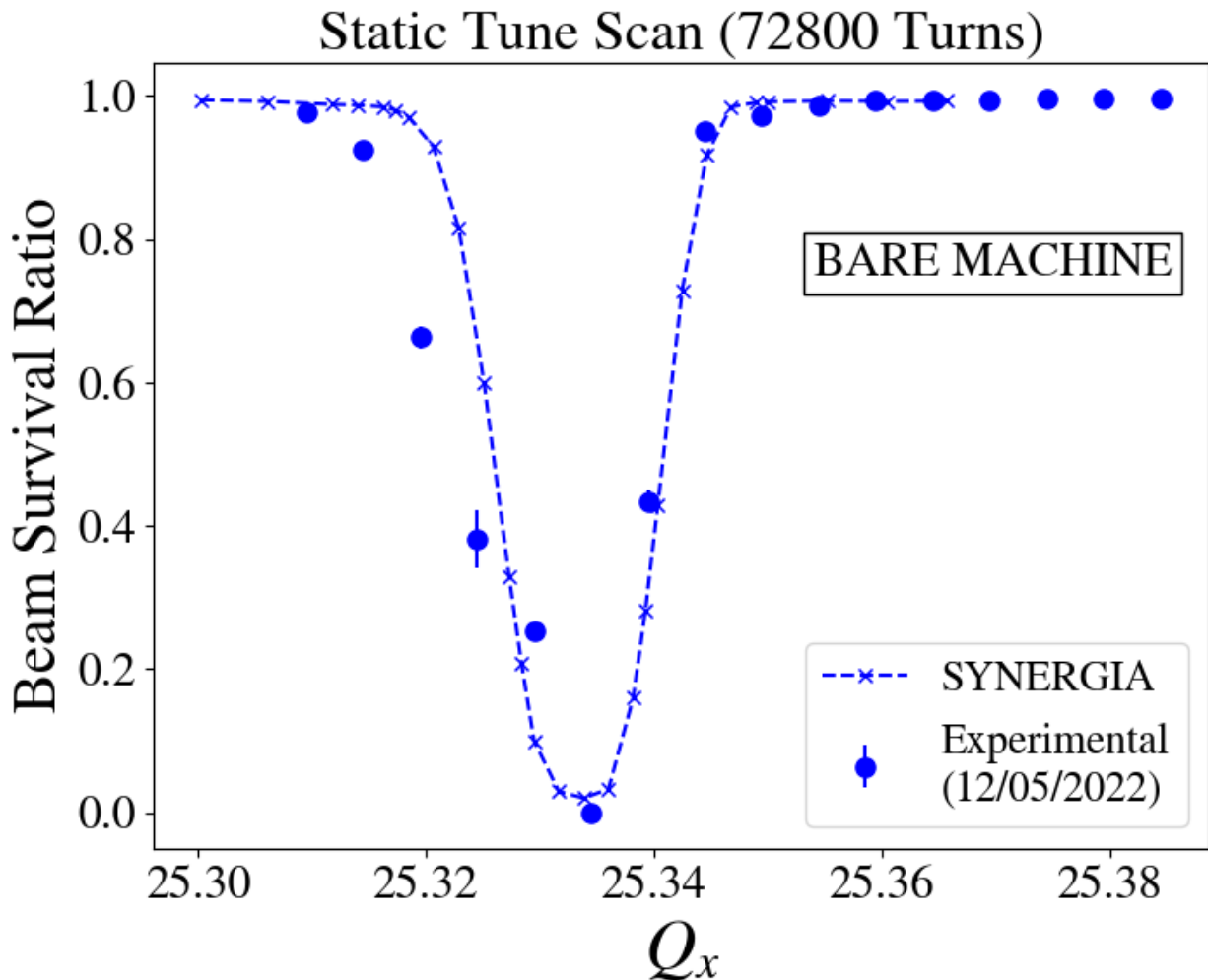


Figure 4.24 Static tune scan for the bare machine with comparisons between experimental data and SYNERGIA simulations at a low intensity of  $0.5\text{e}10$  particles per bunch (2 Booster Turns of equivalent intensity).

Figure 4.24 shows a static tune scan only including beam survival ratio data. This plot includes data from experiments and data from SYNERGIA simulations done with no space charge. No space-charge simulator was needed because these experiments were done at low intensities. The simulations were done for 72800 turns, and the experimental data was partitioned to only this equivalent time window. Figure 4.24 shows the resonance stop band corresponding to the  $3Q_x$  resonance. Effectively, no beam survives when parked on top of the resonance line. There is a good agreement between the stop bandwidth of the resonance from the simulations and the experimental data. This observation hints that the model roughly captures the sextupole component around the ring, even if imperfect. Nevertheless, left of the resonance, the experimental data deviates from the model, given that the Recycler Ring is not optimized to run in this region.

On the other hand, Fig. 4.25 shows a similar comparison between static tune scans done with SYNERGIA simulations and experimental results. The simulations were done by calculating the  $K_2$  coefficients that compensate  $3Q_x$  and then launching the simulations for 72800 turns. The intensity and beam emittance data were recorded every 100 turns for these simulations. Experimentally, the compensation currents were calculated from the response matrix method, and losses on top of  $3Q_x$  were optimized with a Nelder-Mead algorithm as mentioned in Sec. 4.4. The first thing to note is that the beam survival ratio increases close to the resonance line with compensation—for both the simulations and the experiment. Nevertheless, in this case, the simulation data does not agree well with the experiments. In principle, the compensation done experimentally is better than that done with the lattice model. Therefore, something is missing from the compensation algorithm applied to the lattice model. The lattice model is imperfect and does not necessarily capture all the physics in the real accelerator. More work must be done to match the simulations and experiments of static tune scans with resonance line compensation.

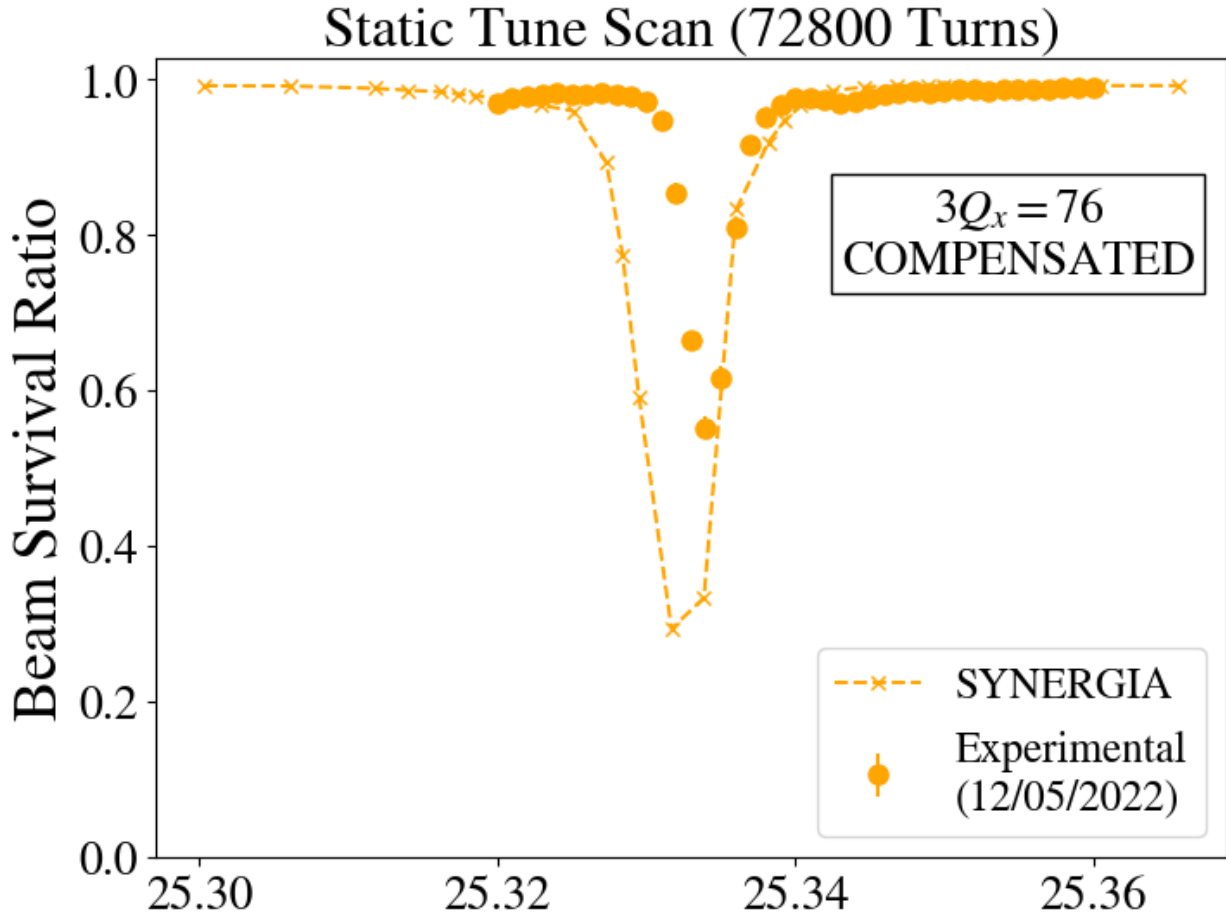


Figure 4.25 Plot for static tune scan for the machine with  $3Q_x$  compensation, including a comparison between experimental data and SYNERGIA simulations.

Additional experiments performing static tune scans were done. Figures 4.26 and 4.27 are additional experiments performed at different dates than the ones presented in Figs. 4.24 and 4.25. An accelerator is a machine that drifts in time; every day, it gets tuned and manipulated. From day to day, different fields can be sampled from different elements. This is why the data can sometimes change from experiment to experiment, especially if it was taken six months apart—such is the case with these datasets.

Nevertheless, these additional experiments allow a better understanding of the accelerator and improve the resonance compensation algorithms. Figures 4.26 and 4.27 show static tune scans with beam size calculated from IPM data. Figure 4.26 shows the case for when the bare machine was sampled—compensation sextupoles were off. As the working tune point gets closer to the  $3Q_x$

resonance line, Fig. 4.26 shows how the beam survival ratio goes down, and the beam size goes up. The losses increase due to the beam size growth coming from the resonance. Eventually, it hits the beam pipe, and losses appear. When operating on top of the resonance with no compensation, almost no beam survives, and the IPM data can not be used.

On the other hand, Fig. 4.27 shows what happens with compensation turned on. Once the compensation currents are set into the sextupoles, the beam survival ratio across the  $3Q_x$  resonance line increases. Up to the point where approximately 95% of the beam survives while operating on top of the resonance line—compare this to the uncompensated case where no beam survives. Nevertheless, this region has some beam size growth, but not as large as the uncompensated case. There is still sufficient beam that can be used to probe the beam size. With compensation at low intensity, the beam size growth is suppressed such that 95% of the beam can now survive for 0.8 seconds on top of this third-order resonance line.

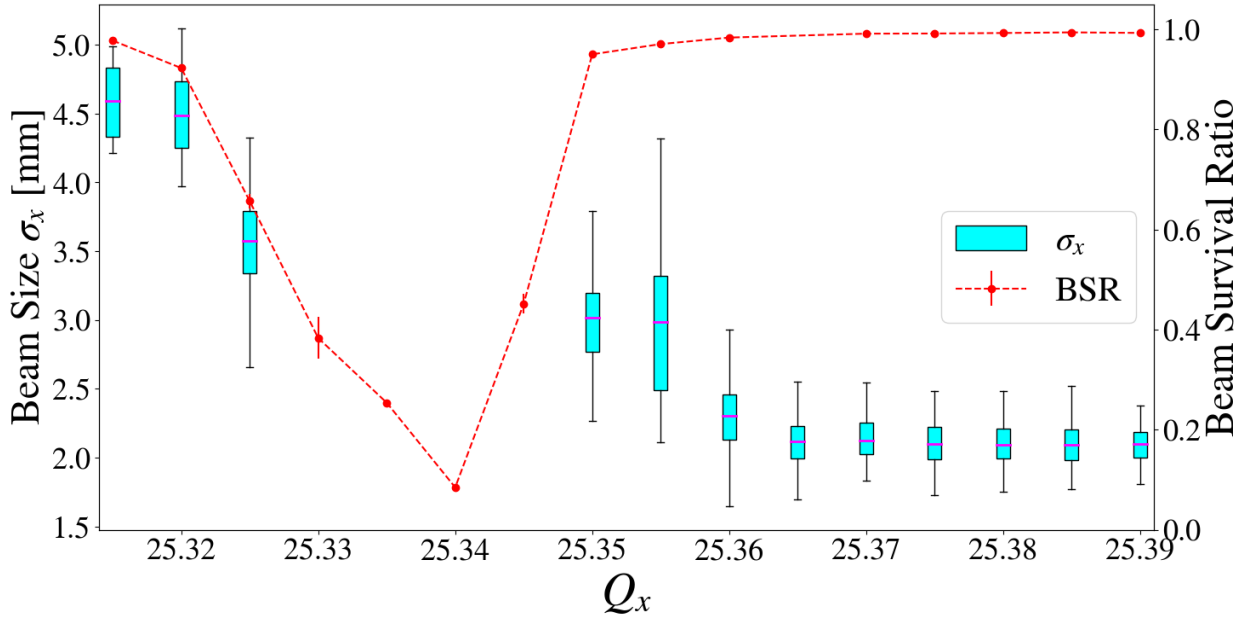


Figure 4.26 Static tune scan with beam survival ratio and IPM data box plots for the bare machine at 2 Booster Turns of equivalent intensity.

It is worth specifying that the plots shown in Figs. 4.26 and 4.27 are box plots of the sigmas of Gaussian-fitted IPM data. Box plots are used to represent distributions. The beam size data is a distribution depending on the number of turns. Ultimately, the beam size can grow with the

number of turns, as shown in Fig 4.28 and in Sec. 6.4. Therefore, a simple scatter plot of the mean with some error bars would be incorrect to illustrate IPM data—this type of plot can only be used with centrally distributed data. This is the reason why box plots have been used in these plots.

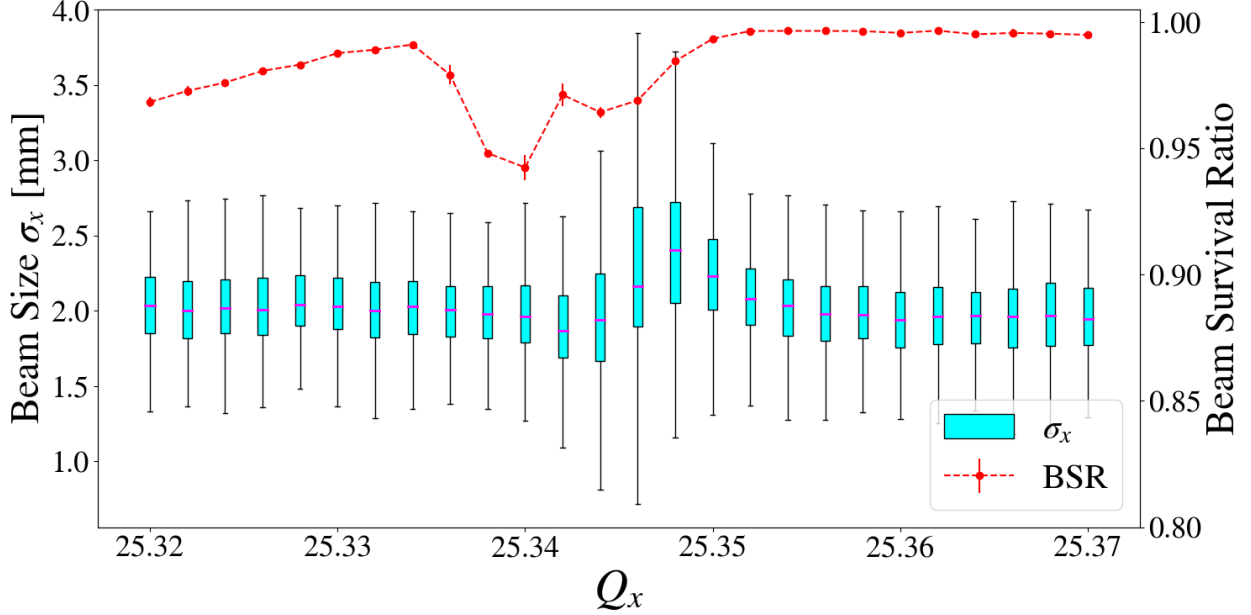


Figure 4.27 Static tune scan with beam survival ratio and IPM data box plots for the machine with  $3Q_x$  compensation at 2 Booster Turns of equivalent intensity.

The 95% normalized emittance  $\varepsilon_{N,95\%}$  of the beam in the  $u$  plane—either horizontal or vertical—is the phase space area that encapsulates 95% of the particles in a beam traveling close to the speed of light. The definition for this quantity is:

$$\varepsilon_{n,u,95\%} = 6\beta_L\gamma_L\varepsilon_u, \quad (4.39)$$

where  $(\beta_L, \gamma_L)$  are the longitudinal relativistic factors. The geometrical RMS emittance  $\varepsilon_u$  was calculated from:

$$\varepsilon_u = \frac{\sigma_u^2}{\beta_u} - \frac{D_u^2}{\beta_u} \left( \frac{\delta p}{p_0} \right)^2, \quad (4.40)$$

where  $\beta_x = 27.10$  meters,  $D_x = 0.32$  meters and  $\delta p/p_0 = 5e - 4$  were the parameters estimated for the horizontal IPM. The data from the horizontal IPM can be used to calculate the beam size  $\sigma_x$ , as shown in Figs. 4.26 and 4.27. All these values were extracted from the Ref. [40] information.

Figure 4.28 shows the 95% normalized horizontal emittance calculation from the IPM data presented in Fig. 4.27. In this case, each point from each scatter plot is indexed by its decimated turn number. The decimated turn number is the data point's position in the IPM return array. Even though the IPM can analyze up to 65000 turns, it can only output an array of 1024 decimated turns. The data analyzed in these plots was for 65000 turns decimated into 1024 data points. As mentioned, this data can not be represented with an error bar plot because it does not necessarily follow a normal distribution. This can be seen in the emittance evolution against the turn number illustrated in Fig. 4.28.

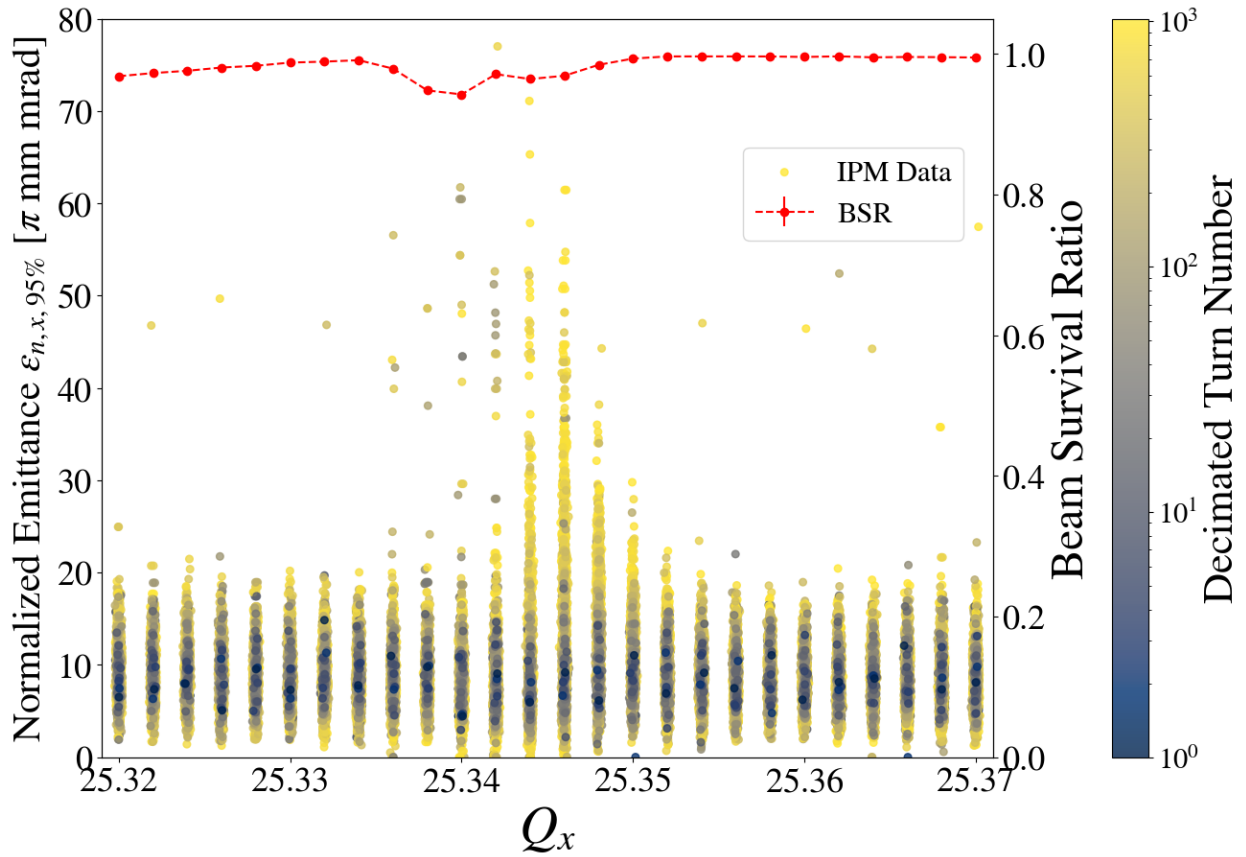


Figure 4.28 Static tune scan with beam survival ratio and emittance data calculated from IPM data for the machine with  $3Q_x$  compensation at 2 Booster Turns of equivalent intensity.

Just as the beam size grows in Fig. 4.27 while on top of the resonance line, this translates into normalized emittance growth shown in Fig. 4.28. Once the beam is injected close to the resonance line at a normalized emittance of around  $11 \pi \text{ mm mrad}$ , it grows with the number of turns. In

particular, the Recycler Ring has an acceptance of  $40 \pi$  mm mrad. This means that particles will start getting lost close to this number. This can be seen for the values of around  $Q_x = 25.344$  where the emittance grows up to values larger than  $40 \pi$  mm mrad, and, indeed, there is some loss in the beam survival ratio plot (red dashed lines). Ultimately, this section has shown how using DCCT and IPM data allows for the characterization of resonance lines and their compensation.

#### 4.6 Additional Sextupoles for Resonance Compensation

As mentioned before in the discussion of Figs. 4.10, 4.11 and 4.23, the currents in the compensation sextupoles that cancel out the  $h_{3000}$  and  $h_{1020}$  RDTs are too large. This section explores the idea of introducing two additional normal compensation sextupoles to bring down the  $K_2$  coefficients that cancel out both of these RDTs, effectively bringing down the currents in all the sextupoles. Therefore, this section looks at optimizing the location for these two new sextupoles. The introduction of two new sextupoles implies that the RDT equation from Eq. 4.16 is modified, and this reads:

$$\begin{bmatrix} -|h_{3000}| \cos \psi_{3000} \\ -|h_{3000}| \sin \psi_{3000} \\ -|h_{1020}| \cos \psi_{1020} \\ -|h_{1020}| \sin \psi_{1020} \end{bmatrix}_{(Bare)} = \mathbf{M}_A \begin{bmatrix} K_2^{(sc220)} \\ K_2^{(sc222)} \\ K_2^{(sc319)} \\ K_2^{(sc321)} \\ K_2^{(1)} \\ K_2^{(2)} \end{bmatrix}. \quad (4.41)$$

In this case, the response matrix gets appended to two new columns with the RDT sensitivity of the two new sextupoles. This reads:

$$\mathbf{M}_A = \begin{pmatrix} \mathbf{M} & \begin{array}{cc} \frac{1}{48} l_{sc} \beta_{x(1)}^{3/2} \cos 3\phi_{x(1)} & \frac{1}{48} l_{sc} \beta_{x(2)}^{3/2} \cos 3\phi_{x(2)} \\ \frac{1}{48} l_{sc} \beta_{x(1)}^{3/2} \sin 3\phi_{x(1)} & \frac{1}{48} l_{sc} \beta_{x(2)}^{3/2} \sin 3\phi_{x(2)} \\ \frac{1}{16} l_{sc} \beta_{x(1)}^{1/2} \beta_{y(1)} \cos(\phi_{x(1)} + 2\phi_{y(1)}) & \frac{1}{16} l_{sc} \beta_{x(2)}^{1/2} \beta_{y(2)} \cos(\phi_{x(2)} + 2\phi_{y(2)}) \\ \frac{1}{16} l_{sc} \beta_{x(1)}^{1/2} \beta_{y(1)} \sin(\phi_{x(1)} + 2\phi_{y(1)}) & \frac{1}{16} l_{sc} \beta_{x(2)}^{1/2} \beta_{y(2)} \sin(\phi_{x(2)} + 2\phi_{y(2)}) \end{array} \end{pmatrix}, \quad (4.42)$$

where the beta functions and phases are evaluated at a lattice location that has still yet to be determined. The original matrix  $\mathbf{M}$  is defined from Eq. 4.27.

The first step was to minimize the function

$$f(\beta_{x(i)}, \beta_{y(i)}, \phi_{x(i)}, \phi_{y(i)}) = \max \left( \begin{bmatrix} K_2^{(sc220)} \\ K_2^{(sc222)} \\ K_2^{(sc319)} \\ K_2^{(sc321)} \\ K_2^{(1)} \\ K_2^{(2)} \end{bmatrix} \right), \quad (4.43)$$

where the max operator takes the absolute maximum of the vector. Therefore, it would correspond to the maximum  $K_2$  coefficient in the vector. The minimization procedure was done using a Nelder-Mead algorithm. Ultimately, the result would be a set of  $\beta_{x(i)}, \beta_{y(i)}, \psi_{x(i)}, \psi_{y(i)}$ , where  $i$  runs from 1 to 2 (representing the two additional sextupoles), and this specifies the location where the maximum  $K_2$  coefficient from all the sextupoles gets minimized. An instance of Nelder-Mead was launched 10000 times; each time, the starting point would be chosen randomly to ensure most of the parameter space was explored. All the results could be plotted in histograms to create constraints for locations depending on the beta and phase advance. Figure 4.29 shows an example of such histograms. This plot shows the relations and constraints the new sextupoles must comply with to minimize the maximum  $K_2$  coefficient. For example, Fig. 4.29 shows that the horizontal beta functions of both sextupoles should have a ratio of around 1. Additionally, it shows that the horizontal phase advances should lie close to thirds of  $\pi$ , e.g.,  $\pi/3, 2\pi/3, \pi$ , etc. . . .

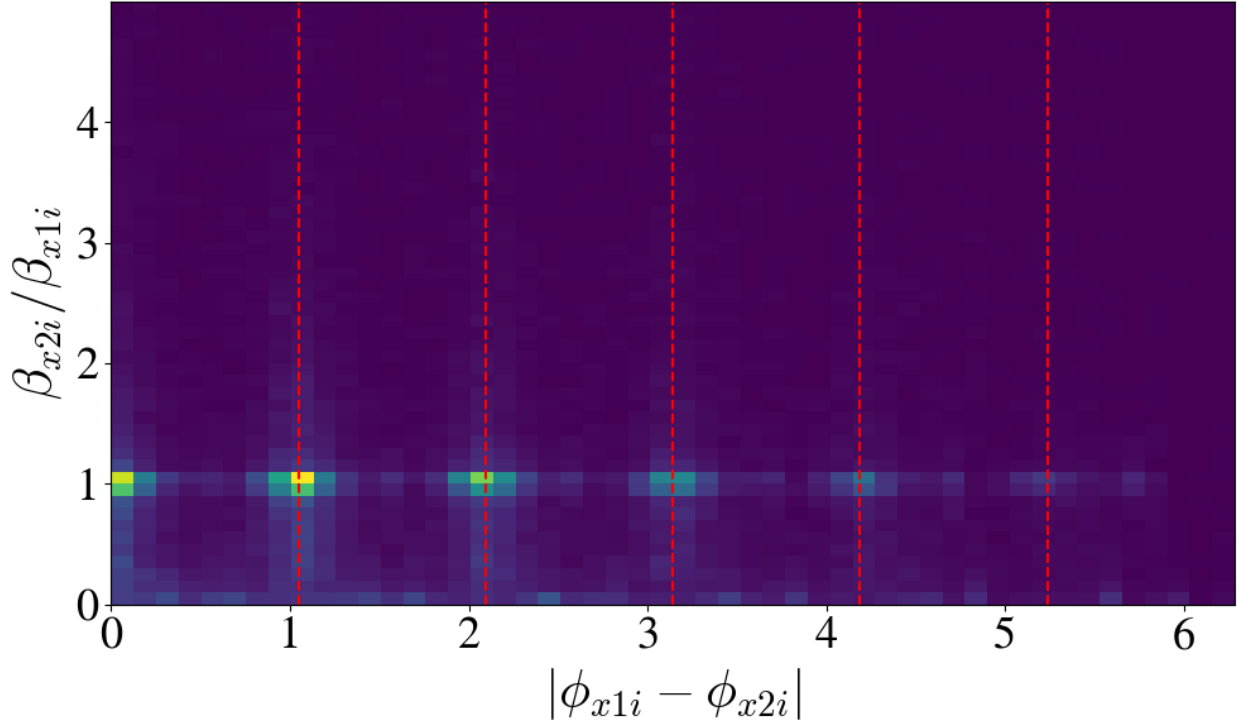


Figure 4.29 2D Histogram of optimum lattice locations where the compensating  $K_2$  coefficients with the two new sextupoles are minimized. Red dashed lines correspond to thirds of  $\pi$ .

With the previous constraints already set up, the next step is to look into all the possible pairs of drift spaces in the lattice where two sextupoles would fit. Therefore, all the possible combinations of two available drift spaces longer than 1 meter and horizontal dispersion less than 0.1 meters were explored. This last constraint came from the fact that these new sextupoles should not introduce any additional chromaticity into the Recycler. In total, the number of total possible combinations was 39340. From all of these possibilities, the first filter analyzed only the combinations that complied with the constraints imposed by minimizing Eq. 4.43. With this first filter, the number of pair candidates was narrowed to 776. In these 776 pairs of locations, the sextupoles were introduced, and the resulting maximum  $K_2$  coefficient was calculated. Figure 4.30 shows these candidates with their corresponding metric for this particular constraint superimposed onto the 2D histogram of Fig. 4.29. The color bar of Fig. 4.30 labels the candidates by their particular maximum  $K_2$  coefficient, as defined in Eq. 4.43.

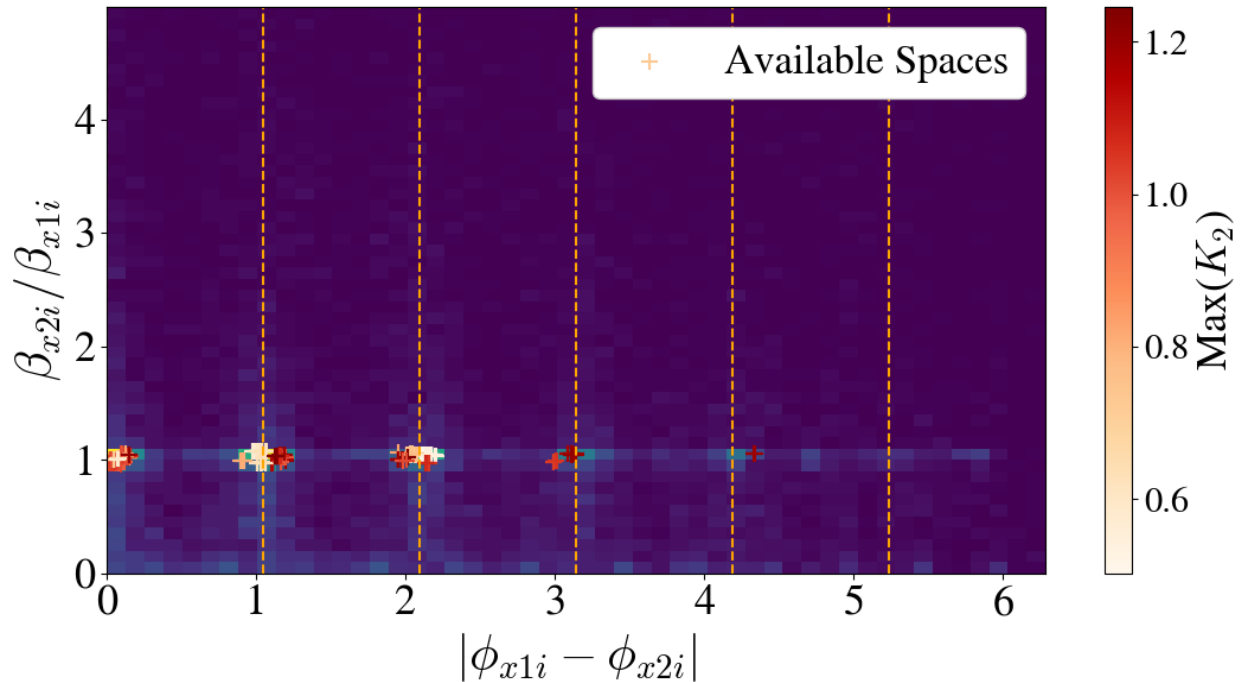


Figure 4.30 2D Histogram of optimum lattice locations where the compensating  $K_2$  coefficients with the two new sextupoles are minimized with available drift spaces candidates scattered on top of it.

With the number of candidates narrowed down, the next step is to select the idle pair of locations to introduce these new sextupoles. Figure 4.31 was used as a tool for this purpose. The left vertical axis shows the dispersion curve (golden solid continuous line) of the Recycler Ring to ensure that the new candidates are indeed in areas of low dispersion. The red crosses and the blue exes represent the pair of drift space candidates where the sextupoles could go. The right vertical axis specifies the maximum  $K_2$  coefficients when the sextupoles are introduced in these locations. The minimum of this quantity is given by the pair of sextupoles introduced in the region 620. By observing Fig. 4.31 and making sure the locations in 620 were viable in terms of space and logistics, the new locations for two new compensation sextupoles were chosen.

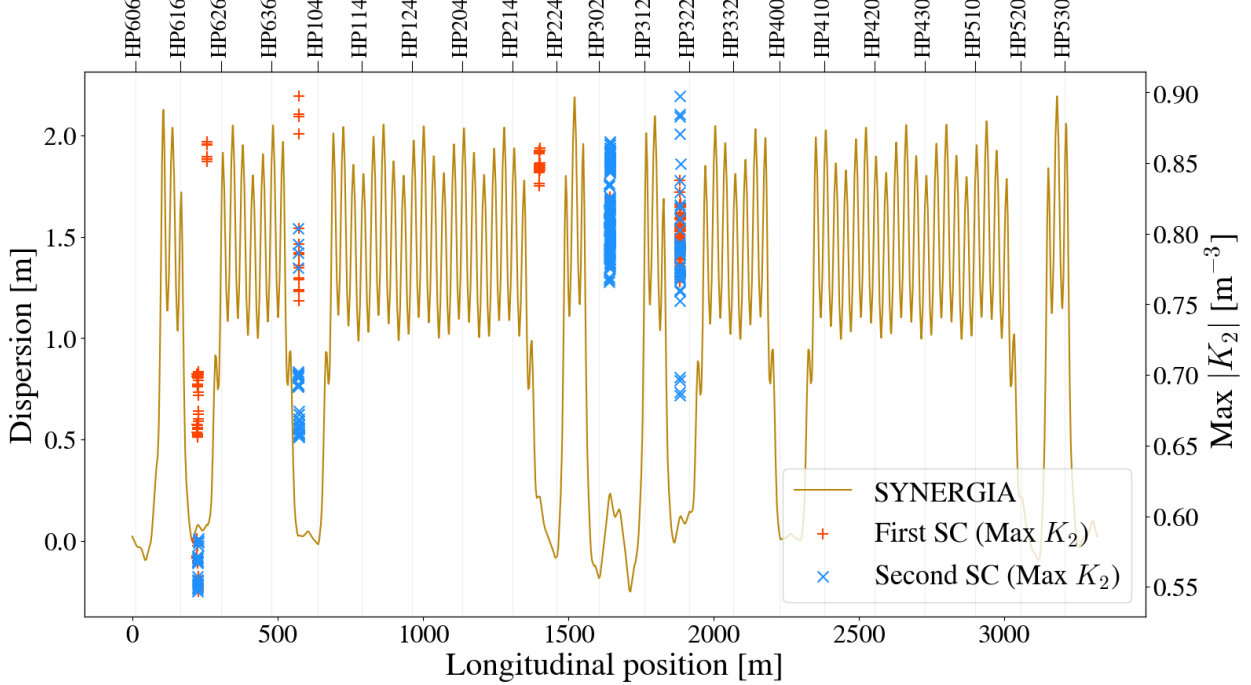


Figure 4.31 Dispersion function of the Recycler Ring with possible new locations to introduce a pair of sextupole magnets that cancel out  $h_{3000}$  and  $h_{1020}$  simultaneously. The right y-axis shows the maximum compensation  $K_2$  coefficient needed with these new candidates.

Once the new locations are pinned down, the compensation of  $h_{3000}$  and  $h_{1020}$  can be verified. Table 4.6 shows the  $K_2$  coefficients that need to go into the sextupoles for  $3Q_x = 76$  and  $Q_x + 2Q_y = 74$  compensation. These values can be compared to those in Table 4.5, which are one order of magnitude less. Furthermore, all the values in Table 4.6 are less than  $1.0 \text{ m}^{-3}$ , the equivalent current limit for the  $K_2$  coefficients. Ultimately, these two new sextupoles, SC620a and SC620b, have brought down the compensating sextupole coefficients by one order of magnitude. Their installation would enable a viable option to compensate both resonance lines simultaneously.

Table 4.6  $K_2$  coefficients that cancel out the  $h_{3000}$  and  $h_{1020}$  term when the two new 620 sextupoles are introduced. These values were calculated for a Recycler lattice tuned to  $Q_x = 25.4422$  and  $Q_y = 24.3915$ .

Sextupole	$K_2$ [m $^{-3}$ ]
SC220	-0.263835
SC222	0.463129
SC319	0.480173
SC321	-0.407482
SC620a	0.581187
SC620b	0.511139

As it was previously done in Sec. 4.1, the  $h_{3000}$  and  $h_{1020}$  RDTs can be calculated after introducing the values of  $K_2$  coefficients specified in Table 4.6. Figures 4.32 and 4.33 show the RDT calculations with these settings. Both plots show how the global RDTs go down to 0 at the end of the sum along the lattice. Nevertheless, more noteworthy is the fact that the RDT calculations do not show huge variations in the cumulative sum, as they did in Figs. 4.12 and 4.13. This means that these two additional sextupoles will delocalize the amount of sextupole that must be introduced into the ring to cancel out both RDTs. Therefore, the RDT variation around the ring will be smaller with these new settings than with the four original compensation sextupoles.

As of Spring 2024, these new 620 sextupoles have been installed in the Recycler Ring. Nevertheless, they have not been commissioned nor tested for operations. The next step would be to verify that both lines can be compensated with these six normal compensation sextupoles. This work is still a work in progress.

### (WITH NEW 620 SEXTUPOLES) LATTICE MODEL

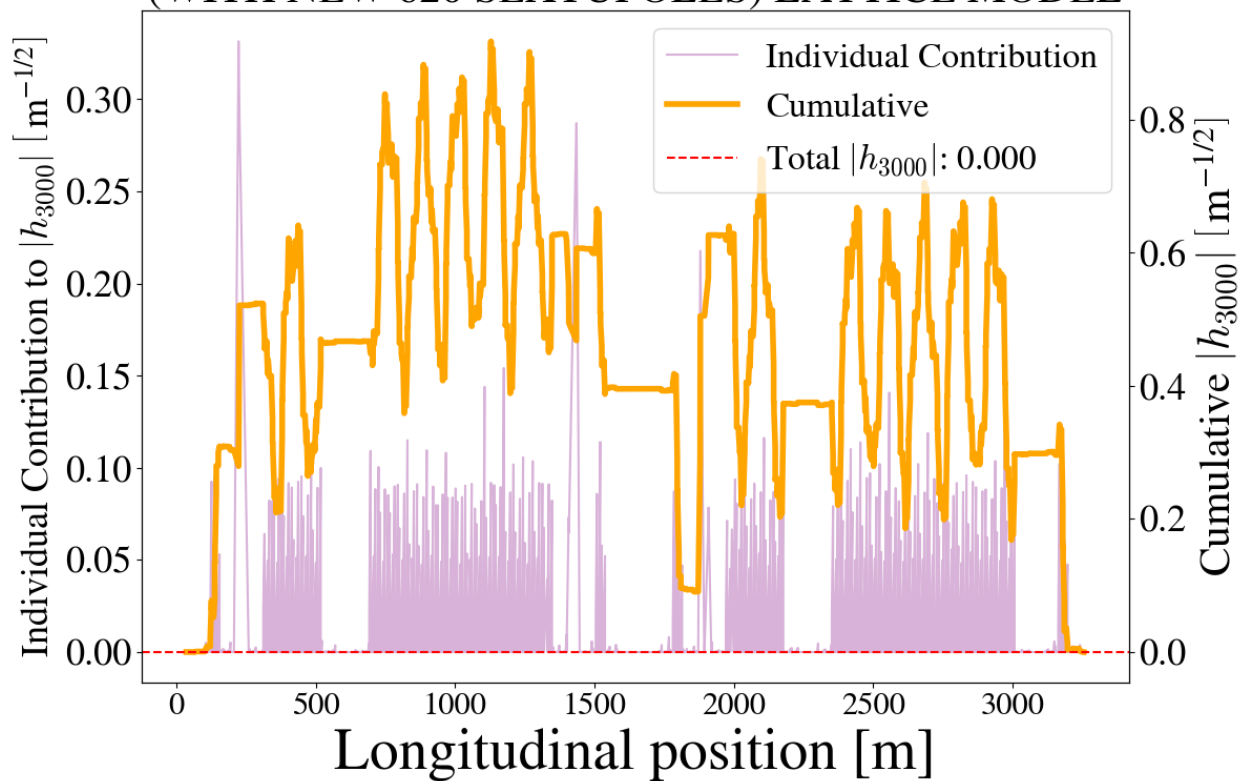


Figure 4.32 Distribution of the  $h_{3000}$  term around the ring with individual contributions from each relevant element and the cumulative sum from an arbitrary starting point. This calculation includes the new 620 sextupoles powered at the correct currents to simultaneously cancel out  $h_{3000}$  and  $h_{1020}$ .

(WITH NEW 620 SEXTUPOLES) LATTICE MODEL

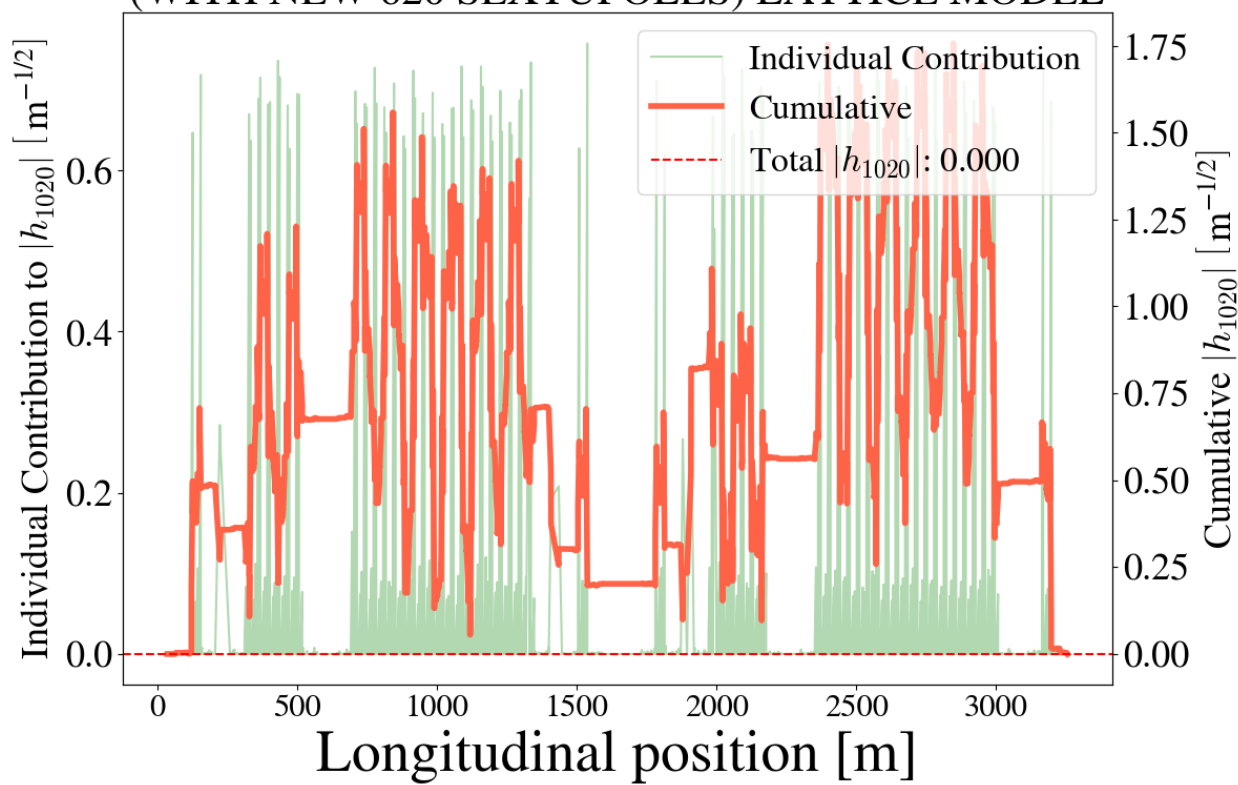


Figure 4.33 Distribution of the  $h_{1020}$  term around the ring with individual contributions from each relevant element and the cumulative sum from an arbitrary starting point. This calculation includes the new 620 sextupoles powered at the correct currents to simultaneously cancel out  $h_{3000}$  and  $h_{1020}$ .

## CHAPTER 5

### RESONANCE COMPENSATION STUDIES AT THE CERN PROTON SYNCHROTRON BOOSTER

#### 5.1 General Description

The Proton Synchrotron Booster (PSB) is the first circular accelerator in the CERN accelerator complex that ultimately leads to the LHC. Figure 5.1 shows the entire chain of accelerators at CERN, feeding a variety of physics experiments [48]. Following the successful implementation of the LHC Injectors Upgrade (LIU) [49], the PSB receives  $H^-$  ion beam from the Linac4 at an energy of 160 MeV. Interestingly, the PSB is not just one ring but four identical synchrotron rings stacked on each other. This design counteracts the space charge effects, which are the largest in low-energy machines. Once the ion beam enters the PSB rings, the electrons are stripped off through a charge-exchange process with a carbon foil, and a proton beam is achieved [50]. The proton beam is then accelerated from an energy of 160 MeV to 2 GeV. Each ring extracts one bunch and is injected in different buckets into the Proton Synchrotron (PS). This description is true for LHC-type beams. Nevertheless, the PSB can also feed protons to other customers such as its highest-intensity user—ISOLDE (Isotope mass Separator On-Line facility) [51].

One ring of the PS Booster has a total circumference of 157.08 meters. Multiplying this quantity by the four rings, one gets a length of 628.32 meters, the exact circumference of the next accelerator, the Proton Synchrotron (PS). The PSB has a superperiodicity of 16, meaning it has 16 identical fundamental cells. Each cell has a length of 9.82 meters, housing a sequence of bending magnet, focusing quadrupole, defocusing quadrupole, focusing quadrupole, and bending magnet [52, 53]. Between these main components are drift spaces used for RF insertions, diagnostic devices, injection and extraction devices, and additional multipole corrector magnets. At injection energy, 160 MeV, protons have a revolution period of  $1.01 \mu s$ , while at the extraction energy of 2.0 GeV, they have a revolution period of  $0.553 \mu s$ . The beam stays in the PS Booster for around 530 microseconds, where CERN and its accelerators are synchronized with a 1.2-second basic period.

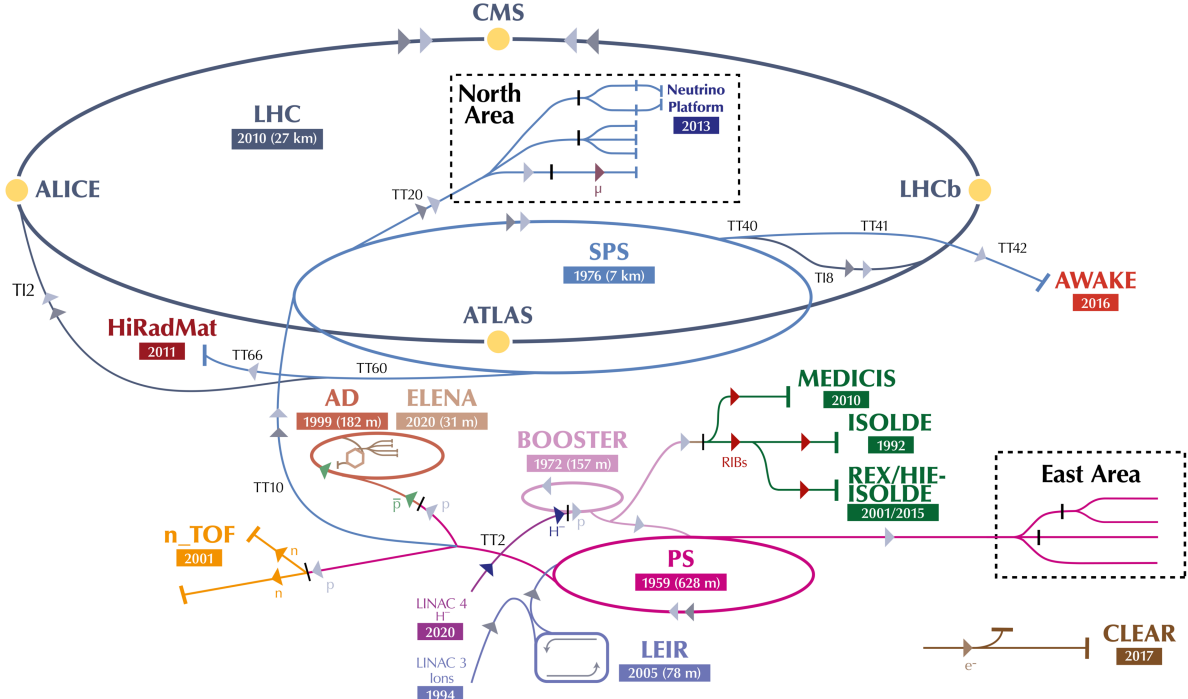


Figure 5.1 A graphic overview of all accelerators in operation at CERN as of 2022. Original image taken from Ref. [48]. This file is licensed under the Creative Commons Attribution 4.0 International license.

## 5.2 Tune Diagram and Operation

Figure 5.2 illustrates the tune diagram dynamics that the LHC-type beam undergoes at the PS Booster [51, 54, 55]. As mentioned before, the beam gets injected at an energy of 160 MeV. At this low energy, the tune footprint is large enough that the spread can reach up to 0.5, i.e.,  $\Delta Q_u \approx -0.5$ . The nominal injection tunes are around  $Q_x = 4.40$  and  $Q_y = 4.45$ , in order to accommodate the footprint between the integer resonance lines  $Q_u = 4.0$  and the half-integer line  $2Q_y = 9$ . As the beam is accelerated, the quadrupoles are ramped up to match the increasing beam rigidity, but, additionally, a tune ramp is introduced to move the shrinking footprint to a less resonance-populated area in the tune diagram. The nominal extraction tunes are around  $Q_x = 4.17$  and  $Q_y = 4.23$ . At extraction, the beam tune footprint has shrunk by a factor of  $(\gamma_L^3 \beta_L^2)$ , as explained by the beam perveance definition in Eq. 2.66. At extraction, the footprint is smaller than 0.05, i.e.,  $|\Delta Q_u| \lesssim 0.05$ .

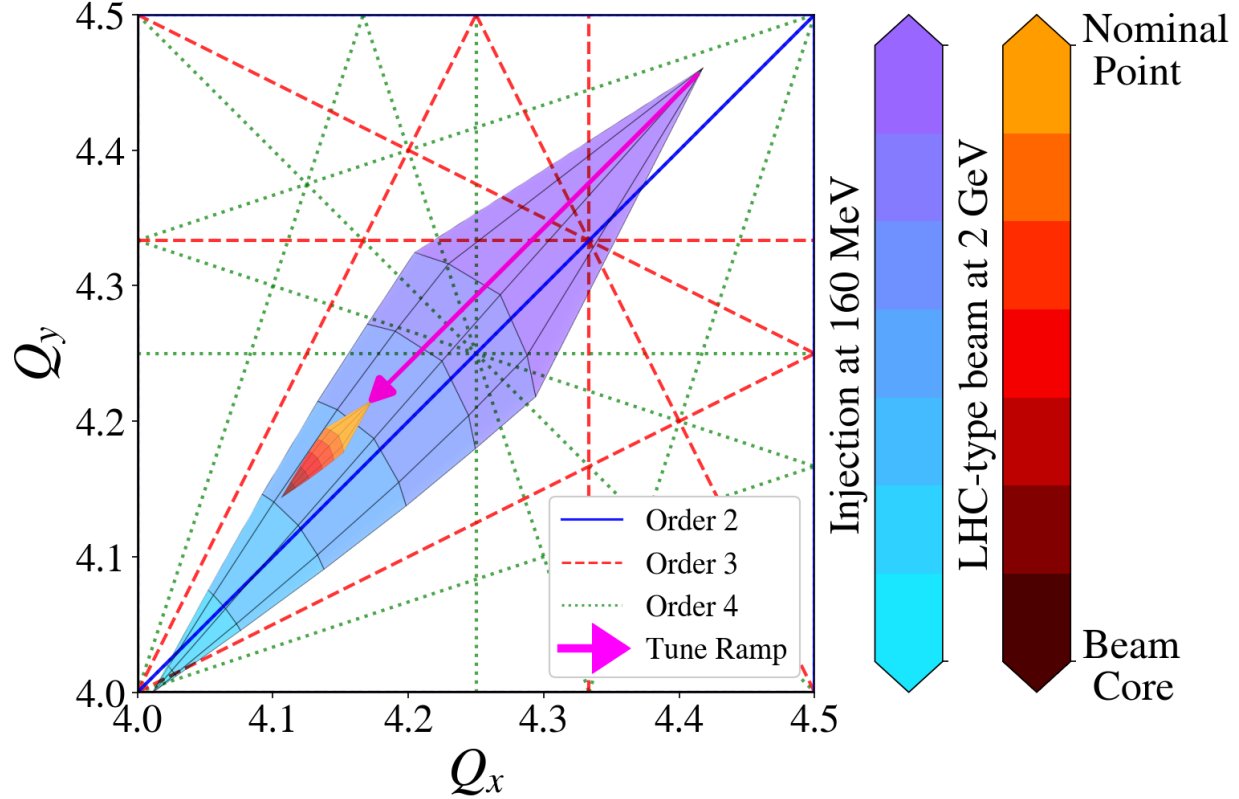


Figure 5.2 Operational tune footprint for PSB beam at injection (cool color map) and footprint after the beam has been accelerated to 2 GeV (warm color map). During acceleration, there is a tune ramp illustrated with the fuchsia arrow.

As illustrated in Fig. 5.2 with the fuchsia arrow, the nominal tune ramp crosses several resonance lines. Uncorrected, these resonance lines will lead to beam loss during the tune ramping. These include four third-order resonance lines and four fourth-order lines. It is worth reminding the reader that the third-order lines are excited by sextupole-like components in the ring, while fourth-order lines are excited by octupole-like fields. The third order resonances include two normal sextupole lines,  $3Q_x = 13$  and  $Q_x + 2Q_y = 13$ , and two skew sextupole lines,  $3Q_y = 13$  and  $2Q_x + Q_y = 13$ . For the octupole case, these include two normal octupole lines,  $4Q_x = 17$  and  $Q_x + 3Q_y = 17$ , two skew octupole lines,  $4Q_y = 17$  and  $3Q_x + Q_y = 17$ , and the octupole coupling sum resonance,  $2Q_x + 2Q_y = 17$ . Figure 5.3 shows all these resonance lines summarized in one tune diagram. All of these resonance lines have different strengths in each Booster ring. It is worth pointing out that the coupling resonance  $Q_x - Q_y = 0$  is not strongly excited in the low-intensity operation of the PSB.

At higher intensities, it has been demonstrated that this resonance line is driven in fourth-order by space charge [53].

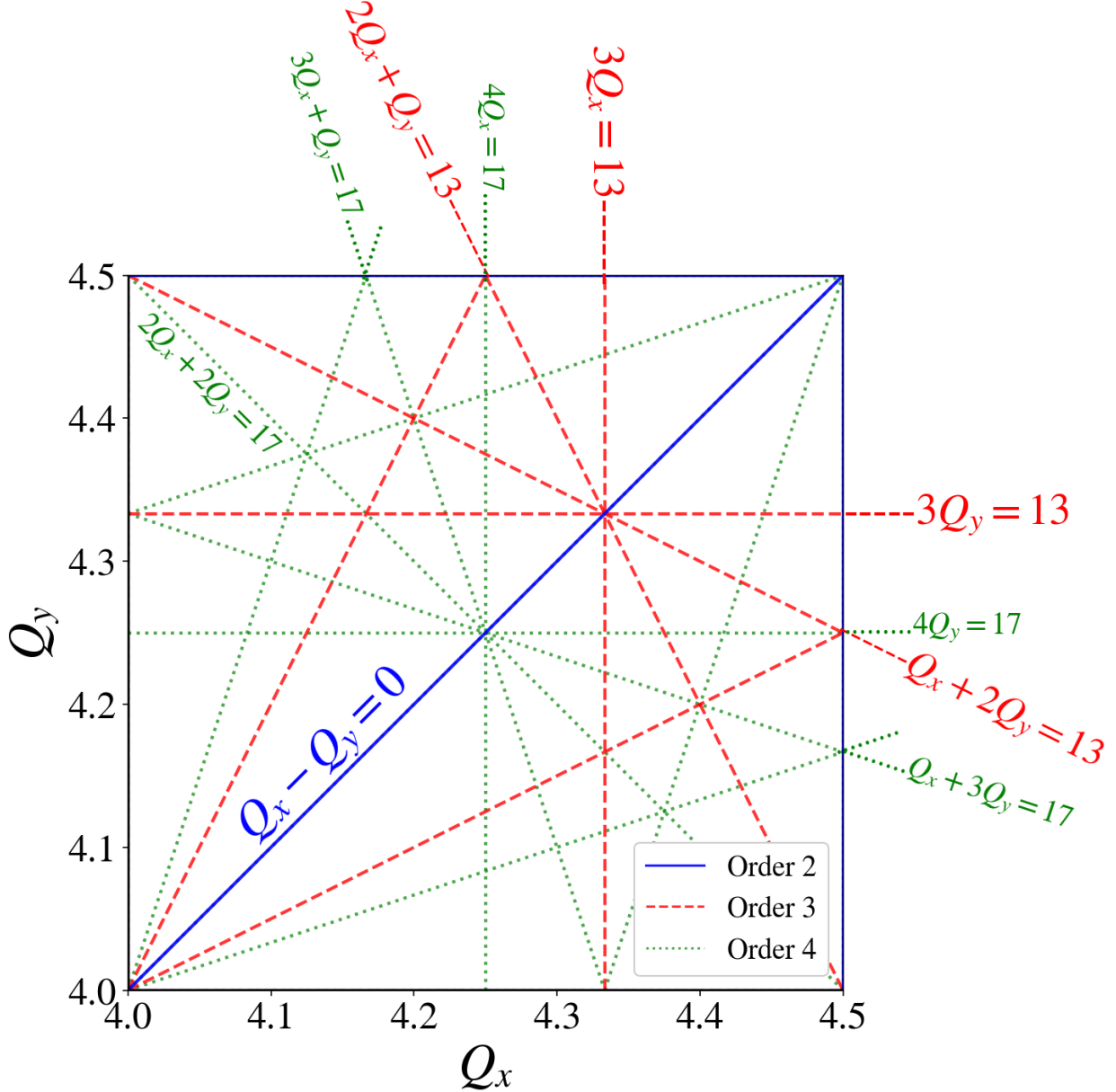


Figure 5.3 Portion of the tune diagram enclosing the operational tunes of the PS Booster with relevant resonance lines labeled.

Like the plots shown in Fig. 4.21 and Fig. 4.22, loss maps can be used to visualize the strength of the resonance lines in the CERN PS Booster. Figure 5.4 shows loss maps for each of the four rings in the PSB. These plots are created slightly differently from the ones in the Recycler Ring.

The plots shown in Fig. 5.4 are an average from four loss maps. One where losses are mapped from (a) left to right, i.e., fixing  $Q_y$  and ramping from  $Q_x \approx 4.49$  to  $Q_x \approx 4.15$ , (b) another one from right to left, (c) one from top to bottom, i.e., fixing  $Q_x$  and ramping from  $Q_y \approx 4.49$  to  $Q_y \approx 4.15$ , (d) and one from bottom to top. Therefore, these plots show an average from mapping the losses in four directions.

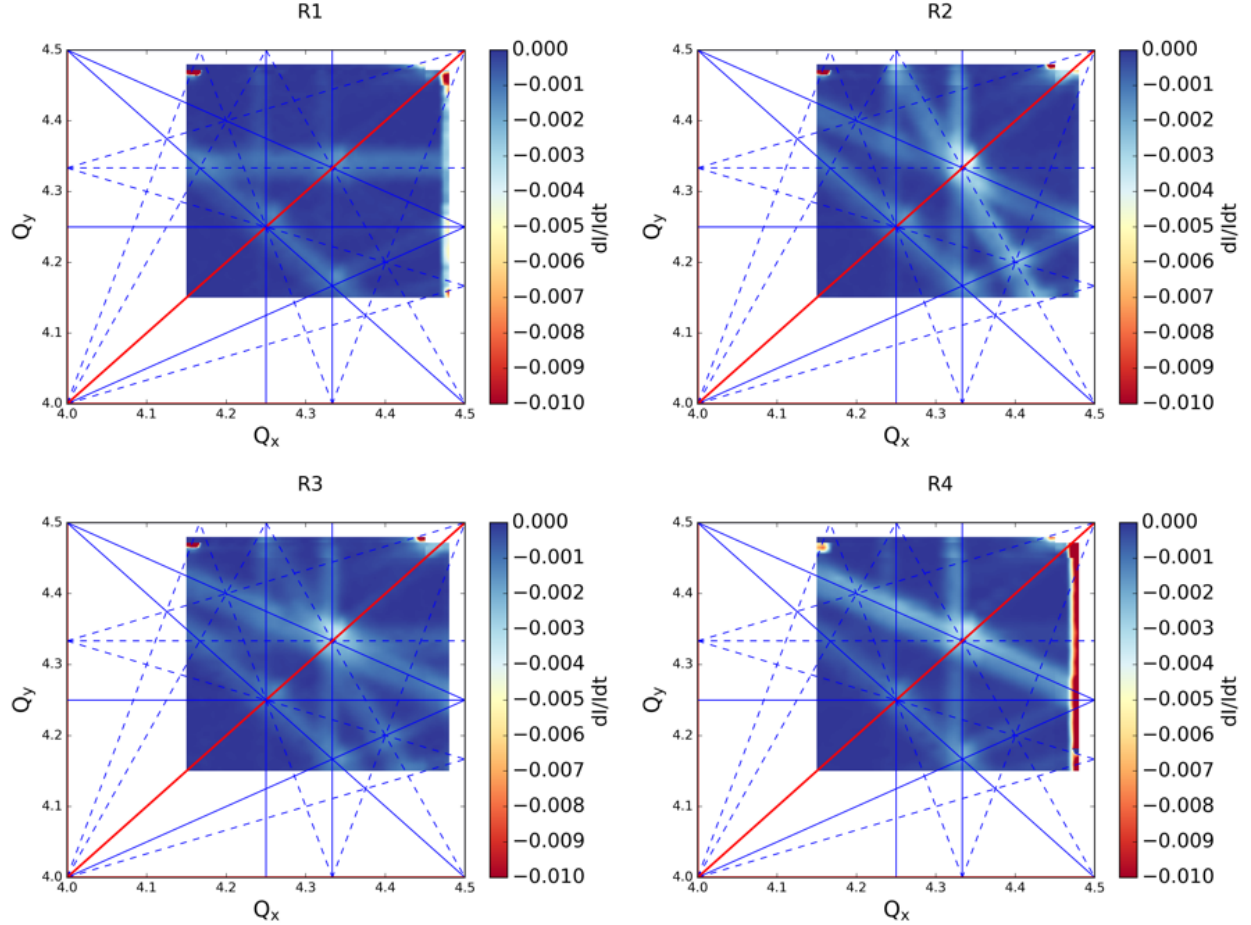


Figure 5.4 Dynamic loss maps for the bare machine of the four rings (R1, R2, R3, and R4) in the PS Booster. The plots are an average of scanning in 4 directions. Plot provided by F. Asvesta.

Figure 5.4 shows how resonances are excited differently for each ring at the Proton-Synchrotron Booster. For example, third-order lines are more excited for Ring 2 than Ring 1. This feature hints that every ring will have different values for the corrector magnets used for resonance compensation. The fourth-order order skew resonances are not observed in this loss map. The work in the following sections looks to calculate the currents of the corrector magnets used for resonance compensation.

This approach involves using two optimization procedures to find the values that clear out the losses from the plots in Fig. 5.4.

### 5.3 Optimization Algorithms for Resonance Compensation

The whole objective of the following work is to minimize the losses during the PS Booster's operational cycle, as explained in Fig. 5.2. The losses during the cycle come from particles falling on top of third-order and fourth-order resonance lines, as identified in Fig. 5.3. In order to decrease the strength of these resonances, sextupoles and octupoles can be used to control their Resonance Driving Terms (RDTs). Nevertheless, measuring and minimizing the RDTs may not always be ideal. For this work, the main observable to optimize was the beam loss from crossing the resonance lines, which is related to the amplitude of the RDTs. Figure 5.5 shows an illustration of the experimental setup used in order to measure this beam loss.

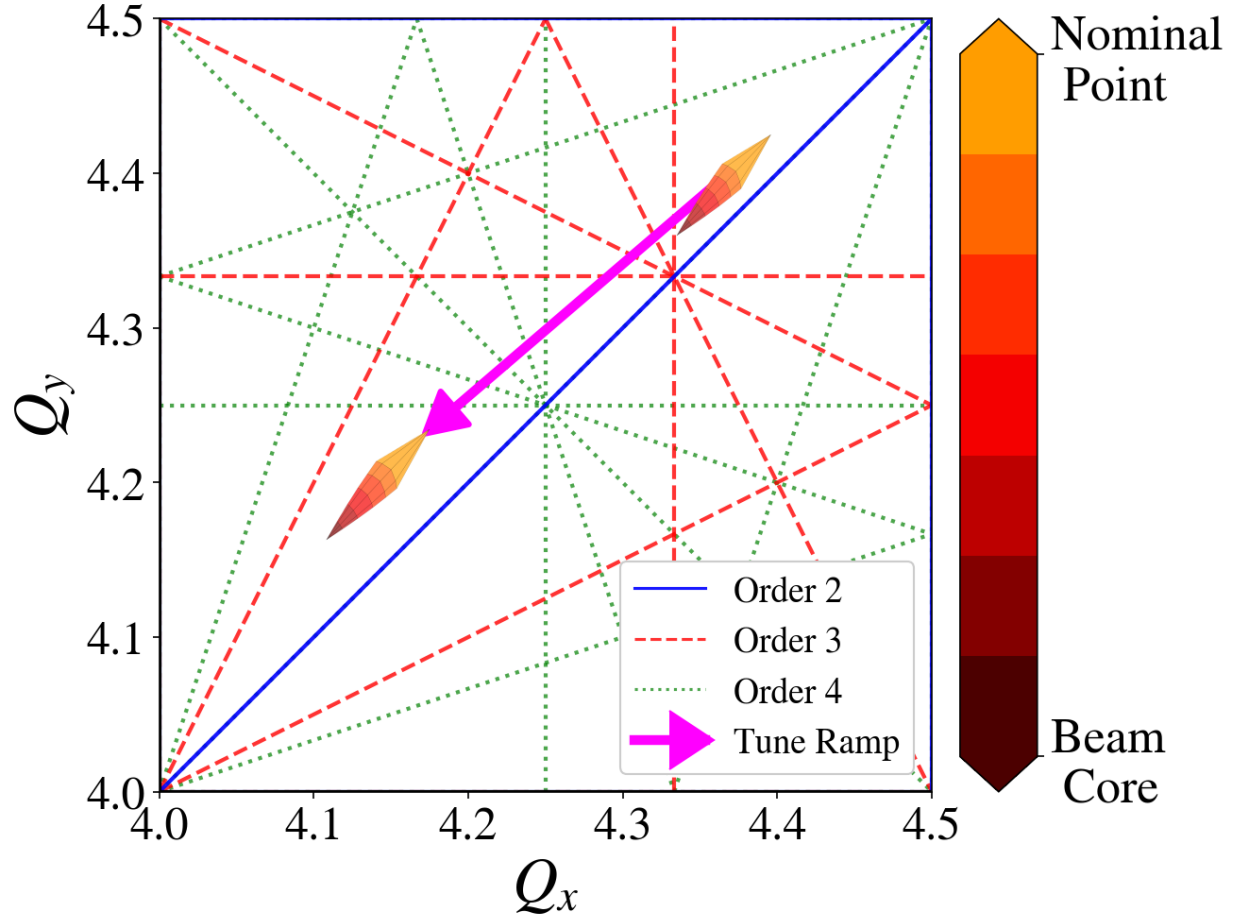


Figure 5.5 Experimental setup of the tune diagram dynamics for optimizing resonance compensation used in the PS Booster.

The experimental setup introduced in the PS Booster involved several steps to find the optimal compensation currents. First, a low-brightness beam was injected into every ring at an energy of 160 MeV. Energy is not ramped up for this configuration, and the machine stays at a flat bottom. Second, a tune ramp was programmed into the quadrupoles in the ring in order to go from initial tunes of  $Q_x = 4.40$  and  $Q_y = 4.45$  to a final setting of  $Q_x = 4.17$  and  $Q_y = 4.23$ . This particular setting was introduced to mimic the operational tune ramp of the LHC-type beam. The start of this tune ramp occurs within  $t_0 = 300$  ms of the start of the cycle and ends at  $t_f = 600$  ms, i.e., all of this occurs within a 300 ms time window. During this time window, the beam loss is measured by comparing the beam current at the end of the window to the initial value of the beam current. The currents fed to the corrector magnets remain constant during this measurement. Figures 5.5 and

5.6 summarize this experimental setup.

While monitoring the beam loss, the corrector magnets used for compensation are varied every cycle according to the optimization algorithm. Table 5.1 summarizes the 11 elements used for resonance compensation for this work. Out of these elements, there are 6 normal sextupoles, 3 skew sextupoles, and 2 normal octupoles. Figure 5.6 shows an example of the power cycle in these magnets for one optimization step. Before the tune ramp, most actors show currents at or near zero. As preparation for the tune ramp, the magnets are powered to the set values—per the optimizer calculation. During the tune ramp, they are set to a constant value and powered off once the cycle is finished. These magnets were varied for each ring, and each ring had its independent optimization run. Theoretically, in order to fully correct eight resonance lines, one needs at least 16 correctors. Nevertheless, this work aimed to find a solution to this over-constrained problem through advanced optimization algorithms.

The two optimization algorithms used were Bayesian Optimization and BOBYQA (Bound Optimization BY Quadratic Approximation). In order to implement these algorithms, the special application GeOFF (Generic Optimization Frontend and Framework) was used [56]. This graphical application is designed to facilitate numerical optimization through various algorithms and reinforcement learning on CERN accelerators. It incorporates programmable interfaces that can be used to specify the hyperparameters of the optimization algorithms.

Table 5.1 List of elements (optimization actors) in the PS Booster at CERN used for resonance compensation optimization as present in all four PS Booster rings.

Actor	Name	Type
1	XN04L1	Normal Sextupole
2	XN06L1	Normal Sextupole
3	XN09L1	Normal Sextupole
4	XN012L1	Normal Sextupole
5	XN0311L1	Normal Sextupole
6	XN0816L1	Normal Sextupole
7	ON0311L1	Normal Octupole
8	ON0816L1	Normal Octupole
9	XSK2L4	Skew Sextupole
10	XSK4L1	Skew Sextupole
11	XSK6L4	Skew Sextupole

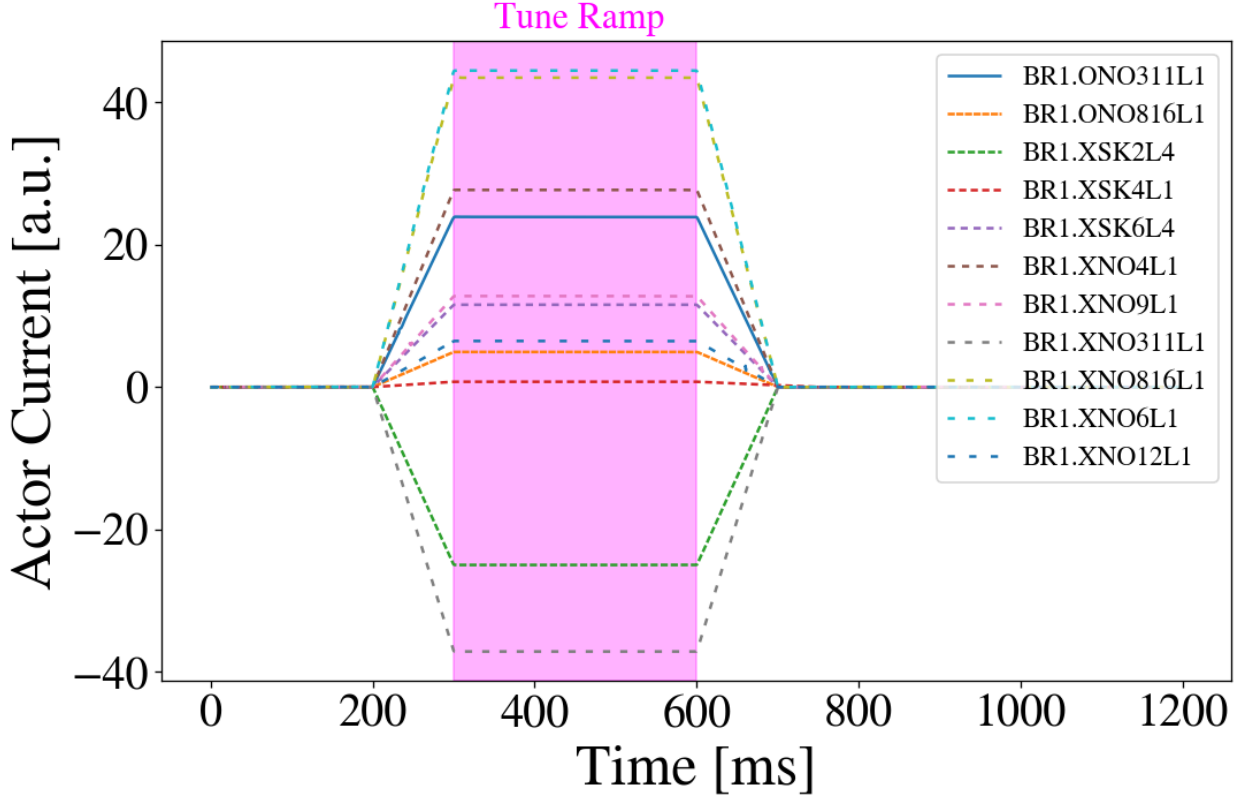


Figure 5.6 Waveform for the currents fed to the correctors (actors) as a function of time in the study cycle for one particular iteration of an arbitrary optimization instance.

### 5.3.1 Bayesian Optimization

Bayesian optimization is a well-established technique used in machine learning and optimization tasks to efficiently search for the optimal solution within a parameter space, particularly when the objective function is expensive or time-consuming to evaluate—this is the case for an accelerator. It combines probabilistic modeling with the principles of Bayesian inference to iteratively update a model of the objective function based on observed data, gradually refining its understanding of the parameter space [47]. By balancing exploration (searching for promising regions) and exploitation (leveraging known information to identify the best areas), Bayesian optimization aims to find the global optimum while minimizing the number of evaluations required. This method is particularly useful in hyperparameter tuning for complex models, where traditional grid search or random search approaches may be impractical due to computational costs.

At the heart of Bayesian optimization are Gaussian processes. A Gaussian process (GP) is

a statistical model representing a collection of random variables, any finite subset with a joint Gaussian distribution [47]. GPs are defined by a mean function and a covariance function, which capture prior beliefs about the underlying function being modeled and the correlations between different points in the input space. These special types of statistical models are key to estimating the underlying function that wants to be optimized. Through Bayesian inference, GPs can be updated with observed data, yielding posterior distributions that can inform predictions and lead to an optimized sampling for the Bayesian optimization algorithm.

Figure 5.7 shows an example of the evolution of the objective function during a Bayesian optimization procedure. In this case, the objective function is the normalized beam loss after the tune ramp illustrated by Fig. 5.5. It can be seen how the Bayesian optimizer finds solutions that effectively cancel out the beam loss from crossing the resonances. Nevertheless, given that this optimizer is built to find a global minimum, it will keep sampling other regions to ensure the best solution is not a local minimum. The color map of Fig. 5.7 shows how for some of these cases, the optimizer prioritizes exploration and drifts to some unknown region where the losses are high. For these cases, the underlying Gaussian process will learn that there is no worth in exploring these regions. Ultimately, the configuration with the least relative beam loss—the best configuration—is saved and kept as the optimum solution.

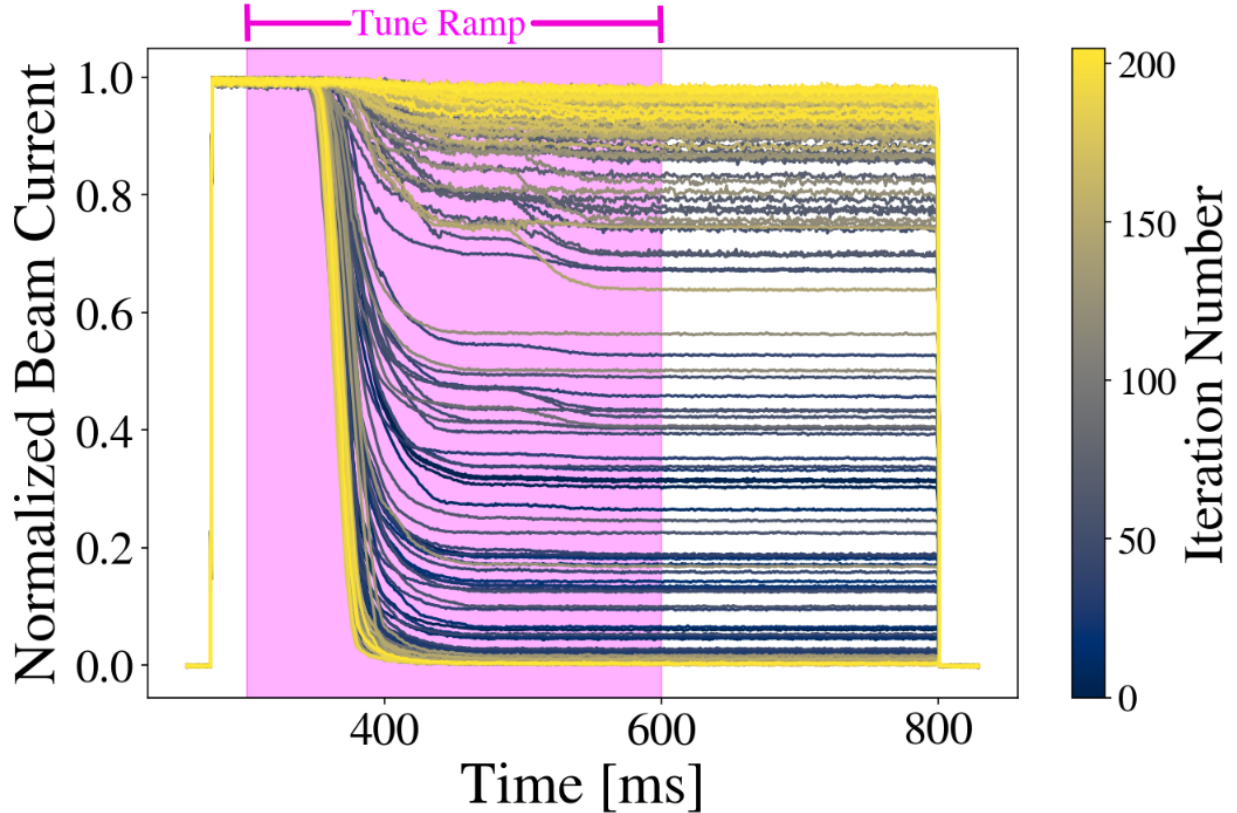


Figure 5.7 Normalized beam current plots for the Bayesian Optimization method done at Ring 1.

The bottom plot of Fig. 5.8 shows the explicit steps of each actor versus the number of iterations. Additionally, the top plot shows the trend of the objective function (relative beam loss) as the number of iterations increases. There are significant oscillations in the relative beam loss values, especially at the beginning, but a general trend towards minimization as the algorithm progresses through iterations. The early iterations reflect the exploration phase. BO is sampling points that give a broad understanding of the objective function's landscape. As iterations progress, there is a trend toward certain regions in the parameter space. This trend indicates a shift from exploration to exploitation, where the algorithm samples more from areas it believes to be near the optimum. The narrowing of actor current variability suggests a reduction in uncertainty about the location of the minimum beam loss. The GP model is becoming more informed and better trained. At the end of the optimization instance, such as the one shown in Fig. 5.8, the configuration that gave the smallest relative beam loss is saved. GeOFF sets the default configuration of the correctors

to these best values.

The corrector values for the best configurations are important to discuss from Fig. 5.8. It can be seen from Fig. 5.8 that some correctors land on the limit values, e.g., the limits for the normal sextupoles (XNO magnets) were [-50,50]. This behavior is especially apparent for the octupole correctors (ONO magnets), which have limits from -80 to 80, e.g., the magnet ONO816L1 is maxed out. Nevertheless, this was expected given that only two octupole correctors were used to correct four fourth-order lines, whereas one would need eight correctors to cancel out all the fourth-order RDTs fully. It is important to remind the reader that to implement these types of algorithms with several actors efficiently, the currents need to be normalized between [0,1] to ensure that all the data is on the same scale and improve the model performance. This procedure is done by GeOFF internally.

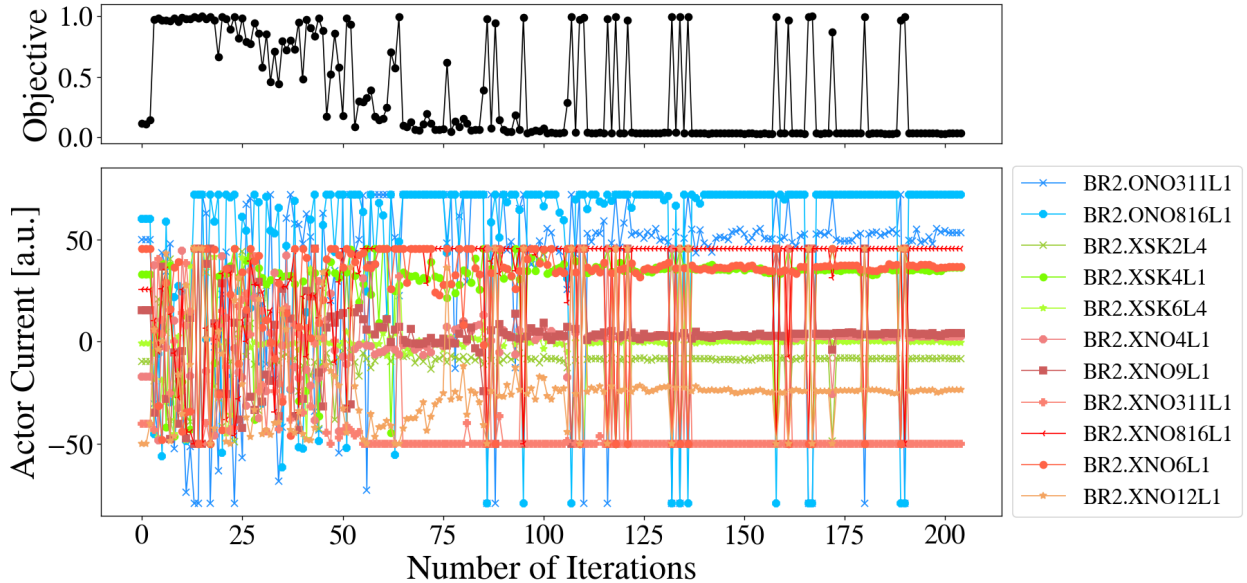


Figure 5.8 Summary for Bayesian optimization of resonance compensation applied to Ring 2 in the CERN PSB.

While Fig. 5.8 shows a relatively smooth Bayesian optimization instance for Ring 2, Figs. 5.9 and 5.10 show a different story for Ring 3. This particular optimization instance failed to find a configuration yielding a relative beam loss of less than 5% after 200 iterations—unacceptable for operation. This feature can be seen on the top plot of Fig. 5.9, which follows the objective function

across iterations. In order to find an acceptable configuration, the BO instance was performed again, but in this case, the initial Gaussian process was trained with the data from the previous incomplete run. The additional 350 iterations from this second instance are shown in Fig. 5.10. This second instance yielded configurations that led to acceptable values for the relative beam loss. Possible explanations for this hurdle include inadequate exploration of the parameter space, poor choice of the kernel for the Gaussian Process, poor choice of hyperparameters for this BO, and noise in the measurements.

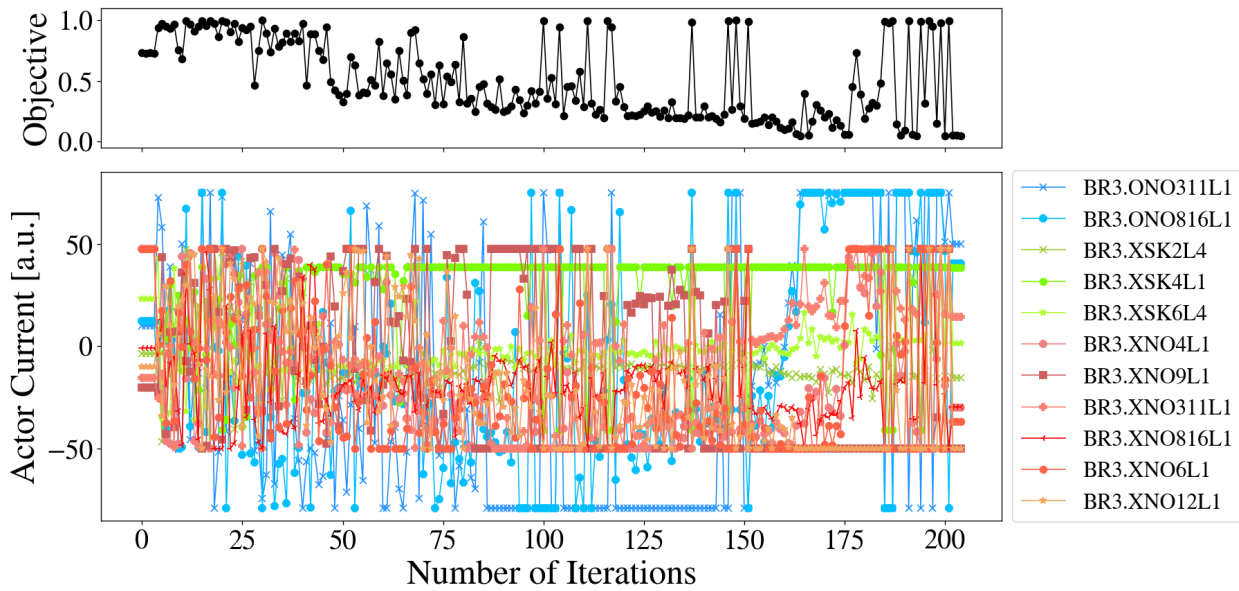


Figure 5.9 Summary for the first instance of Bayesian optimization towards resonance compensation applied to Ring 3 in the CERN PSB.

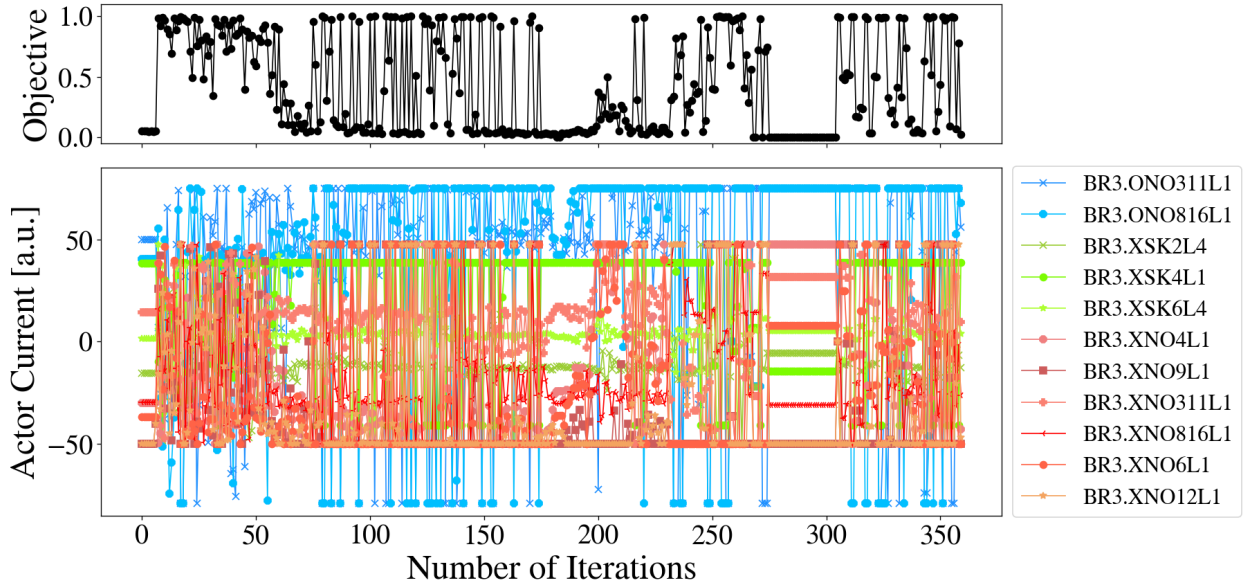


Figure 5.10 Summary for the second instance of Bayesian optimization of resonance compensation applied to Ring 3 in the CERN PSB. This second optimization instance was trained with the data from the first instance.

### 5.3.2 BOBYQA (Bound Optimization BY Quadratic Approximation)

BOBYQA, which stands for Bound Optimization BY Quadratic Approximation, is an optimization algorithm commonly used for solving constrained optimization problems [57]. Unlike gradient-based methods, BOBYQA belongs to the class of derivative-free optimization algorithms, making it suitable for scenarios where the objective function is not differentiable or computationally expensive to evaluate. The algorithm iteratively builds a quadratic approximation of the objective function within a trust region, a bounded area around the current solution. By iteratively updating the quadratic model and moving towards the predicted optimum within the trust region, BOBYQA efficiently explores the search space while minimizing the number of function evaluations. It employs a bound constraint strategy to ensure that the search remains within specified bounds. In this case, BOBYQA was used to solve the same optimization task from the last section but using a special type of beam at the PSB, the BCMS (Bunch Compression Merging and Splitting) beam.

The BCMS configuration is special given that it is produced with a smaller intensity (compared to the LHC-type beam from the previous section), and, hence, it has a smaller tune spread. For

this case, the injection tunes were changed from those shown in Fig. 5.5. The injection tunes were chosen to avoid one normal sextupole and one skew-sextupole resonance. This different configuration changes the optimum compensation currents compared to the Bayesian optimization results.

Similar to the exercise done in Fig. 5.7, Fig. 5.11 shows the relative beam loss profiles for an instance of the BOBYQA optimization done on Ring 1. As the iterations progress (transitioning from blue to yellow), the spread in beam current values decreases. This decrease suggests that the algorithm is refining its search based on the feedback from the objective function and moving towards regions of the parameter space that yield better optimization results. The later iterations, indicated by yellow lines, show beam current trajectories closer together. This convergence pattern signifies that the algorithm has likely identified a promising region in the parameter space and is now fine-tuning the parameters. It minimizes the variance between iterations, suggesting an approach toward a stable solution.

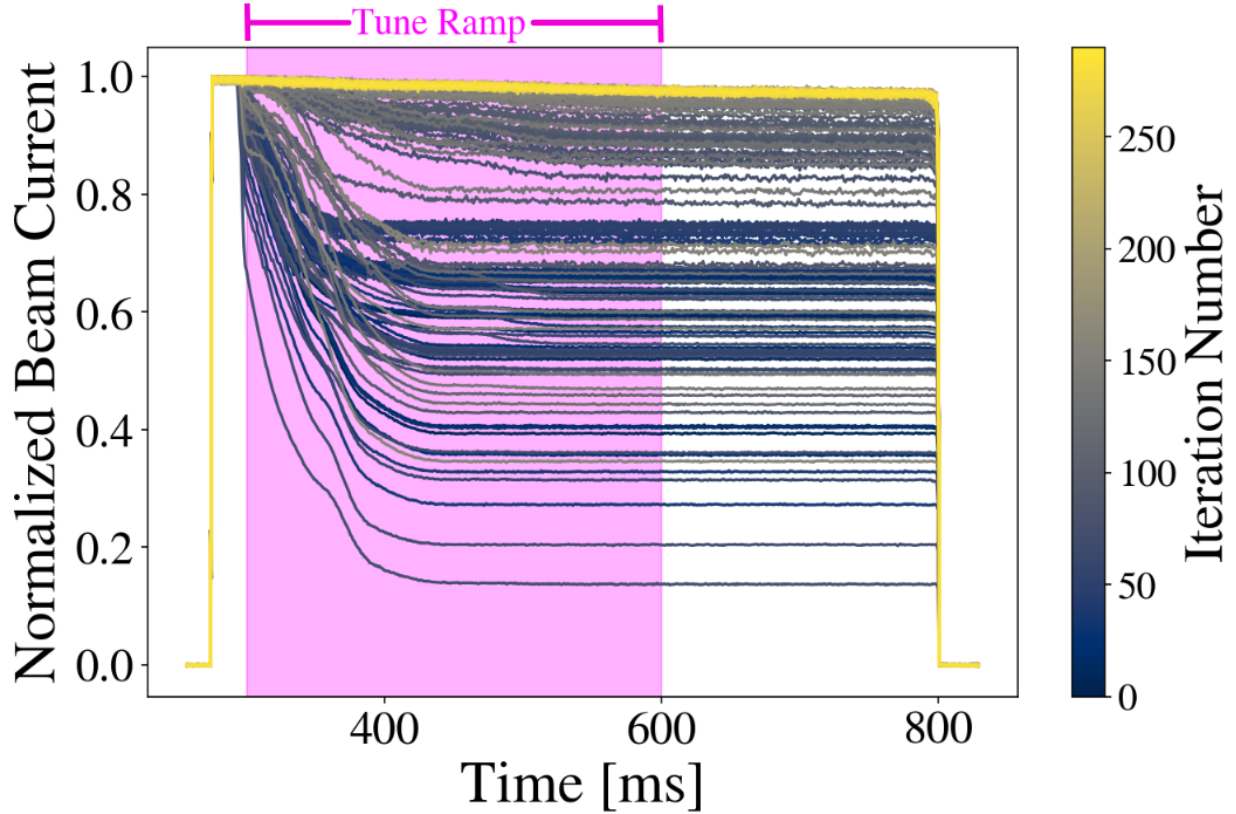


Figure 5.11 Normalized beam current plots for the BOBYQA method done at Ring 1.

Similar to the exercise done for the Bayesian optimization, Fig. 5.12 shows the evolution of the objective function and actor currents for a BOBYQA optimization instance on a BCMS beam. The initial values were set from the Bayesian optimization results for each ring, as discussed in the last section. The trend of the objective function (top plot) shows a general decrease in relative beam loss as the number of iterations increases, indicating that the optimization successfully finds parameters that result in less beam loss. The bottom graph illustrates the variation of the actor currents in arbitrary units across iterations. A unique line pattern and color distinguish each actor. Some correctors are kept at 0, given that they were unavailable for Ring 3. Implementing BOBYQA through GeOFF ensures the algorithm does not fall to a local minimum by bumping the settings to a new configuration once it falls to a stable one. That can be seen from the sudden oscillations in the objective function plot from Fig. 5.12.

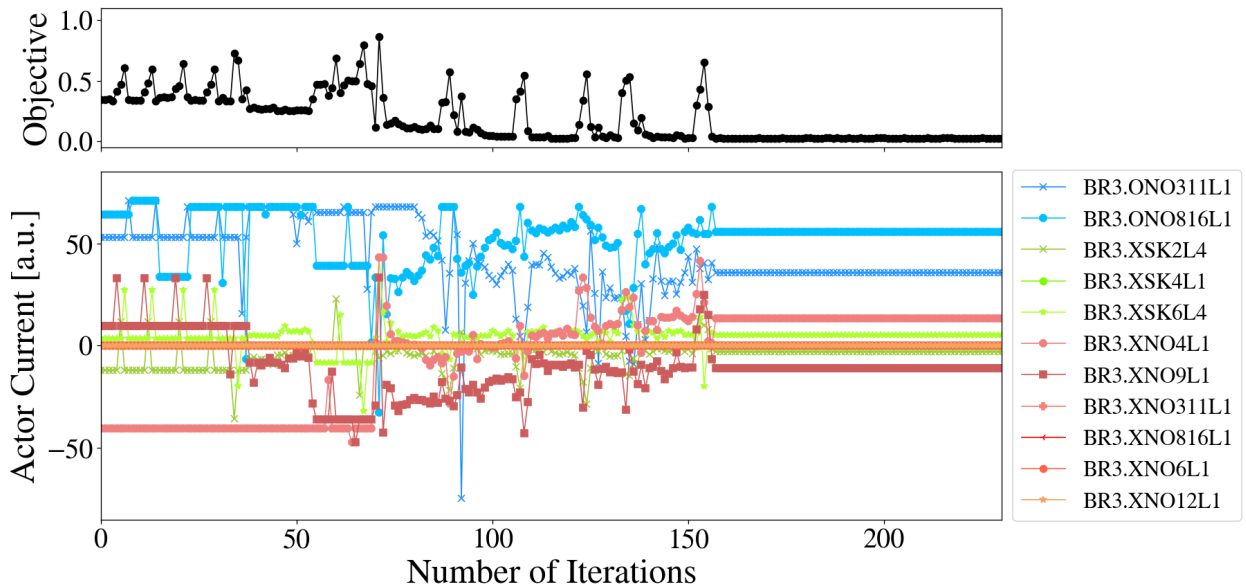


Figure 5.12 Summary for BOBYQA optimization of resonance compensation applied to Ring 3 in the CERN PSB for BCMS (Bunch Compression Merging and Splitting) beam.

Comparing this BOBYQA instance with the Bayesian optimization results, one can see that the exploration phase is much shorter and less broad for the BOBYQA instance. Similarly, the variation steps from BOBYQA in the actor currents are smaller than BO. This comparison is true because of the underlying mechanism used to estimate the objective function and its uncertainty. BOBYQA

uses deterministic local quadratic models, while Bayesian Optimization uses probabilistic models that measure uncertainty. BOBYQA is generally considered a local search technique, meaning it may be more prone to finding a local minimum than a global minimum. Hence, the initial point for BOBYQA holds more importance. Bayesian optimization is generally used for global optimization and is particularly strong in high-dimensional spaces or when function evaluations are very expensive. In summary, while both algorithms are powerful tools for optimization in accelerator physics problems, the choice between BOBYQA and Bayesian optimization will depend on the specific characteristics of the problem at hand, including the nature of the objective function, the presence of constraints, the dimensionality of the problem, practical considerations like the availability of computational and experimental resources, and, ultimately, availability of study/machine development time.

#### 5.4 Experimental Verification of Compensation

The whole point of the optimization algorithms explained in the last sections was to reduce the losses that show up in the loss map from Fig. 5.4. Figure 5.13 shows a new loss map with the best configurations found for each ring using the Bayesian optimization procedure on LHC-type beam. When comparing both loss maps, it is clear that with these new configurations, the loss maps have been cleared out of losses in the region of interest. The immediate losses are decreased by nearly one order of magnitude in the region occupied by the tune ramp. In particular, these new configurations largely suppress the third-order resonances that dominated the losses in Fig 5.4. Nevertheless, some resonance lines are still visible in the loss maps in Fig. 5.13, e.g.,  $Q_x - 2Q_y = -4$ . Given that these lines are not in the region of PSB operation, they are not of particular concern.

This chapter has shown a different approach to resonance compensation from the one presented in Ch. 4. Chapter 4 showed a physics-informed approach by minimizing the Recycler's RDTs and, ultimately, leading to the reduction of beam loss. On the other hand, the previous sections of this chapter showed an optimization-based approach, which can be considered a brute-force line of action. In this approach, all the actors are thrown into an optimization algorithm, which finds a numerical solution that minimizes the objective function. There is no physics involved, just

numerical optimization. In particular, BOBYQA's deterministic approach can quickly determine a solution when the accelerator operates near a resonance compensation optimum. With its probabilistic nature, Bayesian Optimization is better suited for exploring unknown or poorly understood operational regimes. All the previous approaches have been proven to work and yield satisfactory results in the context of resonance compensation. The choice between optimization-based and physics-informed approaches—or a combination thereof—depends on the specific context of the particle accelerator's operational goals, the available data, and the accuracy of the model.

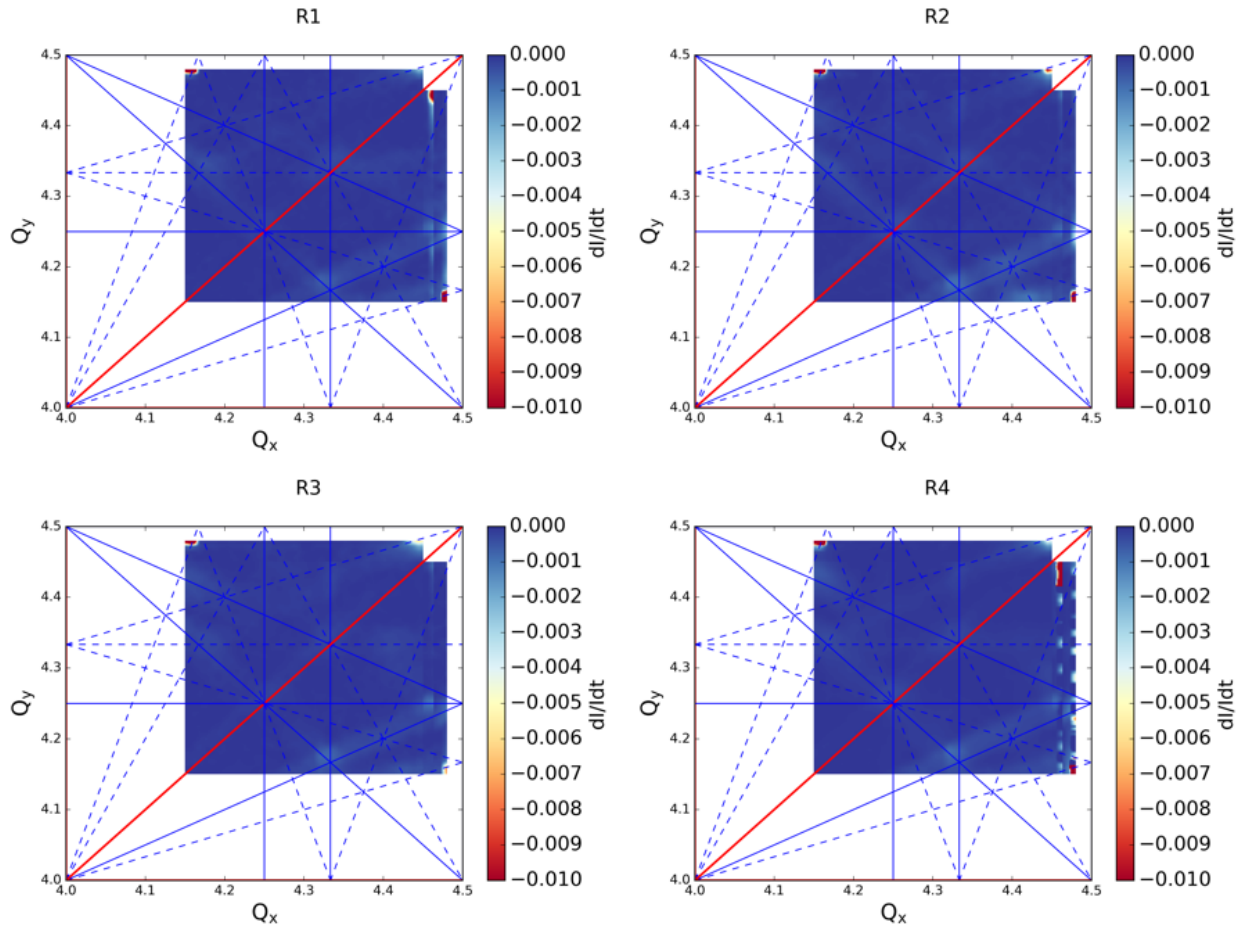


Figure 5.13 Dynamic loss maps for the four rings in the PS Booster with the best configuration from the Bayesian optimization of the resonance compensation. The plots are an average of scanning in 4 directions. Plot provided by F. Asvesta.

## CHAPTER 6

### HIGH INTENSITY STUDIES

#### 6.1 Space Charge Tune Shift

For this chapter, the focus goes back to the Fermilab Recycler Ring. All the experiments and measurements done in Ch. 4 were done at low intensities, i.e., less than  $1\text{e}10$  particles per bunch (ppb). Nevertheless, current operations and future operations under PIP-II objectives are done at higher intensities, i.e.,  $5\text{e}10$  ppb for current operations and  $8\text{e}10$  ppb for PIP-II. Therefore, it is relevant to explore resonance compensation at higher intensities.

An important parameter for high-intensity operation is the space charge tune shift. As mentioned in Ch. 2, the space charge tune shift is incoherent, meaning every particle will feel a different magnitude of this effect. Nevertheless, as shown in Figs. 2.5 and 3.8, this incoherent quantity will be contained within a necktie distribution. This necktie profile will define the space charge tune spread. When particles are in the beam core, they will feel the largest space charge potential, leading to the largest detuning and defining the edge of the necktie distribution.

Equation 2.78 showed a general way to calculate the space charge tune shift for particles at different amplitudes  $J_u$ . Nevertheless, this calculation is an involved process where the envelope equation has to be solved around the ring simultaneously as the Poisson equation, Eq. 2.65. Different approximations can be made in order to make rapid estimates of the space charge tune shift. Furthermore, a more important quantity is the maximum tune shift of the beam core particles. This tune shift will ultimately define the space charge tune spread. While this quantity can be calculated using PySCRDT [27], a cruder estimate can also be calculated. This estimate involves using a smooth-lattice approximation and circular beam pipe approximation, as used in Ref. [58].

With these simplifications, the space charge tune spread can be found as follows:

$$\Delta Q_{u,sc} = \frac{-3N_b r_0 RS}{4\sigma_z \beta_L \gamma_L^2 \varepsilon_{n,u,95\%}}, \quad (6.1)$$

where  $N_b$  is the number of protons per bunch,  $r_0 = 1.535 \times 10^{-18}$  meters is the classical radius of the

proton,  $\sigma_z = 0.5726$  meters is the bunch length,  $R = C/(2\pi)$  is the radius of the Recycler Ring with a circumference of  $C = 3319.4$  meters,  $S = 1.596$  is a geometrical factor of the bunch,  $\varepsilon_{n,u,95\%}$  is the 95% normalized emittance in the  $u$  plane, and  $(\beta_L, \gamma_L)$  are the longitudinal relativistic factors. The following section explores a method to measure this tune spread.

## 6.2 Measurement of Tune Spread

The  $3Q_x = 76$  line can be used to estimate the tune spread of the beam in the Recycler Ring. As seen before, when a dynamic tune ramp is set, and  $3Q_x$  is crossed, 95% of the beam is lost. By monitoring the tune ramp set into the tune trombone and assuming a linear tune ramp, one can correlate the tune instance when losses first appear with the tune spread. The tune distance between the losses first appearing and the  $3Q_x$  line is a crude estimate for the tune spread. This estimate is crude because particles in the beam core—particles with the largest tune shift—will start feeling the resonance and drift to higher amplitudes. The migration of particles from the beam core to the tails means that the tune shift will be smaller. There is a time delay (tune distance delay) between particles touching the resonance and particles being lost to the aperture. While this delay exists given the large strength of the  $3Q_x$  line, just hitting the resonance head-on can still give a crude estimate for the value of the tune spread and its behavior.

Figure 6.1 shows slices of loss maps at different intensities used to measure this tune spread. The top slice corresponds to an intensity of 2 Booster Turns (BTs), i.e., approximately  $0.6 \times 10^{10}$  particles per bunch for this experiment. The bottom slice corresponds to an intensity of 17 BTs, approximately  $6.0 \times 10^{10}$  ppb, close to the maximum intensity Booster can provide in a single batch. The important thing to note here is that as the intensity increases, the losses happen earlier in the tune ramp. This behavior can be correlated to the space charge tune spread using the location of the  $3Q_x$  line, which corresponds to where all the beam is lost. For example, for the bottom slice, the losses start at  $Q_x = 25.36$ , while all beam is lost at  $Q_x = 25.34$ . This feature means the space charge tune spread can be approximated to 0.02. Ultimately, Fig. 6.1 shows beams with space charge tune spreads that range from 0.005 to 0.02.

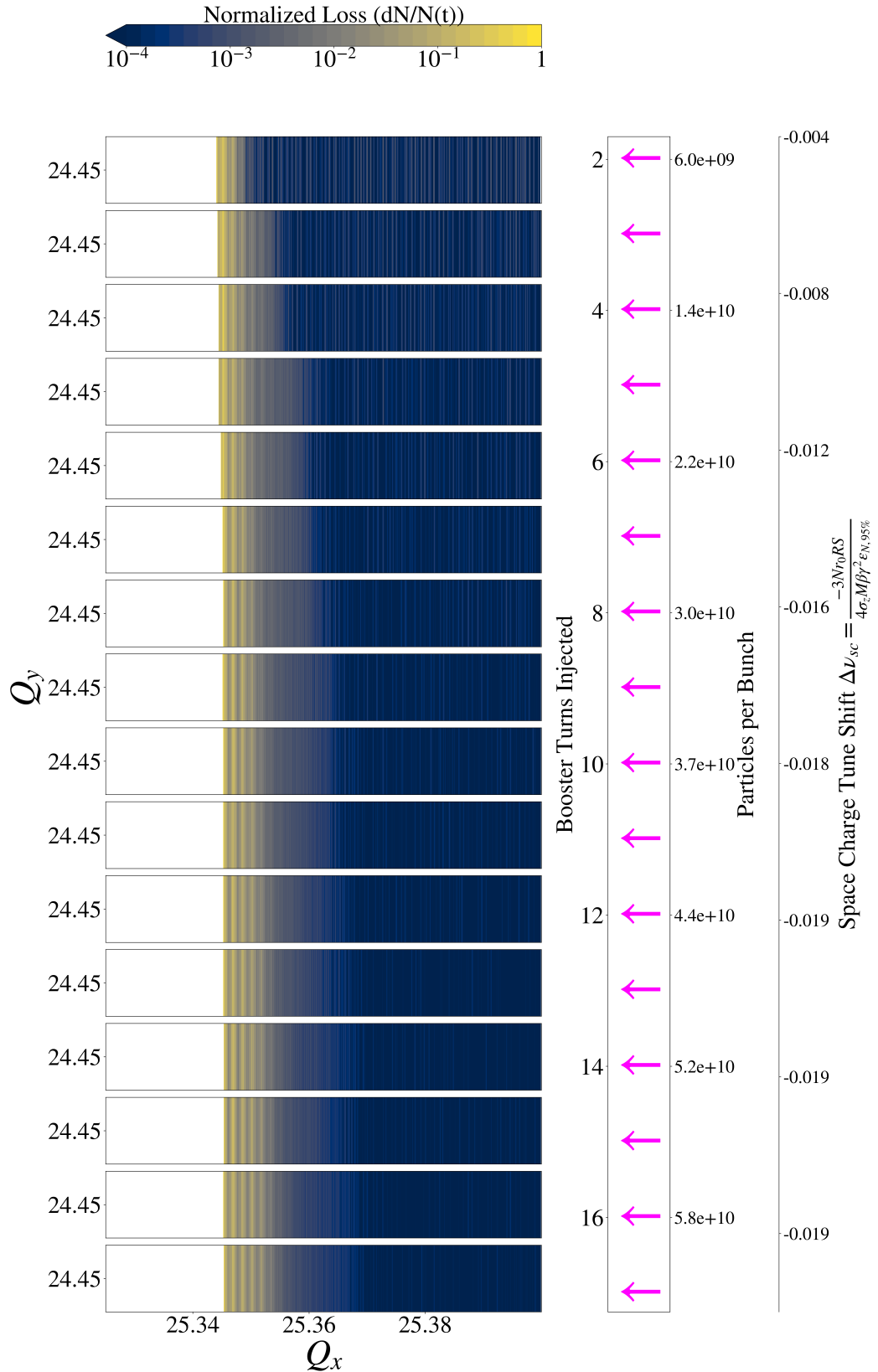


Figure 6.1 Dynamic loss strips at a fixed vertical set tune of  $Q_y = 24.45$  and on a range from  $Q_x = 25.39$  to  $Q_x = 25.32$  for different intensities.

Another thing to note from Fig. 6.1 is how the space charge tune spread tends to stabilize to a value of around 0.02 for intensities higher than 12 BTs or  $4.4 \times 10^{10}$ . This behavior is because the equilibrium emittance grows exponentially at higher intensities. Specifically, Ref. [40] shows how the beam emittance grows with intensity in the Recycler Ring. It looks at the first turn emittance coming from the Booster Ring, which will dictate the initial tune shift of the Recycler Ring. This study, combined with calculations of the space charge tune shift provided in Ref. [58], explains this behavior. The emittance grows exponentially as the beam intensity increases, leading to a saturated tune shift value. Figure 6.2 summarizes this behavior by plotting the measured tune spread from losses, the calculated tune spread from the first-turn abort emittance, and, finally, the first-turn abort 95% emittance on the right vertical axis.

The maximum tune spread shown in Figs. 6.1 and 6.2 is around 0.02, which only compares to 1/5 of the PIP-II projection. It is worth pointing out that these experiments are done for a single batch with no slip stacking. Therefore, with slip stacking and smaller beam emittance coming from Booster, space charge tune shifts in the RR of around 0.1 will be possible in the PIP-II era. For now, Fig. 6.2 shows how the tune spreads are not large enough to consider space-charge-dominated losses in the Recycler Ring relevant. All current losses are emittance-dominated, meaning the beam from Booster is hitting on the acceptance of the Recycler.

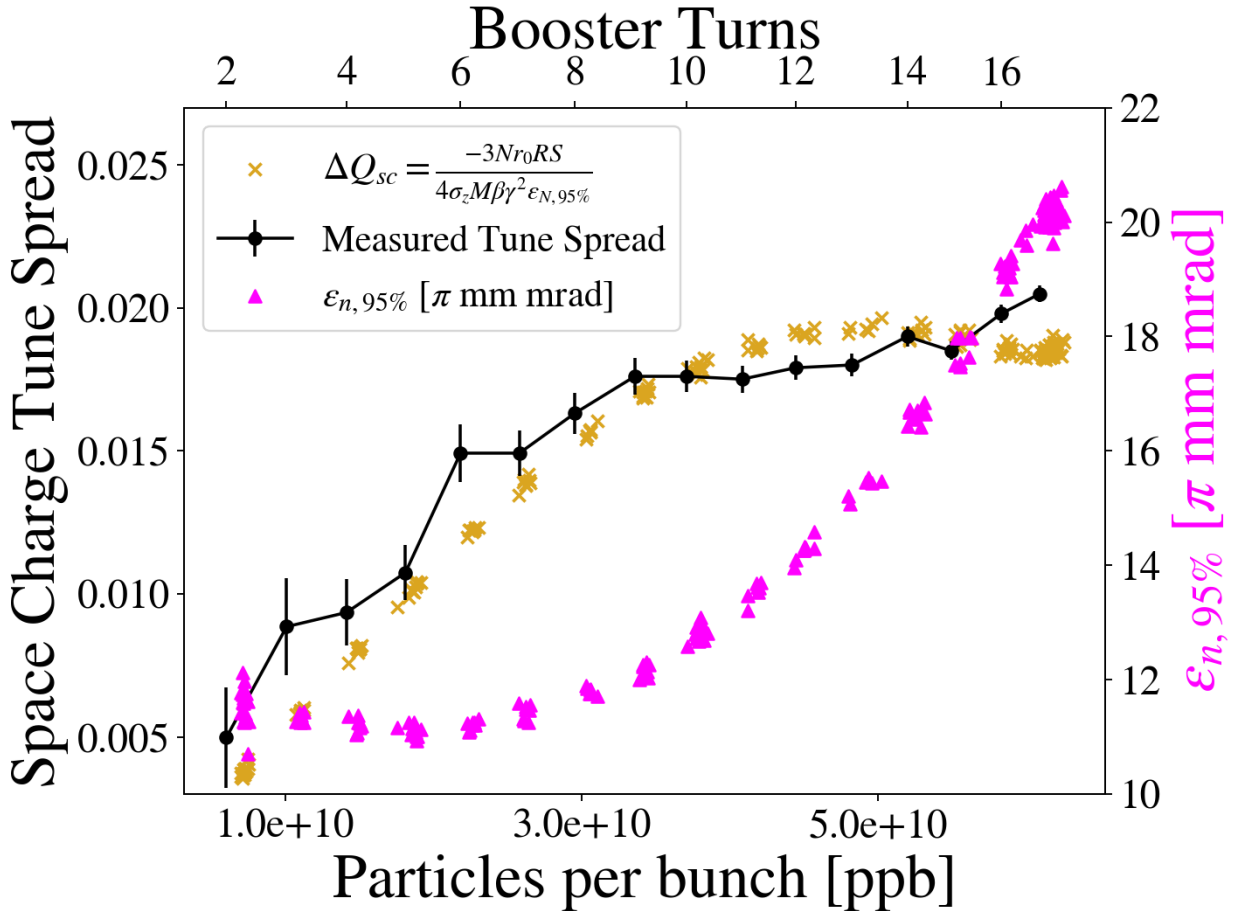


Figure 6.2 Tune spread measurements compared to tune spread calculations from horizontal emittances measured with multiwire data on first-turn abort beam.

### 6.3 Intensity-Dependent Effects and Non-Gaussian Beam Profiles

As mentioned in Sec. 3.5, the Ion Profile Monitor system is useful for extracting information about the transverse beam distribution. In particular, fitting a Gaussian distribution and extracting the scaling parameter or sigma  $\sigma_u$  can help characterize the transverse beam size. Such as it was done in Figs. 4.26 and 4.27, the beam size growth can be correlated to the beam loss in the machine. Nevertheless, one can go further and look into deviations from Gaussian distributions. Reference [59] looks into an application and explanation for these non-Gaussian profiles.

In particular, looking at how the beam tails populate with incoming particles from the beam core is interesting. This population happens when the space charge detuning is large enough for particles in the beam core to start touching resonance lines and, therefore, migrate to larger amplitudes, i.e.,

the beam tails. In order to quantify this effect, one can use q-Gaussian distributions [59, 60]. The definition for the probability density function  $f_q(x)$  of this distribution for a given  $q$  reads:

$$f_q(x) = \frac{1}{\sigma C_q \sqrt{2}} e_q \left( -\frac{x^2}{2\sigma^2} \right), \quad (6.2)$$

where  $\sigma$  is the scale parameter for the distribution and corresponds to the usual standard deviation of a Gaussian  $\sigma$  when  $q = 1$ . Additionally,  $C_q$  is the normalization constant. The auxiliary function  $e_q(x)$  is defined as:

$$e_q(x) = \begin{cases} \exp(x), & \text{if } q = 1 \\ (1 + (1 - q)x)^{\frac{1}{1-q}}, & \text{if } q \neq 1 \text{ and } (1 + (1 - q)x) > 0 \\ 0 & \text{if } q \neq 1 \text{ and } (1 + (1 - q)x) \leq 0 \end{cases}, \quad (6.3)$$

where the usual Gaussian distribution is recovered when  $q = 1$ . The distribution is said to have heavy tails when  $q > 1$  and light tails when  $q < 1$ . The usual Gaussian distribution is recovered when  $q = 1$ , and the usual Cauchy-Lorentzian distribution is recovered when  $q = 2$ . Figure 6.3 compares the probability density function for several values of  $q$ . It shows that tails can become more populated for larger values of  $q$  or under-populated for smaller values of  $q$ .

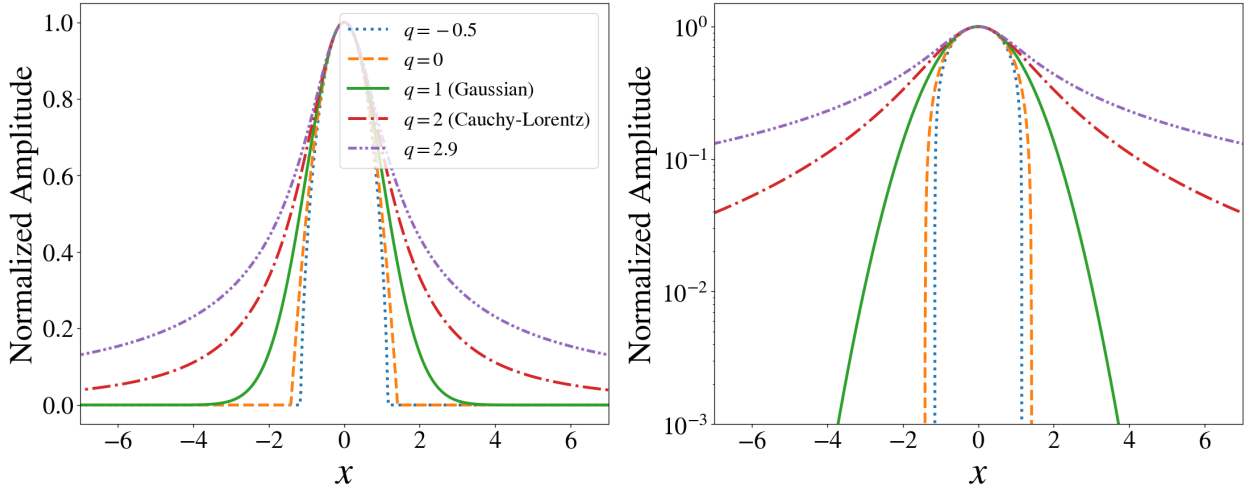


Figure 6.3 Several q-Gaussian distributions for different  $q$  parameters normalized to unit amplitude and with a scale parameter of  $\sigma = 1$ . The left plot uses linear scaling, and the right plot uses logarithmic scaling for the y-axis.

## 6.4 Static Tune Scans at Different Intensities

Section 4.5.2 showed how static tune scans are useful to verify if the resonance compensation scheme benefits the Recycler Ring. Nevertheless, these studies in Ch. 4 were done at low intensities. It is interesting to go to higher intensities and perform these static tune scans with a larger spread. Figure 6.4 shows a static tune scan crossing the  $3Q_x$  line with no compensation at an intensity of approximately  $4.5\text{e}10$  ppb (14 BTs) and a set vertical tune of  $Q_y = 24.44$ . The beam survival ratio drops dramatically after the horizontal tune of  $Q_x = 25.37$ , as the beam starts hitting the resonance line. At the same time, the beam size grows exponentially. If this plot is compared to the low-intensity case from Fig. 4.26, one can see that the losses start earlier at high intensities because the space charge tune spread is larger for this case. The beam size growth is also enhanced at high intensities. With large tune spreads, the beam survival ratio plots get more messy, given that the beam can operate simultaneously on top of multiple resonance lines and there is no stable beam. This process can be seen for horizontal tunes lower than 25.35 in Fig. 6.4. This fact is aggravated by the transverse dampers being on for this particular experiment, but they have been fine-tuned to operate in another tune region.

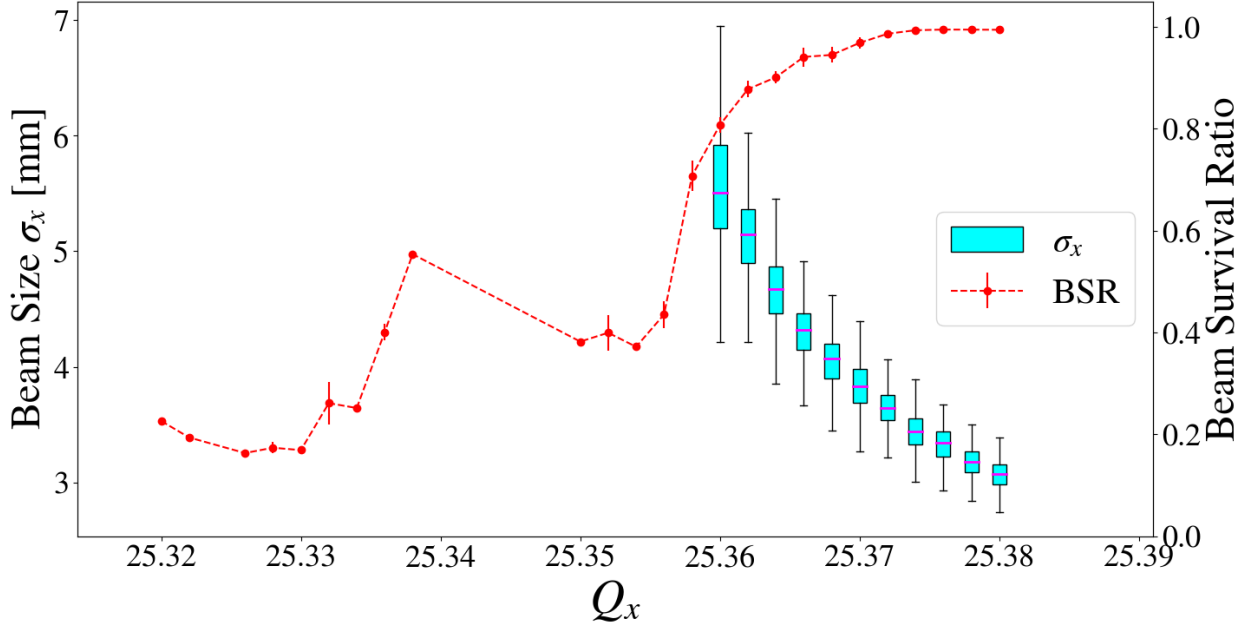


Figure 6.4 Static tune scan at an equivalent intensity of 14 Booster turns or approximately  $4.5\text{e}10$  ppb with no  $3Q_x$  compensation and transverse dampers on.

In Ch. 4, it was shown that when the  $3Q_x$  compensation was introduced, this helped improve the beam survival ratio close to and on top of the resonance line. Figures 6.5, 6.6 and 6.7 show what happens to the beam survival ratio and the beam size at different intensities during these static tune scans. It is worth pointing out that the transverse dampers were turned off for these particular measurements. A deeper discussion into the effect of transverse dampers is done in Sec. 6.5. Additionally, the color map of the scatter plot utilized for these figures represents the decimated turn number of the data point. Blue means that the data point happened earlier in the cycle—closer to injection—and yellow means it happened later in the cycle. A decimated number of turns of 1024 corresponds to 65000 real turns in the machine.

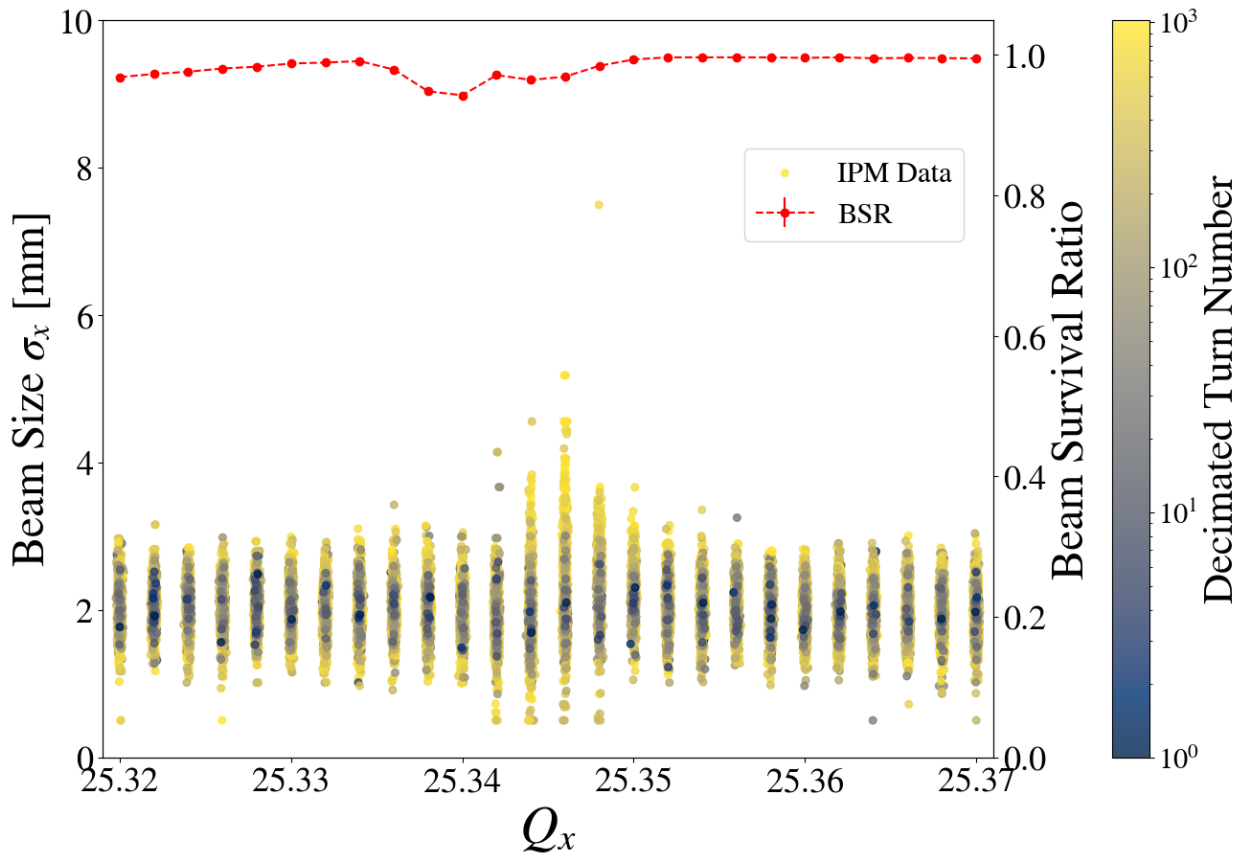


Figure 6.5 Static tune scan at an equivalent intensity of 2 Booster turns or approximately  $0.5\text{e}10$  ppb.

The data for Fig. 6.5 has already been shown in Figs. 4.27 and 4.28. Nevertheless, it is interesting to reference it again as the base case to compare against the high-intensity cases. In

particular, Fig. 6.5 shows the beam size and beam survival ratio as a function of horizontal tune and decimated turn number. When compensated for, more than 95% of the beam survives on top of the  $3Q_x$  resonance for 0.8 seconds. Nevertheless, beam size growth occurs when operating close to a set tune of  $Q_x = 25.345$ , where the  $3Q_x = 76$  resonance lies. This beam size growth does not happen immediately but after many turns, as seen by the yellow color on large beam sizes. Nevertheless, out of this particular region, there is no noticeable growth in beam size for other tune values.

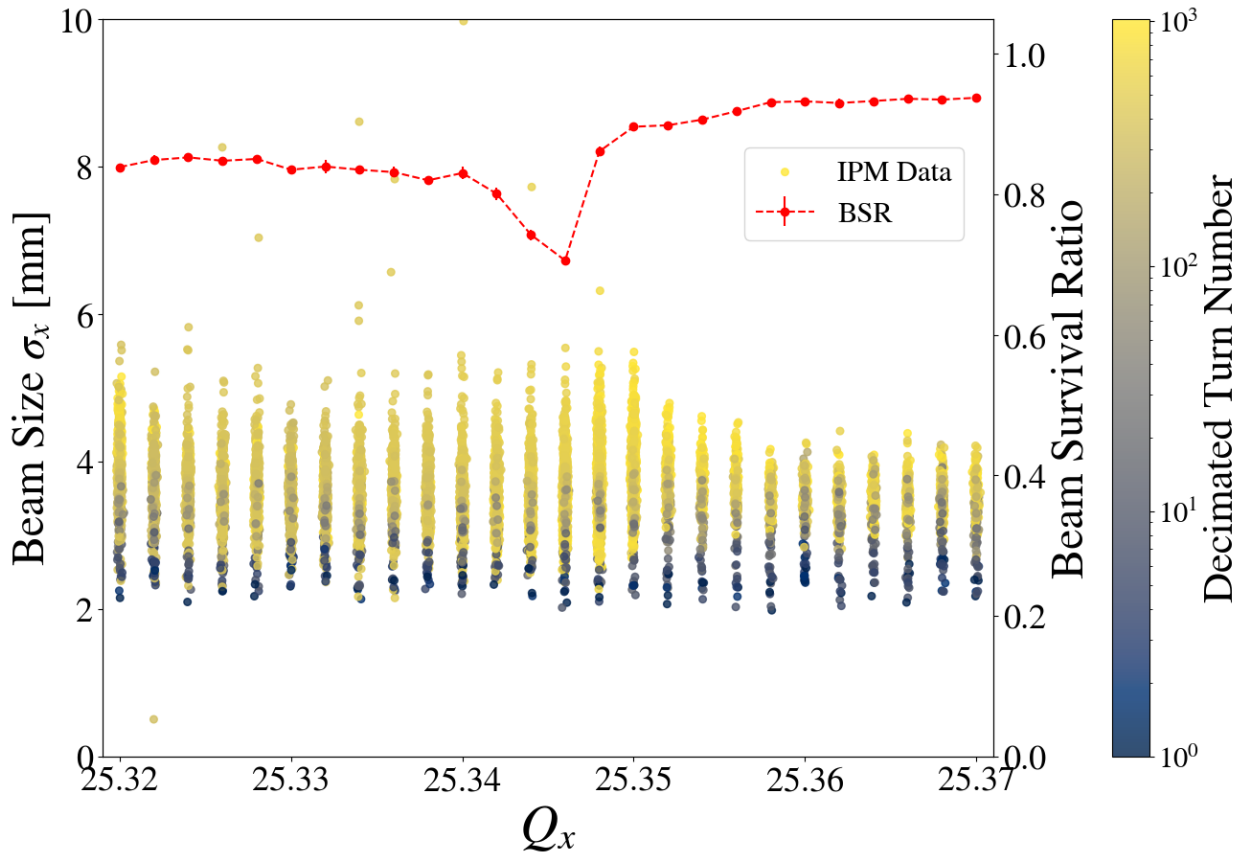


Figure 6.6 Static tune scan at an equivalent intensity of 8 Booster turns or approximately 3e10 ppb.

Figure 6.6 shows a static tune scan done at a higher intensity than the one in Fig. 6.5, i.e., 3e10 ppb, approximately six times larger. From Fig. 6.2, the corresponding space charge tune spread corresponds to approximately 0.015. Therefore, the beam size growth and losses should start earlier in the scan. This process can be seen in Fig. 6.6 compared to the low-intensity case. The other feature is the beam size growth at every tune value for the scan. The beam is injected and

undergoes some mechanism that leads to beam size growth. This mechanism is related to space charge, given that it is not present at low intensities. Furthermore, it can be seen that the beam size grows as a function of tune before leading to a big dip in the beam survival ratio. At this point, the beam size is large enough to hit the aperture of the Recycler. Ultimately, it is interesting to see the interplay between space charge, beam size growth, and the physical aperture of the machine.

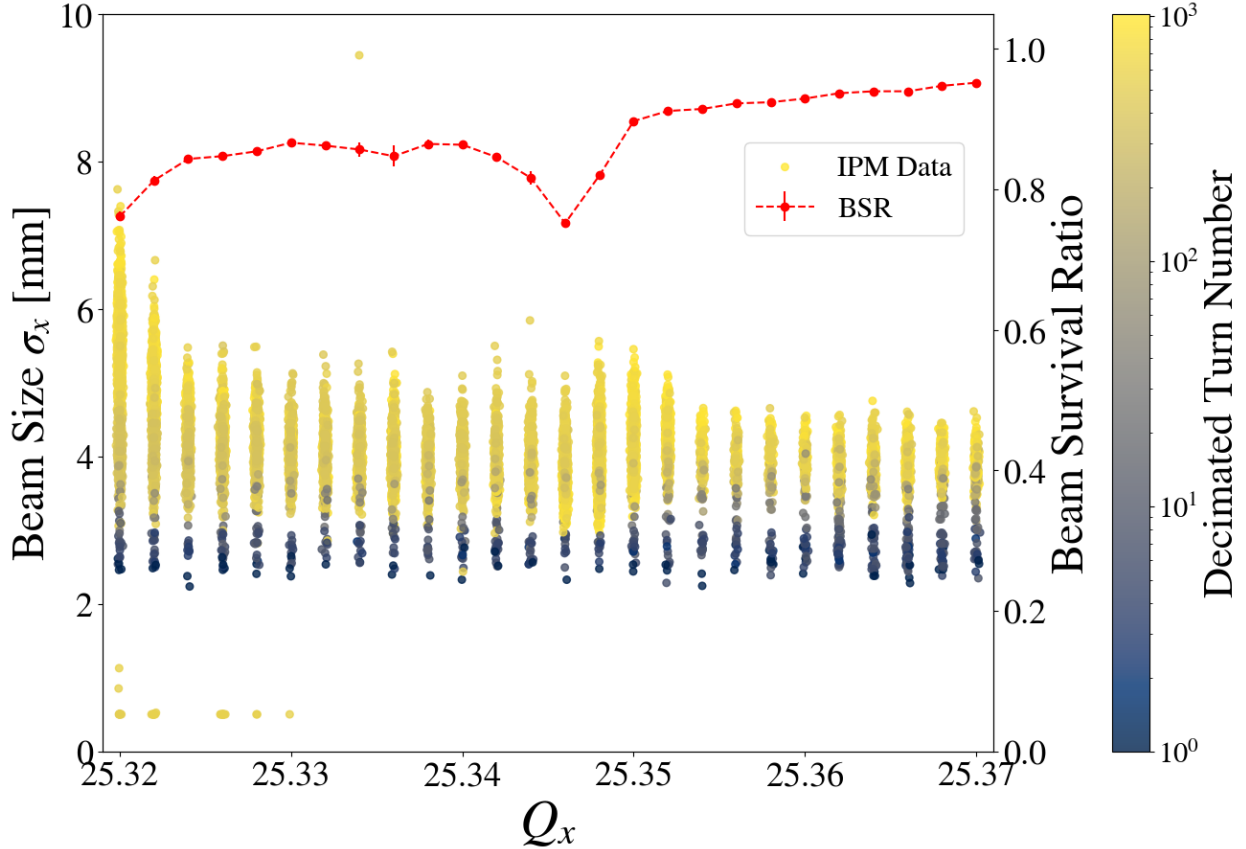


Figure 6.7 Static tune scan at an equivalent intensity of 14 Booster turns or approximately  $4.5 \times 10^{10}$  ppb.

Going almost to double the previous intensity, Fig. 6.7 shows a static tune scan done for intensity of  $5 \times 10^{10}$  ppb (particles per bunch). While the intensity is almost doubled, the tune spread only jumps to 0.02. This is because the emittance grows exponentially, and the tune spread saturates, as shown in Fig. 6.2. This small change in tune shift explains why Figs. 6.6 and 6.7 exhibit very similar behaviors. Nevertheless, a closer look shows that the injection beam size is slightly higher for this higher intensity, as expected from the emittance data shown in Fig. 6.2. Furthermore, the beam

survival ratio also decreases slightly.

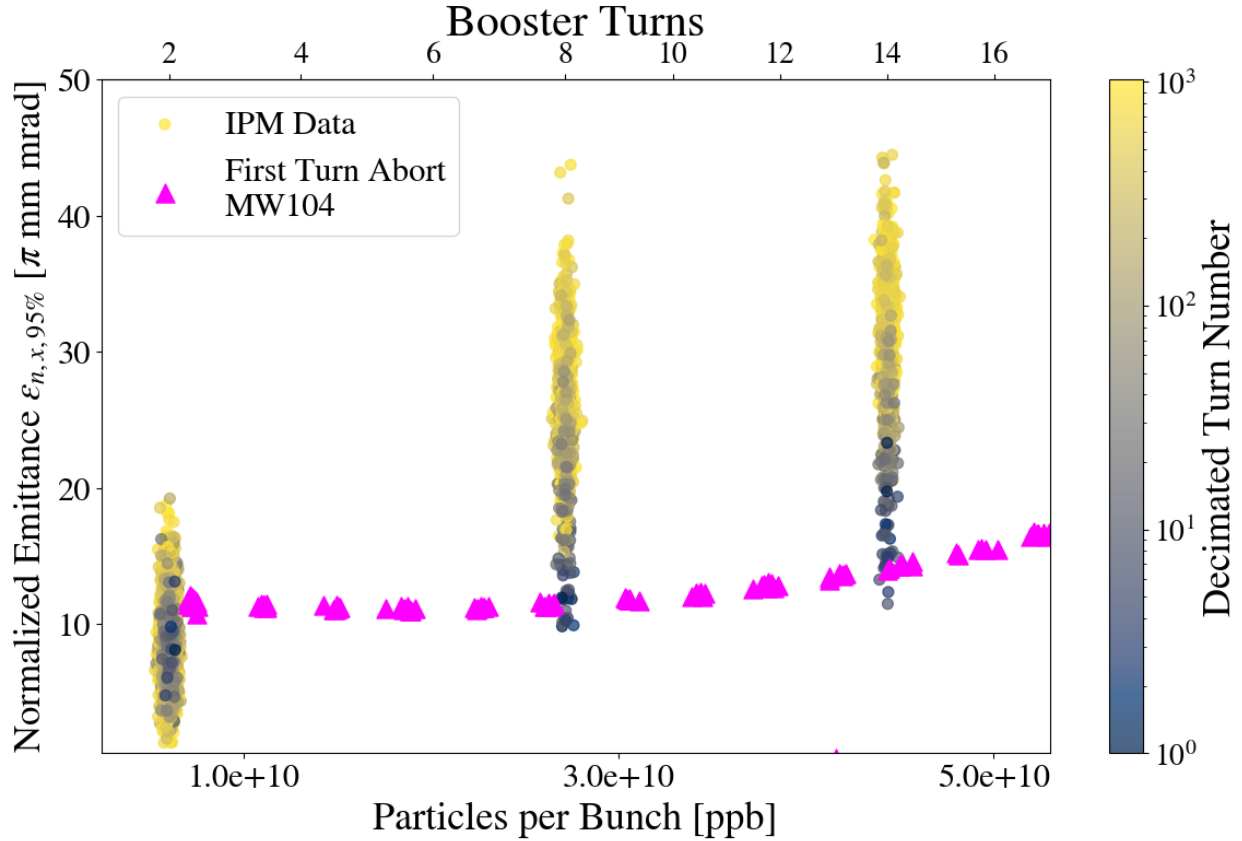


Figure 6.8 IPM data and multi-wire first turn abort data for  $Q_x = 25.370$  at different intensities.

Figure 6.8 compares emittance evolution data at these different intensities, as calculated from Eq. 4.40. A set tune of  $Q_x = 25.37$  was used for comparison. On this plot, first-turn-abort emittances are also plotted as fuchsia triangles. Ideally, these emittances calculated from multiwire data should correspond to those calculated from the IPM data. At low intensities, the emittances from the IPM data are centered around the multiwire value. At higher intensities, the IPM data for the initial number of turns coincides with the first-turn-abort data. Nevertheless, once injected, the beam emittance grows as it circulates many turns around the ring. This growth can ultimately lead to beam loss. Ultimately, the IPM system is a useful tool to characterize the effects of space charge. The multi-wires could not survive such high intensities for many turns.

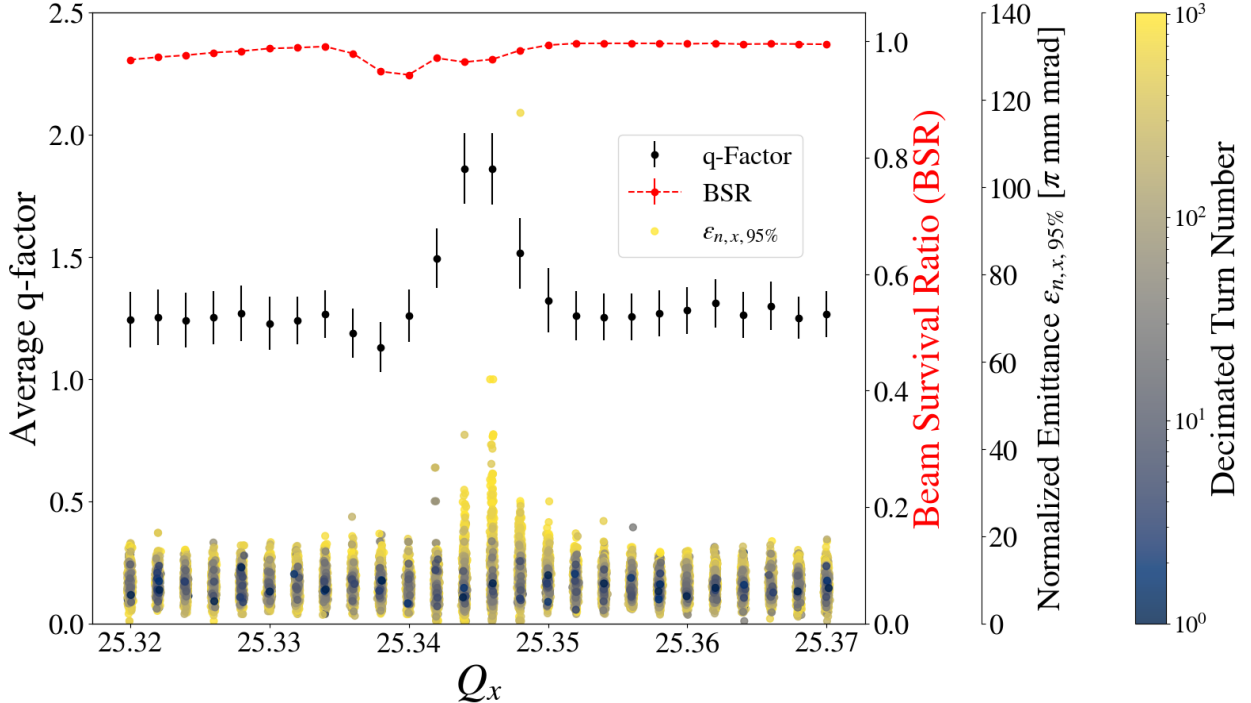


Figure 6.9 Static tune scan with beam survival ratio (BSR), average q-factor for the q-Gaussian fits, and normalized emittance at an equivalent intensity of 2 Booster turns or approximately 0.5e10 ppb.

Going further with IPM data, one can use q-Gaussian distributions to fit raw data from the beam profile. Using Eq. 6.2 to fit IPM data, the  $q$  parameter can be extracted to characterize the beam tails. Figures 6.9, 6.10, and 6.11 show a plot of the average  $q$  values at each tune for the different intensities. These  $q$  values should quantify how populated the tails are. A priori, one would not expect the tails to be underpopulated —all  $q$  values should be above 1,  $q > 1$ . Figures 6.9, 6.10, and 6.11 also plot the beam survival ratio and horizontal normalized emittance calculated from IPM data. Analyzing these quantities together helps one understand the loss mechanism that reduces the beam survival ratio.

For low intensities, it has been shown that the beam survival ratio improves when the  $3Q_x$  compensation is introduced. Figure 6.9 looks at how the small losses develop through the  $q$  factor. Close to  $Q_x = 25.345$ , the beam survival ratio drops slightly, while the normalized emittance and the average  $q$ -factor increase. In particular, the emittance increases after tens of thousands of turns in the Recycler. While the sextupole term that feeds the  $3Q_x$  line has been canceled, higher

order terms still feed the resonance line, causing emittance growth and beam loss in this region. Furthermore, the beam tails are populated in this region—the average  $q$  factor increases. Therefore, a combination of emittance growth and tail population from the resonance line explains the beam losses in this region. It is also worth pointing out that the average  $q$ -factor for these fits is slightly above 1.0, around 1.2, meaning that the raw data from the IPM system is not necessarily Gaussian. This feature is not present in Figs. 6.10 and 6.11, where  $q$  values before the resonance are centered around 1.0. It is worth reminding the reader that the IPM system is designed to operate at higher intensities.

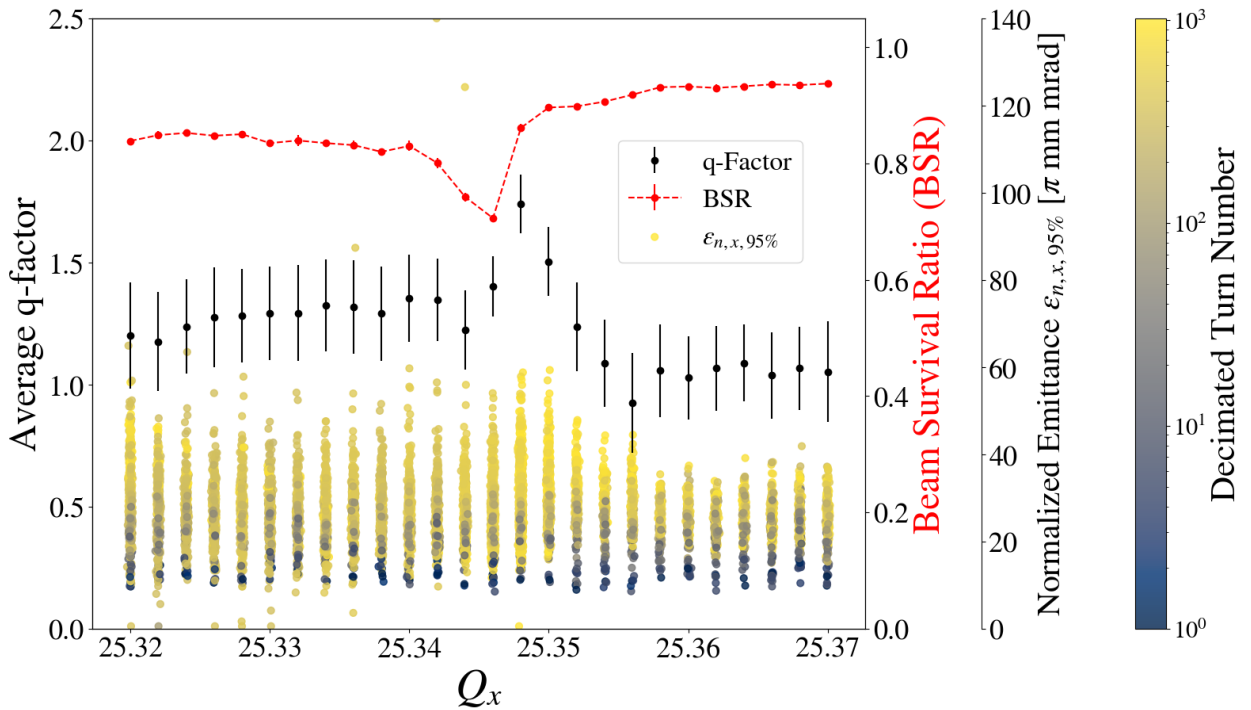


Figure 6.10 Static tune scan with beam survival ratio (BSR), average  $q$ -factor for the  $q$ -Gaussian fits, and normalized emittance at an equivalent intensity of 8 Booster turns or approximately  $3e10$  ppb.

According to Ref. [31], the transverse acceptance of the Recycler Ring is  $40 \pi \text{ mm mrad}$ . Taking a closer look into the emittance plot of Fig. 6.9, it can be seen that when the normalized emittance starts hitting this value, that is where losses start to appear. Figure 6.10 shows how at injection—for the first couple of initial turns of  $3e10$  ppb beam—the emittance is well below  $40 \pi \text{ mm mrad}$ . Nevertheless, as the beam circulates the Recycler Ring, the emittance grows close to the

acceptance of the machine. Given that this is the 95% emittance, there is still some beam outside this phase space region, particularly in the tails of the beam. This beam-tail population is why the beam survival ratio is not necessarily close to 1.0, even far from the resonance. This feature can also be seen at a higher intensity of 4.5e10 ppb beam through Fig. 6.11. While the injection emittance is slightly higher, the beam still grows to the machine's acceptance limit. While the beam emittance grows, the space charge tune spread in the Recycler is decreasing from its original value. Close to the remnants of the resonance, there is a small dip in the beam survival ratio caused by the increase in beam emittance. As long as the emittance comes close to the acceptance of the machine, there will be losses from beam tail particles hitting the machine's aperture.

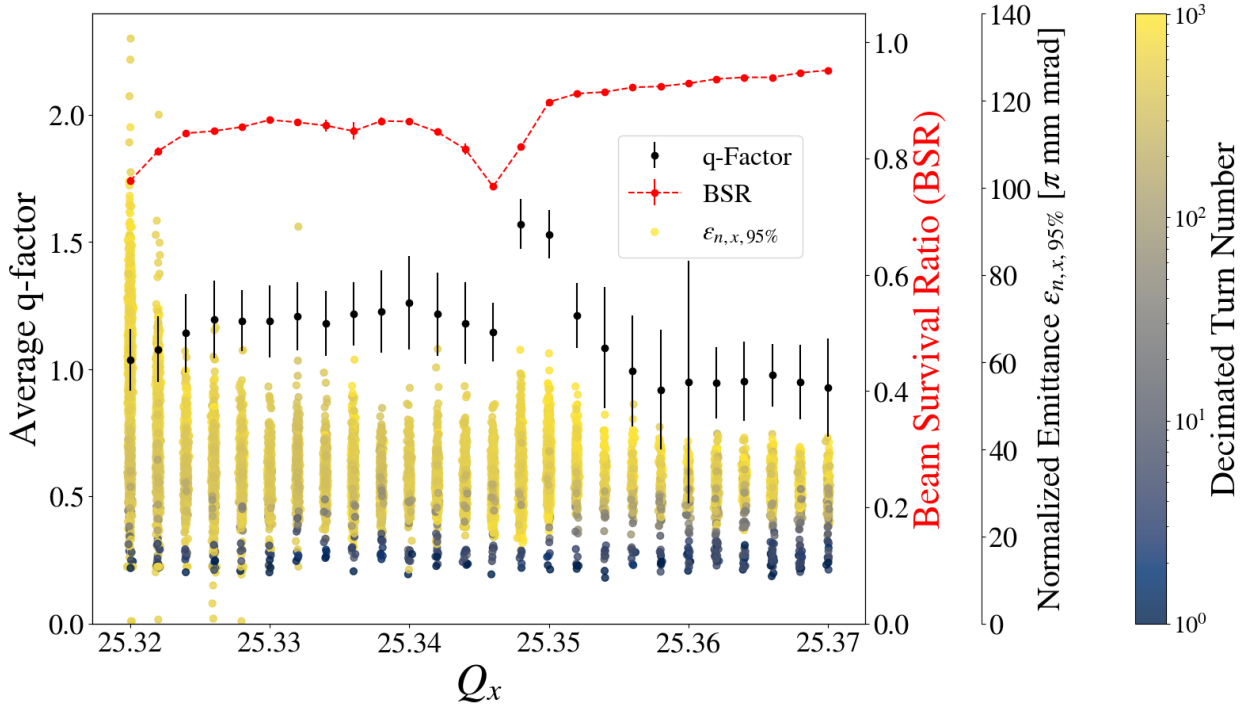


Figure 6.11 Static tune scan with beam survival ratio (BSR), average  $q$ -factor for the  $q$ -Gaussian fits, and normalized emittance at an equivalent intensity of 14 Booster turns or approximately 4.5e10 ppb.

The other important feature from the plots shown in Figs. 6.10 and 6.11 is the average  $q$ -factor behavior. Close to  $Q_x = 25.35$ , the average  $q$ -factor increases. This increase coincides with a dip in the beam survival ratio. Given that the beam is already on the acceptance limit, any increase in the beam tail population will inevitably lead to beam loss. This behavior is what Figs. 6.10 and

6.11 are essentially showing. A point is reached where there is no more space in the beam pipe to accommodate more beam tails. Therefore, any tail population mechanism will lead to beam loss. After this point, if the beam is wide enough, there are no beam tails, given that the beam pipe itself is collimating them, and everything is just the beam core. This is what happens for tunes left of the resonance line. Essentially, while emittance growth exists to the limits of the machine, any beam tail population mechanism will lead to beam loss.

## 6.5 Effect of Transverse Dampers

As hinted, the transverse dampers play a role in the quality of resonance compensation. The transverse dampers at the Recycler Ring are used to suppress the coupled bunch beam instability from the slip-stacked beam [61, 62]. This feedback system consists of a BPM pickup, input filters, digital signal processing, output amplifiers, and stripline kickers—one set for the horizontal direction and another for the vertical. The general knobs to tune the damper system include timing delays and gain settings. For the experiments shown previously, the dampers were completely turned off. Nevertheless, some experiments were done with the damper system turned on to observe its effect. Figures 6.12 and 6.13 show a comparison between static tune scans done at low intensity (0.5e10 ppb) with dampers on and off.

From just looking at Fig. 6.12, one could conclude that the resonance compensation does not fully work because only 60% of the beam survives close to the resonance. Nevertheless, these losses disappear when the dampers are turned off for Fig. 6.13. When the dampers are turned on, they increase beam size when the horizontal tunes are close to the resonance lines. This beam size growth leads to beam loss. The dampers seem to impact the quality of the resonance compensation directly. Nevertheless, the gain and phase of these dampers are not optimized to run too far away from the operational point of the Recycler Ring, i.e.,  $Q_x = 25.40$  and  $Q_y = 24.44$ . Once the set tune strays too far, the dampers will do more harm than good. This behavior occurs because this feedback system will amplify any beam size growth. Further quantifiable studies should be done to understand the interplay between dampers and resonance lines.

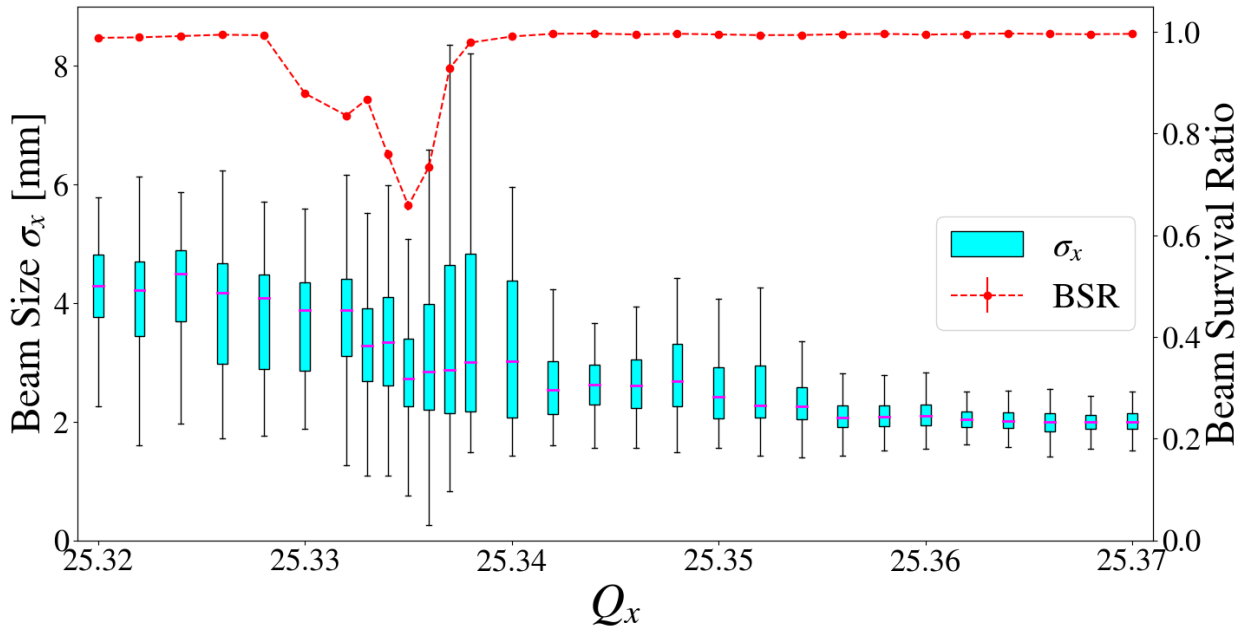


Figure 6.12 Static tune scan with beam survival ratio and IPM data box plots with  $3Q_x$  compensation, transverse dampers ON and 2 Booster Turns of equivalent intensity or approximately  $0.5\text{e}10$  ppb.

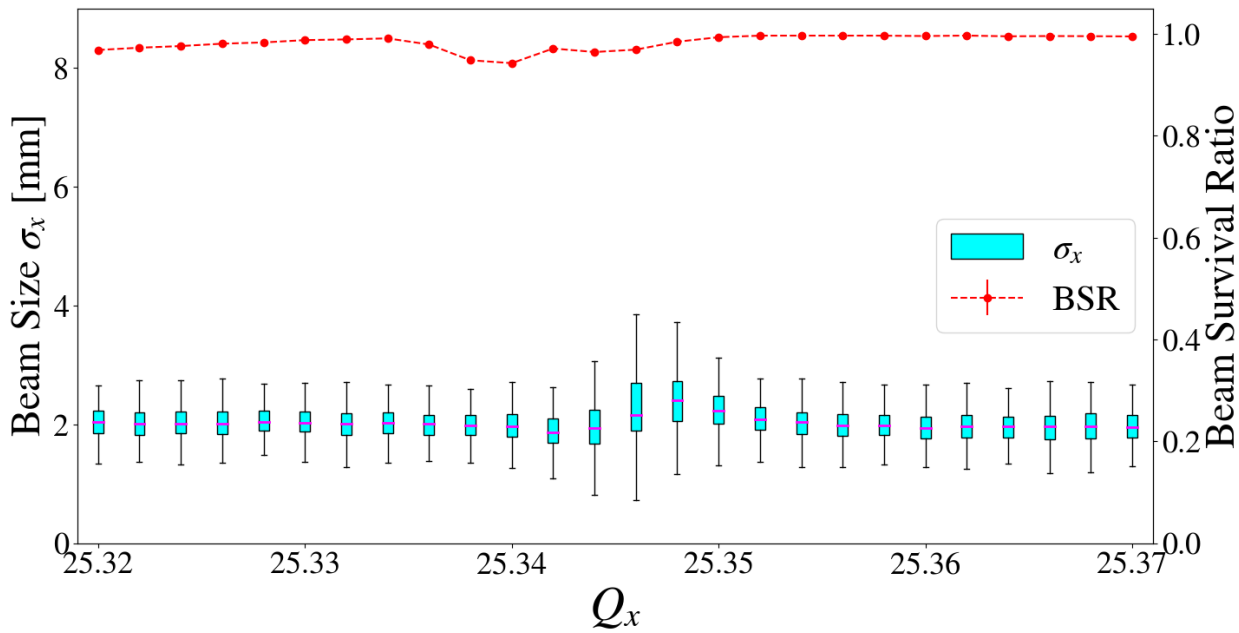


Figure 6.13 Static tune scan with beam survival ratio and IPM data box plots with  $3Q_x$  compensation, transverse dampers OFF and 2 Booster Turns of equivalent intensity or approximately  $0.5\text{e}10$  ppb.

Figure 6.14 looks at how the beam grows when the transverse dampers are activated. It can be seen that once the horizontal tune is set to the left of  $Q_x = 25.36$ , a beam size and emittance growth as a function of the number of turns starts to appear. This feature was absent in its dampers-off counterpart, as shown in Figs. 6.5 and 4.28. Figure 6.14 also shows how tails generate before the beam is lost to the beam pipe. Nevertheless, there seems to be a tune shift with respect to where the losses are now generated. It is also worth noting that the raw data from the IPM follows this trend from Fig. 4.28, where the average q-factor is around 1.2, meaning the data is not truly Gaussian at low intensities.

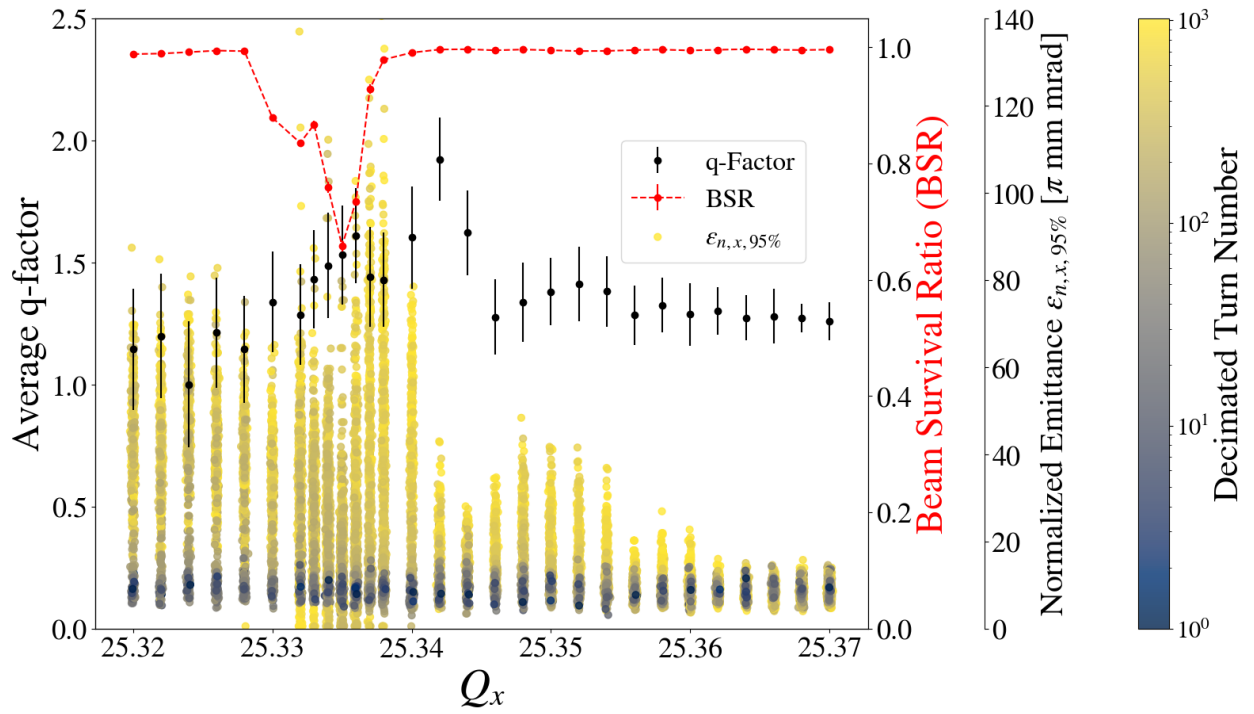


Figure 6.14 Static tune scan with beam survival ratio (BSR), average q-factor for the q-Gaussian fits, and normalized emittance with  $3Q_x$  compensation ON, transverse dampers ON and 2 Booster Turns of equivalent intensity or approximately  $0.5 \times 10^{10}$  ppb.

## CHAPTER 7

### CONCLUSIONS AND FUTURE WORK

The work shown throughout this document can also be found in Refs. [63–65]. This section reports on the conclusions and future work stemming from this thesis.

#### 7.1 Conclusions

##### 7.1.1 RDTs and Resonance Compensation in the Recycler Ring

The measurement and subsequent cancellation of RDTs were investigated in depth in Ch. 4. It was shown that third-order RDTs in the Recycler Ring could be measured and, afterward, canceled with the compensation sextupoles in place. Furthermore, optimization procedures have been developed to have this compensation with physics-informed input and/or numerical optimization. The Recycler Ring now has a resonance compensation method for when large tune spreads are present. Depending on the operational tunes, any setting in the compensation sextupoles from Fig. 4.23 can be enabled to cope with space-charge-induced losses. This advancement is a new operational feature that can be enabled on demand and will be especially useful for the PIP-II era.

##### 7.1.2 Physics-Informed vs. Optimization-Based Compensation

Chapters 4 and 5 showed two different approaches to the same problem of resonance compensation. The first one performed at the Fermilab Recycler Ring showed how to implement the response matrix approach, which can be traced to some underlying physics principles. On the other hand, Ch. 5 shows how to implement numerical optimization algorithms for compensating multiple resonance lines at the CERN PS Booster. Nevertheless, this last approach had no direct physics input. The distinction between a physics-informed approach and a numerical-optimization approach summarizes the differences between both chapters. The numerical-optimization approach is a brute-force one that can be carried out without any physics input—just by minimizing the losses in the resonance lines with the compensation sextupoles. Nevertheless, the physics-informed compensation can significantly enhance numerical optimization by constraining a window in parameter space where the solution lies. The best approach to resonance compensation is to use a hybrid

scheme where the response matrix method sets the limits in parameter space for subsequent and faster numerical optimization.

### 7.1.3 High-Intensity Resonance Compensation

For current operations of the Fermilab Accelerator Complex, the third-order resonance compensation scheme developed in this work will not have an effect on reducing losses in the Recycler Ring. The current tune spreads in the RR need to be larger for the third-order resonances to be especially harmful to operations. The beam coming out of Booster grows exponentially with the beam intensity, as shown in Fig. 6.2. Thus, saturating the tune spread at values close to 0.02—not particularly large. The losses in the Recycler Ring are purely emittance-dominated for current operations. They are not related to space charge effects. Nonetheless, the resonance compensation scheme still benefits operations at high intensities when close to the third-order resonances. The operational tune should remain as far as possible from these lines.

### 7.1.4 Transverse Dampers and High-Intensity Compensation

Section 6.5 showed how the transverse dampers have an effect on the resonance compensation scheme. Figure 7.1 reinforces this statement by showing the beam survival ratio at a high intensity of  $4.5\text{e}10$  ppb without compensation and dampers on (bare machine), with compensation and dampers on, and with compensation and dampers off. Ultimately, the dampers degrade the quality of the compensation. In particular, when turned off, the overall beam survival ratio increases. The configuration of the dampers—gain and phase of feedback—has been optimized away from the resonance lines. The damper settings will create beam size growth when the tunes are set close to the third-order resonance lines. They are not optimized to run in this region and will cause harmful effects on the beam, even with the resonance compensation scheme enabled.

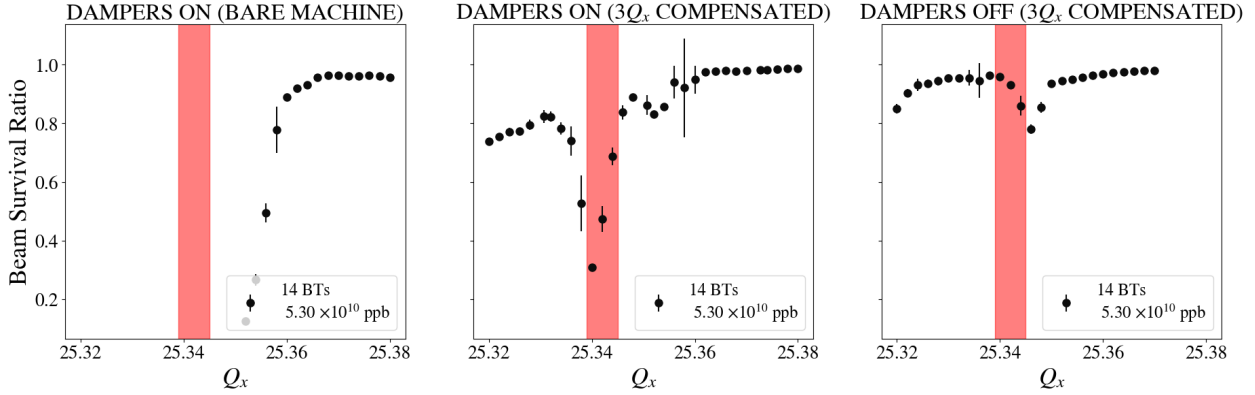


Figure 7.1 Transverse damper effect on resonance compensation for bare machine + dampers ON,  $3Q_x$  compensated + dampers ON, and  $3Q_x$  compensated + dampers OFF configuration. The red band corresponds to the  $3Q_x$  stop band at an intensity of 0.5 ppb with dampers ON.

## 7.2 Future Work

### 7.2.1 Verification of Newly-Installed Sextupoles

Section 4.3 explained the motivation behind installing additional sextupoles that would bring down the currents needed to compensate  $3Q_x = 76$  and  $Q_x + 2Q_y = 74$ . Subsequently, Sec. 4.6 explained the procedure used to pin down the new locations for two new compensation sextupoles. These sextupoles have been installed in the Recycler. There is still future work to be done regarding the commissioning and connection of the new 620 sextupoles. The sextupoles and their power supplies need to be interfaced with ACNET. Furthermore, the resonance compensation enhancement still needs to be verified by performing an RDT scan. Specifically, the response matrix coefficients corresponding to these new sextupoles must be measured and calculated. All of this, following the procedure outlined in Secs. 4.2 and 4.3. Figure 7.2 shows a picture of the newly installed sextupoles.



Figure 7.2 Newly installed compensation sextupoles in the 620 section.

### 7.2.2 Resonances and Transverse Dampers at High Intensities

It was shown in Sec. 6.5 that the transverse dampers in the Recycler Ring can interact with betatron resonance lines depending on their configuration. It would be interesting to perform experiments with the configuration of these dampers to characterize these effects fully, i.e., change the gain and phase of the dampers and study their effect on the strength of the resonance lines. Furthermore, it would also be interesting to use the dampers as anti-dampers to sustain betatron oscillations. With this configuration, one could perform tune measurements and evaluate this alternative method to measure RDTs. This tool would be similar to installing an AC dipole in the Recycler.

### **7.2.3 Effect of MI Ramp on RDTs**

The ultimate objective of this work is to characterize this resonance compensation scheme fully and incorporate it into high-intensity operations. Nevertheless, one additional factor has also been identified as playing a role in this effort. This factor stems from the fact that the Main Injector and the Recycler Ring share the same tunnel. It has been shown that the MI acceleration ramp changes the beam dynamics inside the RR. In particular, it introduces orbit distortions and tune shifts depending on the ramp position [66]. There is an ongoing effort to characterize any higher-order magnetic effect from the MI to RR, e.g., any sextupole term introduced by the MI acceleration ramp. The first results have shown that the compensation currents change depending on the location of the study event with respect to the MI acceleration ramp. Therefore, in the future, the resonance compensation described hereinabove should be modified to accommodate this effect to be fully operational.

### **7.2.4 Limits of Resonance Compensation**

Chapter 4, specifically Sec. 4.5.1, shows how individual and different pairs of resonance lines can be compensated in the Recycler Ring. Nevertheless, there is still a question of whether all four third-order resonance lines can be compensated simultaneously. While the previous thesis does not explicitly answer this question, it does contribute to a better understanding of the resonance lines. The source of these third-order resonance lines is a systematic third-order term in the permanent combined function magnets distributed around the ring. The fact that these are systematic does not allow for a straightforward compensation of the four resonance lines. Whenever more resonance lines try to be corrected, the currents in the compensation sextupoles increase. Therefore, one would need more compensation sextupoles around the ring at specific locations to bring down these currents, just as it was done in Sec. 4.6. Ultimately, the approach to follow would be to try to minimize the RDT fluctuations around the ring with the least amount of correctors. Such is the approach in Ref. [67]. Another thing to consider for future theoretical studies is that introducing too much sextupole in the ring might take the machine closer to an anharmonic regime. In this anharmonic regime, the resonances will not necessarily be straight lines but rather polynomial

curves resulting from motion in a 4D coupled phase space [68, 69]. These are considerations for future exploration of the limits of resonance compensation driven by systematic terms around the ring.

### 7.2.5 Space Charge RDTs

Equation 2.80 shows how the lattice elements and the space charge potential drive betatron resonances. It would be interesting to explore further how to measure space charge resonance driving terms (SCRDTs) and their effect on the operation of the Recycler Ring. Without taking into account any collective instabilities, the ultimate limit of the Recycler Ring will be dictated by how strong these third-order lines become in the space-charge-dominated regime. The current future of the Main Injector and Recycler Ring lies in the high-intensity beam. As the space charge potential grows for the Fermilab beams, it is important to quantify all effects from high-intensity operation—being SCRDTs one of them.

## BIBLIOGRAPHY

- [1] S Y Lee. *Accelerator Physics*. 3rd. WORLD SCIENTIFIC, 2011. doi: [10.1142/8335](https://doi.org/10.1142/8335). eprint: <https://www.worldscientific.com/doi/pdf/10.1142/8335>. url: <https://www.worldscientific.com/doi/abs/10.1142/8335>.
- [2] Lillian Hoddeson, Adrienne W. Kolb, and Catherine Westfall. *Fermilab: Physics, the Frontier, and Megascience*. University of Chicago Press, Dec. 2008. ISBN: 9780226346236. doi: [10.7208/chicago/9780226346250.001.0001](https://doi.org/10.7208/chicago/9780226346250.001.0001). url: <https://doi.org/10.7208/chicago/9780226346250.001.0001>.
- [3] David Griffiths. “Historical Introduction to the Elementary Particles”. In: *Introduction to Elementary Particles*. John Wiley and Sons, Ltd, 1987. Chap. 1, pp. 11–53. ISBN: 9783527618460. doi: <https://doi.org/10.1002/9783527618460.ch1>. url: <https://onlinelibrary.wiley.com/doi/abs/10.1002/9783527618460.ch1>.
- [4] Michigan State University. *Facility for Rare Isotope Beams at Michigan State University*. <https://frib.msu.edu/index.php>.
- [5] SLAC National Accelerator Laboratory. *The Stanford Linear Accelerator Center at SLAC*. <https://www.slac.stanford.edu/gen/grad/GradHandbook/slac.html>.
- [6] S. Holmes et al. “Accelerator physics at the Tevatron Collider: Introduction”. In: *Accelerator physics at the Tevatron Collider*. Ed. by Valery Lebedev and Vladimir Shiltsev. 2014, pp. 1–28. doi: [10.1007/978-1-4939-0885-1\\_1](https://doi.org/10.1007/978-1-4939-0885-1_1).
- [7] CERN. *The Large Hadron Collider (LHC)*. <https://home.cern/science/accelerators/large-hadron-collider>.
- [8] Ferdinand Willeke and J. Beebe-Wang. *Electron Ion Collider Conceptual Design Report 2021*. Tech. rep. BNL-221006-2021-FORE. Brookhaven National Laboratory, Feb. 2021. doi: [10.2172/1765663](https://doi.org/10.2172/1765663). url: <https://www.osti.gov/biblio/1765663>.
- [9] Étienne Forest. *Beam Dynamics: A New Attitude and Framework*. Vol. 8. The Physics and Technology of Particle and Photon Beams. Amsterdam, The Netherlands: Hardwood Academic / CRC Press, 1998. ISBN: 978-90-5702-574-7.
- [10] E Kako, P Pierini, and C.E. Reece. <https://cerncourier.com/a/teslas-high-gradient-march/>. Dec. 2020.
- [11] Reidar Hahn. *Fermilab*. File: <https://upload.wikimedia.org/wikipedia/commons/3/3f/Fermilab.jpg>. 2003. url: <https://en.wikipedia.org/wiki/File:Fermilab.jpg>.
- [12] Swapan Chattopadhyay and Joseph David Lykken. *Fermilab at 50*. WORLD SCIENTIFIC, 2017. doi: [10.1142/10637](https://doi.org/10.1142/10637). eprint: <https://www.worldscientific.com/>.

doi/pdf/10.1142/10637. URL: <https://www.worldscientific.com/doi/abs/10.1142/10637>.

- [13] P. Adamson et al. “The NuMI neutrino beam”. In: *Nuclear Instruments and Methods in Physics Research Section A: Accelerators, Spectrometers, Detectors and Associated Equipment* 806 (2016), pp. 279–306. ISSN: 0168-9002. DOI: <https://doi.org/10.1016/j.nima.2015.08.063>. URL: <https://www.sciencedirect.com/science/article/pii/S016890021501027X>.
- [14] R. Ainsworth et al. “High intensity operation using proton stacking in the Fermilab Recycler to deliver 700 kW of 120 GeV proton beam”. In: *Phys. Rev. Accel. Beams* 23 (12 Dec. 2020), p. 121002. DOI: [10.1103/PhysRevAccelBeams.23.121002](https://doi.org/10.1103/PhysRevAccelBeams.23.121002). URL: <https://link.aps.org/doi/10.1103/PhysRevAccelBeams.23.121002>.
- [15] Andrzej Wolski. *Beam Dynamics in High Energy Particle Accelerators*. 2nd. WORLD SCIENTIFIC, 2023. DOI: [10.1142/13333](https://doi.org/10.1142/13333). URL: <https://www.worldscientific.com/doi/abs/10.1142/13333>.
- [16] Helmut Wiedemann. *Resonances*. Cham: Springer International Publishing, 2015, pp. 539–564. ISBN: 978-3-319-18317-6. DOI: [10.1007/978-3-319-18317-6\\_16](https://doi.org/10.1007/978-3-319-18317-6_16). URL: [https://doi.org/10.1007/978-3-319-18317-6\\_16](https://doi.org/10.1007/978-3-319-18317-6_16).
- [17] T. Satogata. *Lecture Notes on Poisson Brackets and Lie Operators*. <https://toddsatogata.net/2011-USPAS/lieAlgebras.pdf>. Jan. 2008.
- [18] P. Urschutz. “Measurement and Compensation of Betatron Resonances at the CERN PS Booster Synchrotron”. PhD thesis. Vienna, Austria, 2004.
- [19] R. Tomas Garcia. “Direct Measurement of Resonance Driving Terms in the Super Proton Synchrotron (SPS) of CERN using Beam Position Monitors”. PhD thesis. Valencia, Spain, Jan. 2003.
- [20] Rüdiger Achilles and Andrea Bonfiglioli. “The early proofs of the theorem of Campbell, Baker, Hausdorff, and Dynkin”. In: *Archive for History of Exact Sciences* 66.3 (May 2012), pp. 295–358. DOI: [10.1007/s00407-012-0095-8](https://doi.org/10.1007/s00407-012-0095-8). URL: <https://doi.org/10.1007/s00407-012-0095-8>.
- [21] R Bartolini and F Schmidt. “Normal form via tracking or beam data”. In: *Part. Accel.* 59 (1998), pp. 93–106. URL: <https://cds.cern.ch/record/333077>.
- [22] *MAD-X: Methodical Accelerator Design*. <http://madx.web.cern.ch/madx>.
- [23] F. Asvesta. *PySCRDT*. 2019.

- [24] Kouichi Soutome and Hitoshi Tanaka. “Higher-order formulas of amplitude-dependent tune shift caused by a sextupole magnetic field distribution”. In: *Phys. Rev. Accel. Beams* 20 (6 June 2017), p. 064001. doi: [10.1103/PhysRevAccelBeams.20.064001](https://doi.org/10.1103/PhysRevAccelBeams.20.064001). url: <https://link.aps.org/doi/10.1103/PhysRevAccelBeams.20.064001>.
- [25] A. W. Chao. *Physics of collective beam instabilities in high-energy accelerators*. 1993. ISBN: 978-0-471-55184-3.
- [26] Ronald C Davidson and Hong Qin. *Physics of Intense Charged Particle Beams in High Energy Accelerators*. IMPERIAL COLLEGE PRESS CO-PUBLISHED WITH WORLD SCIENTIFIC PUBLISHING CO, 2001. doi: [10.1142/p250](https://doi.org/10.1142/p250). url: <https://www.worldscientific.com/doi/abs/10.1142/p250>.
- [27] F. Asvesta and H. Bartosik. *Resonance Driving Terms From Space Charge Potential*. Tech. rep. CERN-ACC-NOTE-2019-0046. <https://cds.cern.ch/record/2696190/files/CERN-ACC-NOTE-2019-0046.pdf>. 2019.
- [28] George B. Arfken, Hans J. Weber, and Frank E. Harris. “Chapter 10 - Green’s Functions”. In: *Mathematical Methods for Physicists (Seventh Edition)*. Ed. by George B. Arfken, Hans J. Weber, and Frank E. Harris. Seventh Edition. Boston: Academic Press, 2013, pp. 447–467. ISBN: 978-0-12-384654-9. doi: <https://doi.org/10.1016/B978-0-12-384654-9.00010-4>.
- [29] Gabriel Tellez Acosta. *Metodos Matematicos*. Ediciones Uniandes, 2022. ISBN: 9789587981827.
- [30] Oliver Dimon Kellogg. “Foundations of potential theory”. In: Springer, 1967, pp. 192–194.
- [31] G. Jackson. *The Fermilab recycler ring technical design report. Revision 1.2*. Tech. rep. FNAL-TM-1991ON: DE97051388; BR: KAHEP. Fermilab, Nov. 1996. doi: [10.2172/16029](https://doi.org/10.2172/16029). url: <https://www.osti.gov/biblio/16029>.
- [32] S. Nagaitsev. *Fermilab Antiproton source, Recycler ring and Main Injector*. Tech. rep. FERMILAB-FN-0957-AD. Fermilab, Mar. 2013. doi: [10.2172/1127965](https://doi.org/10.2172/1127965). url: <https://www.osti.gov/biblio/1127965>.
- [33] M. Ball et al. *The PIP-II Conceptual Design Report*. Tech. rep. FERMILAB-TM-2649-AD-APC1516858. Fermilab, Mar. 2017. doi: [10.2172/1346823](https://doi.org/10.2172/1346823). url: <https://www.osti.gov/biblio/1346823>.
- [34] Fermi National Accelerator Laboratory. *Deep Underground Neutrino Experiment*. url: <https://www.dunescience.org/>.
- [35] Fermilab Accelerator Division — Operations Department. *Concepts Rookie Book*.

- [36] M. Xiao. “Phase trombone program migration for the recycler ring at Fermilab.” In: *Proceedings of the IEEE Particle Accelerator Conference*. Vol. 2005. Proceedings of the Particle Accelerator Conference, PAC 2005. Fermilab, 2005, pp. 3135–3137 –3137.
- [37] R. Ainsworth et al. “High intensity space charge effects on slip stacked beam in the Fermilab Recycler”. In: *Phys. Rev. Accel. Beams* 22 (2 Feb. 2019), p. 020404. doi: [10.1103/PhysRevAccelBeams.22.020404](https://doi.org/10.1103/PhysRevAccelBeams.22.020404). URL: <https://link.aps.org/doi/10.1103/PhysRevAccelBeams.22.020404>.
- [38] R. Webber et al. “Fermilab Recycler Ring BPM Upgrade Based on Digital Receiver Technology”. In: *AIP Conference Proceedings* 732.1 (Nov. 2004), pp. 190–200. ISSN: 0094-243X. doi: [10.1063/1.1831147](https://doi.org/10.1063/1.1831147). URL: <https://doi.org/10.1063/1.1831147>.
- [39] J. Laskar. “The chaotic motion of the solar system: A numerical estimate of the size of the chaotic zones”. In: *Icarus* 88.2 (1990), pp. 266–291. ISSN: 0019-1035. doi: [https://doi.org/10.1016/0019-1035\(90\)90084-M](https://doi.org/10.1016/0019-1035(90)90084-M). URL: <https://www.sciencedirect.com/science/article/pii/001910359090084M>.
- [40] B. Babacan et al. *The Ionization Profile Monitors in the Recycler Ring*. 2023. arXiv: [2307.07017](https://arxiv.org/abs/2307.07017) [physics.acc-ph].
- [41] M. Xiao. *Recycler Chromaticities and End Shims for NOvA at Fermilab*. 2013. arXiv: [1301.6666](https://arxiv.org/abs/1301.6666) [physics.acc-ph].
- [42] *SUSSIX: A Computer Code for Frequency Analysis of Nonlinear Betatron Motion*.
- [43] R. E. Meller et al. “Decoherence of Kicked Beams”. In: (May 1987).
- [44] S. Y. Lee. “Decoherence of the Kicked Beams II”. in: (Feb. 1991).
- [45] Ming-Jen Yang. *Lattice function measurement with TBT BPM data*. Tech. rep. Fermilab, 1996. URL: <https://lss.fnal.gov/archive/test-tm/1000/fermilab-tm-1922.pdf>.
- [46] Robert Ainsworth et al. “Improvements to the Recycler/Main Injector to Deliver 850 kW+”. In: *JACoW* (Oct. 2022). doi: [10.18429/JACoW-NAPAC2022-WEYE3](https://doi.org/10.18429/JACoW-NAPAC2022-WEYE3). URL: <https://www.osti.gov/biblio/1909888>.
- [47] Roman Garnett. *Bayesian Optimization*. Cambridge University Press, 2023.
- [48] Fabienne Landua. *A graphic overview of all accelerators in operation at CERN*. URL: <https://cds.cern.ch/record/2813716?ln=en>.
- [49] H Damerau et al. *LHC Injectors Upgrade, Technical Design Report*. 2014. doi: [10.17181/CERN.7NHR.6HGC](https://doi.org/10.17181/CERN.7NHR.6HGC). URL: <https://cds.cern.ch/record/1976692>.

- [50] Wim Weterings et al. “The new injection region of the CERN PS Booster”. In: (2019), WEPMP039. doi: [10.18429/JACoW-IPAC2019-WEPMP039](https://doi.org/10.18429/JACoW-IPAC2019-WEPMP039). URL: <https://cds.cern.ch/record/2693918>.
- [51] Foteini Asvesta et al. “Resonance Compensation for High Intensity and High Brightness Beams in the CERN PSB”. in: *JACoW HB 2021* (2022), pp. 40–45. doi: [10.18429/JACoW-HB2021-MOP06](https://doi.org/10.18429/JACoW-HB2021-MOP06). URL: <https://cds.cern.ch/record/2841816>.
- [52] Tarsi Prebibaj. “Optimization of the High Brightness Beam Performance of the CERN PSB with H- Injection”. PhD thesis. Frankfurt am Main, Germany: 2023-06-22, June 2023.
- [53] Foteini Asvesta. “Space charge and lattice driven resonances at the CERN injectors”. PhD thesis. Natl. Tech. U., Athens, 2021.
- [54] F. Asvesta et al. “High Intensity Studies in the CERN Proton Synchrotron Booster”. In: *Proc. IPAC’22* (Bangkok, Thailand). International Particle Accelerator Conference 13. JACoW Publishing, Geneva, Switzerland, July 2022, WEPOTK011, pp. 2056–2059. ISBN: 978-3-95450-227-1. doi: [10.18429/JACoW-IPAC2022-WEPOTK011](https://doi.org/10.18429/JACoW-IPAC2022-WEPOTK011). URL: <https://jacow.org/ipac2022/papers/wepotk011.pdf>.
- [55] Simon Albright et al. “New Longitudinal Beam Production Methods in the CERN Proton Synchrotron Booster.” In: *JACoW IPAC ’21* (2021), pp. 4130–4133. doi: [10.18429/JACoW-IPAC2021-THPAB183](https://doi.org/10.18429/JACoW-IPAC2021-THPAB183). URL: <https://cds.cern.ch/record/2811646>.
- [56] *Generic Optimization Frontend and Framework (GeOFF)*. <https://gitlab.cern.ch/geoff/geoff-app>.
- [57] M. J. D. Powell. “The BOBYQA algorithm for bound constrained optimization without derivatives”. In: 2009. URL: <https://api.semanticscholar.org/CorpusID:2488733>.
- [58] S.Y. Zhang. *CALCULATION OF INCOHERENT SPACE CHARGE TUNE SPREAD*. tech. rep. Brookhaven National Laboratory, 1996. URL: <https://technotes.bnl.gov/PDF?publicationId=30778>.
- [59] S. Papadopoulou et al. “Impact of non-Gaussian beam profiles in the performance of hadron colliders”. In: *Phys. Rev. Accel. Beams* 23 (10 Oct. 2020), p. 101004. doi: [10.1103/PhysRevAccelBeams.23.101004](https://doi.org/10.1103/PhysRevAccelBeams.23.101004). URL: <https://link.aps.org/doi/10.1103/PhysRevAccelBeams.23.101004>.
- [60] Wikipedia contributors. *Q-Gaussian distribution — Wikipedia, The Free Encyclopedia*. [Online; accessed 19-March-2024]. 2023. URL: [https://en.wikipedia.org/w/index.php?title=Q-Gaussian\\_distribution&oldid=1177637416](https://en.wikipedia.org/w/index.php?title=Q-Gaussian_distribution&oldid=1177637416).

- [61] L. R. Prost et al. *Transverse Instabilities in the FERMILAB Recycler*. 2012. arXiv: 1201.4168 [physics.acc-ph].
- [62] Nathan Eddy et al. “Transverse Damper Using Diodes for Slip Stacking in the Fermilab Recycler”. In: *6th International Beam Instrumentation Conference*. 2018, TUPCF21. doi: 10.18429/JACoW-IBIC2017-TUPCF21.
- [63] C.E. Gonzalez-Ortiz, R. Ainsworth, and P.N. Ostroumov. “Third-Order Resonance Compensation at the FNAL Recycler Ring”. In: *Proc. IPAC’22* (Bangkok, Thailand). International Particle Accelerator Conference 13. JACoW Publishing, Geneva, Switzerland, July 2022, MOPOST050, pp. 195–198. ISBN: 978-3-95450-227-1. doi: 10.18429/JACoW-IPAC2022-MOPOST050. URL: <https://jacow.org/ipac2022/papers/mopost050.pdf>.
- [64] C.E. Gonzalez-Ortiz, R. Ainsworth, and P.N. Ostroumov. “Simultaneous Compensation of Third-Order Resonances at the FNAL Recycler Ring”. In: *Proc. IPAC’23* (Venice). IPAC’23 - 14th International Particle Accelerator Conference 14. JACoW Publishing, Geneva, Switzerland, May 2023, pp. 3328–3331. ISBN: 978-3-95450-231-8. doi: doi: 10.18429/jacow-ipac2023-wepl112. URL: <https://www.ipac23.org/preproc/pdf/WEPL112.pdf>.
- [65] C.E. Gonzalez-Ortiz, R. Ainsworth, and P.N. Ostroumov. “Compensation of Third-order Resonances in the High Intensity Regime”. In: *Proc. HB’23* (Geneva). HB’23. JACoW Publishing, Geneva, Switzerland, Oct. 2023. URL: <https://hb2023.vrws.de/papers/wea2i1.pdf>.
- [66] N. Chelidze, R. Ainsworth, and K.J. Hazelwood. “The Effect of the Main Injector Ramp on the Recycler”. In: *Proc. 5th Int. Particle Accel. Conf. (NAPAC’22)* (Albuquerque, NM, USA). International Particle Accelerator Conference 5. JACoW Publishing, Geneva, Switzerland, Oct. 2022, MOPA19, pp. 90–92. ISBN: 978-3-95450-232-5. doi: 10.18429/JACoW-NAPAC2022-MOPA19. URL: <https://jacow.org/napac2022/papers/mopa19.pdf>.
- [67] Bingfeng Wei et al. “Minimizing the fluctuation of resonance driving terms in dynamic aperture optimization”. In: *Phys. Rev. Accel. Beams* 26 (8 Aug. 2023), p. 084001. doi: 10.1103/PhysRevAccelBeams.26.084001. URL: <https://link.aps.org/doi/10.1103/PhysRevAccelBeams.26.084001>.
- [68] H. Bartosik, G. Franchetti, and F. Schmidt. “Observation of fixed lines induced by a nonlinear resonance in the CERN Super Proton Synchrotron”. In: *Nature Physics* (2024).
- [69] Ezio Todesco. “Analysis of resonant structures of 4D symplectic mappings, using normal forms”. In: *Phys. Rev. E* 50.6 (1994), pp. 4298–4301. doi: 10.1103/PhysRevE.50.R4298. URL: <https://cds.cern.ch/record/262010>.